

# **Generation of Activated Carbon from Spent Coffee Grounds: Process Optimization, Kinetics and CO<sub>2</sub> Capture**

A Thesis Submitted to the  
College of Graduate and Postdoctoral Studies  
In Partial Fulfilment of the Requirements  
For the Degree of Doctor of Philosophy  
In the Department of Chemical and Biological Engineering  
University of Saskatchewan  
Saskatoon

By

**ALIVIA MUKHERJEE**

© Copyright Alivia Mukherjee, September 2022. All rights reserved.

Unless otherwise noted, copyright of the material in this thesis belongs to the author

---

## **PERMISSION TO USE**

In presenting this thesis/dissertation in partial fulfilment of the requirements for a Postgraduate degree from the University of Saskatchewan, I agree that the Libraries of this University may make it freely available for inspection. I further agree that permission for copying of this thesis/dissertation in any manner, in whole or in part, for scholarly purposes may be granted by Professor Ajay Kumar Dalai, who supervised my thesis/dissertation work or, in their absence, by the Head of the Department or the Dean of the College in which my thesis work was done. It is understood that any copying or publication, or use of this thesis/dissertation or parts thereof for financial gain shall not be allowed without my written permission. It is also understood that due recognition shall be given to me and to the University of Saskatchewan in any scholarly use which may be made of any material in my thesis/dissertation.

Requests for permission to copy or to make other uses of materials in this thesis/dissertation in whole or part should be addressed to:

Head of the Department of Chemical and Biological Engineering

57 Campus Drive

University of Saskatchewan

Saskatoon, Saskatchewan S7N 5A9 Canada

Or

Dean

College of Graduate and Postdoctoral Studies

University of Saskatchewan

116 Thorvaldson Building, 110 Science Place

Saskatoon, Saskatchewan S7N 5C9, Canada.

## ABSTRACT

Carbon dioxide capture technology is gaining popularity owing to the environmental concerns and deterioration of the climatic conditions related to atmospheric CO<sub>2</sub> emission. Of the candidate, lignocellulose biomass samples have been considered a promising source for producing carbon-based adsorbents that can be utilized to capture recalcitrant CO<sub>2</sub> from the post-combustion capture facility. Recently, the removal of CO<sub>2</sub> using activated carbon (AC) has gained immense attention owing to its environmentally friendly characteristics and low cost for synthesis. Conversely, with the increasing population, the demand for coffee consumption is also accelerating. The generation of coffee residues owing to the increased consumption would increase and demand effective utilization and management. The research primarily focused on utilizing the waste generated from the coffee industries, namely spent coffee grounds (SCG) and coffee husk (CH), to evaluate their potential in synthesizing carbon-based adsorbents for CO<sub>2</sub> removal under the post-combustion capture scenario and propose a cost-effective AC production strategy from lignocellulose-based biomass. This study focused on investigating the influence of different thermochemical conversion techniques on the physicochemical properties of biochar, followed by assessing the impact of activation parameters and the effect of deep eutectic solvent (DES) on the physicochemical characteristics of AC and the removal of CO<sub>2</sub>. Moreover, a techno-economic analysis was performed to assess the economic feasibility of biomass conversion technology used to synthesize AC. Overall, this study is divided into five research objectives with multiple sub-objectives.

The first phase of this research conducted a parametric study of the conventional torrefaction technique. In this regard, SCG and CH were used as the lignocellulose-based precursor. The impact of torrefaction parameter on the physicochemical transformation of biomass was examined by varying each parameter (torrefaction temperature and reaction time) independently. The influence of torrefaction conditions on the precursors' physicochemical changes and structural transformations were analyzed using diverse analytical techniques. This is followed by evaluating the candidacy of the corresponding torrefied biomass samples towards CO<sub>2</sub> capture performance. The physicochemical transformation of torrefied biomass samples mainly synthesized in severe torrefaction conditions (300 °C and 1 h) demonstrated their candidacy for CO<sub>2</sub> removal. The equilibrium CO<sub>2</sub> adsorption capacities of SCG-300-1 and CH-300-1 were 0.38 and 0.23 mmol/g, respectively, at 25 °C of column temperature and in the presence of 30 vol% CO<sub>2</sub> in N<sub>2</sub>.

Comparatively, the torrefied biomass sample derived from SCG displayed superior CO<sub>2</sub> capture performance under a similar capture scenario than CH derived torrefied biomass sample owing to the textural properties and surface chemistry developed during the torrefaction process.

The findings from phase one raised numerous research questions. For instance, is it necessary to study the thermal treatment of biomass at a temperature higher than 300 °C like undergoing slow pyrolysis to elevate the removal of tar from the carbon matrix and accelerate the volatilization reactions to generate biochar with enhanced textural characteristics and improved surface chemistry for superior CO<sub>2</sub> capture performance? Furthermore, evaluating the kinetic and thermodynamic parameters before performing a high-temperature thermal treatment (slow-pyrolysis) is essential to obtain necessary information regarding the feedstock and the process parameters. Hence, phase two implemented the kinetic and thermodynamic study of the slow pyrolysis technique using SCG and CH. In this regard, the kinetic data of SCG and CH during slow pyrolysis were obtained to fit the thermogravimetric data taken using the TGA-DTG analyzer. The kinetic parameters were estimated using different iso-conversational methods followed by estimating thermodynamic parameters. In this regard, the conversion technique using SCG showed higher activity and would be efficient in terms of energy requirement as the requirement of activation energy for SCG was low (90.4-141.7 kJmol<sup>-1</sup>) compared to CH (96.0-162.1 kJmol<sup>-1</sup>). Also, SCG can be identified as a superior lignocellulose-based precursor for further valorization than CH in terms of physicochemical properties.

Appropriate utilization of biochar derived from slow pyrolysis of SCG could improve the overall economics of the post-combustion CO<sub>2</sub> capture facility. In the third phase, the impact of slow pyrolysis process parameters was assessed on biochar yield and specific surface area ( $S_{BET}$ ). Secondly, this research aimed to elucidate the correlation of pyrolysis temperature as a critical parameter with textural properties, surface composition, aromatic structure, and CO<sub>2</sub> mitigation efficiency of SCG-derived biochar samples. The results demonstrated that biochar yield reduced with the rising pyrolysis temperature, but biochar's textural characteristics, surface functionalities and aromatic structure were positively correlated with the increasing temperature conditions. Correspondingly, the impact of pyrolysis process parameters on biochar yield complemented the findings of the second phase of this study. In this study, SCG-600 showed the highest equilibrium CO<sub>2</sub> uptake of 2.8 mmol/g in 30 vol% of CO<sub>2</sub> (in N<sub>2</sub>) and 30 °C (column temperature). It was

evident that the well-developed textural characteristics and porosity, availability of basic surface functional groups, and aromatic structure of SCG-600 influenced the CO<sub>2</sub> removal performance owing to the enhanced acid-base interactions and the presence of Vander Waals force of attraction.

Treating the promising biochar sample derived from SCG at a higher temperature in the presence of a suitable activating agent becomes necessary to improve the physicochemical properties of the carbon-based adsorbent for improved CO<sub>2</sub> capture performance. Therefore, the fourth phase's main objective was to optimize the two-stage CO<sub>2</sub> activation process of SCG-600 using the Box-Behnken design (BBD) method. The impact of activation parameters (activation temperature, holding time, and CO<sub>2</sub> gas flow rate) were investigated on surface area ( $S_{BET}$ ) and AC yield. In addition, the influence of thermal pre-treatment techniques (torrefaction and slow-pyrolysis) for the two-stage physical activation technique were evaluated and compared in terms of textural characteristics and CO<sub>2</sub> adsorption performance. Further, the impact of tailoring the surface functionalities of the pristine AC sample was evaluated using deep eutectic solvent (DES) and compared with pristine AC (AC-CO<sub>2</sub>) through complementary analytical techniques. CO<sub>2</sub> breakthrough experiments were performed under different ranges of temperatures and CO<sub>2</sub> concentration in N<sub>2</sub> to investigate the influence on adsorption performance and selectivity. The estimated highest equilibrium CO<sub>2</sub> uptake for two sets of ACs (pristine and DES-treated) were 4.34 mmol/g and 5.5 mmol/g, respectively, at 25 °C and 15 vol % of CO<sub>2</sub> in N<sub>2</sub>. The DES-treated AC displayed a superior adsorption capacity, selectivity, and regeneration ability due to a well-developed porous structure, morphology, and availability of a wide variety of desired functional groups that facilitated the CO<sub>2</sub> capture process under a simulated post-combustion scenario.

A comparative techno-economic assessment and sensitivity analysis were performed using different AC production scenarios from SCG. The economic viability of the AC production technique using SCG as the potential precursor was assessed based on the discounted cash flow analysis (DCFA) technique. The minimum selling price (MSP) of AC samples derived from different scenarios evaluated were US \$0.15/kg, \$ 0.21/kg, and \$ 0.28/kg, respectively. Comparatively, the MSP of DES functionalized AC was lower than commercial AC (US \$0.45/kg). A positive net rate of return (NRR) for all the production scenarios indicates that AC production using dried SCG is profitable from an economic point of view. The sensitivity analysis demonstrates that the feedstock cost and utility cost influence the MSP of AC production.

## ACKNOWLEDGEMENTS

I would like to express my sincere appreciation to my Ph.D. supervisors, Dr. Ajay K. Dalai, and Dr. Catherine Niu, for their support and guidance during my Ph.D. studies. Their constant encouragement and mentorship ensured that I completed this thesis.

My deepest gratitude goes to my Ph.D. advisory committee members, Dr. Lee Wilson, Dr. Venkatesh Meda, Dr. Amira Abdelrasoul, and Dr. Lifeng Zhang, because their reviews, constructive comments and suggestions helped improve the quality of my thesis. Finally, I thank Dr. Ondrej Masek from the University of Edinburg for taking time out of his busy schedule to serve as my external examiner.

I would also like to thank Mr. R. Lee Prokopishyn, Ms. Heli Eunike, Ms. Rosa Do Phuong, Mr. Richard Blondin and Mrs. Jayasinghe Dushmanthi for their technical assistance in the laboratory. I am thankful to Dr. Jianfeng Zhu (Saskatchewan Structural Sciences Centre) for helping me to execute the NMR analysis and to Danielle Covelli and Dr. Ketan Sandhi (Saskatchewan Structural Sciences Centre) for helping me with the execution of the XPS analysis.

I am grateful to the financial supporters of my research, including the Natural Sciences and Engineering Research Council of Canada (NSERC), BioFuel Net and the Canada Research Chair (CRC) Program. I also recognize that this research would not have been possible without the financial assistance of the College of Graduate Studies and Research and the Department of Chemical and Biological Engineering at the University of Saskatchewan (Graduate Teaching and Laboratory Assistantships).

My sincere thanks to the other members of Dr. Ajay K. Dalai's research group, especially Dr. Jude A. Okolie, Mr. Girish Kamath, Dr. Biswajit Saha, Dr. Sonil Nanda, Dr. Venu B. Borugadda and Dr. Sundar Vedachalam for their technical assistance at the Catalysis and Chemical Reaction Engineering Laboratory (CCREL).

Special thanks to my parents and lovely family, Mr. Biswa Ranjan Mukherjee, Mrs. Shanti Mukherjee, Mr. Shrey Modi, Mrs. Debopriya Mukherjee and Mr. Subhankar Pramanik for their constant support and motivation. I want to thank my extended maternal family for believing in me. I would also like to express my sincere gratitude to my parents-in-law.

## DEDICATION

This thesis is dedicated to:

God Almighty (Shree Sarada Ma and Thakur Ram Krishna Paramahansa) for their benevolence and guidance throughout my studies.

To my late maternal uncles, Mr. Taraknath Sanyal (double mother) and Mr. Shibnath Sanyal (papu), may your soul rest in peace, and I know you are watching me from heaven and showering your blessings and wishes.

To my mother (monai), Mrs. Santi Mukherjee, for being a constant source of love, motivation, and support and also for not giving up on me and my dreams.

To my father (baba), Mr. Biswaranjan Mukherjee. He is someone whose love and blessings are unconditional, and the faith he has in me is unimaginable. I believe it helped me go through even on a very critical day during this time.

To my amazing partner, Mr. Shrey Modi. He supported me when I needed him the most. He is my constant source of motivation and inspiration to work smart and am thankful to him for believing in me through lots of ups and downs.

To my dear sister, Debopriya Mukherjee, and brother-in-law, Mr. Subhankar Pramanik, who believed in me and always gave me the most critical advice when in need.

Lastly, to my mother-in-law and father-in-law, Mrs. Shilpa Modi, and Mr. Sandip Modi. They have always motivated me and believed in me. I know how much proud you are of all my achievements.

## TABLE OF CONTENT

PERMISSION TO USE.....	i
ABSTRACT.....	ii
ACKNOWLEDGEMENTS.....	v
DEDICATION.....	vi
TABLE OF CONTENTS.....	vii
LIST OF TABLES.....	xvi
LIST OF FIGURES.....	xx
LIST OF ABBREVIATIONS.....	xxvi
LIST OF NOMENCLATURES AND SYMBOLS.....	xxviii
GREEK LETTERS.....	xxix
<b>Chapter 1 Introduction.....</b>	<b>1</b>
1.1 Research Background.....	1
1.2 Knowledge Gaps.....	3
1.3 Hypothesis.....	4
1.4 Research Objectives.....	4
1.5 Organization of the thesis .....	7
1.6 Manuscript content of the thesis.....	8
<b>Chapter 2 Literature Review.....</b>	<b>10</b>
2.1 Introduction.....	11
2.2 Carbon dioxide capture technologies.....	18
2.3 Current state in post-combustion capture technology.....	21



2.4 Overview of the ongoing research in post-combustion carbon dioxide capture technology.....	24
2.5 Criteria for selecting carbon dioxide capture adsorbent.....	29
2.5.1 Potential of activated carbon as carbon dioxide separator.....	29
2.6 Pristine and functionalised activated carbon.....	34
2.6.1 Pristine activated carbon.....	37
2.6.2 Chemically functionalised activated carbon.....	38
2.7 Carbon dioxide adsorption techniques.....	39
2.7.1 Pressure swing adsorption technique.....	40
2.7.2 Temperature swing adsorption technique.....	41
2.7.3 Vacuum Swing Adsorption technique.....	41
2.8 Summary.....	41
<b>Chapter 3 Experimental section.....</b>	<b>43</b>
3.1 Biomass collection and pre-treatment.....	43
3.2 Materials section.....	43
3.3 Torrefaction, slow-pyrolysis, and CO <sub>2</sub> activation set-up.....	43
3.4 Experimental procedures.....	45
3.4.1 Torrefaction and slow pyrolysis .....	45
3.4.2 Physical activation and activated carbon production technique.....	45
3.4.3 Preparation of natural deep eutectic solvent.....	46
3.4.4 Impregnation technique and preparation of DES functionalized activated carbon samples .....	46
3.5 Characterizations.....	47

3.6 Breakthrough carbon dioxide adsorption set-up.....	50
3.6.1 CO <sub>2</sub> adsorption capacity.....	51
3.6.2 Selectivity.....	52
3.7 Process safety analysis.....	52

**Chapter 4 Experimental and Modelling Studies of Torrefaction of Spent Coffee Grounds and Coffee Husk: Effects on Surface Chemistry and Carbon Dioxide**

<b>Capture Performance.....</b>	<b>53</b>
4.1 Abstract.....	54
4.2 Introduction.....	55
4.3 Materials and Methods.....	56
4.3.1 Biomass collection and pre-treatment.....	56
4.3.2 Torrefaction set-up and experimental procedure.....	57
4.3.3 Characterizations of the precursors and torrefied biomass samples.....	59
4.3.4 Carbon dioxide capture set-up and adsorption experiments.....	59
4.4 Process Modeling.....	59
4.4.1 Aspen model description and assumptions Validation.....	59
4.5 Torrefaction mass and energy yield .....	63
4.6 Results and discussions.....	63
4.6.1 Ultimate, proximate, and pH analyses of the precursors and torrefied biomass samples .....	63
4.6.2 BET analysis of the precursors and torrefied biomass Samples.....	67
4.6.3 Fourier Transform Infrared Spectroscopic (FTIR) Analysis.....	68
4.6.4 Thermal stability analysis of the precursors and	

torrefied biomass samples.....	71
4.6.5 X-ray Photoelectron Spectroscopic (XPS) analysis.....	75
4.6.6 Mass and energy yield of the precursors and torrefied Samples .....	77
4.6.7 Model Validation .....	78
4.6.8 Parametric studies .....	80
4.6.9 CO <sub>2</sub> capture performance of torrefied samples .....	83
4.7 Conclusions .....	84
<b>Chapter 5 Pyrolysis kinetics and activation thermodynamic parameters of spent coffee</b>	
<b>grounds and coffee husk using thermogravimetric analysis .....</b>	<b>86</b>
5.1 Abstract.....	87
5.2 Introduction.....	88
5.3 Materials and Methods.....	90
5.3.1 Biomass collection and pre-treatment.....	90
5.3.2 Proximate and ultimate analyses of biomass samples.....	90
5.3.3 Calorific value.....	90
5.3.4 Thermogravimetric analysis (TGA) of the precursors.....	91
5.3.5 Sample Preparation for Fourier transform mid-infrared spectroscopy analysis.....	91
❖ FT-MIR Data collection and analysis.....	92
5.4 Kinetic study.....	92
5.5 Iso-conversional models.....	94
5.5.1 Kissinger–Akahira–Sunose (KAS) equation.....	95
5.5.2 Flynn–Wall– Ozawa (FWO) equation.....	95

5.5.3 Kissenger’s method.....	95
5.5.4 Friedman method.....	96
5.6 Evaluation of the thermodynamic parameters .....	97
5.7 Results and discussions.....	97
5.7.1 Physicochemical properties of biomass samples.....	97
5.7.2 Thermogravimetric analysis of biomass samples.....	99
5.7.3 Effects of heating rate on the thermal decomposition of biomass samples.....	101
5.7.4 Kinetic Analysis.....	106
5.7.5 Thermodynamic Parameters estimation.....	116
5.8 Conclusions.....	120
<b>Chapter 6 Carbon dioxide capture from flue gas in biochar produced from spent coffee grounds: Effect of surface chemistry and porous structure.....</b>	<b>122</b>
6.1 Abstract.....	124
6.2 Introduction.....	125
6.3 Materials and methods.....	128
6.3.1 Biomass collection and pre-treatment.....	128
6.3.2 Slow pyrolysis set-up and biochar production.....	128
6.3.3 Characterization of precursor and biochar samples.....	129
C1s Near-edge X-ray Absorption Fine Structure Spectroscopy (NEXAFS).....	129
Sample preparation on gold-coated Si wafers for NEXAFS analysis.....	129
Sample measurement for NEXAFS analysis.....	129
6.3.4 Breakthrough CO <sub>2</sub> adsorption measurements.....	130
6.4 Kinetic study and activation energy evaluation.....	131

6.5 Results and Discussions.....	131
6.5.1 Effects of pyrolysis operating parameters on biochar-yield.....	131
6.5.2 Effects of pyrolysis operating parameters on specific surface area .....	131
6.5.3 Proximate analysis of biomass and biochar samples.....	133
6.5.4 Ultimate analysis and atomic ratios of biomass and biochar samples.....	134
6.5.5 pH analysis of biomass and biochar samples.....	135
6.5.6 Thermal stability analysis of biomass and biochar samples.....	136
6.5.7 BET surface area of biomass and biochar samples.....	137
6.5.8 XRD analysis of biomass and biochar samples.....	139
6.5.9 FTIR analysis of biomass and biochar samples.....	140
6.5.10 Solid-state nuclear magnetic resonance ( <sup>13</sup> C-NMR) spectroscopy.....	142
6.5.11 XPS analysis of biomass and biochar samples.....	143
6.5.12 NEXAFS analysis of biomass and biochar samples.....	148
6.6 Breakthrough CO <sub>2</sub> adsorption performance of SCG derived biochar samples.....	149
6.6.1 Effects of adsorption conditions on CO <sub>2</sub> adsorption capacity.....	150
6.6.2 Breakthrough adsorption capacity of biochar samples.....	151
6.7 Adsorption kinetic study and activation energy.....	155
6.8 Conclusions.....	156
<b>Chapter 7 Preparation of activated carbon from spent coffee grounds a</b>	
<b>functionalization by deep eutectic solvent: Effect of textural properties a</b>	
<b>surface chemistry on CO<sub>2</sub> capture performance.....</b>	<b>158</b>
7.1 Abstract.....	160

7.2 Introduction.....	161
7.3 Box-Behnken experimental design and statistical analysis.....	165
7.4 Materials and Methodology .....	163
7.4.1 Biomass collection, slow pyrolysis, physical activation and DES-functionalization.....	166
7.4.2 Breakthrough carbon dioxide adsorption set-up.....	165
7.5 Results and Discussions.....	167
7.5.1 Development of regression model equation.....	167
7.5.2 Statistical Analysis.....	171
7.5.3 Effects of process parameters on specific surface area.....	174
7.5.4 Effects of process parameters towards activated carbon yield.....	175
7.5.5 Process optimization and validation.....	178
7.5.6 CO <sub>2</sub> adsorption screening of functionalised AC samples.....	177
7.5.7 Evaluation between torrefied biomass and biochar derived activated carbon.....	179
7.5.8 Ultimate analysis and ash content.....	180
7.5.9 XRD analysis.....	181
7.5.10 Thermogravimetric analysis.....	182
7.5.11 Temperature-programmed desorption (TPD) analysis.....	183
7.5.12 Textural properties of the activated carbon samples.....	185
7.5.13 XPS analysis.....	188
7.5.14 Surface morphology.....	190
7.6 Breakthrough CO <sub>2</sub> adsorption performance.....	191

7.6.1 Effects of column temperature on CO <sub>2</sub> capture performance.....	191
7.6.2 Effects of inlet CO <sub>2</sub> concentration on CO <sub>2</sub> capture performance.....	197
7.6.3 Selectivity.....	199
7.6.4 Multiple adsorption-desorption study.....	199
7.7 Conclusions.....	200

**Chapter 8 Techno-Economic analysis of activated carbon production from spent**

**coffee grounds: Comparative evaluation of different production routes .....202**

8.1 Abstract.....	203
8.2 Introduction.....	204
8.3 Research Methodology.....	205
8.3.1 Design Basics.....	205
8.3.2 Process design and simulation.....	206
8.3.3 Economic analysis.....	212
8.4 Results and Discussions.....	215
8.4.1 Model validation, mass and energy analysis.....	215
8.4.2 Economic analysis.....	219
8.4.3 Sensitivity analysis.....	227
8.4.4 Uncertainty analysis using Monte Carlo simulation.....	228
8.5 Conclusions.....	230

**Chapter 9 Summary, Conclusions, and Recommendation.....231**

9.1 Overall summary and conclusions.....	231
9.2 significant Contribution to the knowledge.....	233

9.3 Future Recommendations.....	234
<b>LIST OF REFERENCES.....</b>	<b>236</b>
<b>Appendix A</b> 3-Minutes Thesis Competitions (3MT competitions) .....	259
<b>Appendix B:</b> Torrefaction, slow-pyrolysis, and CO <sub>2</sub> activation for production of torrefied biomass samples, biochar and activated carbons.....	260
<b>Appendix C:</b> CO <sub>2</sub> calibration curve and GC calibration curves for CO <sub>2</sub> adsorption experiment in chapter 3.....	263
<b>Appendix D</b> Additional data for Aspen Plus simulation used in Chapter 4.....	266
<b>Appendix E</b> Additional data for Matlab code for kinetics used in Chapter 5.....	268
<b>Appendix F</b> Additional data for Aspen plus simulation used in Chapter 8.....	270
<b>Appendix G:</b> Permission to use Review and Research Articles.....	273



## LIST OF TABLES

<b>Table 2.1:</b> Flue-gas composition from coal-fired power plants and cement process.....	13
<b>Table 2.2:</b> Comparative analysis of pre-combustion and oxy-fuel combustion carbon dioxide capture technologies.....	20
<b>Table 2.3:</b> The advantages and disadvantages of post-combustion carbon dioxide capture technology.....	22
<b>Table 2.4:</b> Different post-combustion carbon dioxide capture techniques.....	27
<b>Table 2.5:</b> Proximate and ultimate analyses of lignocellulose-based biomass for activated carbon production.....	31
<b>Table 2.6:</b> An overview of the advantages and disadvantages of activated carbon as a CO <sub>2</sub> adsorbent.....	33
<b>Table 2.7:</b> CO <sub>2</sub> adsorption capacities of pristine activated carbon.....	36
<b>Table 2.8:</b> CO <sub>2</sub> adsorption capacities using chemically modified activated carbon species.....	39
<b>Table 3.1:</b> Specifications of torrefaction, slow-pyrolysis, and CO <sub>2</sub> activation set-up.....	44
<b>Table 3.2:</b> Ratio, phase, and abbreviations of the DES-based activated carbon samples.....	47
<b>Table 3.3:</b> Specifications of the CO <sub>2</sub> capture fixed-bed reactor.....	51
<b>Table 4.1:</b> List of assumptions and description of the processing blocks used for the torrefaction model.....	62
<b>Table 4.2:</b> Ultimate, proximate and pH analyses of the precursors and torrefied biomass samples.....	66
<b>Table 4.3:</b> BET analysis of the precursors and torrefied biomass samples.....	68
<b>Table 4.4:</b> Elemental composition of torrefied biomass samples from the XPS analysis.....	75

<b>Table 4.5:</b> Deconvoluted C1s spectra of torrefied biomass samples.....	76
<b>Table 4.6:</b> Deconvoluted O1s spectra of torrefied biomass samples.....	76
<b>Table 4.7:</b> Solid yield (%), HHV, energy density ratio, and energy yield (%) of the precursors and the torrefied biomass samples.....	79
<b>Table 4.8:</b> Breakthrough CO <sub>2</sub> adsorption performance of the torrefied biomass samples.....	84
<b>Table 5.1:</b> Proximate, ultimate, and high heating value of spent coffee grounds and coffee husk.....	98
<b>Table 5.2:</b> The kinetic parameters obtained from the iso-conversional method using the fitted equation for spent coffee grounds.....	110
<b>Table 5.3:</b> The Kinetic parameters obtained from the iso-conversional method using the fitted equation for coffee husk.....	110
<b>Table 5.4:</b> Comparison of activation energies (average, E <sub>A</sub> ) of coffee residues calculated using iso-conversional methods with data reported in the literature.....	115
<b>Table 5.5:</b> The thermodynamic parameters as a function of temperature for spent coffee grounds (SCG).....	117
<b>Table 5.6:</b> The thermodynamic parameters as a function of temperature for coffee husk (CH).....	118
<b>Table 6.1:</b> C 1s NEXAFS assignment of peak energies, bond types, and transitions of SCG and SCG derived biochar samples.....	130
<b>Table 6.2:</b> Effects of process conditions on biochar yield from spent coffee grounds.....	132
<b>Table 6.3:</b> Proximate analysis of biomass and biochar samples derived at different pyrolysis temperatures.....	134

<b>Table 6.4:</b> Ultimate (CHNS) analysis (on a dried-basis) and atomic ratios of biomass and biochar samples.....	135
<b>Table 6.5:</b> pH analysis of biomass and biochar samples.....	136
<b>Table 6.6:</b> Textural properties of biomass and biochar produced at different pyrolysis temperatures.....	139
<b>Table 6.7:</b> Quantitative percentages of various functional groups present in biomass and biochar based on <sup>13</sup> C-NMR spectra.....	143
<b>Table 6.8:</b> XPS derived surface elemental composition (atom ratio %) of biomass and biochar samples.....	145
<b>Table 6.9:</b> Deconvolution results of N1s and O1s spectra of SCG derived biochar samples (relative area percentage %) .....	145
<b>Table 6.10:</b> Breakthrough adsorption performance of SCG-600 under varying column temperatures and initial feed concentration of CO <sub>2</sub> .....	151
<b>Table 6.11:</b> Breakthrough adsorption performance of biochar samples derived from SCG.....	152
<b>Table 6.12:</b> CO <sub>2</sub> adsorption performance of carbon-based adsorbents under the Post-combustion conditions (binary mixture of CO <sub>2</sub> /N <sub>2</sub> ) .....	154
<b>Table 6.13:</b> Values of adsorption kinetic parameters of SCG-600 at varying column temperatures.....	156
<b>Table 7.1:</b> Factors and levels in CO <sub>2</sub> activation.....	166
<b>Table 7.2:</b> Experimental and model predicted responses by varying the activation input parameters.....	170
<b>Table 7.3:</b> Specific Surface area (response: Y <sub>1</sub> ) .....	172
<b>Table 7.4:</b> Activated carbon yield (Y <sub>2</sub> ).....	173

<b>Table 7.5:</b> The model fit summaries for the responses ( $Y_1$ and $Y_2$ ).....	174
<b>Table 7.6:</b> Validation of the actual data evaluated at the optimum activation conditions.....	178
<b>Table 7.7:</b> CO <sub>2</sub> adsorption performance of DES-treated AC samples.....	179
<b>Table 7.8:</b> Ultimate analysis and ash content of pristine and DES-treated samples.....	180
<b>Table 7.9:</b> Distribution of basic sites and temperature range.....	183
<b>Table 7.10:</b> Textural properties of the activated carbon samples.....	186
<b>Table 7.11:</b> O1s and N1s deconvoluted spectra of pristine and DES treated AC samples.....	189
<b>Table 7.12:</b> Breakthrough CO <sub>2</sub> adsorption performance at varying column temperatures.....	193
<b>Table 7.13:</b> CO <sub>2</sub> removal performance of various carbon-based adsorbents reported In the existing literatures (under dynamic conditions).....	195
<b>Table 7.14:</b> Breakthrough CO <sub>2</sub> adsorption performance at varying inlet concentrations of CO <sub>2</sub> .....	197
<b>Table 8.1:</b> Assumptions used in the Aspen plus simulation and economic model.....	212
<b>Table 8.2:</b> CAPEX and OPEX estimation methodology.....	214
<b>Table 8.3:</b> Comparison of the minimum selling price of biochar and activated carbon from different studies.....	225
<b>Table C.1:</b> Composition of standard gas used for GC calibration.....	256
<b>Table C.2:</b> Composition of standard gas used for GC calibration.....	257

## LIST OF FIGURES

<b>Figure 1.1:</b> Schematic of the different research phases of this thesis (phase 1-5) .....	5
<b>Figure 2.1:</b> CO <sub>2</sub> emission from different industrial sectors.....	12
<b>Figure 2.2:</b> (A) Pre-combustion CO <sub>2</sub> capture technology (B) post-combustion CO <sub>2</sub> capture technology and (C) oxy-fuel CO <sub>2</sub> capture technology.....	19
<b>Figure 3.1:</b> Schematic of torrefaction and slow-pyrolysis fixed-bed reactor set-up.....	44
<b>Figure 3.2:</b> Schematic of physical activation fixed-bed reactor set-up (CO <sub>2</sub> activation) .....	45
<b>Figure 3.3:</b> Deep eutectic solvent preparation and AC impregnation technique.....	47
<b>Figure 3.4:</b> Schematic of CO <sub>2</sub> adsorption-set-up (Temperature swing adsorption unit) .....	51
<b>Figure 4.1:</b> Schematic representation of the methodology adapted for research-objective 1.....	57
<b>Figure 4.2:</b> Flow diagram of the coffee residues (SCG and CH) torrefaction model simulated using Aspen Plus.....	61
<b>Figure 4.3:</b> Van Krevelen Plot of the precursors and torrefied biomass samples.....	67
<b>Figure 4.4:</b> FTIR analysis of precursors and torrefied samples at different temperatures (a) SCG (b) CH.....	70
<b>Figure 4.5:</b> TGA-DTG analysis of precursors (a) SCG and (b) CH.....	72
<b>Figure 4.6:</b> TGA-DTG analysis of the torrefied biomass samples at different torrefaction temperatures (a) SCG .....	73
(b) CH.....	74
<b>Figure 4.7:</b> Deconvoluted spectra of SCG-300-1 and Ch-300-1	

(a) C1s and (b) O1s.....	77
<b>Figure 4.8:</b> Model validation for mass yields during torrefaction of coffee residues for (a) SCG torrefied solids and (b) CH torrefied solids.....	80
<b>Figure 4.9:</b> Model validation for HHV during torrefaction of coffee residues for (a) SCG torrefied solids (b) CH torrefied solids.....	80
<b>Figure 4.10:</b> Effect of torrefaction temperatures on the mass yield and HHV values of (a) SCG torrefied biomass samples (b) CH torrefied biomass samples.....	81
<b>Figure 4.11:</b> Effect of torrefaction temperatures on the decomposition of volatile compounds.....	83
<b>Figure 4.12:</b> Breakthrough CO <sub>2</sub> capture performance of torrefied biomass samples.....	84
<b>Figure 5.1:</b> Schematic representation of the methodology adapted for research-objective 2.....	91
<b>Figure 5.2:</b> (a) TGA profiles of spent coffee grounds (SCG) and coffee husk (CH) at a constant heating rate of 10 °C/min; (b) DTG profiles of spent coffee grounds (SCG) and coffee husk (CH) at a constant heating rate of 10 °C/min.....	101
<b>Figure 5.3:</b> TGA and DTG profiles of spent coffee grounds (SCG) at different heating rates 5–20 °C/min: (a) TGA profiles of SCG (b) DTG profiles of SCG.....	103
<b>Figure 5.4:</b> TGA and DTG profiles of Coffee husk (CH) at different heating rates 5–20 °C/min: (c) TGA profiles of CH (d) DTG profiles of CH.....	104
<b>Figure 5.5:</b> (a) Effects of heating rate on the kinetics for an initial conversion	

of 5% for SCG and CH (b) Effect of heating rate on the temperature at which the maximum weight loss is attained ( $T_{peak}$ ) for SCG and CH.....	105
<b>Figure 5.6:</b> Linear least square regression plot for spent coffee grounds at different conversions used for the determination of activation energy by (a) FWO; (b) KAS and (c) Friedman. The lines in figure (c) reflects the values of $\alpha$ ranging from 0.1 to 0.7 starting from left to right.....	107
<b>Figure 5.7:</b> Linear least square regression plot for coffee husk at different conversions used for the determination of activation energy by (a) FWO; (b) KAS and (c) Friedman. The lines in figure (c) reflects the values of $\alpha$ ranging from 0.1 to 0.7 starting from left to right.....	108
<b>Figure 5.8:</b> Change in activation energy with conversion for different the iso – conversional methods for (a) spent coffee grounds (b) coffee husk.....	114
<b>Figure 5.9:</b> Change in enthalpy with conversion for different iso – conversional methods for (a) spent coffee grounds (b) coffee husk .....	119
<b>Figure 6.1:</b> Schematic representation of the methodology adapted for research-objective 3.....	128
<b>Figure 6.2:</b> Effects of pyrolysis temperatures and heating rate on specific surface area of biochar samples.....	132
<b>Figure 6.3:</b> (a) TGA and (b) DTG analysis of SCG and SCG derived biochar samples.....	138

<b>Figure 6.4:</b> Wide-angle XRD patterns of SCG and SCG derived biochar samples.....	140
<b>Figure 6.5:</b> FTIR spectra of SCG and the corresponding biochar samples.....	142
<b>Figure 6.6:</b> <sup>13</sup> C-Nuclear Magnetic Resonance (NMR) spectra of SCG and SCG derived biochar samples.....	144
<b>Figure 6.7:</b> Deconvoluted N1s and O1s spectra of SCG-400 and SCG-600.....	146
<b>Figure 6.8:</b> Deconvoluted O1s spectra of SCG-400 and SCG-600.....	147
<b>Figure 6.9:</b> Stacked C1s NEXAFS spectra of SCG and SCG derived biochar.....	149
<b>Figure 6.10:</b> (a) Breakthrough curve of SCG-600 at varying column temperatures.....	153
(b) Breakthrough adsorption curve of biochar samples derived from SCG.....	153
<b>Figure 6.11:</b> Arrhenius plot.....	156
<b>Figure 7.1:</b> Schematic representation of the methodology adapted for research-objective 4.....	165
<b>Figure 7.2:</b> (a) Perturbation plot of specific surface area (response: Y <sub>1</sub> ) (b) 3D response of specific surface area (CO <sub>2</sub> flow-rate constant) .....	176
<b>Figure 7.3:</b> (a) Perturbation plot of activated carbon yield (response: Y <sub>2</sub> ) (b) 3D response of AC yield (CO <sub>2</sub> flowrate constant) .....	177
<b>Figure 7.4:</b> XRD analysis of pristine (AC-CO <sub>2</sub> ) and DES-treated AC sample.....	181
<b>Figure 7.5:</b> Thermogravimetric analysis of AC samples.....	183
<b>Figure 7.6:</b> CO <sub>2</sub> TPD profile of pristine and DES-treated samples.....	184
<b>Figure 7.7:</b> N <sub>2</sub> adsorption isotherms of AC samples: AC-CO <sub>2</sub> and AC-DES-0.4.....	187
<b>Figure 7.8:</b> (a): Pore size distribution of the AC-CO <sub>2</sub> sample and (b) Pore size distribution of AC- DES-0.4 obtained using N <sub>2</sub> at 77K.....	188
<b>Figure 7.9:</b> Deconvoluted N1s spectra of DES-treated and pristine AC samples.....	189



<b>Figure 7.10:</b> SEM analysis of (a) AC-CO <sub>2</sub> and (b) AC-DES-0.4.....	190
<b>Figure 7.11:</b> Effect of adsorption temperature on CO <sub>2</sub> capture performance (a) AC-CO <sub>2</sub> and (b) AC-DES-0.4.....	194
<b>Figure 7.12:</b> Effect of CO <sub>2</sub> concentration on adsorption performance (a) AC-CO <sub>2</sub> and (b) AC-DES-0.4.....	198
<b>Figure 7.13:</b> Multiple adsorption and desorption cycle study.....	200
<b>Figure 8.1:</b> Schematics of the design procedure for activated carbon production techno-economic analysis using dried SCG.....	206
<b>Figure 8.2:</b> Flowsheet of the proposed design, (scenario 1): slow pyrolysis and physical activation; (scenario 2): slow pyrolysis, physical activation, and flue gas combustion; (scenario 3): slow pyrolysis, physical activation, DES functionalization, and flue gas combustion.....	209
<b>Figure 8.3:</b> Comparison of biochar yield from experimental and model results.....	216
<b>Figure 8.4:</b> Mass and energy balance for scenarios 1-3.....	217
<b>Figure 8.5:</b> Breakdown of the equipment purchase costs for all the three scenarios.....	220
<b>Figure 8.6:</b> Overall cost of equipment for all the three scenarios.....	221
<b>Figure 8.7:</b> Total CAPEX and OPEX for the three scenarios and the OPEX breakdown.....	222
<b>Figure 8.8:</b> Discounted and undiscounted cash flow analysis for the three scenarios for AC production.....	224
<b>Figure 8.9:</b> Sensitivity analysis showing the influence of several independent.....	227
<b>Figure 8.10:</b> Monte Carlo simulation results on the MSP of AC for the three scenarios.....	229
<b>Figure B.1:</b> Temperature calibration data for the furnace installed on the torrefaction, slow-pyrolysis, and CO <sub>2</sub> activation set-up.....	260

<b>Figure B.2:</b> Calibration data for N <sub>2</sub> mass flow controller used in the torrefaction, slow-pyrolysis and CO <sub>2</sub> activation set-up.....	261
<b>Figure B.3:</b> Calibration data for CO <sub>2</sub> mass flow controller used in the CO <sub>2</sub> adsorption set-up.....	262
<b>Figure C.1:</b> Calibration data for N <sub>2</sub> mass flow controller used in the torrefaction, slow-pyrolysis and CO <sub>2</sub> activation set-up.....	264
<b>Figure C.2:</b> Calibration data for CO <sub>2</sub> mass flow controller used in the torrefaction, slow-pyrolysis and CO <sub>2</sub> activation set-up.....	265
<b>Figure G.1:</b> Permission to use the published paper “Review of post-combustion carbon dioxide capture technologies using activated carbon.”.....	273
<b>Figure G.2:</b> Permission to use the published paper “Experimental and Modeling Studies of Torrefaction of Spent Coffee Grounds and Coffee Husk: Effects on Surface Chemistry and Carbon Dioxide Capture Performance.”.....	274
<b>Figure G.3:</b> Permission to use the published paper “Pyrolysis kinetics and thermodynamic activation parameters of exhausted coffee residue and coffee husk using thermogravimetric analysis.”.....	275
<b>Figure G.4:</b> Permission to use the published paper “Carbon dioxide capture from flue gas in biochar produced from spent coffee grounds: Effects of surface chemistry and porous structure.”.....	276
<b>Figure G.5:</b> Permission to use the published paper “Techno-Economic Analysis of activated carbon production from spent coffee grounds: Comparative evaluation of different production routes.”.....	277

## LIST OF ABBREVIATIONS

AC	Activated Carbon
AOE	Total annual production cost
ANOVA	Analysis of variance
ASTM	American society for testing and materials
BBD	Box-Behnken design
BET	Brunauer-Emmett-Teller method
BJH	Barret-Joyner-Halenda
CAPEX	Capital expenditure
CCD	Central composite design
CO <sub>2</sub>	Carbon dioxide
CCS	Carbon capture and sequestration
CEPCI	Chemical engineering plant cost index
CLS	Canadian Light Source
CH	Coffee husk
DBEP	Discounted break-even point
DCFR	Discounted cash flow rate of return
DEA	Diethanolamine
DES	Deep eutectic solvent
DFT	Density functional theory
DGA	Diglycolamine
DOE	Design of experiment
ESP	Electrostatic Precipitator
FC	Fixed Carbon
FGD	Flue gas desulphurization
FTIR	Fourier Transform Infrared Spectroscopy
FWO	Flynn–Wall- Ozawa method
GA	Glucosamine
GHGs	Greenhouse gases
HHV	Higher heating value
IPCC	Intergovernmental panel of climate change
IUPAC	International Union of Pure and Applied Chemistry
KAS	Kissenger–Akahira-Sunose method
LCA	Life cycle assessment
MEA	Mono ethanolamine
MFC	Mass Flow Controller
MSP	Minimum selling price
NEXAFS	Near-edge X-ray absorption fine structure spectroscopy
NLDFT	Non-linear density functional theory

NMR	Nuclear Magnetic Resonance
NPV	Net present value
NRR	Net rate of return
OPEX	Operating expenditure
PBP	Payback period
PSA	Pressure swing adsorption
PSD	Particle size distribution
R	Universal gas constant, JKmol <sup>-1</sup>
RSM	Research surface methodology
SCG	Spent coffee grounds
TCD	Thermal conductivity detector
TCI	Total investment capital
TEA	Techno-economic analysis
TEI	Total electron yield
TG/DTG	Thermogravimetric/derivative thermogravimetry
TSA	Temperature swing adsorption
TPD	Temperature Programmed Desorption
SP	Slow pyrolysis
SEM	Scanning electron microscope
SGM	Spherical grating monochromator
VM	Volatile matter
VSA	Vacuum swing adsorption
WC	Working capital
XPS	X-ray Photoelectron Spectroscopy
XRD	X-ray Diffraction

## LIST OF NOMENCLATURES AND SYMBOLS

$A_0$	Frequency factor ( $s^{-1}$ )
AC-CO <sub>2</sub>	Pristine activated carbon synthesized using CO <sub>2</sub> activation
AC-DES-0.4	Functionalized activated carbon synthesized using deep eutectic solvent (1:0.4)
$C_{CO_2}$	CO <sub>2</sub> concentration (vol%) in N <sub>2</sub>
CH-200-0.5	Torrefied biomass sample derived from coffee husk at 200 °C and 0.5 h
CH-200-1	Torrefied biomass sample derived from coffee husk at 300 °C and 1 h
CH-250-0.5	Torrefied biomass sample derived from coffee husk at 250 °C and 0.5 h
CH-250-1	Torrefied biomass sample derived from coffee husk at 250 °C and 1 h
CH-300-0.5	Torrefied biomass sample derived from coffee husk at 300 °C and 0.5 h
CH-300-1	Torrefied biomass sample derived from coffee husk at 300 °C and 1 h
$E_A$	Activation Energy ( $kJmol^{-1}$ )
$F(\alpha)$	Reaction model
$k(T)$	Temperature dependent rate constant
$m_0$	Initial mass of the reactant in mg
$m_f$	Final mass of the reactant in mg
$m_t$	Mass of the reactant at any time t in mg
TAC-CO <sub>2</sub>	Activated carbon synthesized using torrefied biomass sample
t	Time in s
$t_B$	Breakthrough time in s
$T_E$	Exhaustion time in s
$T_{mp}$	Peak temperature obtained from the DTG (K)
$T_{peak}$	Temperature at which maximum weight loss occurs from DTG curve (K)
$T_{5\%}$	Initial decomposition temperature (%/°C)
SCG-200-0.5	Torrefied biomass sample derived from spent coffee grounds at 200 °C and 0.5 h
SCG-200-1	Torrefied biomass sample derived from spent coffee grounds at 200 °C and 1 h
SCG-250-0.5	Torrefied biomass sample derived from spent coffee grounds at 250 °C and 0.5 h
SCG-250-1	Torrefied biomass sample derived from spent coffee grounds at 250 °C and 1 h
SCG-300-0.5	Torrefied biomass sample derived from spent coffee grounds at 300 °C and 0.5 h
SCG-300-1	Torrefied biomass sample derived from spent coffee grounds at 300 °C and 1 h
SCG-400	Biochar derived from spent coffee grounds at 400 °C
SCG-500	Biochar derived from spent coffee grounds at 500 °C
SCG-600	Biochar derived from spent coffee grounds at 600 °C

SCG-600-10	Biochar derived from spent coffee grounds at 600 °C and at 10 °C/min heating rate
SCG-600-15	Biochar derived from spent coffee grounds at 600 °C and at 15 °C/min heating rate
SCG-600-20	Biochar derived from spent coffee grounds at 600 °C and at 20 °C/min heating rate
$\Delta H$	Change in enthalpy ( $\text{kJmol}^{-1}$ )
$\Delta G$	Change in Gibbs free energy ( $\text{kJmol}^{-1}$ )
$\Delta S$	Change in entropy ( $\text{Jmol}^{-1}$ )

**GREEK LETTERS**

$\alpha$	Conversion
$\beta$	Heating rate

## **Chapter 1 Introduction**

### **1.1 Research Background**

The global change in the weather pattern and climate deterioration has substantially motivated controlling the carbon dioxide (CO<sub>2</sub>) emission into the atmosphere from large point industrial sources (Fiuza-Jr et al., 2016). CO<sub>2</sub> is one of the principal greenhouse gases (GHGs) contributing substantially to climate change and global warming effects (Li et al., 2015). In the past decades, global industrialization has amplified the consumption of non-renewable fossil-based solid and liquid fuels, escalated greenhouse gas (GHGs) emissions in the atmosphere and the associated anthropogenic activities, which are the subject of widespread public concern (Goel et al., 2015). The Fossil-fuel processing units are considered the dominant contributors to the anthropogenic emission of CO<sub>2</sub> at least until 2050. The plausible explanation for this emission could be the rapid industrialization, explosive growth in population and exponential rise in demand for energy consumption. If the emission increases at the same rate, it corresponds to a rise in average global temperature by 4.1-4.8 °C by the end of the 21st century (Al-Wabel et al., 2019). It is estimated that by 2030 coal-fired power generation facilities, mainly industrial and thermoelectric power plants alone, will contribute to the increase in atmospheric CO<sub>2</sub> emission by more than 50% (Yadavalli et al., 2017). To prevent the rise in global temperature by more than 2 °C above the pre-industrial age and to avert the severe environmental consequences and impact on the global ecosystem, it is suggested to reduce the anthropogenic emission of greenhouse gases, mainly CO<sub>2</sub>, by 2035 (Rashidi et al., 2014).

In this regard, numerous global efforts are being implemented to reduce and stabilize the anthropogenic emission of CO<sub>2</sub>, including promoting the usage of low-carbon based fuels, renewable energy, and CO<sub>2</sub> capture and storage (CCS) technology (Yadavalli et al., 2017). Among the available reduction techniques, CCS technology is an apparent and comprehensive technology that can reduce the emission of CO<sub>2</sub> by 90% from gigantic stationary sources, stabilize the density of CO<sub>2</sub> in the atmosphere, and prevent the rise in global temperature. However, much effort is essential to reduce the energy penalty and operation cost associated with the total cost of CCS. Depending on the layout of the CO<sub>2</sub> emission capture facility and the fuel type, carbon capture facilities can be broadly categorized into three leading technologies: pre-combustion CO<sub>2</sub> capture technique, post-combustion CO<sub>2</sub> capture technique, and oxy-fuel combustion CO<sub>2</sub> capture

technique. Among the CO<sub>2</sub> capture technologies, the post-combustion technique is a dominant strategy that has gained immense popularity. It is the preferred CO<sub>2</sub> removal technique owing to its ease of incorporation and operation and can retrofit easily to an existing unit on a short scale time. The leading post-combustion capture technology commercially includes a chemical absorption technique using liquid amines. However, liquid amine-based technology possesses multiple drawbacks, such as energy penalty associated with CO<sub>2</sub> stripping, regeneration and corrosion of equipment (Tiwari et al., 2018). Research efforts are implemented to investigate alternative techniques to address the operational shortcomings associated with liquid amine technology. In this regard, CO<sub>2</sub> adsorption on solid adsorbents such as activated carbon (AC) can be proposed as a potential alternative to the chemical absorption technique. The use of AC has multiple advantages, such as preparation from low-cost precursors (lignocellulose-based biomass, municipal solid wastes etc.), robustness, thermal stability, tuneable textural properties and surface chemistry, low energy penalty and ease of regeneration (Dilokekunakul et al., 2020). For effective removal of CO<sub>2</sub> from flue gas composition, intensive research interests have been paid to preparing adsorbents that should possess some essential characteristics such as high adsorption capacity and selectivity over N<sub>2</sub> and stability over multiple cycles of adsorption and desorption process.

Coffee is one of the most significant agricultural products and the second-largest commodity exported worldwide after petroleum (Anastopoulos et al., 2017). The International Coffee Organization reported a tremendous increase in the production of coffee in 2010, from 8.4 to 9.1 million tons (Janissen and Huynh, 2018). Moreover, with the increasing world population, coffee demand is expected to rise continuously. As a result of the growing demand and consumption of coffee, a considerable amount of low value residues is generated worldwide. The primary coffee residues generated mainly include coffee husk (CH) and spent coffee grounds (SCG). Discarding coffee residues mainly in landfills presents a severe environmental challenge due to the release of methane (CH<sub>4</sub>), a greenhouse gas, upon natural decomposition. Conversely, the coffee residues generated could be valorized to produce value-added products. For instance, coffee residues (SCG and CH) were used as the lignocellulosic precursors to synthesize carbon-based adsorbents, biofuels and fertilizers that can be utilized for environmental remediation like CO<sub>2</sub> capture from post-combustion capture facility (Janissen and Huynh, 2018).

To address the challenges and fulfil the knowledge gaps, this Ph.D. thesis proposes the development of a low-cost and effective carbon-based adsorbent. This study presents a detailed



impact of precursor type, thermal pre-treatment techniques and activation conditions on breakthrough CO<sub>2</sub> capture performance in adsorption capacity, selectivity and regenerability. In addition, the overall economic viability of the biomass conversion technology to generate AC is evaluated in terms of economic and sensitivity analyses.

## **1.2 Knowledge Gaps**

To identify the knowledge gaps for this study, a comprehensive literature review was done, and the following knowledge gaps were identified and outlined below:

1. A comparative analysis investigating the impact of a conventional torrefaction parameters on the physicochemical properties of torrefied biomass samples and CO<sub>2</sub> capture performance using SCG and CH is scarce in the literature. Furthermore, a few studies have validated the experimental findings of mass and energy yields with the simulated model developed using the Aspen-plus simulation technique.
2. Minimal studies are available that comprehensively evaluated and compared the thermal degradation pattern using different iso-conversional models and estimated the kinetics and thermodynamics parameters of the slow pyrolysis technique of SCG and CH, respectively.
3. Evaluating the influence of operating parameters, physical and chemical properties of low-cost lignocellulose biomass (SCG) on textural properties, surface chemistry, and aromatic structure of biochar for breakthrough CO<sub>2</sub> capture performance is missing from the literature.
4. Examining the impact of AC production conditions from SCG using the Box-Behnken (BBD) methodology is scarce in the literature. Comparative analysis of different thermal treatment techniques (torrefaction and slow pyrolysis) for the two-step physical activation process is missing. To the best of our knowledge, functionalized AC samples derived from SCG impregnated with DES to examine their potential to capture CO<sub>2</sub> under simulated flue gas compositions are very limited.
5. Study related to a comprehensive economic and sensitivity analyses study of the thermal conversion of SCG as a potential lignocellulose-based precursor to synthesize AC is undetermined. Comparing the overall cost of pristine and DES impregnated AC production from SCG with commercially available AC require attention.

### **1.3 Hypothesis**

The following hypotheses are outlined based on the knowledge gaps identified above:

1. The torrefaction of SCG and CH over a varied range of process conditions will reflect the transformation in physicochemical properties and their suitability for CO<sub>2</sub> capture. Also, a comprehensive torrefaction model of SCG and CH would provide theoretical information on the change in mass and energy yield after the thermal treatment. The validation of the theoretical findings with the experimental values are desirable to scale up the technology and bridge the gap between academia and industry.
2. The thermal degradation pattern, kinetics, and thermodynamic analyses of SCG and CH using the thermogravimetric analysis (TGA-DTG) technique would add value to comprehend the role of precursors and pyrolysis process parameters on decomposition pattern as well as are crucial for optimizing the thermal conversion technique. In addition, it would help to identify the promising precursor for further high temperature valorization and application.
3. Understanding the role of surface chemistry on CO<sub>2</sub> removal performance along with the textural properties of the SCG derived biochar samples could shed light upon the interaction between the CO<sub>2</sub> molecules and the basic functionalities or aromatic structure in biochar under simulated post-combustion scenario.
4. Optimizing the activation parameters using statistical tool could help comprehend the impact of the process parameters on textural properties and total AC yield. Furthermore, it is anticipated that the low-cost and non-toxic DES on AC's surface could help enhance the CO<sub>2</sub> capture performance than pristine AC (AC-CO<sub>2</sub>).
5. Assessing the economic viability of thermochemical conversion technology is necessary. Techno-economic sensitivity analyses would help determine the economic feasibility of the overall multi-stage thermal conversion of SCG to generate AC.

### **1.4 Research Objectives**

The abundance of coffee residues generated from the coffee industries due to its increasing demand and availability and the need for attention to environmental remediation by controlling the atmospheric CO<sub>2</sub> emission using carbon-based adsorbents mainly AC as well as the necessity to propose an economically viable thermochemical conversion technology is the motivation behind

this Ph.D. research. The underlying principle behind this research was to: undergo mild (torrefaction) to the extreme (slow-pyrolysis) thermochemical treatment of SCG and CH to synthesize torrefied biomass and biochar samples, undergo kinetic and thermodynamic study of the slow-pyrolysis technique and compare the physicochemical characteristics of SCG and CH to select the promising precursor to produce biochar, converting biochar derived from SCG to synthesize AC and functionalize the surface of the pristine AC with DES and study the influence on the removal of CO<sub>2</sub> under post-combustion conditions. Finally, determine the economic viability of the AC production from SCG. The Figure 1.1 presents the research objectives and sub-objectives performed in this study. The objectives and sub-objectives executed in each phase of this research work are outlined below.

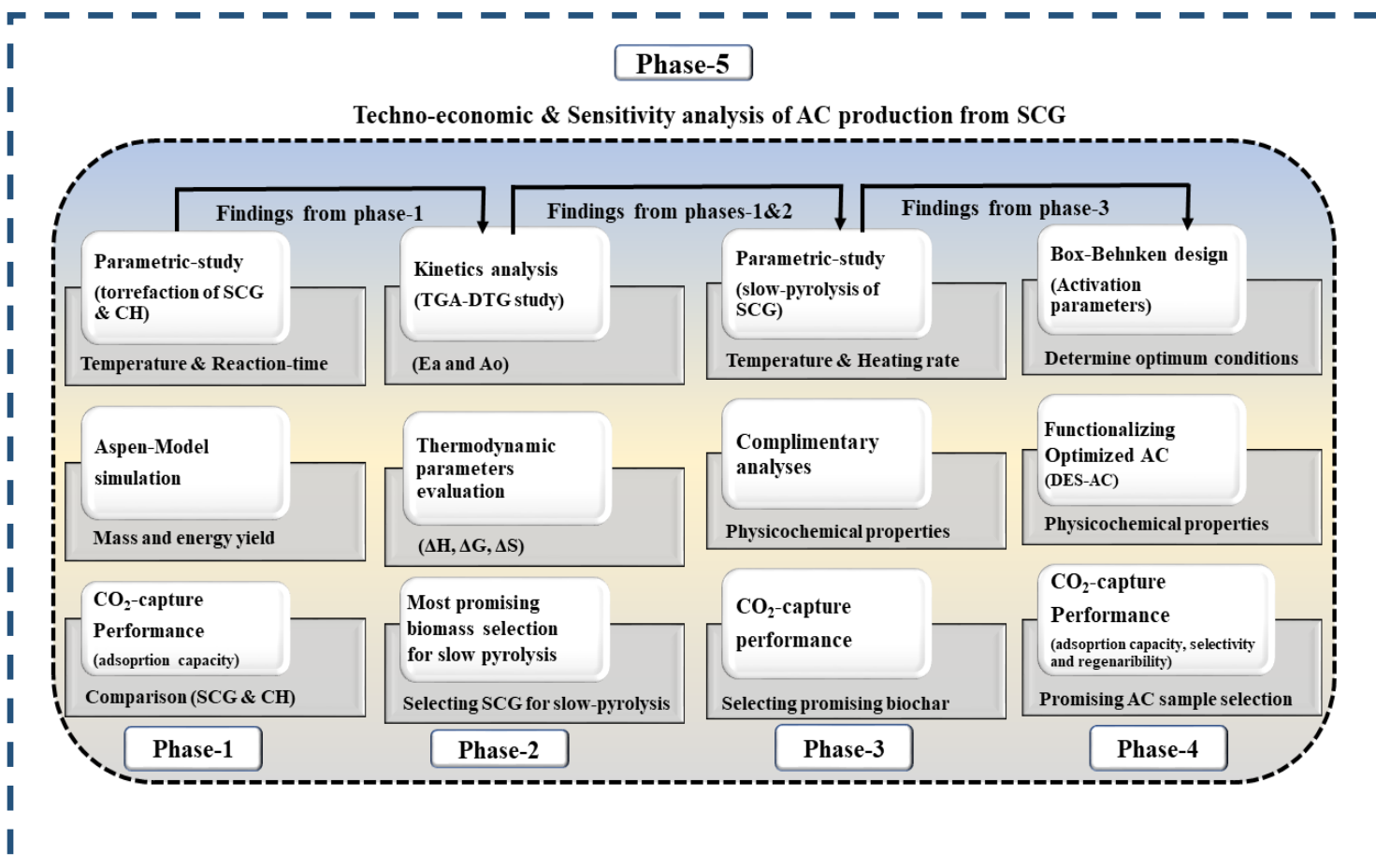


**Figure 1.1:** Schematic of different research phases of the thesis (phase 1-5).

**Phase 1:** To examine how torrefaction parameters effects the mass yield, energy yield, HHV, physicochemical characteristics, and CO<sub>2</sub> capture capacity of corresponding torrefied biomass samples.

- Impact of torrefaction temperature and reaction time on SCG and CH were investigated in terms of the transformation in the physicochemical properties in biomass samples through various complementary analytical techniques.
- Use of Aspen plus v12.1 (Aspen Plus®) to simulate, develop and validate the experimental mass and HHV of the corresponding torrefied biomass samples synthesized over a wide range of torrefaction conditions.
- Use of the most promising torrefied biomass samples for comparative evaluation of CO<sub>2</sub> capture performance under simulated post-combustion conditions.

**Phase 2:** Conduct the kinetics and thermodynamic studies of the slow pyrolysis technique and study the thermal decomposition pattern of SCG and CH using the Matlab®.

- Characterize the feedstock in terms of physicochemical properties and correlate the thermal degradation pattern during slow pyrolysis using a TGA-DTG analyzer with their physicochemical properties.
- Evaluate the kinetic parameters, including pre-exponential factor ( $A_0$ ) and activation energy ( $E_A$ ) using different iso-conversional models and determine the thermodynamic parameters ( $\Delta H$ ,  $\Delta G$  and  $\Delta S$ ) at different conversions for SCG and CH, respectively.
- Compare the thermochemical conversion efficacy of the precursors in terms of energy requirement and physicochemical properties to select the promising precursor for further valorization.

**Phase 3:** To identify the potential of biochar produced through slow pyrolysis using SCG for CO<sub>2</sub> removal.

- Examine the influence of significant pyrolysis process parameters on biochar yield (wt. %) and specific surface area ( $S_{BET}$ ) of the corresponding biochar samples.
- Using complimentary analytical techniques, assess the impact of pyrolysis temperature on the textural characteristics and surface chemistry of the corresponding biochar samples.

- Evaluate the impact of varying column temperatures and initial CO<sub>2</sub> concentration on CO<sub>2</sub> removal performance and choose the promising biochar sample for further activation.

**Phase 4:** Examine the influence of activation parameters (activation temperature, holding time and CO<sub>2</sub> flow rate) to optimize the specific surface area and total AC yield. This is followed by a detailed CO<sub>2</sub> capture performance in presence of simulated flue gas composition under post-combustion scenario.

- To examine the influence of activation factors on specific surface area and activated carbon yield using the statistical tool (BBD) methodology.
- Comparative evaluation of thermal treatment techniques for two-step physical activation in terms of specific surface area ( $S_{BET}$ ) and breakthrough CO<sub>2</sub> adsorption performance.
- Evaluating and comparing the influence of tailoring the surface of pristine AC with DES on the physicochemical characteristics and CO<sub>2</sub> capture performance in terms of adsorption capacity, selectivity, and regeneration study (multiple adsorption-desorption cycles).

**Phase 5:** Perform techno-economic and sensitivity analyses of AC production using SCG through thermochemical conversion techniques.

- Design and simulate the conversion of SCG to produce AC through different scenarios and perform the techno economic analysis (TEA) of different production scenarios derived from the 3<sup>rd</sup> and 4<sup>th</sup> phases using the Aspen Plus® (v12.1) simulation tool.
- Conduct the sensitivity analysis of the AC production routes using SCG and execute a comparative economic evaluation of the AC in terms of minimum selling price (MSP) with the data reported in the literatures.

### **1.5 Organization of the thesis**

The College of Graduate and Postdoctoral Studies (CGPS) provided guidelines for manuscript-style thesis and is followed in this regard to format the manuscript-style thesis. The thesis starts with an introduction and research background with literature review provided in chapters 1 and 2, respectively. This is followed by highlighting knowledge gaps identified from a detailed comprehensive literature review (as discussed in Chapter 2), hypothesis and research objectives presented in Chapter 1. Chapter 2 (Journal of Environmental Sciences) has been published as a

review article. It should be highlighted here that an extensive portion of this thesis consists of published manuscripts. Therefore, the original manuscripts have been altered accordingly to include in this thesis. The manuscripts described in Chapters 4 (ACS Omega), 5 (The Canadian Journal of Chemical Engineering), 6 (The Journal of Environmental Chemical Engineering) and 8 (Energy and Conversion Management: X) were all published to peer reviewed journals. With an intention for possible publication of **Chapter 7** (The Journal of Environmental Chemical Engineering) and is submitted to a peer reviewed journal (status: accepted with revision).

### **1.6 Manuscript content of the thesis**

How all aforementioned research objectives have been addressed in this thesis are presented below. However, the use of manuscript-style thesis structure and written format can cause in overlap amongst parts of the research objectives and sub-objectives. Therefore, the introduction, results and discussion parts are modified (either extended or simplified) in this thesis when needed to minimise possible redundancies.

**Chapter 2** is written based on the comprehensive literature review studied for this thesis.

**Chapter 3** demonstrates in detail the experimental procedure including the precursor collection and pre-treatment, materials used, set-up used and experimental procedure (CO<sub>2</sub> activation, DES preparation, and impregnation of AC using DES) and CO<sub>2</sub> capture performance. Moreover, in Chapter 3, analytical techniques used to characterise the precursors and the products (torrefied biomass samples, biochar, pristine and DES functionalised AC samples) have been described. The adsorption capacity and selectivity of the CO<sub>2</sub> capture performance are also mentioned in this chapter. This is followed by highlighting the process safety analysis followed while performing each experimental run (thermal treatments). Finally highlighting subsequent chapters based on the research objectives and sub-objectives of this thesis.

**Chapter 4** investigates how the process parameters influence physicochemical properties, mass, and energy yield during torrefaction of SCG and CH. Furthermore, the influence of process parameters in torrefied biomass samples was also assessed in terms of transformation in textural characteristics, surface properties using complimentary analytical techniques and CO<sub>2</sub> capture performance under simulated flue gas stream.

**Chapter 5** compares the thermal degradation pattern of lignocellulosic-based precursor (SCG and CH) undergoing slow pyrolysis at varying heating rates using a TGA-DTG analyzer. Furthermore, kinetics and thermodynamic parameters were evaluated using different iso-conversional models, and the thermochemical conversion efficiency of the precursors were compared in terms of activation energy along with the physicochemical properties of the precursors to select the promising precursor for further thermal treatment.

**Chapter 6** purposes to select the best pyrolysis conditions to generate biochar with high specific surface area and tailored surface chemistry for CO<sub>2</sub> capture. This chapter investigates the influence of pyrolysis process parameters on biochar yield and specific surface area on the corresponding biochar samples. This is followed by examining the influence of pyrolysis temperature as one of the crucial pyrolysis parameters significantly affecting the physicochemical characteristics of the biochar samples derived from SCG using complimentary analytical techniques. Finally, examining the influence of column temperatures and CO<sub>2</sub> concentration followed by comparing the CO<sub>2</sub> capture performance of the biochar samples using flue gas composition.

**Chapter 7** aims to select the optimized AC production conditions and investigates how activation parameters, and their interactions could influence the specific surface area and AC yield during the activation process using CO<sub>2</sub> as the activating agent. Furthermore, the impact of torrefaction and slow-pyrolysis on two-stage physical activation was assessed in terms of textural properties and breakthrough CO<sub>2</sub> adsorption performance. Finally, in this chapter, the impact of DES impregnation on the change in surface and textural properties along with CO<sub>2</sub> adsorption behaviour was evaluated and compared with pristine AC in terms of adsorption capacity, selectivity and regenerability.

**Chapter 8** aims to suggest a conceptual design for SCG valorization as one of the potential feedstocks to synthesis AC. A detailed techno-economic assessment and sensitivity analysis of the AC production routes were evaluated and compared to propose a cost-effective production strategy and analyse the economic viability of the thermochemical conversion technology.

The overall conclusions of Chapters 4-8 are summarized and presented in **Chapter 9** and provides some possible research work as the future recommendations. The list of references used to undergo this research is presented in the "**List of References**" section. The appendices section (**Appendix A-G**) highlights the additional data and supporting information used in this study.

## **Chapter 2 Literature Review**

This section provides an overview of the thermochemical conversion and activation technologies available to valorize the lignocellulose-based waste biomass for biochar and AC production to capture recalcitrant CO<sub>2</sub>. The unique properties of carbon-based adsorbents favourable for CO<sub>2</sub> removal are also summarised. A review of different capture techniques, precursor types and activation methods affecting the physicochemical properties of activated carbon and CO<sub>2</sub> removal performance is also mentioned in this section.

Most of the content of this chapter have been published as a review article in the Journal of Environmental Sciences. The permission to use the article in this thesis has been obtained from the Elsevier as the journal holds the copyright as presented in Appendix G (Figure G.1).

### **Citation:**

**Mukherjee, A.**, Okolie, J. A., Abdelrasoul, A., Niu, C., & Dalai, A. K., (2019). Review of post-combustion carbon dioxide capture technologies using activated carbon. Journal of Environmental Sciences, 83, pp.46-63.

In addition, some portion of this chapter was presented at the following conference presentation and 3 minutes thesis (3MT) competition provided in appendix A.

### **Conference Presentation:**

**Mukherjee, A.**, Niu C., & Dalai, A.K., "Review on the performance of activated carbons from spent materials for carbon dioxide capture", oral presentation at 71st Annual Session of Indian Institute of Chemical Engineers (CHEMCON 2018), NIT-Jalandhar, India, December 27-30<sup>th</sup>, 2018.

### **Contribution of the Ph.D. Candidate**

Alivia: Conceptualization, writing the manuscript, and responding to reviewer's comments. Dr. Jude A. Okolie: Reviewing the manuscript. Dr. Amira Abdelrasoul, Dr. Catherine Niu and Dr. Ajay K. Dalai: coordinated the manuscript preparation, provided comments and supervised through discussions.



## 2.1 Introduction

The 20th century has witnessed explosive growth in population and energy utilization. This trend is likely to increase exponentially in the 21<sup>st</sup> century because of the rapid rate of industrialization. Presently, about 85% of the global energy demand is supplied by petroleum-based solid and liquid fuels such as gasoline, natural gas and coal (Nanda et al., 2016). Although fossil fuels have amplified worldwide industrialization in the past years, the amplified consumption has resulted in the increase of greenhouse gas (GHGs) concentration in the atmosphere, which is now a matter of global concern (Goel et al., 2016). Over the past decades, the catastrophic impact on the global economy and ecosystem due to GHGs includes a rise in global average temperature beyond the normal from 0.6 to 1°C (Saxena et al., 2014). In addition, the increase in water level in the sea, floods, and droughts have also become a severe threat to all people around the world, which needs to be evaded (Rashidi and Yusup, 2016).

Among various CO<sub>2</sub> contributors around the globe, about 60% is credited to large stationary emission sources, which include fossil-fuelled power plants, mainly thermoelectric power plants and industrial plants, cement industries, iron and steel mills, petrochemical industries, gas processing industries and refineries, that gratify diverse purposes such as generation of electricity, transportation and industrial sector (Yaumi et al., 2017). The previously mentioned stationary emission sources are considered the dominant contributor to the emission of greenhouse gases (GHGs) because of the combustion of fossil fuels and will likely remain so for the next several decades. For instance, electricity generation and agriculture and forestry account for 25% and 24% of the total CO<sub>2</sub> emissions (Yaumi et al., 2017). Additionally, due to its cheap and abundant nature, coal is widely used in thermal power plants and is considered one of the major emission sources. The emission can amount to 2249 lbs/MWh (Spigarelli and Kawatra, 2013). Figure 2.1 represents the emission of CO<sub>2</sub> from different industrial sectors. Additionally, the conditions of a typical flue gas stream emitted from the coal-fired plants and cement processes are also summarized and presented in Table 2.1.

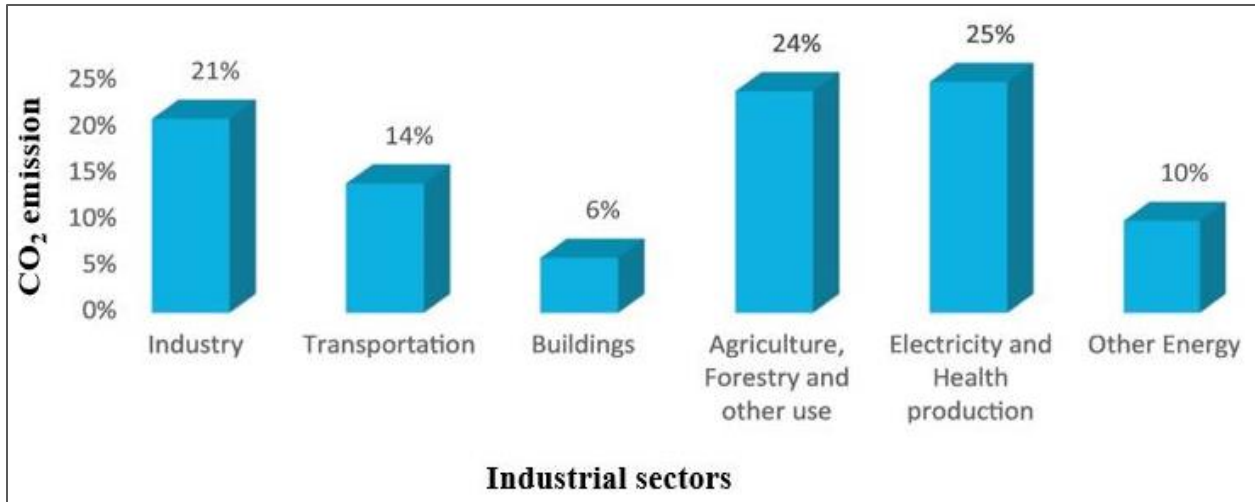


**Figure 2.1:** CO<sub>2</sub> emission from different industrial sectors (United States Environmental Agency, 2018).

In 2014, the International Panel on Climate Change (IPCC) confirmed that global warming and the associated climate change because of the greenhouse gas effect is caused by increased anthropogenic activities. Humans are endangered by two significant problems in the form of global warming and climate change caused by anthropogenic activities such as the release of carbon dioxide (CO<sub>2</sub>), nitrous oxide (N<sub>2</sub>O), methane (CH<sub>4</sub>) and water vapour (H<sub>2</sub>O) into the atmosphere since industrialization (Lee and Park, 2015). At present, CO<sub>2</sub> is 76% of the total source of greenhouse gases (GHGs); because of the enormous amounts released into the atmosphere as the by-product of the combustion of fossil fuels in power plants, it is found to be one of the most predominant anthropogenic greenhouse gases (GHGs) contributing to the global warming causing detrimental impacts on both the environment and ecosystem conditions (Siqueira et al., 2017) . According to the report by most world environmental organizations in May 2013, the alarming increase of the average carbon dioxide (CO<sub>2</sub>) concentration in the ambient air from 120 to 400 ppm volume (ppmv) from the beginning of the industrial revolution has become a primary contributor towards global warming scenario (Rashidi and Yusup, 2016).

**Table 2.1:** Flue-gas composition from coal-fired power plants and cement process (Rashidi et al., 2016; Bosoaga et al., 2009; Granite and Pennline, 2002).

Components	Concentration* (Coal-fired power plants)	Concentration* (Cement process)	Kinetic diameter (nm)
N <sub>2</sub> (Vol %)	70-80		0.364
CO <sub>2</sub> (Vol %)	11-15	14-33% (w/w)	0.330
H <sub>2</sub> O (Vol %)	5-12		0.280
O <sub>2</sub> (Vol %)	3-6	8-14 % (v/v)	0.346
SO <sub>2</sub> (ppm)	200-4000	<10-3500 mg/Nm <sup>3</sup>	0.360
SO <sub>3</sub> (ppm)	0-20		--
NO <sub>x</sub> (ppm)	200-800		0.317-0.340
CO (ppm)	50-<100		0.376
CH <sub>4</sub>	10		0.380
Hg/As (ppb)	1-7		--
<b>Flue gas process conditions</b>			
Temperature	25-180 °C		
Pressure	1 atm		

\* Before flue gas treatment-FGD and deNO<sub>x</sub>

The never-ending emission of GHGs gases like carbon dioxide (CO<sub>2</sub>) and methane (CH<sub>4</sub>) from both mobile and fixed sources led to the enforcement of the Kyoto Protocol in 2005, which has the sole purpose of reducing GHG to a minimum level in the atmosphere. The annual emission of CO<sub>2</sub> of 7 gigatons needs to be minimized by a factor of two-thirds by the end of this century. This is required to mitigate the effect of CO<sub>2</sub> on the environment in the coming decades (Stephens, J.C., van der Zwaan, 2005). This scenario has triggered intensive research, and countless organizations are finding alternatives to reduce the CO<sub>2</sub> concentration to reduce its harmful impacts on the rapidly changing climatic conditions (Gassensmith et al., 2011). CO<sub>2</sub> mitigation scenarios include reduction in fossil fuel burning, energy efficiency optimization, zero and low carbon energy supplies with carbon dioxide capture and storage units, renewable energy sources, and biological sinks (Wang et al., 2011). However, the associated countries of the United Nations Framework Convention on Climate Change (UNFCCC) suggested that one of the unprecedented measures to stabilize CO<sub>2</sub> in the atmosphere is to mitigate the CO<sub>2</sub> emission from large point sources of the energy-related sectors. Hence, to address the devastating effects of global warming, capture technologies of CO<sub>2</sub> from large point sources such as coal-based power plants, cement plants, and

natural and synthesis gas processing plants before direct sequestration is identified as a mid-term solution (Sengupta et al., 2015). In addition, the International Energy Agency (IEA) and the Organisation for Economic Co-operation and Development (OECD) forecast that CO<sub>2</sub> capture and storage (CCS) technology could contribute to the reduction of 14 vol% of CO<sub>2</sub> emission into the atmosphere (Lee and Park, 2015).

Carbon dioxide capture and storage (CCS) technology is an apparent comprehensive technology that will allow the continuing usage of fossil fuels until renewable energy technologies mature and can also stabilize the density of GHGs by 85% or more in the atmosphere. The basic concept of CCS technology is to capture high-density CO<sub>2</sub> emitted from industrial or energy-related sectors before emitting into the atmosphere, followed by compression, transportation to a storage site and sequestration or depositing it safely in the ground or ocean-bedrock sediment layer by a method that will permanently isolate it from the atmosphere and monitoring it continuously and possibly recycling the stored carbon dioxide for future use (Samanta et al., 2012). The CO<sub>2</sub> capture technology for fossil fuel-powered plants is the core of CCS and is classified as pre-combustion, post-combustion and oxy-fuel combustion capture technologies (Spigarelli and Kawatra, 2013). Post-combustion capture technique provides retrofit options for existing large point source emissions. However, the capture of CO<sub>2</sub> from fossil fuel-based power plants' flue gas accounts for three-fourths of the total cost of carbon capture and is one of the energy-intensive steps, and the rest one-fourth is accounted for the transportation and storage. The CCS technology can reduce the total cost of CO<sub>2</sub> capture, and to achieve mid-to-long-term CO<sub>2</sub> reduction approaches, cost-effective capture in a relatively concentrated stream focusing mainly on fossil fuel-based power plants and subsequent sequestration options need to be researched, keeping in view the progressing energy demand globally (Mondal et al., 2012).

To date, a range of integrated post-combustion capture technologies has been designed and built to mitigate the emission of CO<sub>2</sub> and the associated global warming problems by capturing it from the flue gas mixtures such as membrane-based separation, cryogenic separation (Song et al., 2012), physical and chemical absorption (amine scrubbing) (Spigarelli and Kawatra, 2013), solid adsorption (physical and chemical) (Dantas et al., 2011), etc. Among these, chemical absorption with an aqueous amine-based solvent such as MEA (mono-ethanolamine) is one of the current benchmark technologies in terms of CO<sub>2</sub> capture technologies because of its high process

efficiency and has been performed in the industries for over 60 years (Ben-Mansour et al., 2016; Shafeeyan et al., 2010). For several years, most of the commercial CO<sub>2</sub> capture facilities have used amine-based chemical absorption processes with mono-ethanolamine (MEA) to remove carbon dioxide from flue streams in natural gas, refinery off-gases, synthesis gas process and coal-based fossil fuel power plants, which suffer from several shortcomings, including the requirement of enormous energy and cost for solvent regeneration, equipment corrosion and degradation of absorbent. Thus, the energy penalty associated with the absorption of CO<sub>2</sub> using amine is the leading technology challenge associated with it (Rashidi and Yusup, 2016). On the other hand, industrialists do not generally consider cryogenic distillation because of the considerable energy and cost the process demands.

Due to operational challenges and technical shortcomings associated with the existing technologies, adsorption is considered the emerging alternative to the current technology by several research groups. Adsorption using solid adsorbent allows exploring various solid sorbents prepared from inexpensive and abundantly available precursors making the CO<sub>2</sub> capture set-up cost-effective (Sengupta et al., 2015). But the goal is to prepare easily regenerable and durable solid sorbents by incorporating foreign particles to make the adsorption-mediated separation and capture of CO<sub>2</sub> from flue gases a cost-effective and successful approach on an industrial scale than the current technologies. Nowadays, arduous research focuses on the preparation of efficient CO<sub>2</sub> adsorbents such as activated carbon (AC) (Alabadi et al., 2015), zeolites (Akhtar and Saidina Amin, 2012), metal-organic frameworks (Wu et al., 2010) and nitrogen-enriched microporous polymers. Carbonaceous materials such as activated carbons are very competitive among these adsorbents. They are considered a promising porous motif because of their advantages, such as large specific surface area, wide availability, high thermal stability, and good chemical resistance (Dodevski et al., 2017).

Activated carbon (AC) offers tuneable textural characteristics crucial for CO<sub>2</sub> capture from flue gas streams under the post-combustion scenario. Additionally, AC demonstrates excellent potential in providing a wide variety of surface functional groups favourable in the adsorptive process. The purpose of activation is to modify the textural properties of carbon-based precursors through opening new pores or changing the existing pores. Furthermore, activation can alter the surface chemical nature of AC with specific unique characteristics. Understanding the influence

of both textural properties and surface chemistry is crucial as the physicochemical properties of AC influence the adsorption capacity. However, many investigations have been reported demonstrating the role of textural properties in terms of specific surface area on CO<sub>2</sub> adsorption. Activation techniques are broadly categorized into two main methods based on the activating agents used: physical and chemical activations. Both physical and chemical activation techniques are performed to modify the textural and surface properties and exert significant influence on the properties of carbon-based materials. In general, physical activation of biochar is performed at a higher activation temperature (>700 °C), and it consists of oxidation of carbon-based material in the presence of oxidizing agents such as air, steam (H<sub>2</sub>O) or CO<sub>2</sub>. Among the oxidizing agents, CO<sub>2</sub> is often favoured owing to its lower reactivity at higher activation temperature, rendering the activation process easier to regulate (Firdaus et al., 2021). Moreover, CO<sub>2</sub> activation has displayed the potential of developing narrow micropores in the early stage of the activation process, unlike steam activation, which owing to its higher reactivity, enhances the broadening of micropores. On the other, chemical activation comprises several steps, including one thermal treatment of the precursor with several chemical approaches, including impregnation, and washing. Different activation agents have been studied traditionally in the literature, such as potassium hydroxide (KOH), phosphoric acid (H<sub>3</sub>PO<sub>4</sub>) or zinc chloride (ZnCl<sub>2</sub>). Among the chemical activating agents, NaOH and KOH have been the most preferred chemical agents used to modify the surface (Shahkarami et al., 2015a). Most recently, Rashidi and Yusup (2016) reviewed the current performance of the AC for CO<sub>2</sub> capture in relation to activation techniques and CO<sub>2</sub> adsorption capacity. However, the paper was focused on post-combustion CO<sub>2</sub> capture by AC and did not provide a comparative analysis of the three CO<sub>2</sub> capture technologies together.

Biomass can be transformed into value-added products like biofuels, green chemicals and solid adsorbents owing to its abundant availability and interesting inherent physicochemical properties. For instance, coffee is one of the significant agricultural products and the second-largest commodity exported worldwide after petroleum (Anastopoulos et al., 2017). With growing demand and consumption of coffee, low-value residues are generated and are usually discarded in landfills in Canada. The primary coffee residues generated mainly include coffee husk (CH) and spent coffee grounds (SCG). Conversely, the coffee residues generated could be valorized to produce value-added products through thermochemical conversion pathways. Also, coffee residues (SCG and CH) were used as the lignocellulosic precursors to synthesize carbon-based

adsorbents, biofuels and fertilizers that can be utilized for environmental remediation like CO<sub>2</sub> capture from post-combustion capture facility (Janissen and Huynh, 2018). In this regard, biomass can be transformed through various thermochemical conversion techniques (e.g. torrefaction, pyrolysis and activation) (Okolie et al., 2021a). The thermochemical pathway uses heat and chemical energy to decompose biomass compounds and organic waste into sustainable fuels. Thermochemical conversion routes have several advantages, such as short residence time, high conversion efficiency and the ability to use several lignocellulose-based feedstock that are abundant and cheap, making the valorization pathway cost-effective (Okolie et al., 2020a). Compared to all other thermochemical conversion techniques, torrefaction and slow pyrolysis is of interest for this study and could be attributed to the following reasons. Firstly, torrefaction and slow-pyrolysis of biomass feedstock generate solid residue, also known as torrefied char and biochar, and the aqueous phase also referred to as bio-oil and non-condensable gas (mainly syngas) in an inert environment (mainly in the presence of N<sub>2</sub>) without the usage of sophisticated equipment or costly chemicals. The thermochemical conversion pathway is primarily influenced by different operating factors but mainly by the feedstock type, pyrolysis temperature, heating rate and reaction time (Mishra and Mohanty, 2018). The products generated from pyrolysis, mainly biochar, can be readily used to substitute fossil-based energy sources owing to their longevity and ease of transportation, making them a highly attractive alternative for generating clean fuel, especially for environmental-related issues (Hu et al., 2016). In addition. The solid by-products derived from torrefaction and slow pyrolysis are also used to produce solid adsorbents that are mainly explored for environmental remediation. For instance, biochar derived from slow pyrolysis of lignocellulose biomass has been used to synthesize AC for CO<sub>2</sub> removal (Shahkarami et al., 2015b). In this regard, the production of AC from lignocellulose-based biomass through different thermochemical conversion pathways would be an economical approach as it will also allow the usage of abundant and cheap precursors that are usually discarded in a landfill.

Despite the popularity of this topic and the vast importance of GHGs reduction to our environment, limited studies have been reported on the advantages and limitations of the three major CO<sub>2</sub> technologies. This provides a current understanding of the three leading present carbon dioxide capture technologies and the unattended challenges associated with post-combustion capture technology. This review discusses existing post-combustion capture technologies from large point source emissions. Despite the extensive laboratory works and theoretical studies on post-

combustion technology, there is no full-scale, cost-effective, and energy-efficient commercialization of this process in progress. Hence, there is a need to critically evaluate the techniques based on previous studies and existing literature and provide recommendations for further improvements. Different types of post-combustion carbon capture technologies such as adsorption and absorption are also detailed in the remaining portion of this study. Additionally, this review updates the recent performance of ACs as an efficient solid adsorbent in the post-combustion capture technology regarding surface modification, textural properties, and adsorption capacity are limited literature reviews available on them.

## **2.2 Carbon dioxide capture technologies**

CO<sub>2</sub> capture is the core of CCS technology. Depending upon the configuration of a fossil fuel-based power plants, CO<sub>2</sub> partial pressure and gas stream pressure, three approaches are envisaged by which CO<sub>2</sub> can be trapped and sequestered. Figure 2.2 presents an overview of the three main technologies for carbon dioxide capture. Referring to Figure 2.2, the CO<sub>2</sub> capture technologies are classified into three main capture technologies as pre-combustion, post-combustion and oxy-combustion CO<sub>2</sub> capture technologies (Kanniche et al., 2010). As the name implies, pre-combustion involves the capture of CO<sub>2</sub> in the synthetic gas or fossils before combustion is completed, and the fuel is converted into a mixture of H<sub>2</sub> and CO (Syngas). It is mainly employed in integrated gasification combined cycle (IGCC) plants, fertilizer, or hydrogen production plants (Samanta et al., 2012). The separation process utilizes low-cost physical solvents such as rectisol, exploiting a moderate amount of energy compared to post-combustion capture (Mondal et al., 2012). In the pre-combustion process, the fuel conversion process prior to combustion is a more complex process and demands a considerable cost (Ben-Mansour et al., 2016). While in the post-combustion process, the CO<sub>2</sub> is captured in the flue gas after the combustion of fuel is completed. Whereas, in the oxy-fuel combustion process, fuel is combusted in a mixture of highly purified oxygen (> 95%) and recycled flue gas to produce a mixture of CO<sub>2</sub> and water vapour ready for sequestration (Buhre et al., 2005). The process demands substantial energy to separate oxygen from the air. Among all the current technologies, post-combustion carbon capture is a feasible capture technology because it can be applied to the existing emission technologies without employing significant changes to them. The Table 2.2 represents a comparative analysis between pre-combustion and oxy-fuel combustion CO<sub>2</sub> capture technologies.



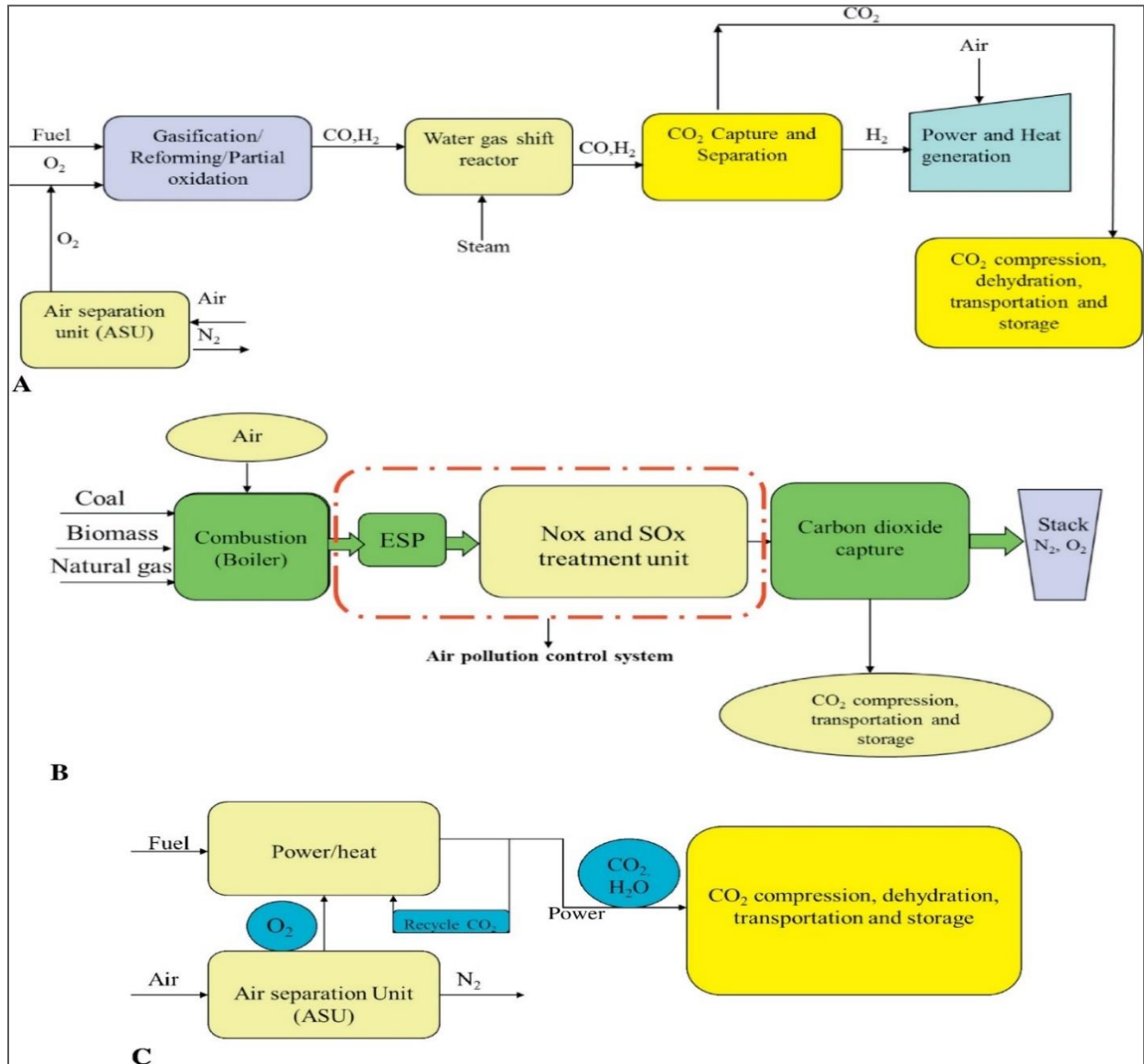


**Figure 2.2:** (A) Pre-combustion CO<sub>2</sub> capture technology, (B) post-combustion CO<sub>2</sub> capture technology and (C) oxy-fuel CO<sub>2</sub> capture technology.

**Table 2.2:** Comparative analysis of pre-combustion and oxy-fuel combustion carbon dioxide capture technologies.

<b>CO<sub>2</sub> capture technologies</b>	<b>Advantages</b>	<b>Disadvantages</b>
<b>Pre-combustion capture technology</b>	The process enables the production of carbon-free fuel and CO <sub>2</sub> capture at high-pressure conditions.	The process has a limitation of high cost and greater risk.
	A wide range of hydrocarbon fuels such as petroleum, coal, natural gas, and biomass can be used.	The process seems complicated due to the mandatory requirement of the Fuel conversion before the combustion into syngas.
	Syngas, the main product of pre-combustion capture, can be used in a combined cycle to generate power or as feedstock for synthesizing a wide range of chemical	
<b>Oxy-fuel combustion capture technology</b>	The process allows the production of a very high purity CO <sub>2</sub> stream. Compared to other CO <sub>2</sub> removal technologies, it is easier to purify the stream once trace contaminants have been removed.	High capital cost requirements are significant because of the need for a considerable amount of electric power required to separate oxygen from the air.
	There is a substantial reduction in NO <sub>x</sub> emission during the oxy-fuel combustion process. Aside from the advantages this poses to the environment, a decrease in NO <sub>x</sub> also reduces the exit gas flow rate, significantly reducing all equipment's size and capital cost.	There are a lot of risk and safety issues related to oxygen management and its effect on the boiler.
	In terms of flexibility in design and operation, oxy-fuel combustion has the potential for storage of energy through cryogenic liquids, and it is also non-intrusive in the steam turbine cycle	

### **2.3 Current state in post-combustion capture technology**

The post-combustion involves the capture of CO<sub>2</sub> from treated flue gas and is widely deployed in the chemical processing industries. The post-combustion capture technology can be retrofitted to the existing large point source of fossil fuel power plants, cement manufacturing industries, or refineries. These are the primary source of CO<sub>2</sub> emission in the atmosphere. It mainly uses wet/dry adsorbents and the principle of adsorption/desorption to collect and capture carbon dioxide. In post-combustion capture technology, the exhaust stream is treated before combustion to reduce the concentration of secondary species in the flue gas, such as nitrogen oxide (NO<sub>x</sub>), sulphur oxide (SO<sub>x</sub>), water vapour and particulate matter as it might significantly affect the operation, even if present in dilute concentrations (Spigarelli and Kawatra, 2013). The capture plant is often located between the stack and the flue gas desulfurization unit. At this point, flue gases are maintained at near atmospheric pressure and temperature in the range of 50–150 °C (Chen et al., 2013) and represent between 10% and 15% by volume of CO<sub>2</sub> concentration (Hornbostel et al., 2013). CO<sub>2</sub> from conventional thermoelectric power plants is often subjected to post-combustion capture. The fuel is burned to produce a flue gas and the subsequent compression, transportation and separation or sequestration of CO<sub>2</sub> from the flue gas. The Figure 2.2 shows how the flue gas from a coal-fired plant is treated using post-combustion technology. The hot flue gas is made to flow through an electrostatic precipitator (ESP) after leaving the boiler. At the ESP, most of the large particulate matter is removed. After leaving the ESP, the gas is sent to a flue gas desulphurization (FGD), where a limestone slurry contractor is used to absorb SO<sub>2</sub> gas to meet the local environmental specification. Carbon capture technologies such as adsorption, absorption or membrane separation are applied to treat the flue gas in order to remove the CO<sub>2</sub> from the flue gas exiting the FGD unit (Merkel et al., 2010).

Despite the number of advantages, the process must overcome the technical challenges before implementation on a commercial scale can become a reality. Researchers are putting in arduous efforts to address the technical challenges associated with it to make the CO<sub>2</sub> capture technology efficient in terms of cost and energy. The Table 2.3 provides an insight into the advantages and disadvantages of post-combustion CO<sub>2</sub> capture technology.

**Table 2.3:** The advantages and disadvantages of post-combustion carbon dioxide capture technology.

SI No.	Post-combustion carbon dioxide capture technologies		Reference
	Advantages	Disadvantages	
1.	Most easily applied technology for existing sources of emissions. Considered one of the essential green and economical technologies	Require the development of efficient adsorbents (dry) for relatively concentrated streams to make it more efficient in terms of cost and energy.	(Mittal et al., 2015)
2.	An effective means of reducing the density of greenhouse gases can be applied to existing power plants after retrofitting	Limited availability of ideal sorbent for post-combustion carbon dioxide capture	(Hornbostel et al., 2013)
3.	Compatible with retrofitted combustion technologies without radical changes in them.		(Tiwari et al., 2017)
4.	Its maintenance does not require stopping the operation of the plant and can be regulated or controlled easily.	The additional energy required to compress the captured carbon dioxide, the need for treatment of high gas volumes as to the partial pressure, and the concentration of carbon dioxide is low in the flue gas, the enormous energy requirement for the regeneration of sorbent, e.g., Amine solvent.	(Ben-Mansour et al., 2016)
5.	Post-combustion capture technology has higher thermal efficiency for conversion to electricity		(Mondal et al., 2012)
6.		Development of suitable solid adsorbent to make the process effective	(Titinchi et al., 2014)
7.		In post-combustion CO <sub>2</sub> capture applications, the gas mixture to be	(Zanco et al., 2017)

		separated is composed predominantly of CO <sub>2</sub> /H <sub>2</sub> and CO <sub>2</sub> /N <sub>2</sub> , respectively. However, the presence of other secondary species is inevitable and can significantly affect the separation, even if present in dilute concentrations, so pre-treatment of the flue gas is a must	
8.	The use of activated carbon (AC) as one of the adsorbents makes the process environmentally friendly.	In post-combustion, the operating temperatures are low. As a result, the appropriate solid adsorbents that can be used for this purpose are limited to activated carbon and zeolites, as these adsorbents belong to the low-temperature application.	(Rashidi and Yusup, 2016)
9.	It is widely believed that post-combustion technologies present the most significant near-term potential for reduction of CO <sub>2</sub> emissions because they can be retrofit to existing fossil-fuelled power plants and may be applied to other industrial emitters of CO <sub>2</sub> as well (e.g., the cement industry and iron and steel production)	The CO <sub>2</sub> is captured from low pressure (1 bar) and low CO <sub>2</sub> content (3–20 vol%) gas streams, often at high temperatures (120–180 °C) containing the impurities SO <sub>x</sub> and NO <sub>x</sub>	(Spigarelli and Kawatra, 2013)
10.	These technologies have the most significant potential for reduction of CO <sub>2</sub> emissions in the short term		(Bonaventura et al., 2017)

## 2.4 Overview of the ongoing research in post-combustion carbon dioxide capture technology

Several separation technologies for CO<sub>2</sub> post-combustion capture from flue streams have been investigated and developed to mitigate the harmful effects of global warming. In terms of the mechanism, generally, they are categorized as wet/dry absorption (Aaron and Tsouris, 2005), membrane separation (Lv et al., 2012), cryogenic distillation (Chapel et al., 1999), microalgal bio-fixation (Pires et al., 2012), condensed centrifugal separation and dry adsorption (Aaron and Tsouris, 2005). CO<sub>2</sub> separation on a large scale is an essential task in many industrial processes. For instance, for the scrubbing of CO<sub>2</sub> from petroleum industries, the post-combustion amine-based solvent systems, mainly mono-ethanolamine (MEA) are commercially used. Capturing CO<sub>2</sub> using physical or chemical absorption technology is a process whereby slightly acidic carbon dioxide is embedded from flue gas into amines-based solvents to form dissolved carbamates and bi-carbamates by chemical means until equilibrium is reached. Chemical absorption utilizes mono-ethanolamine (MEA) and other amine-based solvents such as diethanolamine (DEA), tri-ethanolamine (TEA) diglycolamine (DGA), N-methyl diethanolamine (MDEA), and 2-amino-2-methyl-1-propanol (AMP), glucosamine (GA) to dissolve CO<sub>2</sub> and the selection of the alkanol amines are done based on their ability to absorb CO<sub>2</sub> over the other gases such as nitrogen, oxygen or other flue gases (Aaron and Tsouris, 2005). According to the available works of literature, the amine-based regenerative chemical absorption process appears to be the most suitable method to treat large emission volumes from combustion, generating a concentrated CO<sub>2</sub> stream for requisitioning with almost 98% efficacy and is very useful for changing the density of CO<sub>2</sub>.

Though the absorption technology uses amine-based solvents in capturing CO<sub>2</sub>, it provides plenty of disadvantages in terms of a substantial amount of energy requirement for solvent regeneration, making the process a large consumer of auxiliary power and thus cost more (González et al., 2013). Additional method challenges often encountered include heated absorbents, materials erosion, slow solid-gas reactions, high corrosion, high energy intensity and amine degradation either through oxidative or thermal degradation (Mittal et al., 2015). In addition, the potential of the amine compounds to degrade and accumulate in the solvent phase results in insufficient CO<sub>2</sub> absorption capacity and kinetic rate. Therefore, it demands a regular injection of fresh absorbent, which increases operating cost. Additionally, the high volatility of the amine compounds could lead to the evaporation of a large portion of the chemical and water, which may enter the cleaner

flue gas, thereby releasing amines (as gas and liquid) and accordingly impact the ecosystem during the heating process (Ogungbenro et al., 2017). A wide range of potential materials and technologies for CCS applications has been suggested and explored to overcome the limitations of traditional chemical adsorption techniques.

Selective membrane separation of CO<sub>2</sub> involves the use of polymer or ceramic-based material or mixed matrix membranes to filter out the CO<sub>2</sub> gas faster at elevated pressure produced from a polymer such as a polyaniline (Illing et al., 2001) or polyethylene oxide (Lin and Freeman, 2004) ceramics or combination of both types of materials to allow successful permeation of CO<sub>2</sub> to the shell side along with their configurations specially designed for CO<sub>2</sub>/H<sub>2</sub> and CO<sub>2</sub>/N<sub>2</sub> selectivity in the flue gas. The separation of the gases relies on the nature of the membrane's physical and chemical properties, the diffusivity of gas molecules in the membrane and the gradient in partial pressures of gases (Yang et al., 2008). Membrane-based separation provides ease of operation with low energy consumption as its brighter side. On the other hand, the cryogenic CO<sub>2</sub> separation technique is based on liquid state temperature and pressure gradient in each gas present in the flue gas. CO<sub>2</sub> is cooled and condensed in this technique, thereby removing flue gases from the stream. Its initial investment is low and highly reliable as one of the post-combustion capture technologies. However, challenges are still there in applying these techniques on a large industrial scale. Cryogenic separations become unsuitable for the post-combustion method because of the vast number of impurities and incondensable gases in the flue gas coupled with the reduction in pressure of CO<sub>2</sub> at the post-combustion exhaust from coal/natural gas-fired boilers (Kanniche et al., 2010). Also, cryogenic distillation is not preferred by the industrialists because of the high energy consumption for refrigeration, which makes the process uneconomical for large plants.

Recently, there has been renewed interest in research areas about new post-combustion capture processes (Raynal et al., 2011). Some challenges, such as the high cost of post-combustion methods and the selection of appropriate techniques with lesser technical challenges to separate CO<sub>2</sub> from the flue gas, have been studied to provide maximum CO<sub>2</sub> separation and lower the capture cost. For repeated use, adsorption on porous solid adsorbents using pressure (PSA) or thermal swing approaches (TSA) for the removal of CO<sub>2</sub> from a mixture is considered a competitive post-combustion capture mechanism and a promising alternative to the amine scrubbing process that has been explored in the industry (Saxena et al., 2014). The adsorption

process is significant because it is reversible, and the adsorption efficiency can be improved by functionalizing the surface of the adsorbent materials (Saxena et al., 2014). Adsorption is considered as one of the emerging cost-effective options for CO<sub>2</sub> separation due to its advantages like reduction in regeneration energy requirement either by thermal or pressure modulation mainly attributed to the absence of amounts of water, effective in the dilute gas mixture, increased CO<sub>2</sub> carrying capacity, ease in terms of handling over a relatively wide range of temperatures and pressures, faster reaction rates and minimum pressure drop (Leung et al., 2014). In addition, the adsorption system is attractive since it can reduce the total maintenance requirements with reduced secondary waste generation and long-term stability, owing to the lower heat capacity of adsorbent compared to water and evading moisture removal from flue gas (Shafeeyan et al., 2010). However, the success of such an approach will depend on some imperative factors such as (i) ease of regeneration of adsorbed CO<sub>2</sub>, (ii) durability of adsorbent, (iii) selectivity of adsorbent for CO<sub>2</sub>, (iv) adsorption capacity and (v) stability of adsorbent once several adsorption/desorption cycles are carried out (Ben-Mansour et al., 2016). Table 2.4 provides a comparative analysis of the different available techniques for post-combustion CO<sub>2</sub> capture technology.



**Table 2.4:** Different post-combustion carbon dioxide capture techniques.

Post-combustion carbon dioxide capture techniques		Capture Efficiency (CO <sub>2</sub> )	Reference
<b>Chemical solvent scrubbing</b>			
<b>Advantages</b>	<b>Disadvantages</b>	90%	(Yang et al., 2008)
Maturity of technology	High thermal energy demand for solvent regeneration		
High capture efficiency	Cost of solvent		
Regeneration of solvent possible	Equipment corrosion Emissions related to solvent degradation.		
<b>Physical adsorption</b>		55-92%	(Mondal et al., 2012)
Reversible process	Cooling and drying of the flue gas		
Adsorbent recycling possible	High energy demand for CO <sub>2</sub> desorption		
High adsorption efficiency (> 85%–mainly with PSA)	High adsorbent temperature		
Resistant to long-term use	Influence of SO <sub>x</sub> and NO <sub>x</sub> on sorbent performance		
<b>Calcium looping</b>		>70%	(Dean et al., 2011)
Low energy efficiency loss (4–7%)	Attrition depending on raw meal/limestone hardness		
An up-and-coming technology for the cement industry due to heat recovery			
<b>Membrane separation</b>			
The process has been adopted for the separation of other gases	Influence of minor components (i.e., water, SO <sub>2</sub> ) on gas permeation performance		

High separation efficiency is achievable	High cost and high energy demand of compression equipment	Up to 90%	(D'Alessandro et al., 2016)
	Limited CO <sub>2</sub> purity and demand for large facility area		
<b>Biological capture with algae</b>			
Oil produced can be used as biodiesel or coal replacement	Need of process up-scaling to industrial level		(Packer, 2009)
Economically competitive compared to other capture technologies.	Creation of algae products and markets		

## **2.5 Criteria for selecting carbon dioxide capture adsorbent**

The capture and separation of CO<sub>2</sub> from a large volume of combustion gases are still expensive and characterized by colossal energy consumption; therefore, it is invaluable to develop efficient adsorbents for relatively concentrated streams to reduce the overall cost of the adsorption process. Presently, for post-combustion capture from large point sources, no ideal sorbent is available yet due to various shortcomings associated with low CO<sub>2</sub> capture capacity or selectivity under realistic pressure conditions or high cost, slow kinetics, and sensitivity to moisture. Hence, research studies are being geared toward developing advanced sorbents with lower regeneration energy, high adsorption/desorption rates and better stability for the cost-effective performance of adsorption (Rashidi and Yusup, 2016). There have been many different carbonaceous (activated carbon, carbon nanotubes) and non-carbonaceous solid adsorbents (zeolites, metal-organic frameworks, metal oxides-based adsorbents) available to remove CO<sub>2</sub> in post-combustion separation processes (Hedin et al., 2010). According to the literature, these sorbents have been successfully and vastly utilized for pressure swing adsorption (PSA), which has recently proven to be a promising technology even with low-cost technologies such as amine scrubbing. The adsorbents of CO<sub>2</sub> should meet the following requirements: (i) high CO<sub>2</sub> uptake, (ii) high adsorption rate, (iii) high selectivity against other molecules (i.e., N<sub>2</sub>) competing for adsorption sites, (iv) easy regeneration without any significant cyclic performance loss, (v) low operational cost and high availability, (vi) stable adsorption capacity of CO<sub>2</sub> after repeated adsorption/desorption cycles, (vii) adequate mechanical strength, (viii) high specific surface area, (ix) relevant pore size distribution and (x) tolerant towards moisture and impurities. For instance, non-polar adsorbents like activated carbon, the van der Waals forces with bonding energy between 5 and 10 kJmol<sup>-1</sup> are dominant, and the size and polarizability of adsorbate and pore size distribution of adsorbent (ultra-micropore or micropore) are the main factors for enhanced CO<sub>2</sub> removal performance.

### **2.5.1 Potential of activated carbon as carbon dioxide separator**

In post-combustion capture, adsorbents capable of performing at low-temperature conditions are preferred because the operating temperature ranges from low to moderate and pressure is maintained at atmospheric pressure. Activated carbon has been widely recognized as a potential adsorbent for low temperature recalcitrant CO<sub>2</sub> capture. This is attributed to the large specific surface area and small pores in the range of micropores or ultra-micropore. Compared with other

carbonaceous adsorbents such as zeolite, the AC has been deemed a superior adsorbent for CO<sub>2</sub> separation from the flue gas stream and could be attributed to its hydrophobicity that will avert the extra step of moisture removal before CO<sub>2</sub> adsorption. Also, AC is an excellent choice as carbonaceous adsorbents. They exhibit unique features, including superior CO<sub>2</sub> adsorption capacity, selectivity, and stability in adsorption–desorption cycles and low adsorption and desorption temperatures (below 373K). Moreover, high resistivity to alkaline and acidic conditions, an effective porosity network that assists in the adsorption process and gas diffusion into the interior side of AC, and ease in modification in terms of surface chemistry and physicochemical characteristics via pre- or post-modification method, aside from their low cost (Chen et al., 2013).

The adsorption capacity/quality of activated carbon depends significantly on the source of the precursors. The carbonaceous materials from non-expensive sources must possess a significant amount of carbon along with low ash and important volatile matter. This is because, during the heat treatment, the evolution of contained volatile matter will help form pores on the surface of activated carbon (Rashidi and Yusup, 2016; Herawan et al., 2013). A wide range of renewable, inexpensive carbonaceous precursors ranging from waste biomass (agricultural waste, wood, leaves, bagasse, various seeds, etc.), biochar, coal, and petroleum pitch to waste material such as scrap tires can be explored to prepare activated carbons (Serafin et al., 2017). Among all, biochar seems to be a promising candidate. It is highly desirable because it is highly porous and contains substantially fixed carbon which can be further processed (carbonized/activated) to produce microporous AC. Therefore, the selection of proper precursors before the preparation of activated carbon is essential since the composition of the material structure, such as carbon, hydrogen, nitrogen, oxygen, and sulphur, influences the physicochemical properties of the synthesized activated carbon. In addition, the origins of the raw material also play a significant role in the properties of activated carbon. Table 2.5 shows the ultimate and proximate analyses of different precursors of the activated carbon materials.

**Table 2.5:** Proximate and ultimate analyses of lignocellulose-based biomass for activated carbon production.

Precursor	Proximate analysis (wt. %)				Ultimate analysis (wt. %)					Reference
	Moisture	VM	Ash	FC*	C	H	N	S	O*	
Canadian pinecones (type I)	7.54	74.2	1.42	16.8	46.7	5.9	0.30	0.08	7.5	(Jain et al., 2014)
Canadian pinecones (type II)	2.66	71.12	1.89	24.33	49.48	6.05	0.52	0.09		
Petroleum coke		8.50			76.5	1.5	1.8	6.5	5.5	(Rambabu et al., 2015)
Cotton stalks	4.7	74.6	4.6	16.1	45.2	6.3	1.2	0.3	17.8	(Xiong et al., 2013)
Macadamia nutshell	10	71	0.4	18.6	57.5	5.9	0.3	0.06	36.2	(Bae and Su 2013)
Raw coconut shell	1.91				50.08	6.02	0.05	0.62	43.23	(Rashidi et al., 2014)
Barley straw		77.2	5	17.3	45.4	6.1	0.7	0.07	41.92	(Pallarés et al., 2018)
Coconut shell					50.08	6.02	0.05	0.62	43.25	(Rashidi et al., 2013)
Coconut fibre					45.86	5.72	0.42	0.61	47.40	
Olive stones		85.4	0.6	14						(Plaza et al., 2014)
Almond shells		82.3	1.3	16.4						
Spent coffee grounds		82.9	1.3		56.4	7.0	2.6	34	56.4	(Plaza et al., 2012)
Luscar char		83.7	3.76	0.11	78.34	2.07	0.85	0.01	5.14	(Azargohar and Dalai, 2005)

\*FC (calculated by difference):  $100 - (M + VM + Ash)$  wt.%, \*O (calculated by difference):  $100 - (C + H + N + S + Ash)$  wt.%.

Here, Moisture is denoted as M; Volatile matter is denoted as VM; Fixed carbon is denoted as FC.

From Table 2.5, it is evident that Macadamia nutshell, Canadian pinecones (type I and II), Barley straw and Cotton stalks among all can be the suitable precursors for the preparation of AC, formerly in terms of the high volatile matter content of approximately in the range of 71-74.6 wt. %. Extensive research has shown promising results in the post-combustion capturing CO<sub>2</sub> by using activated carbon at different temperatures and pressure. Both synthetic and natural adsorbents have been used for this process. AC has attracted much attention for capturing CO<sub>2</sub> from the post-combustion process because of its plenty, inexpensive precursors, ease of separation, and a wide range of pH coupled with its high porosity and large surface area and adsorption capacity. These salient features encourage the use of AC for CO<sub>2</sub> adsorption in various industrial processes. However, its utilization as an adsorbent for CO<sub>2</sub> capture is limited by its responsiveness to high-temperature conditions. At near power plant flue gas temperature, AC adsorption capacity drops drastically. To overcome the limitations, several studies on the modification of activated carbons and the synthesis of high-performance adsorbents to treat GHG gases have been carried out. One of the well-known methods is the use of metal oxides to modify activated carbon. Modifying the surface of AC with metal oxides may provide a structure with enhanced porosity, which can vary in pore structure and surface functional groups, thereby altering its adsorption properties.

Several studies have been carried out using different adsorbents, both synthetic and natural. However, AC has shown much promise in this process; hence, there is a need to critically evaluate various sources of AC to improve their adsorption properties. AC has numerous advantages as adsorbent for CO<sub>2</sub> capture, as mentioned previously. In addition, about 98% efficiency was observed in the capture of CO<sub>2</sub> using AC adsorbents (Liu et al., 2012). Table 2.6 outlines the advantages and disadvantages of AC as an adsorbent for CO<sub>2</sub> capture.

**Table 2.6:** An overview of the advantages and disadvantages of activated carbon as a CO<sub>2</sub> adsorbent.

Advantages	Disadvantages
It can be synthesized from any carbonaceous raw material containing high carbon content, which is a non-expensive resource.	The porosity of the AC depends on various factors like temperature and agent. Hence an optimum process needs to be developed to achieve the maximum surface area.
The manufacture of AC is not a cumbersome process. There are two methods: physical and chemical activation.	Sometimes, only pristine AC is not sufficient to capture CO <sub>2</sub> from the post-combustion process. So foreign martial needs to be added to increase the selectivity of CO <sub>2</sub> .
Separating AC from the process is relatively very easy	
AC can operate under a wide range of pH	
AC dose not react with various chemicals easily and hence it can resist corrosion.	
Easy to regenerate	
Activated carbons can be prepared in the form of granules, powders, fibers, or beads from suitable	
Thermosetting precursors by either physical or chemical means	

## 2.6 Pristine and functionalized activated carbon

This section distinguishes between modified and non-modified AC as adsorbents for CO<sub>2</sub> capture. Current research pertaining to the use of pristine and functionalized AC is also elucidated to differentiate between the two types of AC.

Pristine AC is simply AC manufactured from carbonaceous raw material via physical or chemical activation. The precursor is cut into small pieces, which are washed repeatedly to get rid of the unwanted dust particles. After cutting it into smaller dimensions, it is fed to the pyrolysis or carbonization reactor. In physical activation after carbonization, the char is activated in another reactor with a continuous flow of oxidizing agents such as CO<sub>2</sub>, O<sub>2</sub> or steam. In addition, it contributes to the enhancement of the textural surface characteristics of the carbon material. In chemical activation, the chemical agents that are used are basically dehydrating agents that enhance the yield of carbon by influencing pyrolytic decomposition. The chemicals react with the carbon chains forming a rigid matrix by cross-linking reactions. This step reduces the volatile loss which occurs during carbonization. Since this type uses chemicals, the produced activated carbon needs to be washed repeatedly before using it.

Non-modified AC is modified to change the surface chemistry of the adsorbent to enhance its basicity. The surface functionalization and formation of different compounds help in capturing CO<sub>2</sub> by increasing the adsorption capacity and selectivity. According to literature, the metal doping technique includes various ranges of metals starting from alkaline earth metal (Mg or Ca) to transition metals such as Cu, Cr, Ni or Fe have been explored to impregnate activated carbon to enhance its adsorption capability or improve its catalytic oxidation capability for CO<sub>2</sub> capture (Rashidi and Yusup, 2016). In addition, due to the acidic nature of CO<sub>2</sub> (weak Lewis acid), it is expected that introduction of Lewis bases onto the activated carbon surfaces may also favour the CO<sub>2</sub> capture performance (Shafeeyan et al., 2010).

The surface area, pore diameter and functional groups play a significant role in the adsorption of CO<sub>2</sub>. The specific surface area is determined by Brunauer–Emmett–Teller (BET) test. The surface area and the number of pores is interrelated. The higher the surface area, the greater the number of pores. The surface area, pore diameter and pore distribution depend on the thermal treatment of the AC. Activation temperature has a significant effect on the porosity of activated carbon. However, there is an intermediate optimum temperature range where the porosity is maximum



because, at low temperatures around 700°C, the micro-pores develop, which increases the surface area of the AC, whereas, at high temperatures of 1000 °C, the developed micro-pores fuse to form macro-pores. As a result, the surface area decreases. The process conditions for preparing activated carbon to directly affect the capture capacity. Table 2.7 describes in brief the preparation process of activated carbon from different precursors.

**Table 2.7:** CO<sub>2</sub> adsorption capacities of pristine activated carbon.

Precursor	Carbonization temperature	Activating agent	Activation temperature	Specific surface area, m <sup>2</sup> /g	CO <sub>2</sub> capture capacity, 1 bar (mmol/g)	Reference
<b>Physical activating agents</b>						
Coconut shell	-	CO <sub>2</sub>	900 °C	371	2.5 (25 °C)	(Rashidi et al., 2014)
					1.5 (50 °C)	
					0.4 (100 °C)	
Palm kernel shell	700 °C	CO <sub>2</sub>	800 °C	-	7.32	(Nasri et al., 2014)
Olive stone	-	CO <sub>2</sub>	800 °C	1215	3.1 (25 °C)	(Gonzalez et al., 2013)
Almond shell	-	O <sub>2</sub>	650 °C	557	2.1 (25 °C)	(Plaza et al., 2014)
Nutshell	700 °C	CO <sub>2</sub>	900 °C	573	3.5 (25 °C)	(Bae and Su 2013)
HTC biomass (grass cuttings)	-	CO <sub>2</sub>	800 °C	841	1.5	(Hao et al., 2013)
<b>Chemical activating agents</b>						
Spent coffee grounds	400 °C	KOH	600 °C	1082	3.0 (25 °C)	(Plaza et al., 2012)
Sawdust	-	KOH	600 °C	1260	4.8 (25 °C)	(Environ et al., 2011a)
Paulownia sawdust biomass	-	KOH	700 °C	1643	8.0	(Zhu et al., 2014)
HTC beer waste	-	H <sub>3</sub> PO <sub>4</sub>	600 °C	1073	0.80	(Hao et al., 2013)
Rice husk	-	ZnCl <sub>2</sub>	500 °C	927	1.3 (25 °C)	(Boonpoke et al., 2013)

### 2.6.1 Pristine activated carbon

Activated carbon can be prepared either by physical or chemical activation (Dodevski et al., 2017). The physical activation of the raw material has two different treatment stages: the carbonization under an inert atmosphere (Ar or N<sub>2</sub>) followed by the activation of char at oxidizing (high) temperature. This can be done by using steam or CO<sub>2</sub> as the source of activating agents. Among all the physical activating agents, CO<sub>2</sub> is preferred the most because it is inexpensive and contributes to the formation of ultra-micropores. It should be noted that single-stage activation can be more economical in terms of reducing the temperature and energy intensity due to dual cooling, operational costs and installation costs (Yaumi et al., 2017). Chemical activation involves impregnating the precursors or physically mixing the chemical compounds by dehydrating or chemical activating agents. The process involves only one step where both carbonization and activation co-occur using either alkali or metal salt-based chemical activating agents such as KOH, H<sub>3</sub>PO<sub>4</sub>, NaOH and ZnCl<sub>2</sub>. However, ZnCl<sub>2</sub> is not suitable for chemical activation due to zinc emissions in the environment. Solutions of H<sub>3</sub>PO<sub>4</sub> are made with the raw material, which is then inserted into the reactor. Furthermore, either wet impregnation or solid-solid mixing, chemical activation can be performed by wet impregnation. In chemical activation, the size of the activator plays an essential role in the formation of porosity in the carbon matrix. Also, the flow rate of steam/CO<sub>2</sub> significantly contributes to the development of porosity on the surface of activated carbon during physical activation. The pore formation mechanism is different in chemical than physical activation.

Shahkarami et al. (2016) investigated the effects of metal impregnation technology containing magnesium salt before and after activation. The result showed that the addition of metal oxide in a one-step and two-step process exploring steam activation enhanced the property of the carbon sorbent in terms of the development of micro- and mesopores. Sethia and Sayari (2015) took a mixture of trimethylsilyl imidazole (4.6 g, 0.033 mol) and chloroacetonitrile (4.9 g, 0.033 mol) and stirred it at room temperature for 24 hr under an inert atmosphere to form 1,3-bis (cynomethyl imidazolium) chloride a white solid material. The solid was washed with diethyl ether (three 30 mL) and dried under vacuum for 24 hr to form the raw material for activated carbon. A wide range of activation conditions, including the KOH to carbon weight ratio (1–2), temperature (550–700°C) and time (1–2 hr), were explored to generate activated carbons with adjustable pore sizes and nitrogen contents. The optimized materials exhibited unusually high nitrogen content (22.3 wt.%) and high surface area (1317 m<sup>2</sup>/g), in addition to a large pore volume (0.27 cm<sup>3</sup>/g) comprised of ultra-micropores less than 0.7 nm in diameter.

This material showed an extraordinary CO<sub>2</sub> uptake of 23.7 wt% (5.39 mmol/g) at 25°C, and 1 bar, one of the highest uptakes reported for any activated carbon. Its CO<sub>2</sub>/N<sub>2</sub> selectivity at 25°C was 237 and 62 at 0.01 and 1 bar, respectively (Sethia and Sayari, 2015). Thus, from this study, it is evident that chemical activation also leads to efficiency in the adsorption of CO<sub>2</sub>. The affinity of the AC was also found to be substantial. Table 2.6 shows the different non-modified AC produced from various sources and their CO<sub>2</sub> adsorption capacities.

### **2.6.2 Chemically functionalized activated carbon**

The adsorption capacity of AC significantly increases with the impregnation of various foreign particles onto the carbon matrix that contributing to the enhancement of the basicity of the solid sorbent in terms of chemical reaction at elevated temperature. The use of the metal impregnation technique is called wet impregnation, where an inorganic salt containing specified metal, as mentioned, is mixed with the carbon material that alters the surface chemistry. Yadavalli et al. (2017) used Douglas fir sawdust pellets as the raw material for the chemical activation of AC. The precursor was soaked at room temperature (25°C) in phosphoric acid solution (85% mass fraction aq. soln.) with a 1.5:1 mass ratio of acid to biomass. To modify the AC, 100 g of unmodified AC was mixed with a saturated solution (25°C) of ammonium sulphate salt prepared using 5, 7.5 and 10 g of dry ammonium sulphate. This carbon adsorbed 97% carbon dioxide from the inlet stream containing methane and other gases with a carbon dioxide over methane selectivity of 5.27. The highest breakthrough and exhaustion times of 3.5 and 13.5 min, respectively, were obtained.

The one-hour exposure of the used carbon at 105°C regeneration removed a majority of the carbon dioxide and methane on the carbon surface, facilitating regeneration. The addition of various functional groups on the surface of the AC by the addition of acid or alkalis can affect the chemistry. The thermal and chemical treatment can be manipulated during the modification of AC for specific applications (Chingombe et al., 2005). The surface of the AC must be evaluated thoroughly to increase the affinity towards CO<sub>2</sub> selection from a mixture of gases after the post-combustion process. In general, the modification of AC takes place after the activation has been carried out. The modification process can be classified into three types: heat treatment, chemical impregnation, or biological modification (Yin et al., 2007). CO<sub>2</sub> is considered a weak Lewis Acid, and the adsorption capacity depends on the surface chemistry of the solid material. Thus, basic functional groups are preferable on the surface of the AC, which increases the affinity of the CO<sub>2</sub> capture, and the acidic functional groups must be

substituted by basic functional groups (Shafeeyan et al., 2010). Introducing nitrogen-containing groups, sulphur and other metals or amines groups will enhance the basicity of activated carbon due to the contribution of delocalized pi electrons and unsaturated valences in the carbon matrix by them (Yaumi et al., 2017). Table 2.8 shows the CO<sub>2</sub> adsorption capacity of AC impregnated with various functional groups and metals.

**Table 2.8:** CO<sub>2</sub> adsorption capacities using chemically modified activated carbon species.

Precursor	Surface modification	Specific surface area, m <sup>2</sup> /g	CO <sub>2</sub> capture capacity (mmol/g)	Reference
Cotton stalk	NH <sub>3</sub> treatment at 900 °C	435	1.8 (25 °C)	(Xiong et al., 2013)
Coconut shell activated carbon	Cu impregnation at 900 °C	1339	0.4 (50 °C)	(Yi et al., 2014)
Commercial activated carbon	Pre-oxidation NH <sub>3</sub> treatment at 800 °C	826	1.6 (25 °C)	(Shafeeyan et al., 2011)
Bagasse activated carbon	Aniline (ANL)	574	0.3 (25 °C)	(Boonpoke et al., 2012)
Biochar	3 and 10 wt% of magnesium salt solution	760	1.1 (25 °C)	(Shakarami et al., 2016)
Hybrid sorbent materials	Cao and MgO impregnation		CO <sub>2</sub> removal increased with increasing the oxide concentration	(Prepiorski et al. 2013)

## 2.7 Carbon dioxide adsorption techniques

The CO<sub>2</sub> capture by adsorption is usually carried out in a packed column filled with dry carbonaceous adsorbents, and the CO<sub>2</sub> bearing stream is passed through the column at moderate temperature (25-65°C) and atmospheric pressure. The entire mechanism involves two stages, and they are CO<sub>2</sub> adsorption followed by desorption to get pure CO<sub>2</sub> through a pressure swing (PSA), thermal swing (TSA) approach or the combination of both to make the entire process cost-effective. Firstly, CO<sub>2</sub> molecules are adsorbed on activated carbon's non-polar surface, which is mainly dominated by oxygenated functional groups such as carboxylic, lactonic (acidic) and carbonyl or ether (non-acidic), followed by achieving the equilibrium between

adsorbate and adsorbent under moderate temperature as it is exothermic. Finally, the surface of the adsorbent is regenerated by reversing the adsorption condition. It can be further reused for the next adsorption cycle contributing to the high efficiency of the multiple adsorption-desorption cycles. CO<sub>2</sub> capture on activated carbon surface is mainly governed by the principle of physical adsorption/physisorption, such as weak Van der Waal's force evident from its reversible nature of adsorption, so easy recovery of the adsorbent is achievable. In addition, the lower value of isosteric (Q<sub>st</sub>) heat of adsorption of carbon materials such as activated carbon is attributed to the lower electrostatic interactions between the CO<sub>2</sub> molecule and the non-polar surface of the carbon material. It is also a sign of weak interaction between adsorbate and adsorbent. Hence, the energy penalty is reduced at the final step. However, such an approach's success depends on developing narrow micro-pores (ultra or super) with a high adsorption capacity and selectivity for CO<sub>2</sub>, followed by high stability, easy regeneration, and potential corrosion problems with surface chemistry of activated carbon less dominant.

Moreover, the incorporation of amine or nitrogen (electron acceptor) groups into solid adsorbing materials are expected to enhance the polarization and improve the CO<sub>2</sub> capture as the CO<sub>2</sub> molecule is Lewis-acid. Moreover, the success of the capture technology will also equally depend on the regeneration capacity of the amine or nitrogen functionalized solid adsorbents. The regeneration of adsorbents by pressure swing adsorption (PSA), temperature swing adsorption (TSA) or vacuum swing adsorption (VSA) is discussed below.

### **2.7.1 Pressure swing adsorption technique**

The pressure swing adsorption (PSA) technique is a cyclic adsorption process that allows continuous and bulk separation of the desired constituent from a mixture/gas streams under pressure according to an adsorbent material's molecular characteristics and affinity. This process relies on the phenomenon that high-pressure gases (the desired constituent) are attracted to the surface of the adsorbent. The technique is called PSA because it is performed by a periodic change in pressure between the adsorption and desorption. Firstly, the mixture of gases flows through the bed at high pressure and low temperature until the adsorption of CO<sub>2</sub> reaches equilibrium conditions at the exit of the bed (Illing et al., 2001). The beds are then regenerated by tumbling the pressure and elutriating the adsorbed constituents with a gas having low absorptivity. After regeneration, the beds are equipped for another adsorption cycle.

### **2.7.2 Temperature swing adsorption technique**

This technique is called temperature swing adsorption (TSA) because the bed temperature alternates between adsorption and regeneration. It is an alternate swing adsorption approach in which flue gas is passed over the bed. After which, selective adsorption occurs on the adsorbent until equilibrium is achieved. Desorption of gas can be done at high temperature by providing additional heat (hot, pure, and relatively inert gas). For further adsorption cycle to be continued, the regenerated bed is cooled down. The regeneration temperature is chosen based on the stability and characteristics of the adsorbent and adsorbate. The additional requirement of heat in TSA makes it costlier than PSA. The possibility of using available waste heat suggests using TSA processes for post-combustion capture. Usually, PSA and TSA processes are combined in the industries, i.e., adsorption at a low temperature followed by desorption/regeneration by heating or lowering the pressure.

### **2.7.3 Vacuum swing adsorption technique**

Other adsorption-based technologies, such as pressure/vacuum swing adsorption (PVSA/VSA) with a regeneration pressure that is significantly below ambient, have frequently been investigated because of their simplicity and low energy requirements. Summing up, all these technologies are similar regarding how species present in the feed are separated. A solid medium undergoing alternating loading and regeneration phases is driven by the process.

## **2.8 Summary**

The exponential growth of anthropogenic CO<sub>2</sub> in the atmosphere from different industrial and energy sectors is the primary contributor to global warming and climate change. Therefore, various post-combustion capture processes are developed to recover CO<sub>2</sub> from point sources, and they are liquid solvent-based absorption, membrane separation, cryogenic distillation, and adsorption, etc. The technical challenges associated with the as-mentioned processes shifted the focus to the use of solid sorbents prepared from lignocellulose-based inexpensive precursors for CO<sub>2</sub> adsorption because of the plethora of advantages associated with it. Despite the number of benefits related to the technology, certain limitations/disadvantages are still associated with the approach. The adsorption capacity of AC significantly increases with the impregnation of various functional groups mainly basic owing to the Lewis acidic nature of CO<sub>2</sub>. From this study, it is evident that chemical activation leads to favourable results in the adsorption of CO<sub>2</sub>. The affinity of the AC was also found to be vastly improved. Non-modified/pristine AC is made to change the surface chemistry of the adsorbent to basic. The

surface modification can contribute to the ultra-micropores development that can help trap CO<sub>2</sub> by enhancing the selectivity. The addition of various functional groups on the surface of the AC by the addition of acid or alkalis can affect the surface chemistry. This study shows that PSA is a promising option for CO<sub>2</sub> capture due to its low energy and capital requirements coupled with the ability to operate over a wide range of temperature and pressure conditions. For this, it is widely believed that post-combustion technologies present the most significant near-term potential for reduction of CO<sub>2</sub> emissions because they can be retrofit to existing fossil-fuelled power plants and may be applied to other industrial emitters of CO<sub>2</sub> as well (e.g., the cement industry and iron and steel production). Nevertheless, there is a need to scale up the novel technologies from a laboratory to an industrial scale. This review paper is a reasonable overview of the recent technologies used in post-combustion capture of CO<sub>2</sub>, and it also outlines its drawbacks and advantages in detail. The knowledge gaps are addressed in this research.



## **Chapter 3 Experimental Section**

In Chapter 3 biomass collection and pre-treatment, materials section (gases and chemicals), thermal treatment set-up, CO<sub>2</sub> capture set-up, impregnation technique and CO<sub>2</sub> capture process are included in detail. In addition, the complimentary analytical techniques used to characterize the precursors and the products (solid samples) are also described in depth. Finally, the process safety analysis followed while performing each experimental run are included in this chapter.

### **3.1 Biomass collection and Pre-treatment**

SCG and CH were collected from a local coffee café located at the University of Saskatchewan, Saskatoon campus, and Road Coffee Inc. (Saskatoon). The biomass samples without any modification were referred to as the "as-received samples." The as-received precursors were thoroughly washed with distilled water to eliminate any impurities and then oven-dried at 105±5 °C for 12±3 h to remove the presence of excess moisture from SCG and CH. The moisture content in SCG was reduced to less than 5 wt. %. The dried biomass samples with medium sized particle fraction of d<sub>50</sub> = 522 and 611 µm for SCG and CH were preferred and stored in airtight glass containers to avoid any moisture absorption for further thermal treatment and analyses.

### **3.2 Materials section**

In this work, high-purity (> 98%) nitrogen (N<sub>2</sub>) and carbon dioxide (CO<sub>2</sub>) cylinders were obtained from the Praxair Co. Saskatoon. High purity choline chloride (ChCl) and urea were obtained from the Sigma Aldrich.

### **3.3 Torrefaction, slow-pyrolysis, and CO<sub>2</sub> activation set-up**

The torrefaction, slow-pyrolysis and CO<sub>2</sub> activation set-up included a fixed bed Inconel reactor, as shown in Figures 3.1 and 3.2, respectively. The specifications of the fixed-bed reactor are summarized in Table 3.1. Heat to the reactor for thermal treatment was supplied by an external tubular furnace mounted on the steel frame. As mentioned in Table 3.1, the temperature controller (Eurotherm) was used to control and monitor the furnace temperature. The actual temperature inside the bed and the temperature ramp was observed instantly with the aid of the K-type thermocouple (Omega, K-type) positioned in the middle of the bed. Using time as the function, heating rate during each run was determined by monitoring the change in reactor temperature through the temperature controller. The temperature calibration of the bed was recorded before the thermal treatment and is displayed in Figure B.1. The condenser placed

inside an ice-bath and was used to collect the hot vapours from the fixed-bed reactor generated during each experimental run. The thermal treatments conducted under N<sub>2</sub> flow (to maintain inert environment), and under CO<sub>2</sub> flow for physical activation. The gas flow rates were controlled by using a mass-flow controllers (MFCs). The mass flow rates of N<sub>2</sub> and CO<sub>2</sub> were calibrated prior to the experimental run. The N<sub>2</sub> and CO<sub>2</sub> calibration curves are shown in Appendix B (Figures B.2 and B.3).

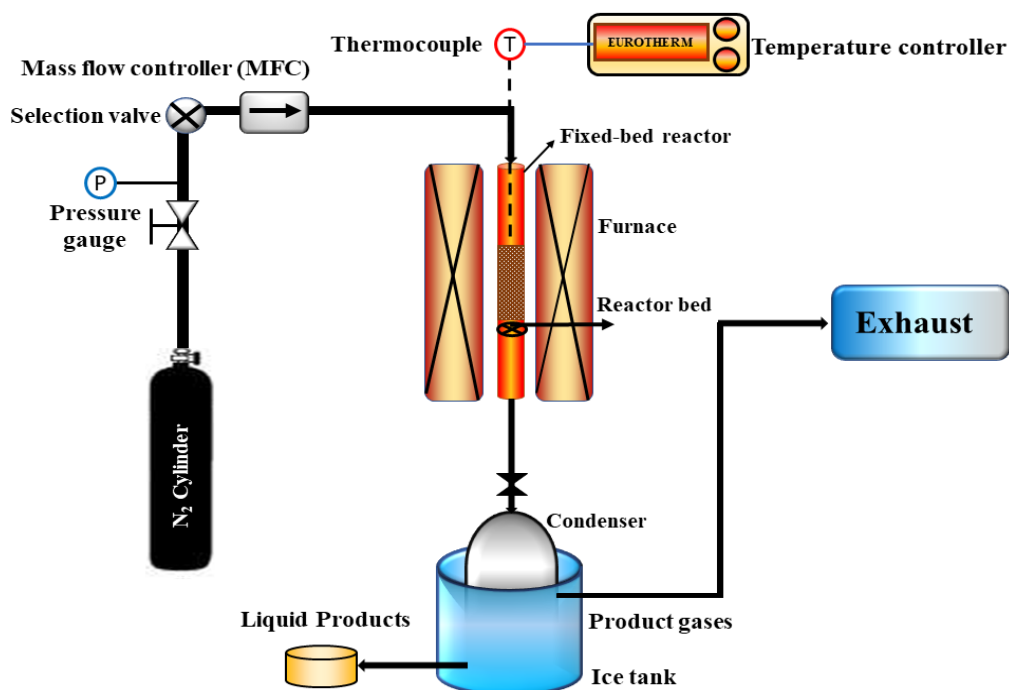


**Figure 3.1:** Schematic of torrefaction and slow-pyrolysis fixed-bed reactor set-up.

**Table 3.1:** Specifications of torrefaction, slow-pyrolysis, and CO<sub>2</sub> activation set-up.

Reactor	Specifications and unit (mm)
Column length	870
Outer Diameter (O.D)	25.4
Inner Diameter (I.D)	22
<b>Specifications of the fixed-bed reactor components</b>	
Vertical Furnace	3210 series, Applied Test System Inc., max temperature (1200 °C)
Temperature controller	Eurotherm 2416
Thermocouple	Omega, K-type
Mass Flow Controller (CO <sub>2</sub> )	Brooks instrument, 5850S (A)
Mass Flow Controller (N <sub>2</sub> )	Brooks instrument, 5850S (B)
Condenser (stainless steel)	SS316

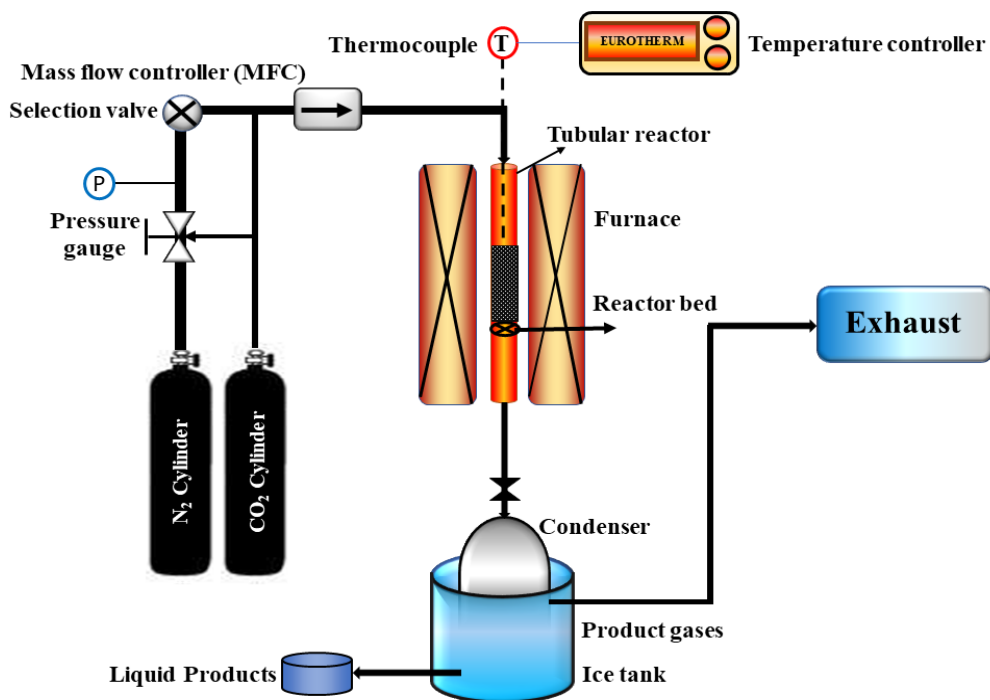


**Figure 3.2:** Schematic of physical activation reactor set-up ( $\text{CO}_2$  activation).

### 3.4 Experimental procedures

#### 3.4.1 Torrefaction and slow pyrolysis

The details regarding the torrefaction experimental procedure and the slow-pyrolysis technique are outlined in detail in chapters 4 and 6, respectively.

#### 3.4.2 Physical activation and activated carbon production technique

The physical activation setup included a lab-scale fixed bed reactor made of Inconel tubing as shown in Figure 3.2. The specification of the fixed-bed reactor is mentioned in section 3.3 and summarized in Table 3.1. The preparation of biochar from SCG through slow pyrolysis technique is mentioned in chapter 6 (section 6.3.2). In this regard, the physical activation of SCG-600 (SCG-600,  $>500 \mu\text{m}$ ) was conducted using  $\text{CO}_2$  as the activating agent. A sample size of  $20 \pm 0.5 \text{ g}$  was used per batch of an experiment run. To ensure inert condition maintained inside the reactor system,  $\text{N}_2$  gas was fed inside the fixed-bed reactor initially for 30 min under a flow rate of  $100 \text{ mL/min}$ , controlled and monitored by MFC. This is followed by subsequent heating to activation temperatures in the range of  $600$  to  $800 \text{ }^\circ\text{C}$  increased from the ambient temperature at a constant ramping rate of  $5 \text{ }^\circ\text{C/min}$  conducted under  $\text{N}_2$  flow ( $100 \text{ mL/min}$ ). Once the peak temperature was reached, the gas was switched from  $\text{N}_2$  to desired flow rates of

CO<sub>2</sub> maintained in the range of 150 to 250 mL/min, controlled and monitored by MFC. Upon reaching the activation temperature, the system condition was maintained in that state for 60 to 120 min to further allow CO<sub>2</sub>–carbon reaction, widening of unreachable pores and elimination of carbon monoxide from the carbon matrix. After completion of the CO<sub>2</sub> activation, the reactor was allowed to cool to ambient temperature by natural cooling performed under N<sub>2</sub> flow. The resultant AC samples were appropriately labelled as AC-CO<sub>2</sub>. The activated carbon derived from two stage physical activation using CO<sub>2</sub> as the activating agent and torrefied biomass as the starting material was labelled as TAC-CO<sub>2</sub>. The AC samples were stored in glass vials and kept inside a desiccator to avoid absorption of moisture or any contamination for further analyses, functionalization, and breakthrough CO<sub>2</sub> adsorption experiments. Consequently, the AC yield from each run was also measured according to the Eq. (3.1).

$$\text{AC yield (\%)} = W_2/W_1 * 100 \dots \dots \dots (3.1)$$

where, W<sub>2</sub> is the final weight of the AC synthesized and W<sub>1</sub> is the initial weight of the biochar (dried SCG-600).

### **3.4.3 Preparation of natural deep eutectic solvent**

In this regard, to functionalize the surface of pristine and optimized AC sample (AC-CO<sub>2</sub>), natural deep eutectic solvent (DES) was prepared by mixing choline chloride (ChCl) and urea in different molar ratios according to the method stated below. Firstly, to remove any excess moisture, urea was pre-dried at 45±5 °C in a vacuum oven for 48 h, before synthesizing the solvent. Choline chloride and urea were stirred at different molar ratios ranging from 1:0.1-1:0.5 maintained at a temperature of 80 °C for 2 h, until a homogeneous and transparent liquid phase was obtained after mixing as demonstrated in Figure 3.3. In this regard, the molar ratios were designated as 1-4 as shown in Figure 3.3 and the 5<sup>th</sup> DES sample was not included owing to the presence of solid with liquid phase. Finally, all the as-synthesized DES samples were dried in an oven at 110 °C to remove the traces of excess moisture and collected in a well-sealed glass containers for further functionalization of the pristine AC sample.

### **3.4.4 Impregnation technique and preparation of DES functionalized activated carbon samples**

The optimized AC sample derived from SCG was thoroughly mixed with DES at a fixed ratio of 1:2, at approximately 65±5 °C for 2 h using ultra-sonication.

In this regard, impregnation has been defined as the mass of optimized pristine AC to the mass of DES that was used to synthesize functionalized AC. The Figure 3.3 demonstrates the natural DES preparation technique and DES impregnation procedure. For the impregnation, the DES mixed AC samples were left at the room temperature for 24 h. Once the impregnation was over, the AC samples were washed thoroughly with distilled water, filtered and subsequently oven dried over-night at  $110 \text{ }^{\circ}\text{C} \pm 5 \text{ }^{\circ}\text{C}$ . Once the drying was over, the samples were collected and labelled accordingly and kept in a desiccator. The samples obtained were labelled as AC-DES-x where x denotes the molar ratio at which choline chloride and urea have been mixed to prepare DES. For instance, AC-DES-0.1 means AC sample functionalized using DES solution of choline chloride and urea mixed at a molar ratio of 1:0.1. Table 3.2 demonstrates the list of DES solvents used to tailor the surface of pristine and optimized AC (AC-CO<sub>2</sub>).

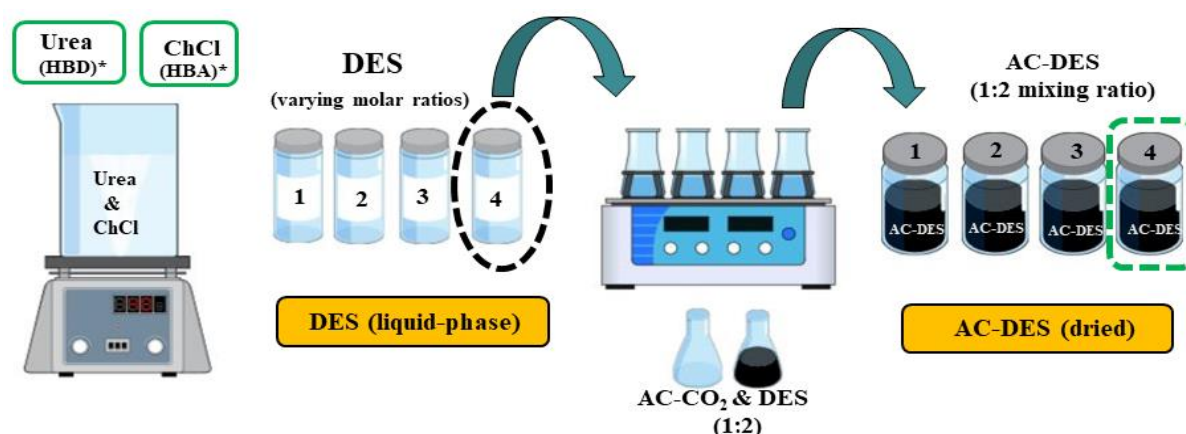


**Figure 3.3:** Deep eutectic solvent preparation and AC impregnation technique.

**Table 3.2:** Ratio, phase, and abbreviations of the DES-based activated carbon samples.

SI No.	Ratio	Phase	Abbreviations of AC
	ChCl: urea		
1	1:0.1	Liquid (transparent)	AC-DES-0.1
2	1:0.2	Liquid (transparent)	AC-DES-0.2
3	1:0.3	Liquid (transparent)	AC-DES-0.3
4	1:0.4	Liquid (transparent)	AC-DES-0.4
5	1:0.5	Liquid with solid phase	AC-DES-0.5

### 3.5 Characterizations

Following characterizations were performed to analyse the transformation in physicochemical characteristics of the precursors (SCG and CH), torrefied biomass samples, biochar samples

derived from slow pyrolysis, pristine AC (AC-CO<sub>2</sub>) and DES-functionalised (AC-DES-0.4) and are described in the section below:

- Using the Malvern Mastersizer 3000 (Malvern Instruments, UK) the particle size of the tested samples was determined and scanned within the range of 4-3500 μm.
- The amount of ash, moisture, and volatile matter content (proximate analysis) in the tested samples was assessed based on the standard ASTM methods as described below. Each analysis was carried out on a dried-basis and repeated in triplicates to estimate the error.
  - i. Moisture content (ASTM E871-82): Moisture content was assessed by heating a crucible containing approximately 1 g of solid sample at 105±5 °C in a furnace maintained for 2 h. This is followed by estimating the difference in weight of the sample (before and after heating) (ASTM, 2006).
  - ii. Ash content (ASTM E1755-01): Subsequently the ash content was evaluated by heating the sample at a temperature of 575±10 °C for 4 h in a muffle furnace. Ash content is estimated by calculating the weight loss of the sample (before and after heat treatment) (ASTM, 2007).
  - iii. Volatile matter (VM) content (ASTM D3175-11): Volatile matter content in the tested sample was measured by heating the tested sample at 950±10 °C maintained for 7 min in the furnace followed by cooling the in the desiccator (ASTM, 2011).
  - iv. Fixed carbon (FC) content: The fixed carbon content in the tested sample was measured by mass balance as shown below in Eq. 3.2:

$$\text{FC content (wt. \%)} = 100 - (\text{moisture} + \text{ash} + \text{VM}) \text{ wt. \%} \dots\dots\dots(3.2)$$

- Using the Vario EL III CHNS Analyzer, the elemental compositions (C, H, N and S) were determined in the tested samples through high temperature decomposition technique. The oxygen content (O) was determined using the technique of mass-balance as shown in the Eq. (3.3). Each analysis was repeated in triplicate to estimate the error and the average value has been reported each time.

$$\text{Oxygen content (O) wt. \%} = 100 - (\text{C} + \text{H} + \text{S} + \text{N} + \text{Ash}) \text{ wt. \%} \dots\dots\dots(3.3)$$

Where, C (carbon, wt. %); H (hydrogen, wt. %); N (nitrogen, wt. %) and S (sulphur, wt. %).

- The pH analysis was determined with the aid of an Elite PCTS pH meter. Before conducting the pH analysis, the tested sample and de-ionized water was mixed in a ratio of 1: 5. The solution was mixed for 24 h with sporadic agitation.
- The higher heating value (HHV) of the tested sample was obtained by using an oxygen bomb calorimeter (Parr 6400). Before estimating the calorific value, the calorimeter was first

calibrated using benzoic acid pellets as the standardized material. In this regard, each experimental run was repeated in triplicates to determine the error.

- The textural properties of the tested sample were determined using a Micromeritics instrument (Model ASAP-2020). The surface area ( $S_{\text{BET}}$ ) of the tested sample was determined by using the BET method, whereas to evaluate the pore-size distribution and pore volume of the tested sample the BJH model was used. The IUPAC classification (International union of pure and Applied Chemistry) was considered for the pore size distribution. Before the analysis, the tested sample was degassed at 300 °C for 4 h under vacuum maintained at 500 mm Hg to eliminate excess moisture and traces of absorbed gases present in the surface of the tested samples. This is followed by N<sub>2</sub> adsorption-desorption analysis performed at a temperature of -196 °C. To determine the micropore size distribution of the tested sample, the non-local Density Functional Theory (NLDFT) was applied using N<sub>2</sub> adsorption at -196 °C on slit-pore carbon.
- The FTIR spectroscopy was done to recognize different surface functional moieties in the samples. This analysis was executed with the aid of a Bruker VERTEX 70v Fourier Transform spectrometer. The spectra were obtained in the range of 4000–400 cm<sup>-1</sup> using a diamond ATR crystal obtained at a resolution of 4 cm<sup>-1</sup> and 32 scans.
- The TGA-DTG analysis was performed to examine the devolatilization behaviour of the tested samples. Using the TGA Q500 instrument the analysis was executed. About 10–20 mg of the tested sample was heated in an inert environment at a temperature range of 25–800 °C in the presence of Nitrogen gas (N<sub>2</sub>) purged at 60 mL/min of flow rate. The heating rate during the thermal degradation was maintained at 10 °C/min.
- The X-ray diffraction (XRD) technique was used to analyse the X-ray diffractogram of the tested samples. The analysis was performed using an Advance D8 Diffractometer equipped with Cu K- $\alpha$  source of radiation ( $\lambda=1.5418$  nm). In this regard, the data were collected in the two-theta range of 10-80°.
- To determine the carbon-containing groups in the tested samples, solid-state <sup>13</sup>C-NMR spectroscopy was studied using the Bruker Avance NMR spectrometer (500 MHz). The analysis was performed at a spinning speed of 6 kHz, accumulating 2048 scans in 90 min. The data was processed by using the Topspin version 4.0.7 software.
- The X-ray photoelectron spectroscopy (XPS) analysis was performed using a Kratos AXIS Supra instrument. The spectrometer is equipped Al K- $\alpha$  source with a combined hemi-spherical and spherical mirror analyzer. To conduct a high-resolution analysis, an accelerating voltage of 15 keV and current of 10 mA was maintained at each run of the analysis.

- The CO<sub>2</sub>-Temperature-programmed desorption (TPD) study of the activated carbon samples (pristine and DES functionalized) was performed with the aid of Micromeritics chemisorption Analyzer (AutoChem, 2950 HP). In a typical CO<sub>2</sub>-TPD experiment, before performing the TPD analysis, the sample was first degassed at a temperature of 300 °C under He flow maintained for 30 min. With anhydrous CO<sub>2</sub> gas (5.21% CO<sub>2</sub> in He) the adsorption was performed at 100 °C maintained for 30 min. This is followed by flushing the sample with He for 30 min to remove the physically adsorbed CO<sub>2</sub> and recording the desorption profile at 100 to 700 °C under He purged at a rate of 50 ml/min.
- The morphologies of the tested samples were acquired using a scanning electron microscope (SEM, Hitachi SU8010) The imaging of the tested samples was functioned at a voltage of 3 kV voltage maintained under a high vacuum. Prior to SEM imaging, gold was used to coat the tested samples with the aid of A Q150T ES sputter coating instrument.

Details regarding the analytical techniques mentioned above are also provided in the previous work done from our research group (Mukherjee et al., 2021a; Mukherjee et al., 2021b; Chand et al., 2019; Azargohar et al., 2019a).

### **3.6 Breakthrough Carbon dioxide adsorption set-up**

The breakthrough CO<sub>2</sub> capture performance was evaluated by conducting adsorption runs in a fixed-bed tubular reactor. The schematic diagram of the CO<sub>2</sub> adsorption set-up is demonstrated in Figure 3.4. Specification of the fixed-bed laboratory-scale reactor is summarized in Table 3.3. To supply heat to the reactor, silicone rubber insulated heating tape was used with a maximum operating temperature of 232 °C. The CO<sub>2</sub> and N<sub>2</sub> gases were calibrated before performing the experiments presented in Appendix C, Figures C.1 and C.2, respectively. The mixture of pure CO<sub>2</sub> and N<sub>2</sub> was fed through the bed of adsorbents, and the flow rates (maximum 200 mL/min) were controlled by using a mass-flow controllers (MFC) and a metering valve coupled with a mass flow meter (maximum 500 mL/min). The micro-GC calibration is presented in Appendix C, Tables C1 and C2, respectively. In this regard, the micro-GC analyzer (CP-4900, Micro-GC) with a thermal conductivity detector ( $\mu$ TCD) was used to determine the dynamic concentration of the gas. Each experimental runs were performed in triplicates and the mean value of adsorption capacity is reported in this study.



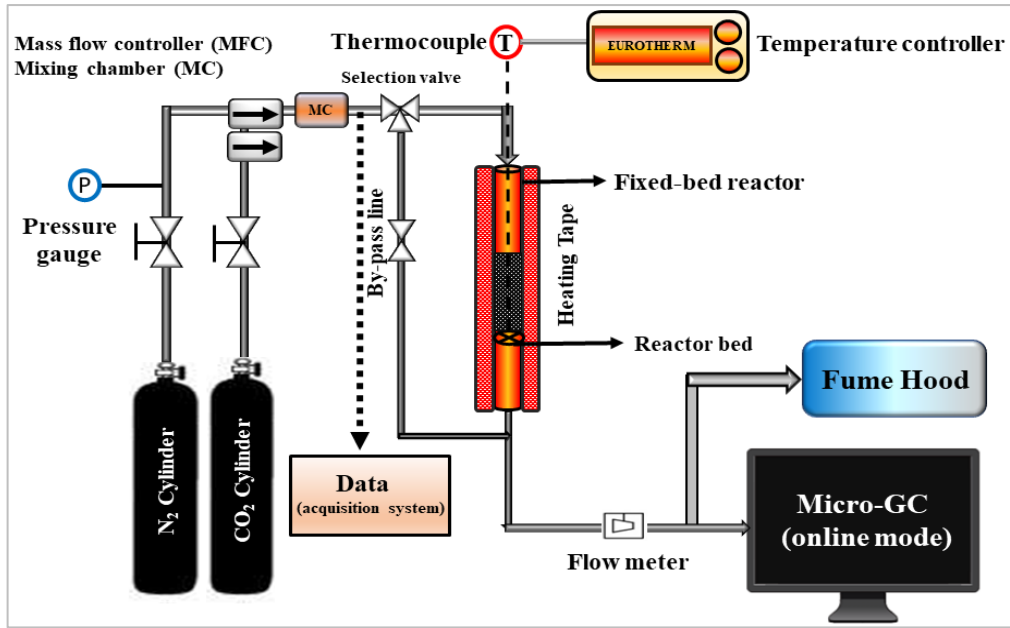


**Figure 3.4:** Schematic of CO<sub>2</sub> adsorption set-up (temperature swing adsorption unit).

**Table 3.3:** Specifications of CO<sub>2</sub> capture fixed-bed reactor.

Reactor	Specifications and unit
Bed-Diameter	2.5 cm
Bed height	6 cm
Column length	42 cm
<b>Specifications of the components of CO<sub>2</sub> capture set-up</b>	
Heating Tape	Silicone insulating heating tape, Cole-Parmer
Mass Flow Controller	Brooks instrument, 5850S (A/B)
Flow Meter	Brooks instrument, 5860S

### 3.6.1 CO<sub>2</sub> adsorption Capacity

The breakthrough CO<sub>2</sub> adsorption and desorption performance is described in chapters 4, 6 and 7. The CO<sub>2</sub> adsorption capacity in this study is determined by using the Eq. 3.4 and is expressed in mmol of CO<sub>2</sub>/g of adsorbent (Singh et al., 2019). It can also be converted to mg/g by multiplying the adsorption capacity expressed in mmol/g by 44.01 (molecular weight of CO<sub>2</sub>). The breakthrough adsorption capacity was calculated using the Eq. (3.4) as stated below:

$$q_t = \frac{1}{m_0} \int_0^t Q(C_0 - C) dt$$

where,  $q_t$  is the adsorption capacity expressed in mmol/g,  $m$  is the mass of adsorbent used to perform the experimental run expressed in g,  $Q$  is the gas flow rate expressed in mL/min,  $C_o$  and  $C$  are the  $CO_2$  inlet and outlet concentrations expressed in volume %, and  $t$  is the time expressed in min. The multiple adsorption-desorption cycles performed to assess the thermal stability or the extent of regeneration of the AC samples are described in detail in chapter 7.

### 3.6.2 Selectivity

The selectivity of binary mixture of  $CO_2$ :  $N_2$  was measured using the breakthrough adsorption capacities (Igalavithana et al., 2020). The gas mixture contained  $CO_2$  and  $N_2$  at 0.15:0.85 ratio (15 vol% of  $CO_2$  in  $N_2$ , flue gas composition) and the following Eq. (3.5) was used to determine the selectivity of the AC samples:

$$S = q_1 * p_2 / q_2 * p_1 \dots\dots\dots (3.5)$$

Where,  $q_1$  and  $q_2$  represents the breakthrough adsorption capacities of  $CO_2$  and  $N_2$  at 25 °C and at 1 bar and  $p_1$  and  $p_2$  represents the partial pressure of  $CO_2$  and  $N_2$ , respectively.

### 3.7 Process Safety Analysis

Thermal treatments were carried out under high temperatures. Hence, the following safety protocol outlined below were strictly followed while performing each experimental run:

**Outlet of the reactor:** All the outlet of the reactor must be cleaned before starting each experimental run.

**Leak Detection Test:** All the experimental runs were performed after undergoing a leak-detection test. The experiments were performed if the test result was positive (no leak detected). Apply anti-sieve before starting the experimental run and close the reactor.

**Reactor temperature:** During each experimental performance, the temperature of the reactor temperature was monitored continuously through the temperature controller (Eurotherm).

**Gas flow rate:** During each experimental run, the gas flow rate was monitored constantly through the mass flow controller (MFC).

**$N_2$  and  $CO_2$  cylinders:** During each experimental run, the  $N_2$  and  $CO_2$  cylinders were monitored continuously. The valves of  $N_2$  and  $CO_2$  cylinders were closed after each experimental run and the pressure gauge was set at the lowest point when not in use for any experimental run.

## **Chapter 4 Experimental and Modeling Studies of Torrefaction of Spent Coffee Grounds and Coffee Husk: Effects on Surface Chemistry and Carbon Dioxide Capture Performance**

Most of the content of this chapter has been published as a research article in the American Chemical Society (ACS), Omega. The ACS publication holds the copyright and the permission to use the aforementioned article in this thesis has been obtained from the ACS and is presented in Appendix G (Figure G.1).

### **Citation :**

**Mukherjee, A.**, Okolie, J. A, Niu, C, Dalai, A.K., (2021). Experimental and Modeling Studies of Torrefaction of Spent Coffee Grounds and Coffee Husk: Effects on Surface Chemistry and Carbon Dioxide Capture Performance. ACS Omega, 7(1), pp. 638-653.

In addition, some portion of this chapter was presented at the following conference presentation and 3 minutes thesis (3MT) competition provided in appendix A.

**Mukherjee, A.**, Niu C., & Dalai, A.K. (2019). "Capture of carbon dioxide in post-coal combustion conditions by ground coffee Wastes: Influence of torrefaction of coffee waste," oral presentation at 69<sup>th</sup> Canadian Chemical Engineering Conference (CCEC), October 20<sup>th</sup>-23<sup>rd</sup> 2019, Halifax, Nova Scotia, Canada.

### **Contribution of the Ph.D. Candidate**

Alivia Mukherjee: Biomass collection, pre-treatment, performed the experiment and analyzed the desired products and interpreted the related data, calibrated the CO<sub>2</sub> adsorption set-up, and performed breakthrough CO<sub>2</sub> capture experiments, validated the experimental findings with the modelling studies, writing the manuscript and provided response to the reviewers through discussions with Dr. Ajay K. Dalai. Dr. Jude Okolie helped to develop the model using Aspen Plus. Dr. Catherine Niu and Dr. Ajay K. Dalai guided to draft the manuscript through suggestions and guidance.

### **Contribution of this chapter to the overall Ph.D. research**

The first objective and the subsequent sub-objectives is highlighted in this chapter: To investigate the influence of process parameters to transform the physicochemical characteristics of the biomass samples. Furthermore, validated the experimental findings of mass and HHV with the theoretical observations. Finally, this section demonstrates the candidacy of the torrefied biomass samples in removing CO<sub>2</sub> under post combustion scenario.

## 4.1 Abstract

Torrefaction of biomass is a promising thermochemical pre-treatment technique used to upgrade the properties of biomass to produce solid fuel with improved fuel properties. A comparative study of the effects of torrefaction temperatures (200, 250, and 300 °C) and residence times (0.5 and 1 h) on the quality of torrefied biomass samples derived from spent coffee grounds (SCG) and coffee husk (CH) was conducted. An increase in torrefaction temperature (200–300 °C) and residence time (0.5– 1 h) for CH led to an improvement in the fixed carbon content (17.9–31.8 wt. %), calorific value (18.3–25 MJ/kg), and carbon content (48.5–61.2 wt. %). Similarly, the fixed carbon content, calorific value, and carbon content of SCG rose by 14.6–29 wt. %, 22.3–30.3 MJ/kg, and 50–69.5 wt.%, respectively, with increasing temperature and residence time. Moreover, torrefaction led to an improvement in the hydrophobicity and specific surface area of CH and SCG. The H/C and O/C atomic ratios for both CH and SCG-derived torrefied biomass samples were in the range of 0.93–1.1 and 0.19–0.20, respectively. Moreover, a significant increase in volatile compound yield was observed at temperatures between 250 and 300 °C. Maximum volatile compound yields of 11.9 and 6.2 wt. % were obtained for CH and SCG. A comprehensive torrefaction model for CH and SCG developed in Aspen Plus provided information on the mass and energy flows and the overall process energy efficiency. Based on the modelling results, it was observed that with increasing torrefaction temperature to 300 °C, the mass yield values of the torrefied biomass samples declined remarkably (97.3 wt.% at 250 °C to 77.5 wt.% at 300 °C for CH and 96.7 wt.% at 250 °C to 75.1 wt.% at 300 °C for SCG). The SCG-derived torrefied biomass tested for CO<sub>2</sub> adsorption at 25 °C had a comparatively higher adsorption capacity of 0.38 mmol/g than CH-300-1 (0.23 mmol/g) owing to its better textural characteristics and surface chemistry. Although, SCG would need further thermal treatment or functionalization to tailor the surface and textural characteristics to attract more CO<sub>2</sub> molecules under a typical post-combustion scenario.

## 4.2 Introduction

The post-combustion CO<sub>2</sub> capture units are considered one of the feasible solutions to reduce CO<sub>2</sub> emissions (Deshani et al., 2020; Mukherjee et al., 2019). The post-combustion method involves capturing CO<sub>2</sub> from the mixed flue gas stream after the complete combustion. Compared to other existing CO<sub>2</sub> capture technologies (pre-combustion or oxy-fuel combustion) the post-combustion capture technique can be retrofitted to the existing industries without significant modifications (Shewchuk et al., 2021). In addition, the post-combustion method is easy to set up and is also a cost-effective CO<sub>2</sub> capture technology. Post-combustion CO<sub>2</sub> capture technology uses wet/dry adsorbents and the principle of adsorption/desorption to trap CO<sub>2</sub> molecules from the flue gas stream. Activated carbon (AC) and biochar are widely studied as the carbon-based adsorbents for post-combustion capture techniques due to the availability of a large specific surface area, microporous structure, hydrophobicity, and superior CO<sub>2</sub> adsorption capacity (Mukherjee et al., 2019). Activated carbon can be produced from a single or two-step thermal treatment technique (thermally treating biomass/organic wastes in an inert environment, slow pyrolysis) and subsequent physical or chemical activation.

Few studies have evaluated carbonaceous materials' post-combustion CO<sub>2</sub> capture potential produced from thermochemical conversion methods such as torrefaction. Furthermore, most reports in this field are related to either experimental studies and physicochemical findings (Jiang et al., 2021) or kinetics analysis (Ugochukwu Michael Ikegwu et al., 2021). However, it is challenging to scale up a process without implementing and comparing modelling studies to the experimental results. For instance, it is challenging to calculate the energy requirements of an entire process with experimental results alone (Bach et al., 2017). Also, experimental results alone do not provide adequate information needed for preliminary economic evaluation.

Torrefaction is fundamentally a mild thermochemical pre-treatment exploited mainly for upgrading biomass characteristics. The thermal treatment is conducted at a moderate temperature ranging from 200 to 300 °C in an oxygen-deficient condition. Moreover, torrefaction is characterized by lower heating rates and long reactor residence time under atmospheric conditions (Yan et al., 2017). The fundamental advantage of torrefaction is that the biomass samples are converted into high-quality fuels with lower atomic ratios and high energy density. The properties of torrefied biomass are comparable to those of conventional fossil fuels such as coal (Chen et al., 2015). Hydrophobicity properties in torrefied biomass make it easier for efficient storage, handling, and long-distant transportation.

Several researchers have studied and reported the torrefaction process as a biomass pre-treatment technique for improving its fuel characteristics (Barskov et al., 2019; Ribeiro et al., 2018). In a recent study, Sarker et al. (2020) reported the improvement in biomass characteristics after undergoing mild to severe torrefaction treatment using barley straw (BS), canola hull (CH), and oat hull (OH). Chen et al. (2012) showed that torrefied biomasses fall in the periphery of high-volatile bituminous coal when synthesized at high temperatures. Despite many impressive studies related to biomass torrefaction, a few studies have reported the effect of torrefaction on the fuel properties of SCG and coffee husk (CH) as well as their candidacy for CO<sub>2</sub> capture. To the best of our knowledge, no study has reported the possibility of using torrefied SCH or CH as solid material for post-combustion CO<sub>2</sub> capture.

In contrast, numerous studies have reported using AC for post-combustion CO<sub>2</sub> capture (Dilokekunakul et al., 2020; Tiwari et al., 2017). Tiwari et al. (2017) showed that almond shell-prepared AC is effective for CO<sub>2</sub> removal. In another study, (Dilokekunakul et al., 2020) prepared activated carbon from bamboo waste and studied the effect of N, O, and different functional groups on CO<sub>2</sub> capture.

This study aims to evaluate the impacts of temperature and residence time on the yield and physicochemical properties of torrefied SCG and CH to fill the knowledge gaps. Another novelty of this study is developing a comprehensive biomass torrefaction model. The model is essential for process optimization and techno-economic analyses. Furthermore, the torrefaction model can estimate the product distribution and by-products of the process. Furthermore, torrefaction models provide the information required to bridge the gap between academia and industry research. SCG and CH have no significant applications as they are mostly discharged into landfills, causing a detrimental impact on the environment owing to the emission of toxic materials. Therefore, their valorization would help minimize environmental pollution originating from their disposal.

## **4.3 Materials and Methods**

### **4.3.1 Biomass collection and pre-treatment**

The biomass collection (SCG and CH) and pre-treatment techniques before undergoing torrefaction are described in detail in section 3.1 (chapter 3). The methodology followed to execute the research objective is outlined and is schematically represented in Figure 4.1.

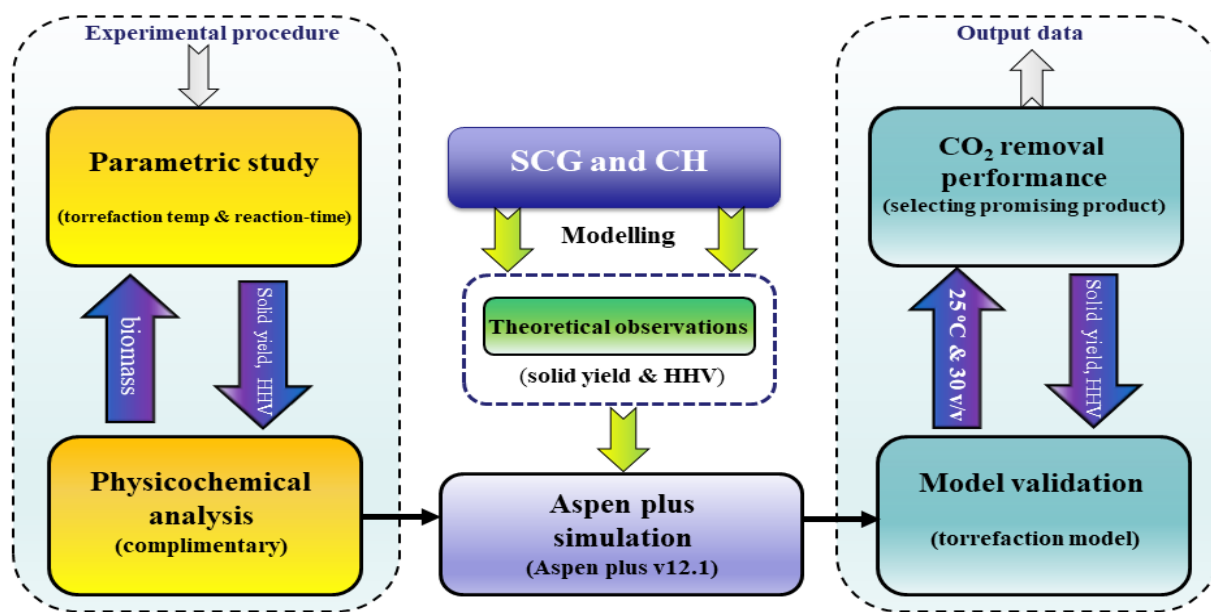


**Figure 4.1:** Schematic representation of the methodology adapted for research-objective 1.

#### 4.3.2 Torrefaction set-up and experimental procedure

The overall details of the torrefaction reactor system have been meticulously explained in the section 3.3 (chapter 3). A schematic representation of the fixed-bed reactor for torrefaction is presented in Figure 3.1. The torrefaction of SCG and CH was performed in a one inch fixed-bed Inconel tubular reactor. The average geometric mean particle size of dried biomasses (SCG and CH) was already small and in the range of 0.52–0.61 mm, so they were fed directly into the reactor. The temperature was raised from 25 °C to the desired peak temperatures (200, 250, and 300 °C) during torrefaction. In addition, a constant heating rate of 10°C/min was maintained throughout the reaction. Like torrefaction temperature and residence time, the heating rate influences the properties in torrefied biomass samples. However, the influence is minimal compared to the other parameters (torrefaction temperature and residence time). Usually, the heating rate range studied for torrefaction is between 10 and 50 °C/min. The heating rate of 10 °C/min was selected because a lower heating rate favoured the generation of higher torrefied biomass (solid) yield. As the corresponding torrefied biomass is the main product of consideration in this study, the heating rate was kept at the lower level and fixed at 10 °C/min. N<sub>2</sub> gas was added at 100 mL/min to maintain an inert atmosphere and avoid undesirable reactions (oxidation or ignition) during the reaction. The flow rate of gas was continuously monitored using a mass-flow controller (MFC). Once the desired torrefaction temperature was reached, a known amount of biomass (10 ± 0.5 g) was loaded into the reactor

and then tightly sealed to ensure that the inertness and temperature inside the reactor were well maintained. It should be emphasized that two sets of residence times were considered in this study (0.5 and 1 h). Once the experiment was completed, the reactor was cooled down to the ambient temperature ( $25 \pm 5$  °C) in the presence of N<sub>2</sub>. The final products (torrefied biomass and liquid samples) were collected for further mass balance. The torrefied biomass samples were stored in a glass container inside a desiccator at room temperature until another chemical analysis and adsorption performance study was performed. The corresponding torrefied biomass samples were labelled according to the precursor-torrefaction temperature–residence time. For instance, SCG-200-0.5h implies a torrefied biomass sample derived from SCG at 200 °C and 0.5 h hold time, or CH-300-1h indicates a torrefied biomass sample derived from CH at 300 °C and 1 h hold time. The torrefied biomass yield is calculated using the following Eq. (4.1):

$$\text{Torrefied biomass Yield (wt. \%)} = (M_{\text{TB}}/M_{\text{B}}) * 100 \% \dots\dots\dots(4.1)$$

where, M<sub>TB</sub> represent the weight of the torrefied biomass sample obtained after torrefaction and M<sub>B</sub> represent the initial weight of the biomass sample (SCG/CH) used for torrefaction.

Temperature and reaction time ranges of 200–300 °C and 0.5–1 h were defined in this study for the following reasons:

- The devolatilization and depolymerization of lignocellulosic components (hemicellulose and cellulose) occur within the temperature range (200–300 °C) (Prins et al., 2006).
- The objective of the present study is to improve the solid physicochemical properties and yield for potential CO<sub>2</sub> capture. An increase in the temperature beyond 300 °C could lead to a drastic decline in solid yield. Therefore, 300 °C was selected as the maximum temperature.
- The torrefaction temperature range of 200–300 °C was used to prevent excessive mass loss in the precursors.
- The residence time range of 0.5–1 h was selected for this study because previous studies reported a decline in solid yield with a residence time above 1 h (Trubetskaya et al., 2020; Prins et al., 2006).
- Furthermore, a residence time below 0.5 h does not provide enough duration for intermediate reactions such as depolymerization, dehydration, and deoxygenation to occur.



### **4.3.3 Characterizations of the precursors and torrefied biomass samples**

The complimentary analytical techniques performed to analyse the transformation of the biomass samples before and after torrefaction is provided in previous chapter (section 3.5, chapter 3).

### **4.3.4 Carbon dioxide capture set-up and adsorption experiments**

The information on the CO<sub>2</sub> capture set-up and the schematic (Figure 3.4) has been meticulously described in section 3.6 of previous chapter (chapter 3). Before each adsorption experiment, the set-up was loaded with  $2 \pm 0.2$  g of torrefied biomass samples and then preheated to  $160 \pm 5$  °C for 2 h in the presence of N<sub>2</sub> gas at  $50 \pm 0.5$  mL/min. N<sub>2</sub> gas was used to maintain the inertness and to remove excess moisture inside the reactor. After dehydration, the reactor was cooled down to 25 °C, after which pure CO<sub>2</sub> (30 vol %) balanced by N<sub>2</sub> was fed through the bed of torrefied adsorbents, controlled, and monitored by MFCs (as summarised in Table 3.3) to study the CO<sub>2</sub> capture performance. The adsorption capacity was evaluated by using Eq. (3.4) as provided in detail in previous chapter (chapter 3).

## **4.4 Process Modeling**

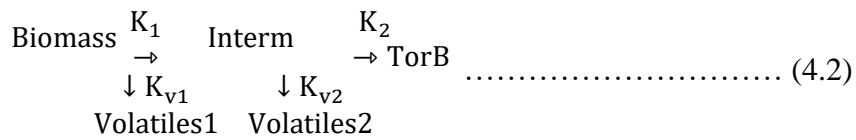
### **4.4.1 Aspen plus Model Description and Assumptions**

Biomass torrefaction is a highly complex process with a series of intermediate reactions. Therefore, it is challenging to model such systems in Aspen Plus. This is because biomass contains several complex components, including lignocellulosic compositions (hemicellulose, cellulose, and lignin) (Okolie et al., 2021b). The thermal degradation of these lignocellulosic components comprises several intermediate and complex reactions that could possibly yield various intermediate products. Therefore, the modeling and identification of these products are complicated and equally challenging. Consequently, the entire torrefaction process was simulated by considering different unit operations.

The Figure 4.2 shows the flow diagram of the torrefaction model. Together with the unit operations arrangement, the flowsheet was designed to be as simple as possible. That way, it is easier for future adjustments and scale-up. The model consists of a dryer, a series of heaters and compressors, two yield reactors, and flash separators. The description of each unit operation and the assumptions are summarized and presented in Table 4.1. It should be emphasized that Aspen Plus does not contain a predefined feedstock for SCG and CH. Therefore, a nonconventional stream was used to define the heterogeneous solid feedstock based on proximate and ultimate analyses and a calculator block. A detailed description of the

nonconventional stream modeling and the assumptions were adapted from Okolie et al., (2020). Moreover, it should be noted that a steady-state system was assumed in all calculations, while the Redlich–Kwong–Soave equation was used to simulate the fluid properties. Based on the flowsheet in Figure 4.2, the coffee residues (SCG and CH) are fed into a convective air dryer (DRYER) operating for 12 h. The dryer was designed to mimic the feedstock pre-drying steps and reduce the feedstock moisture content. Air at ambient temperature (ARN) is compressed and sent to the dryer for feedstock drying. The dried feedstock exiting the dryer is named as DRIEDSCG. The dried coffee residues enter the heater (HEATER1), where the temperature is elevated to a preheating temperature (200-300 °C) before entering the torrefaction reactor.

The torrefied unit was modeled with unit operations comprising the stoichiometric reactor, two RGibbs reactors, and two separator blocks. The entire torrefaction system was modeled in three sequential steps: initial heating and moisture removal, biomass decomposition, and intermediate decomposition. The first step in the torrefaction module is the moisture removal step. This step was modeled using the stoichiometric reactor (DRY-REC) and solid/gas phase separator (Onsree et al., 2020). The mass balance calculations to ensure that the final moisture content is the same as the torrefied solid were solved with a calculator block with an embedded FORTRAN code. The dried solid stream (S3) leaving the stoichiometric reactor is fed to the solid separator, where the inbound moisture is separated from the solids, after which the hot stream containing dried solids (DRYSCG) is fed to the Ryield reactor (RYIED1). The two yield reactors were used to model the intermediate steps during coffee residue torrefaction based on Eq. 4.2. The two yield blocks were selected for several reasons. The torrefaction kinetic models assume that the reaction occurs in two-step processes, including biomass decomposition into intermediates and volatiles. They are followed by intermediate degradation to form the torrefied solids (Bach et al., 2017). In addition, a similar approach was employed in previous studies related to the development of biomass torrefaction models (Manouchehrinejad and Mani, 2019). The first yield reactor represents the decomposition of coffee residues into volatile compounds and solid intermediates, while the second reactor models the intermediate decomposition into other volatile compounds and torrefied biomass samples. It is vital to note that the density and enthalpy of the nonconventional solid feedstock were determined by the specific property methods of DCOALIGT and HCOALGEN, respectively (Okolie et al., 2020).



The torrefaction models in this study could be applied to other types of coffee residues and might not be helpful for lignocellulose-based biomass or agricultural residues due to the varying chemical compositions. The disparity in chemical compositions could lead to different product distributions and torrefaction behaviour.

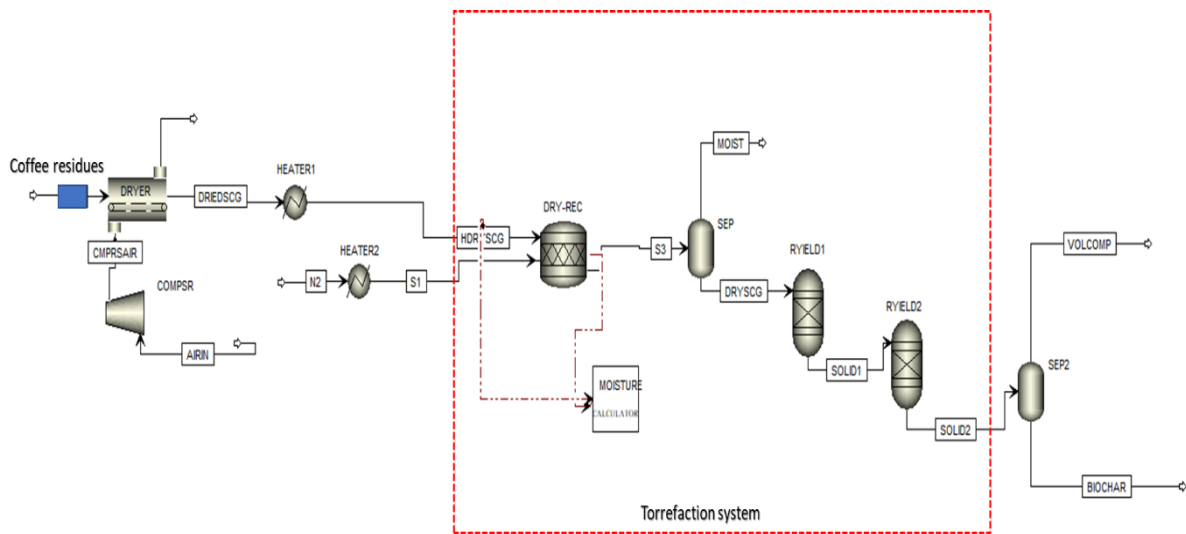


**Figure 4.2:** Flow diagram of the coffee residues (SCG and CH) torrefaction model simulated using Aspen Plus.

**Table 4.1:** List of assumptions and description of the processing blocks used for the torrefaction model.

Default block ID in Aspen Plus	Unit operations used in the flowsheet	Descriptions and Assumptions
<b>Dryer</b>	DRYER	<ul style="list-style-type: none"> <li>• This convective air-drying unit was used to simulate the pre-drying steps.</li> <li>• A continuous operation mode was assumed with a plug flow operation.</li> </ul>
<b>Compressor</b>	COMPSR	<ul style="list-style-type: none"> <li>• The compressor helps to increase the pressure of the incoming air that is fed to the dryer.</li> <li>• Isentropic operation mode was assumed.</li> </ul>
<b>Heater</b>	HEATER1	<ul style="list-style-type: none"> <li>• Heats air-dried feedstock to the desired preheating temperature.</li> </ul>
<b>Rstoic</b>	DRY - REC	<ul style="list-style-type: none"> <li>• Simulate the moisture removal step in the torrefaction process.</li> <li>• Operates under atmospheric pressure.</li> </ul>
<b>Sep</b>	SEP	<ul style="list-style-type: none"> <li>• Separate liquid products from other reaction products.</li> </ul>
<b>Sep</b>	SEP2	<ul style="list-style-type: none"> <li>• Separate volatile products from solid products.</li> </ul>
<b>Ryield</b>	RYIELD1	<ul style="list-style-type: none"> <li>• This unit helps to simulate the decomposition of coffee residues into volatiles and intermediate products.</li> <li>• Operates under atmospheric pressure.</li> </ul>
<b>Ryield</b>	RYIELD2	<ul style="list-style-type: none"> <li>• The unit helps to simulate different solid intermediate decomposition into volatiles and torrefied biomass.</li> <li>• Operates under atmospheric pressure.</li> </ul>

## 4.5 Torrefaction mass and energy yield

The main parameters that are exploited to determine the efficacy of the torrefaction process are the mass and energy yields. They indicate how much dry mass is removed or lost during the torrefaction process and the amount of energy retained in the torrefied biomass samples (solid residues). The mass yield is calculated from Eq. (4.3) as follows:

$$M_y (\%) = \frac{M_{\text{TORR}}}{M_{\text{RAW}}} \times 100\% \dots \dots \dots (4.3)$$

Where,  $M_y$ ,  $M_{\text{TORR}}$ , and  $M_{\text{RAW}}$  represent the mass yield, the mass of torrefied biomass sample (solid-residue), and the mass of raw feedstock (biomass).

The energy yield was determined from the expression in Eq. (4.4) as follows:

$$E_y (\%) = M_y (\%) \times \frac{\text{HHV}_{\text{TORR}}}{\text{HHV}_{\text{RAW}}} \times 100\% \dots \dots \dots (4.4)$$

Where  $E_y$ ,  $\text{HHV}_{\text{TORR}}$ , and  $\text{HHV}_{\text{RAW}}$  represent the energy yield and higher heating values of torrefied biomass and raw feedstock (biomass), respectively.

## 4.6 Results and discussions

### 4.6.1 Ultimate, proximate, and pH Analyses of the precursors and torrefied biomass samples

The ultimate, proximate, and pH analyses reveal the modifications in chemical composition before and after the exposure of the precursors (SCG and CH) to torrefaction, and the findings are summarized in Table 4.2. The carbon, hydrogen, nitrogen, sulfur, and oxygen compositions of SCG and CH were characteristics of typical lignocellulosic (agricultural) biomass materials such as bamboo, rice husk, and oil palm (Chen et al., 2012a). The carbon contents of SCG (50 wt. %) and CH (48.5 wt. %) fall in the periphery of typical lignocellulosic biomasses. On the contrary, SCG has superior hydrogen (6.7 wt. %) and sulfur content (0.9 wt. %) compared with CH. The higher C and H content in SCG could depict that it could be further valorized to produce energy and fuels. Furthermore, it should be emphasized that both coffee residues showed a low sulfur content of less than 1 wt.% and nitrogen content (<3 wt.%). Low sulfur and nitrogen contents are desirable for thermochemical conversion processes, especially the reactions involving a catalyst. Moreover, low sulfur and nitrogen contents mean that there will be fewer emissions of nitrous and sulfides during thermochemical conversion processes.

The ultimate analysis of the torrefied biomass samples reveals a change in elemental composition for both precursors. The results indicate that notable alterations in composition occur during torrefaction regardless of the type and nature of the precursor. Moreover, an elevation in the torrefaction temperature from 200 to 300 °C at 0.5 h led to a significant improvement in C content for both the precursors. For instance, the C content of SCG-derived torrefied solid was 52.8 wt % at 200 °C and 0.5 h residence time. However, a rise in the torrefaction temperature to 300 °C and 1 h produced an elevation in the C content to 69.5 wt.%. On the contrary, the torrefaction temperature and residence time increased the torrefied biomass samples' oxygen, hydrogen, and sulfur contents reduced, irrespective of the biomass. The reduction in oxygen fraction could be attributed to the disruption of the polymeric structure, mainly hemicellulose followed by cellulose, between 200 and 300 °C during torrefaction. Moreover, due to the series of devolatilization and decomposition reactions of the lignocellulosic components during torrefaction, the oxygen content was reduced sharply. The decline in hydrogen content with elevating torrefaction temperatures to 300 °C could also be attributed to the release of hydrocarbons (CH<sub>4</sub> and C<sub>2</sub>H<sub>6</sub>) during torrefaction (Sarker et al., 2020). It should also be highlighted that no clear pattern was evident in the change in nitrogen composition in torrefied biomass samples with variations in torrefaction temperatures or residence time. Similar observations were reported in previous studies (Ren et al., 2017; Acharya et al., 2015).

The proximate analysis presented in Table 4.2 indicates that both SCG and CH showed a high content in the volatile matter range of 77.7–81.2 wt. % and, therefore, could exhibit poor fuel characteristics. However, torrefaction of the precursors led to a decline in the volatile matter and moisture content with increasing process severity (Table 4.2). Surprisingly, the ash content of all the torrefied solids is more significant than those of the precursors. However, all the ash contents are still low and less than lignite coal (8.5 wt. %, ash content). Decreasing ash content is favourable for thermochemical conversion processes. Biomass ash contains inorganic elemental composition that often creates operating challenges such as slagging, fouling, or obstruction in the combustion units (Ugochukwu M Ikegwu et al., 2021). For that reason, a low ash content of the torrefied solid residues is desirable. Significant changes in the proximate analysis were not evident at a lower range of temperature (200 °C) because only moisture and light volatile compounds were eliminated from the biomass samples.

The Van Krevelen diagram presented in Figure 4.3 shows the extent of reactivity and fuel characteristics of the precursors and the torrefied biomass samples. Compared to the

precursors, the torrefied biomass samples showed lower atomic ratios (H/C and O/C) owing to low H and O content. Moreover, comparatively, CH-derived torrefied biomass samples under the most severe conditions (300 °C and 1 h) had the lowest values of H/C (0.93) and O/C (0.19). Both the atomic ratios (H/C and O/C) declined remarkably and were influenced by increasing torrefaction temperature and longer residence time. The atomic ratios of the torrefied biomass samples are within the periphery of lignite coal (Table 4.2). The atomic ratios reveal that torrefaction of both the precursors improved their fuel properties for subsequent biological or thermochemical conversion processes.

The pH analysis was used to assess the acidity or basicity of the torrefied samples. The pH values of the tested samples are also summarized and presented in Table 4.2. The pH of SCG and CH were 5.5 and 6.8, respectively. These values are often regarded as very weak acidic values. However, torrefaction of the precursors led to an increase in pH values beyond neutral values to the very weak to the mild basic range. Therefore, it can be inferred that torrefaction of SCG and CH improved their pH values. An increase in pH for both the precursors also indicates a decrease in acidic functional groups in the torrefied solids, and a similar finding was observed from the FTIR analysis. Owing to the Lewis acid nature of CO<sub>2</sub> molecules, the improvement of pH for both the precursors to the basic range could facilitate the CO<sub>2</sub> capture process owing to acid–base interactions between the adsorbent (torrefied biomass sample) and adsorbent (CO<sub>2</sub>).

**Table 4.2:** Ultimate, proximate and pH analyses of the precursors and torrefied biomass samples.

Precursor	Torrefaction conditions (Temperature-Time) (°C-h)	Ultimate analysis (dry-basis)					Proximate analysis (dry-basis)				Atomic ratios		pH
		C (wt. %)	H (wt. %)	N (wt.%)	S (wt.%)	O* (wt.%)	Volatile matter (wt.%)	Ash (wt.%)	Moisture (wt.%)	Fixed carbon* (wt.%)	H/C	O/C	
Coffee Husk (CH)	Raw material	48.5	5.9	2.8	0.6	40.6	77.7	1.7	2.7	17.9	1.43	0.63	6.8
	200-0.5	50.5	5.6	2.8	0.2	36	75.3	1.9	2.2	20.6	1.31	0.53	7.1
	200-1	51.6	5.5	2.9	0.1	33	74.6	2.1	1.9	21.4	1.26	0.48	7.2
	250-0.5	56.3	5.4	3.3	0.1	25.6	71.1	2.2	1.8	24.9	1.13	0.34	7.4
	250-1	58.6	5.3	3.3	0.1	22.1	70.4	2.7	1.7	25.2	1.07	0.28	7.7
	300-0.5	60.3	5.0	3.3	0.1	17.6	64.8	3.1	1.5	30.6	0.99	0.22	8.3
	300-1	61.2	4.8	3.5	0.2	15.3	63.5	3.3	1.4	31.8	0.93	0.19	8.8
Spent coffee grounds (SCG)	Raw material	50	6.7	2.3	0.9	39.0	81.2	0.9	3.3	14.6	1.6	0.60	5.5
	200-0.5	52.8	6.6	2.2	0.06	37.3	79.7	1.07	3.5	15.7	1.5	0.53	5.6
	200-1	54.4	6.5	2.8	0.1	35.1	78.3	1.1	2.5	18.1	1.45	0.48	5.9
	250-0.5	56.3	6.3	2.4	0.03	33.5	73.2	1.3	2.2	23.3	1.37	0.45	6.1
	250-1	59.4	6.3	2.7	0.04	30.1	72.6	1.6	2.1	23.7	1.3	0.38	6.3
	300-0.5	67.8	6.2	3.0	0.03	21	68.3	1.8	1.8	28.1	1.13	0.23	6.4
	300-1	69.5	6.0	3.2	0.03	19	67.8	2.0	1.2	29	1.1	0.20	6.7
Lignite		61.9	4.3	0.9	-	16.4	-	8.5	-	-	0.80	0.20	-

\*Calculated by the difference; O (wt. %) = 100 - (C + H + N + S + Ash) wt. %; Fixed carbon content (wt. %) = 100 - (Volatile matter + Ash + Moisture) wt. %

\*Standard deviations for the pH measurements of the tested samples were  $\pm 0.02$ ; Values for lignite are obtained from Kim et al., (2017)



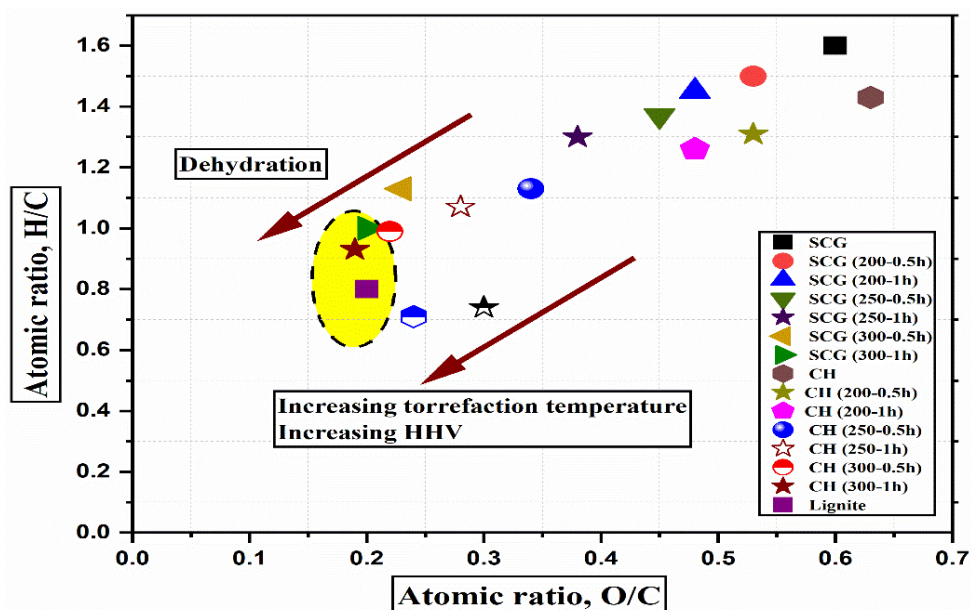


**Figure 4.3:** Van Krevelen Plot of the precursors and torrefied biomass samples.

#### 4.6.2 BET analysis of the precursors and torrefied biomass samples

A summary of the textural properties of the precursors and torrefied biomass samples is presented in Table 4.3. As evident irrespective of the precursors, the torrefaction temperature significantly influenced the specific surface area. The specific surface area for SCG-derived torrefied biomass samples increased from 11 to 100 m<sup>2</sup>/g when the torrefaction temperature and residence time rose from 200 °C for 0.5 h (mild) to 300 °C for 1 h (severe). A similar trend in the improvement of the specific surface area was observed for CH-derived torrefied biomass samples, as highlighted in Table 4.3. The specific surface area of CH-derived torrefied biomass samples is within the range of 15-24 m<sup>2</sup>/g for mild-severe treatment conditions. More porous structure in SCG-derived torrefied samples when torrefied at 300°C and 1 h obtained could be attributed to the removal of volatiles, tars, degradation of lignin and loss of oxygenated species from the pores creating a network of void spaces in the carbon-matrix. A similar finding was reported by (Sarker et al., 2020), where they have said that with increasing the harshness of the torrefaction process conditions, the biomass structures rupture to produce a more porous structure and higher specific surface area as evident from Table 4.3.

**Table 4.3:** BET analysis of the precursors and torrefied biomass samples.

Samples	BET surface area (m <sup>2</sup> /g)	Total pore volume (10 <sup>-3</sup> *cm <sup>3</sup> /g)	Mean pore size (nm)
<b>Spent Coffee Grounds (SCG)</b>			
SCG	2.3	1.2	10.1
SCG-200-0.5	11	7.2	8.4
SCG-300-1	100	10.4	5.8
<b>Coffee Husk (CH)</b>			
CH	3.5	2.4	23.1
CH-200-0.5	15	3.7	13.4
CH-300-1	24	5.5	8.1

#### 4.6.3 Fourier Transform Infrared Spectroscopic (FTIR) Analysis

To determine the impact of torrefaction conditions on the chemical structure of the biomasses and torrefied biomass samples, the Fourier transform infrared spectroscopy (FTIR) analysis were conducted as shown in Figures 4.4 (a) & (b). The FTIR spectra of the biomasses and torrefied samples heated up to 250 °C are almost similar in shape, owing to the absence of significant changes in their chemical structure. However, the changes in the vibration intensity of the FTIR spectra at 300 °C for 1 h (severe treatment conditions) are more pronounced than precursors and torrefied samples synthesized at 200 and 250 °C. The characteristic peak at around 3200–3400 cm<sup>-1</sup> characterizes O–H vibration (stretching), mainly in the lignocellulosic component (cellulose). The peak reduced drastically and disappeared with increasing torrefaction temperature due to partial dehydration and carbohydrate decomposition with increasing severity of torrefaction conditions (Azargohar et al., 2019). The inception of the peaks at around 2980–2850 cm<sup>-1</sup> is attributed to the presence of vibrations (stretching) of asymmetric and symmetric aliphatic groups (C–H), which narrowed and disappeared in the torrefied samples (Y. Chen et al., 2016). The band at around 1730 cm<sup>-1</sup> in both precursors and torrefied biomass samples could be attributed to the carbonyl stretching (C=O) of acetyl, carboxylic acid, aldehyde, or ketone groups in hemicellulose. It starts to disappear from 250 °C and with increasing temperature progressively to 300 °C and 1 h duration. The peak at around 1730 cm<sup>-1</sup> is eliminated owing to the complete decomposition of the carbonyl group in hemicellulose present in the torrefied biomass samples. This demonstrates that a chemical change appears from the decomposition of hemicellulose and the disintegration of long-chain

polysaccharides in the tested samples. The peak at 1620–1600  $\text{cm}^{-1}$  represents the aromatic skeletal vibration of C=O, with no significant change in the vibrational intensity of this peak observed at a lower range of temperatures (Jiang et al., 2021). The inception of the peak reveals the aromatization of the torrefied samples. This characteristic reflects its stability in the torrefied biomass samples and enrichment of lignin components.

Among all the build block components found in biomasses, hemicellulose is the most reactive biopolymer due to its lack of crystallinity and lower polymerization (Okolie et al., 2021b). Therefore, hemicellulose undergoes the most significant decomposition reactions during torrefaction, as evident from the less intensified peaks at 300 °C for the respective torrefied samples. From the spectrum presented in Figures 4.4 (a) & (b), it can be concluded that by increasing the temperature to mild conditions (200 and 250 °C), the peaks are retained, but under the severe torrefaction conditions (300 °C & 1 h), noticeable changes in the spectra of the tested samples are observed. The changes are attributed to the release of oxygenated species mainly from the complete destruction of hemicellulose and the limited disintegration of cellulose.

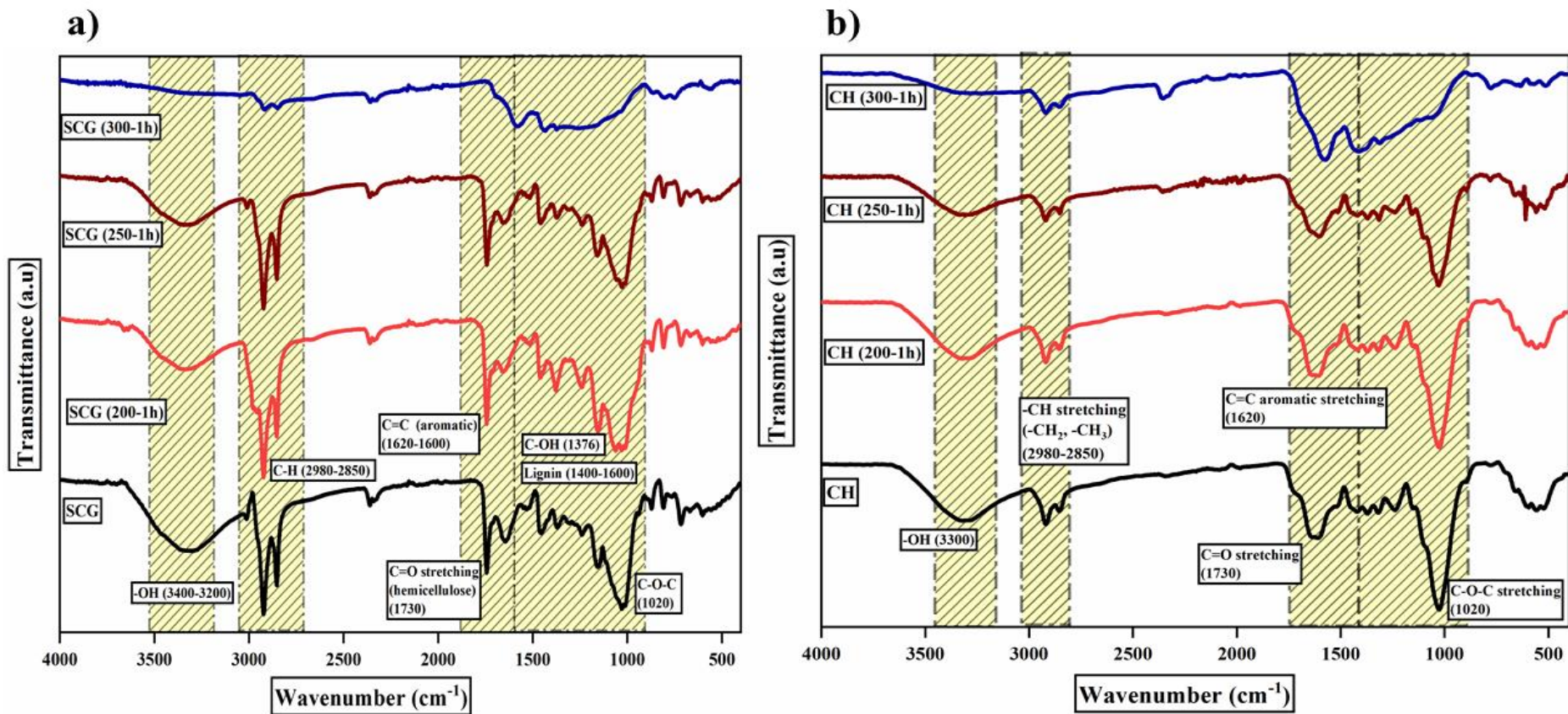


**Figure 4.4:** FTIR analysis of precursors and torrefied samples at different temperatures (a) SCG (b) CH.

#### 4.6.4 Thermal stability analysis of the precursors and torrefied biomass samples

The TGA-DTG profiles for SCG and CH and the torrefied biomass samples are presented in Figure 4.5. Moreover, the devolatilization profiles of the torrefied samples are shown in Figures 4.6 (a) & (b). The thermal decomposition pattern of the torrefied biomass samples differs from that of the precursors, most significantly for the sample synthesized under mild to severe torrefaction conditions (250 and 300 °C). From the DTG curve, the two prominent peaks observed for the precursors overlapped for the torrefied biomass samples, and the peaks represent the disintegration temperature of cellulose and lignin. Owing to the loss of hemicellulose as the main lignocellulosic component at around 320 °C, the lignin content increased in both the tested samples. Additionally, the decline in the rate of mass loss of the torrefied biomass samples and the peak shifting to a higher temperature also indicated the attainment of thermal stability of the torrefied biomass samples compared to the precursors. Irrespective of the precursors, the thermal stability is attained under the severe torrefaction conditions (300 °C and 1 h), and the CH-derived torrefied biomass sample is thermally more stable than SCG.

As can be seen in Figures 4.5 and 4.6 (a) & (b), the thermal decomposition process of the precursors and torrefied samples can be separated into three distinct stages. The first stage, which occurs at a temperature of up to 200 °C, corresponds to dehydration and the removal of light volatile matter content from the precursors. However, the mass loss associated with dehydration was insignificant for the torrefied samples, confirming the tested samples' hydrophobic nature compared to the raw precursor. The second stage occurs at temperatures ranging from 200 to 500 °C. This stage is characterized by volatile pyrolytic combustion and is termed the active phase (Ren et al., 2017).

Decomposition of the basic lignocellulosic building blocks, including hemicellulose (220–315 °C), cellulose (315–400 °C), and lignin (160–900 °C), occurred at this stage. This stage could proceed in one or two phases depending on the torrefaction temperature. The first phase corresponded to the combustion of hemicellulose and cellulose components within the temperature range of 190–400 °C. Two visible peaks with maximum mass loss in DTG curves can be observed in this stage, as shown in Figures 4.6 (a) & (b).

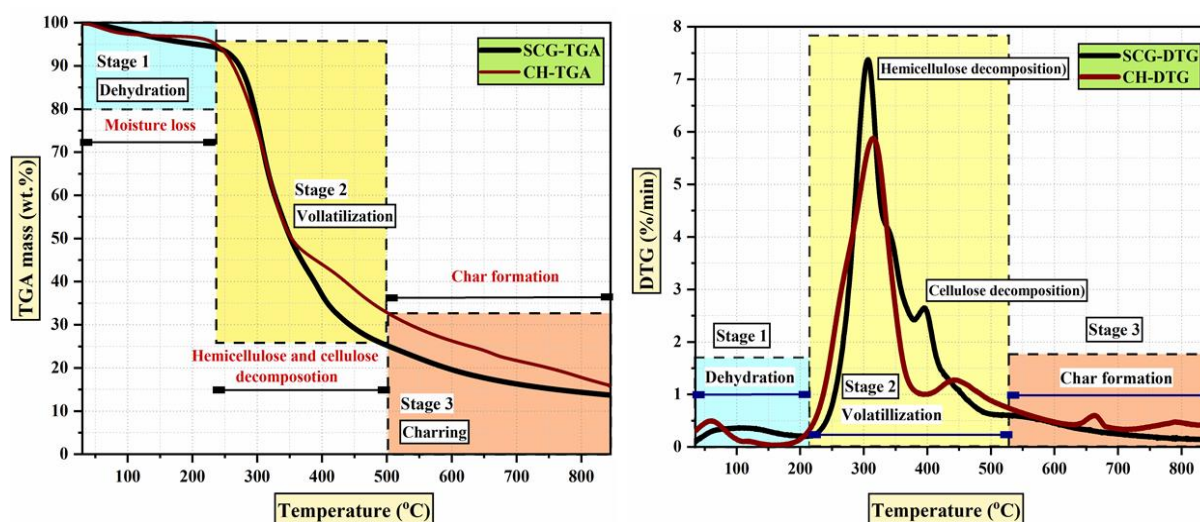
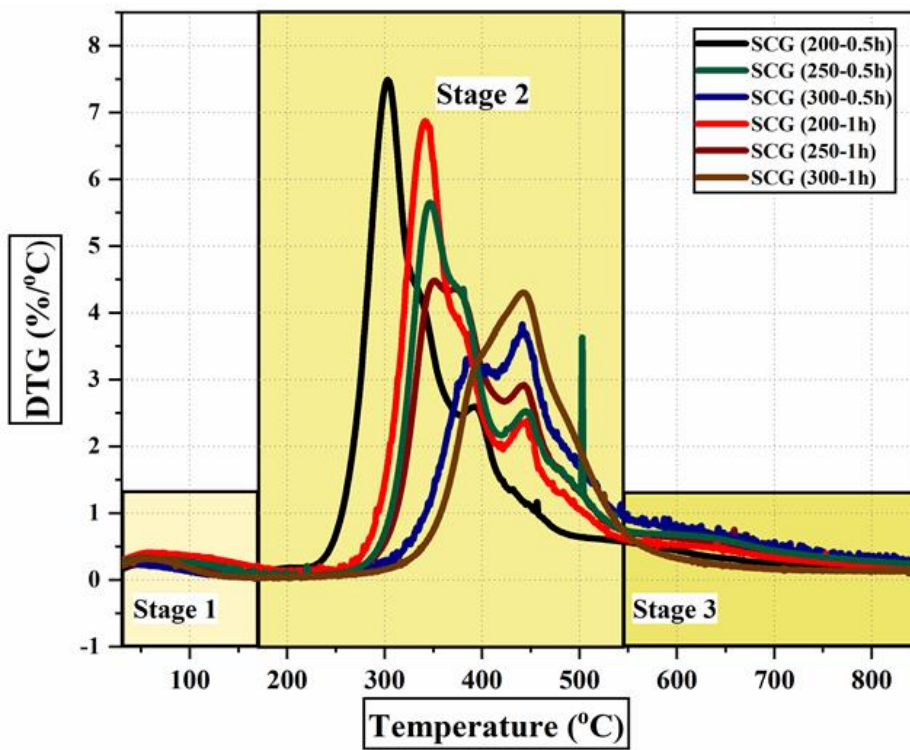
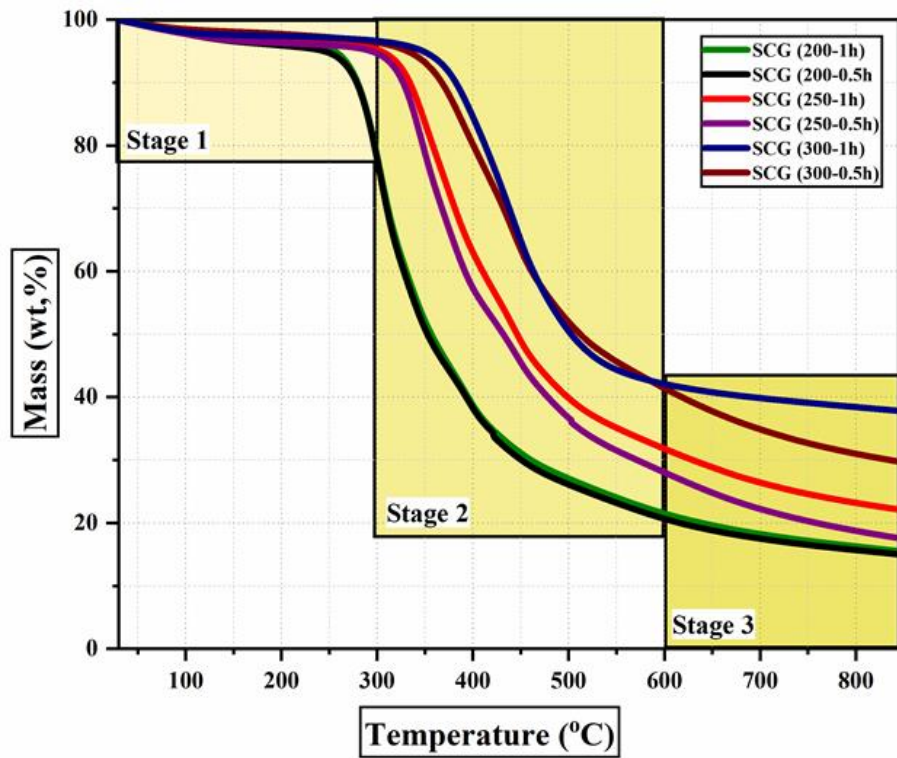


**Figure 4.5:** TGA-DTG analysis of precursors (a) SCG and (b) CH.

The first peak corresponds to the degradation of hemicellulose at 322 °C with a maximum mass loss rate of 1.02%/°C, and the second peak relates to cellulose degradation at 400 °C with a maximum mass loss rate of 1.03%/°C. Moreover, the weight loss at the first phase was approximately 70% for raw precursors, which decreased to about 30% for the torrefied 300 °C–1 h samples and corresponded to the maximum devolatilization process. It should be observed that the decomposition of hemicellulose in the first peak had the highest reactivity compared to cellulose and lignin for both the precursors. This indicates the high reactivity of hemicellulose, as also confirmed from the FTIR analysis (section 4.6.3). Moreover, the peak representing the decomposition of hemicellulose did not appear for the torrefied samples at 300 °C–1 h, which further highlights the loss and disintegration of hemicellulose during torrefaction. The third stage (500–800°C) corresponded to char oxidation. Residue fixed carbon is combusted in this stage, which has the lowest reactivity, and the mass-loss rate declines. As seen in Figures 4.6 (a) & (b), no peak appeared in the DTG curve during this stage. The decline in the rate of mass loss of the torrefied biomass samples and the peak shifting to a higher temperature also indicated the attainment of thermal stability of the torrefied biomass samples compared to the precursors. Irrespective of the precursors, the thermal stability is attained under the severe torrefaction conditions (torrefaction temperature of 300 °C and longer residence time of 1 h). The CH-derived torrefied biomass sample is thermally more stable than SCG, owing to a lesser mass loss rate and peak shifting to a higher temperature.

(a)



(b)

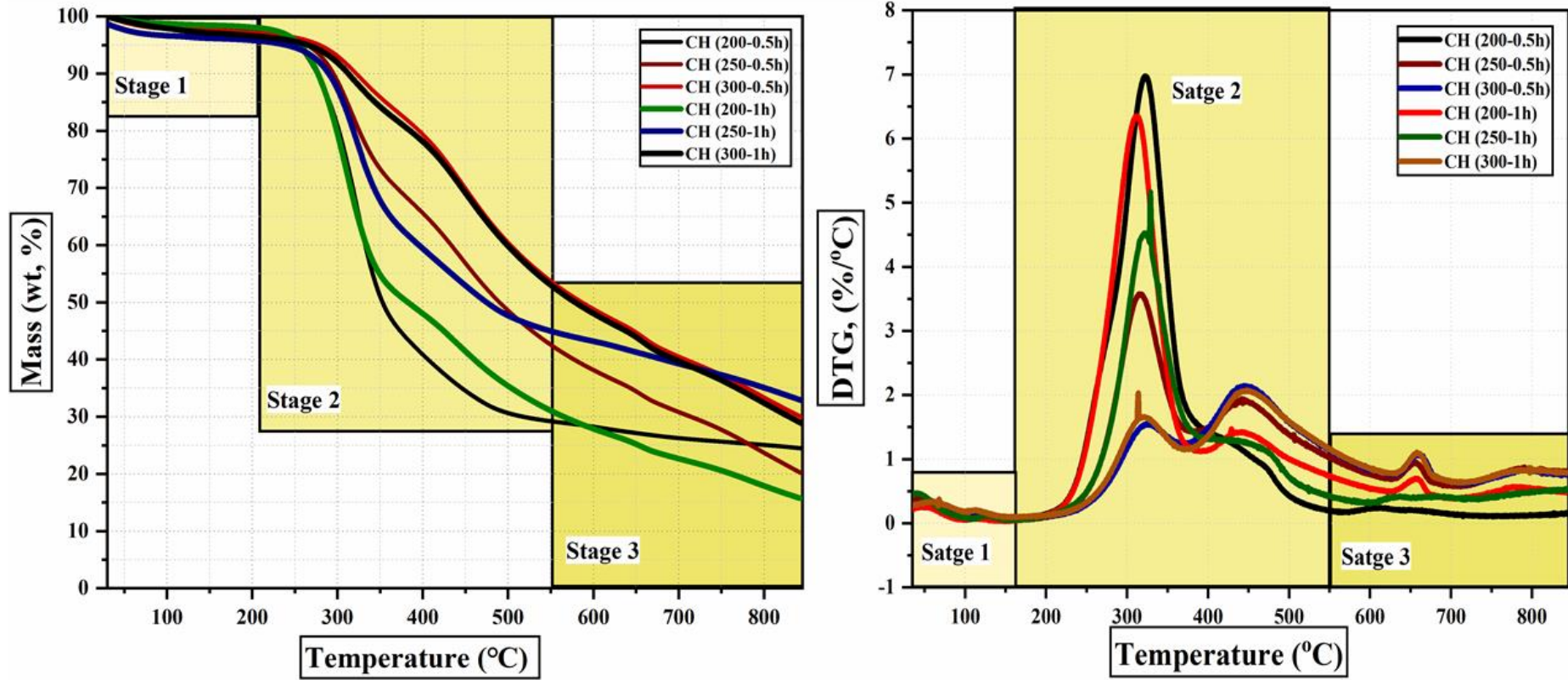


Figure 4.6: TGA-DTG analysis of the torrefied biomass samples at different torrefaction temperatures (a) SCG (b) CH.



#### 4.6.5 X-ray Photoelectron Spectroscopic (XPS) analysis

X-ray photoelectron spectroscopy is carried out to understand the impact of torrefaction temperatures and residence time on the elemental composition and surface functional groups in the torrefied biomass samples. Moreover, it also provides information on the qualitative and quantitative analyses of the different amounts of elements in the torrefied biomass samples. The findings of the survey scan for the respective torrefied biomass samples are presented in Table 4.4. The elemental composition obtained from the wide survey scan of the tested samples reveals a similar trend where the surface is dominated by carbon content (C1s), followed by oxygen (O1s), nitrogen (N1s), and a small amount of Silicon (Si2p), irrespective of the precursors. The XPS analysis findings complement the ultimate analysis (bulk) results (Table 4.2), where SCG-derived torrefied biomass samples were predominantly carbonaceous, followed by CH-derived torrefied biomass samples synthesized at 300 °C for 1 h (Table 4.4). The C content increased to 90.8-85.9 wt.% and O reduced slightly to 8.7-10.9 wt.% for SCG and CH-derived torrefied biomass samples synthesized at 300°C-1h. The increase in C content, a decline in O content and O/C demonstrate the carbonization, cracking of bonds, aromatization, and decarboxylation during biomass torrefaction.

**Table 4.4:** Elemental composition of torrefied biomass samples from the XPS analysis.

Sample	C1s	O1s	O/C	N1s	Si 2p
SCG-200-0.5h	84.9	15.3	0.14	1.3	2.2
SCG-300-1h	90.8	8.7	0.07	1.6	0.5
CH-200-0.5h	83.4	14.2	0.13	1.2	1.1
CH-300-1h	85.9	10.9	0.09	2.4	0.7

The deconvoluted C1s and O1s spectra of the respective precursors and the SCG and CH-derived biochar at 300°C for 1h are shown in Figures 4.7 (a) & (b), respectively and the variation in content obtained from the survey scan is presented in Tables 4.5 and 4.6. Azargohar et al. (2019b) suggested the C1s spectra contain the following functional groups in the carbon matrix: Peak (I) for aromatic /aliphatic sp<sup>2</sup> carbon (C-C/C=C/C-CH<sub>x</sub>) observed at B.E=284.1-284.6 eV, Peak (II) for sp<sup>3</sup>-C and C-O bonding at B.E=285.5-285.9 eV peak (III) for -C-OR for ether and hydroxyls/phenol group (C-OH) observed at B.E=286.4 eV, and Peak (IV) for C=O for carboxylic acids or ester observed at B.E=288.0-288.8 eV. Also, Azargohar et al. (2019b) suggested the O1s spectra could be deconvoluted into three peaks; peak (I) at 531.2-531.5 eV for carbonyl, ketone/lactone; peak (II) at 532.04-532.3 eV for C-OH functional

groups and peak (III) at 533.3 eV for ether oxygen atoms in anhydrides and esters as both SCG and CH are dominated by C-C/C-Hx functional groups. Also, the relative proportion of C-C/C=C/C-Hx functional groups increased from 25.2-24.4 wt% to 34.3-31.0 wt% for SCG and CH-derived torrefied samples, respectively, when the torrefaction conditions changed from mild to severe conditions. The trend of increasing -C-C/C=C/C-Hx, confirmed the increment in aromatic content and disintegration of aliphatic. On the contrary, the hydroxyl, carbonyl and ester functional groups reduced with torrefaction harshness. These findings indicated the occurrence of a series of dehydration and decarboxylation reactions releasing CO<sub>2</sub> and H<sub>2</sub>O during torrefaction and agree with the findings of the FTIR analysis (section 4.6.3).

**Table 4.5:** Deconvoluted C1s spectra of torrefied biomass samples.

Sample	Peak I (C1)	Peak II (C2)	Peak III (C3)	Peak IV (C4)
	284.1-284.7 eV	285.5 eV	286.1 eV	288.0-288.8 eV
SCG-200-0.5h	25.2	28.7	40.4	8.7
SCG-300-1h	34.3	63.5	11.3	3.5
CH-200-0.5h	24.4	39.1	28.1	6.9
CH-300-1h	31.0	49.1	19.3	7.2

**Table 4.6:** Deconvoluted O1s spectra of torrefied biomass samples.

Sample	Peak I (O1)	Peak II (O2)	Peak III (O3)
	B.E (531.2-531.5 eV)	B.E (532.04-532.3 eV)	B.E (533.3 eV)
SCG-200-0.5h	67.30	22.8	9.9
SCG-300-1h	47.03	44.7	8.3
CH-200-0.5h	60.4	29.3	1.3
CH-300-1h	39.2	59.4	2.7

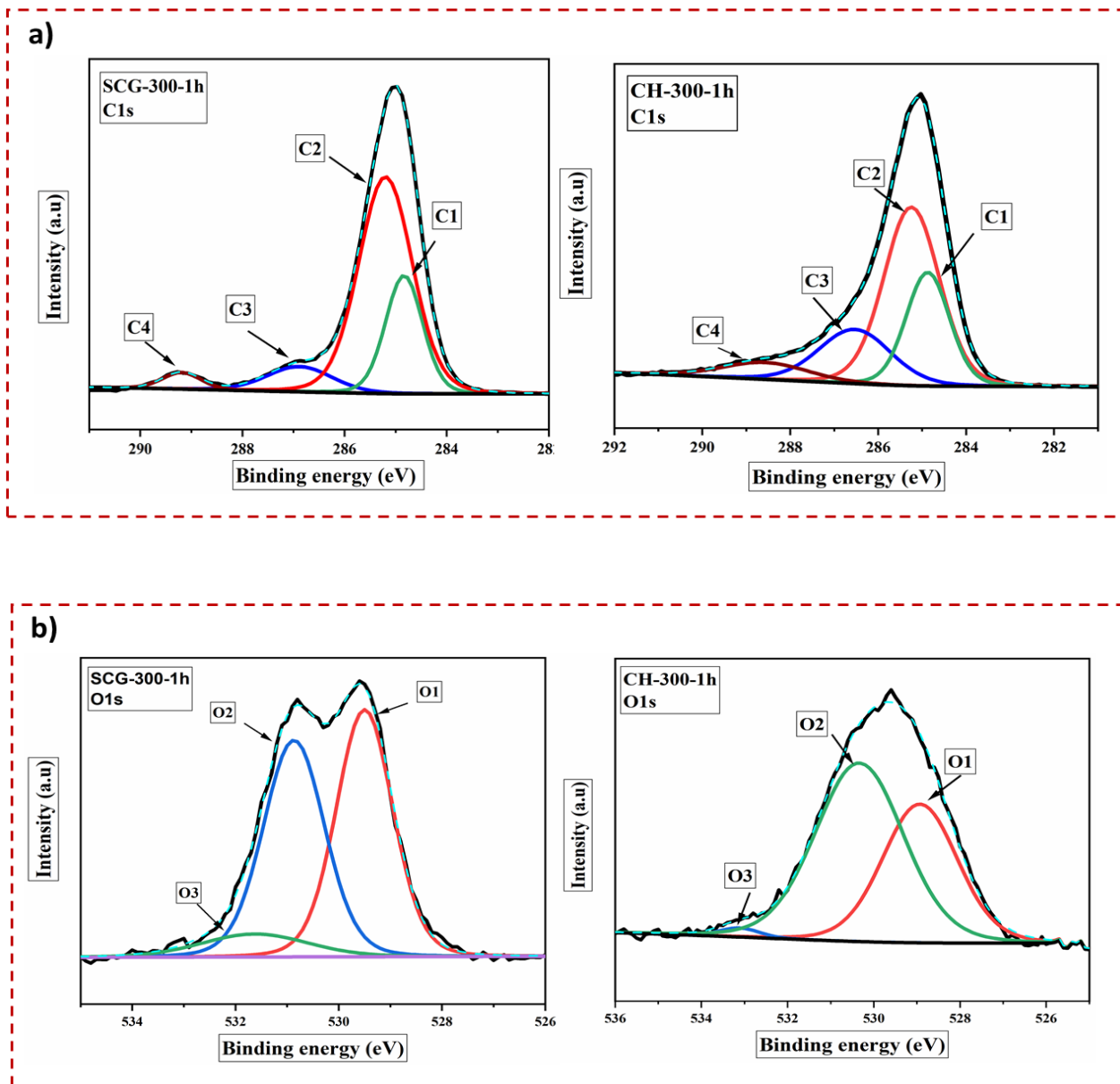


**Figure 4.7:** Deconvoluted spectra of SCG-300-1 and CH-300-1 (a) C1s and (b) O1s.

#### 4.6.6 Mass and energy yield of the precursors and the torrefied Samples

The resultant mass yield, higher heating value (HHV), energy yield of CH and SCG, and torrefied samples are summarized in Table 4.7. The results show that biomass exposure to higher temperatures had significantly negative impact on the mass yield (wt.%) compared to the residence time. For instance, at a constant residence time of 0.5 h, an increase in temperature from 200 °C to 300 °C led to a decline in mass yield from 93.2 wt. % to 55.1 wt. % for SCG. This behaviour could be because of the decomposition of volatile components into liquid and gaseous products between 200 and 300 °C (Dai et al., 2019).

It could also be attributed to the accelerated thermal degradation of the lignocellulosic components mainly hemicellulose, without any significant degradation on cellulose or lignin in precursors as also observed from the thermogram derived from the TGA-DTG analysis (Acharya et al., 2015).

Considerable decreases in the mass yield of torrefied CH and SCG to 48.1 and 54.3 wt.%, respectively, were observed at 300 °C and 1 h of residence time. This finding implies that approximately 51.9 and 45.7 wt. % of coffee residues degraded thermally as the temperature increased and prolonged duration. Moreover, due to the inherent difference in composition, the SCG had a superior solid yield compared to CH.

The energy yield ranged between 67.1-70.6% for SCG and CH-derived torrefied samples. However, CH-derived torrefied samples have a superior energy yield compared to SCG samples. It should be highlighted that the energy yield of the torrefied samples at all temperatures was below 100% due to the loss in energy during the torrefaction process. Additionally, from Table 4.7, it is evident that the energy density ratio improved for both the precursors with increasing severity of the torrefaction. Fuel with high energy density is always desirable. It will be less expensive in transportation and storage because it would occupy less storage or unit energy for transportation. The HHV values of the torrefied solids also increase with the severity of torrefaction conditions. Furthermore, when compared with the raw precursor, torrefied solids have higher HHV values. The HHV values are widely represented in the Van Krevelen diagram (Figure 4.3), where torrefied samples obtained at 300 °C and 1 h were found at the lower end of the diagram, demonstrating an improved HHV.

#### **4.6.7 Model Validation**

Experimental data for mass yields and HHV values from SCG and CH torrefaction at different torrefaction temperatures and residence times were used to validate the accuracy of the torrefaction model in this regard. The model validation plots for mass yields from the respective biomasses are presented in Figures 4.8 (a) & (b). It can be seen from Figures 4.8 (a) & (b) that the experimental mass yield correlates with the model predictions at a lower range of torrefaction temperature (200 °C). However, the model predictions are higher than the experimental results for both the biomasses at mild-higher torrefaction temperatures (> 250 °C). The variation of solid yield (wt.%) exists between the experimental and model results at higher torrefaction temperatures (> 250 °C) and could be attributed to multiple factors such as the reactor type, execution of the torrefaction process, type of precursors, mass loss during

biomass handling, product collection, temperature, and heating rate. Also, the model is not able to predict the complete decomposition of hemicellulose that occurs between the temperature range of 220-315 °C, which is responsible for drastic mass loss between 250-300 °C. On the other hand, Figures 4.9 (a) & (b) compare the HHV values from the experimental and model values. From Figures 4.9 (a) & (b), the HHV values from experimental data are close to the model values, with a deviation of less than 7% observed at 300 °C. For the HHV values, the deviations are relatively small and are permissible for engineering applications in the industries for the generation of energy. Also, the trends for both HHV values and solid yields are similar for the biomass samples. Therefore, the model could be used further to explain different phenomena occurring during the torrefaction process but would need detailed information regarding the lignocellulosic decomposition occurring between the temperature range of 200-300 °C.

**Table 4.7:** Solid yield (%), HHV, energy density ratio, and energy yield (%) of the precursors and the torrefied biomass samples.

Material	Torrefaction conditions (Temperature-residence time) (°C-h)		Solid mass yield (%)	HHV (MJ/kg, dry basis)	Energy density ratio	Energy yield (%)
	Temperature (°C)	Residence time (h)				
Coffee Husk (CH)	Raw material	Dried	100	18.3	1	100
	200	0.5	93.3±1.7	19.3±0.7	1.05	97.9
	200	1	89.6±1.2	20.03±0.5	1.09	97.6
	250	0.5	72.0±1.4	23.8±0.9	1.3	93.6
	250	1	68.3±1.1	24±1.1	1.3	89.5
	300	0.5	49.7±2.5	24.6±1.3	1.34	68
	300	1	48.1±3.3	25±1.6	1.4	67.1
Spent coffee grounds (SCG)	Raw material	Dried	100	22.3	1	100
	200	0.5	93.2±1.3	23±0.5	1.03	96.5
	200	1	90.4±1.6	23.6±0.3	1.06	95.6
	250	0.5	78.6±2.2	25.5±1.1	1.14	90
	250	1	77.1±2.1	25.7±1.7	1.15	89
	300	0.5	55.1±3.1	28.6±1.9	1.24	74.4
	300	1	54.3±2.9	30.3±1.6	1.3	70.6

*The solid mass yield for SCG and CH were performed in triplicates and the average values are reported. Similarly, the data reported for HHV are the average values of the triplicates. As can be observed for the solid mass yield (wt.%) and HHV, the standard deviation was within ±5 for both the biomasses.*

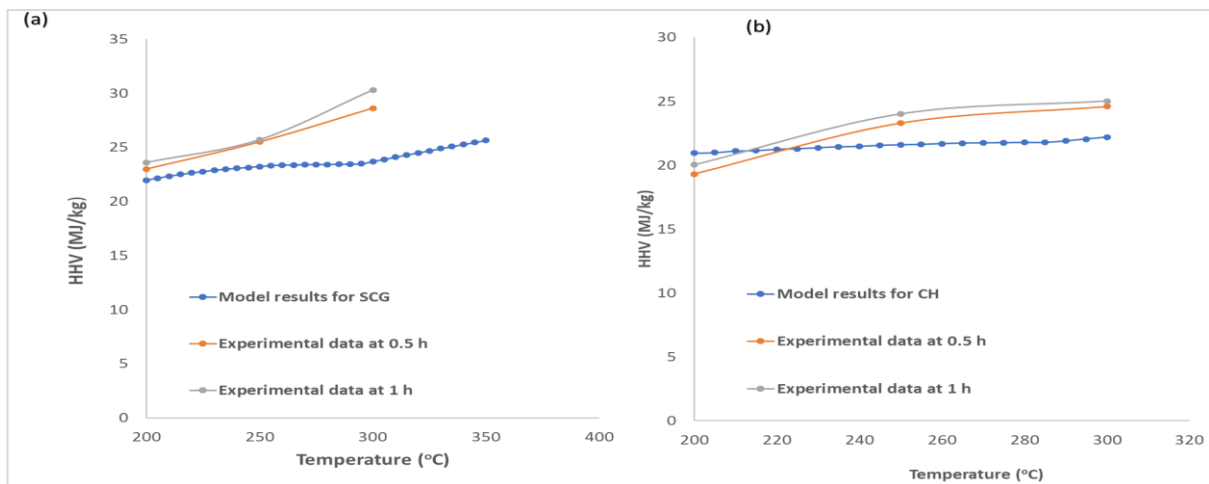


**Figure 4.8:** Model validation for mass yields (wt.%) during torrefaction of coffee residues for (a) SCG torrefied solids and (b) CH torrefied solids.

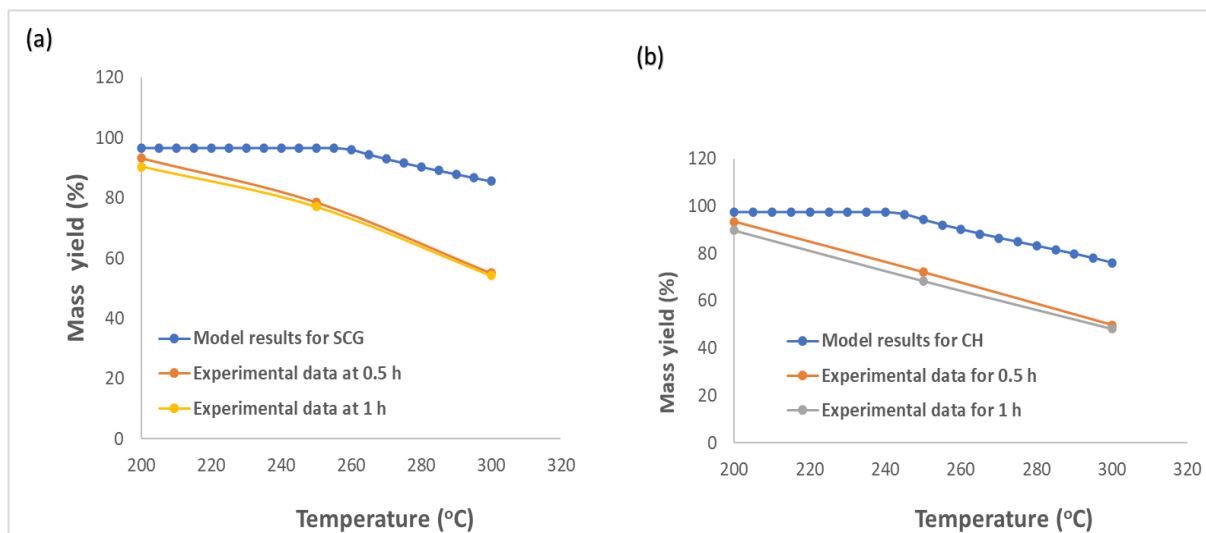


**Figure 4.9:** Model validation for HHV during torrefaction of coffee residues for (a) SCG torrefied solids (b) CH torrefied solids.

#### 4.6.8 Parametric Studies

The impacts of torrefaction temperatures on the mass yield (wt. %) and HHV values (MJ/kg) of the torrefied biomass samples are studied, and the modelling data obtained from process simulation are presented in Figures 4.10 (a) & (b) for SCG and CH. The simulation was performed at a temperature range of 200–300 °C. It should be noted that the effect of time was less pronounced when compared to torrefaction temperature as evident from the findings reported in the Table 4.7; therefore, the residence time was kept constant at 1 h.

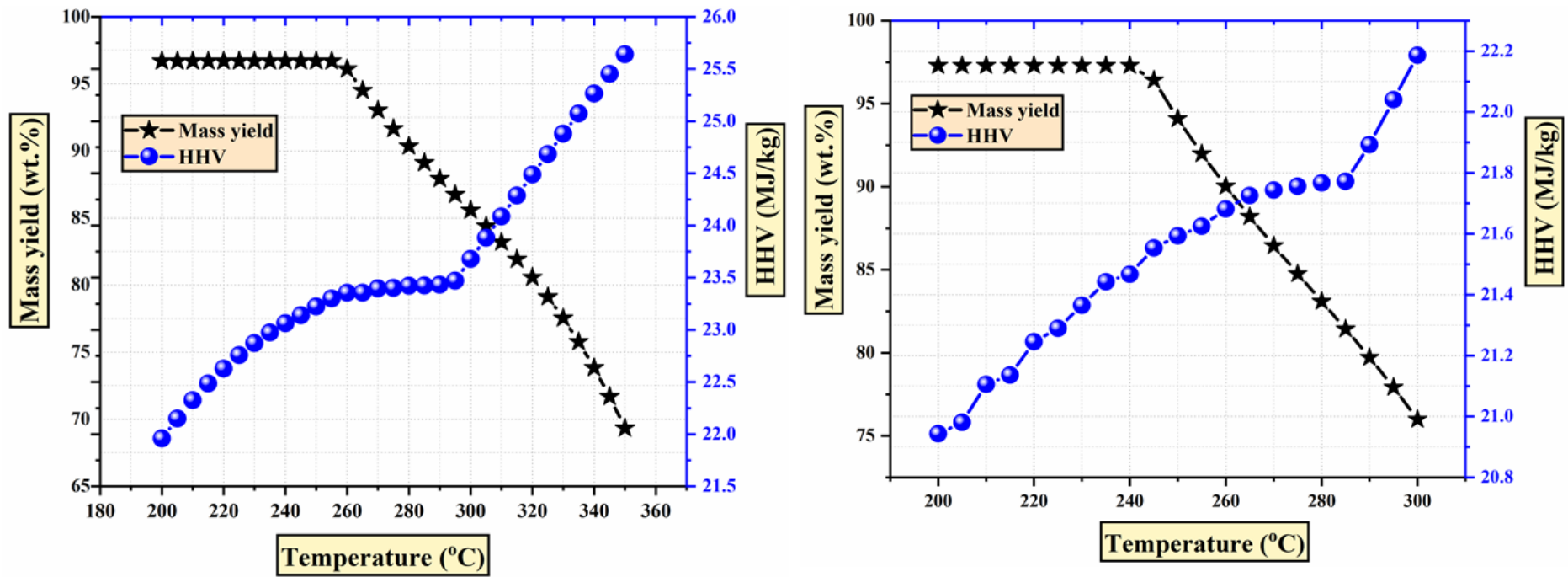


**Figure 4.10:** Effect of torrefaction temperatures on the mass yield and HHV values derived from the modelling data (a) SCG torrefied biomass samples (b) CH torrefied biomass samples.

It can be observed from Figures 4.10 (a) & (b) that the mass yield remains almost the same at a lower range of temperature between 200 and 250 °C for both the biomasses. However, when the temperature rose above 250 °C, a significant decline in mass yield was observed for both precursors. For example, the mass yield of SCG solid at 250 °C was reported as 96.7 wt.%. Moreover, a rise in temperature to 300 °C led to a significant decline in the mass yield to approximately 75.1 wt.% at 300 °C. Similarly, the mass yields of CH solids decreased from 97.3 wt.% at 250 °C to 77.5 wt.% at 300 °C. This behaviour of significant mass loss after 250 °C for both the biomasses can be attributed to the complete decomposition of hemicellulose that occurs in the temperature range of 220-315 °C and partial decomposition of cellulose (315-400 °C) and lignin (160-900 °C), also evident from the TGA-DTG thermogram of the precursors and the torrefied biomass samples in Figures 4.5 and 4.6.

Regarding the HHV values, it was observed that there is a consistent increase in the HHV values of the torrefied biomass samples with temperature, irrespective of the precursor type. For instance, the HHV values of SCG solids rose from 22 MJ/kg at 200 °C to 23.7 MJ/kg at 300 °C. In the same way, CH solid HHV values increased from 20.9 MJ/kg to 22.2 MJ/kg. The increase in HHV values and the decline in mass yields with temperature confirm the trend obtained from the experimental findings and analytical characterization results reported in the previous sections. To understand why there is a significant decline in mass yields with temperature and an elevation in HHV values, the yields of volatile components were also simulated.

The change in volatile compound yields with torrefaction temperature is shown in Figure 4.11. As shown in Figure 4.11, at temperatures between 200 and 250 °C for both biomasses, the amount of volatiles decomposed is almost negligible. This explains why there is an increase in mass yield at this temperature range. On the contrary, beyond 250 °C, a significant increase in volatile compounds yield was observed. Maximum volatile compound yields of 11.9 and 6.2 wt % were obtained for CH and SCG, respectively.

The simulation result of volatile yield decomposition aligns with the TGA findings reported in the previous section. Additionally, the increased HHV values of the torrefied samples could be attributed to the change in their elemental compositions (CHNSO values) compared to the raw precursors, as reported in Table 4.2. The C content of the torrefied biomass samples increases when compared with the biomasses, although the oxygen (O) and hydrogen (H) content is reduced. These changes in ultimate composition promote the elevation in HHV values. These



findings are in agreement with the previously reported literature (Azargohar et al., 2019a ; Bach et al., 2017).

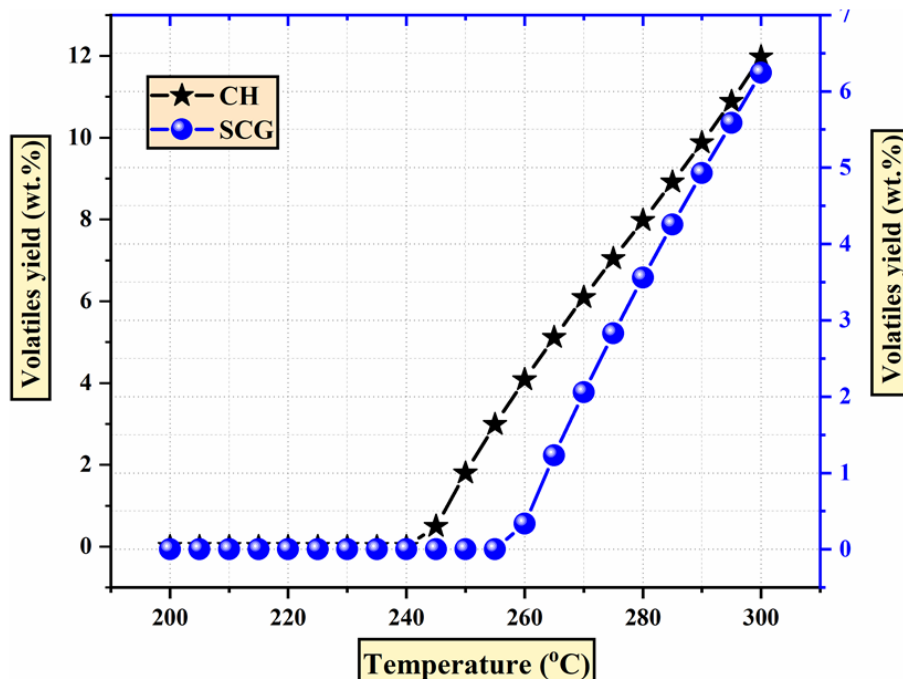


**Figure 4.11:** Effect of torrefaction temperatures on the decomposition of volatile compounds.

#### 4.6.9 CO<sub>2</sub> capture performance of torrefied samples

The CO<sub>2</sub> adsorption performance of SCG- and CH-derived torrefied biomass samples at 300 °C and 1 h was executed in a fixed-bed reactor at 25 °C under atmospheric pressure and in the presence of 30 vol % CO<sub>2</sub> (balanced by N<sub>2</sub>). The breakthrough capture performance of the tested samples is shown in summarised in Table 4.8 and demonstrated in Figure 4.12. As can be observed from Figure 4.11, the adsorption of gases proceeds continuously until the point of saturation is attained by the bed of torrefied biomass samples.

In general, under a similar capture scenario (25 °C and 30 vol % CO<sub>2</sub> balanced by N<sub>2</sub>), the torrefied sample derived from SCG presents a higher adsorption capacity ( $0.38 \pm 0.03$  mmol/g) at equilibrium than that derived from CH ( $0.23 \pm 0.08$  mmol/g).

**Table 4.8:** Breakthrough CO<sub>2</sub> adsorption performance of the torrefied biomass samples.

Sample	Exhaustion time (min)	Adsorption capacity at 25 °C and 1 bar (mmol/g)	Standard deviation
SCG-300-1	2.07	0.38	0.03
CH-300-1	1.1	0.23	0.08

The physiochemical transformation of SCG-derived torrefied samples under severe conditions (300 °C and 1 h) could probably account for a higher equilibrium adsorption capacity under a similar capture scenario. It presents a comparatively porous structure, higher specific surface area, and well-developed basic functional species on the surface of the SCG-derived torrefied biomass sample. It had a significant impact on the capture performances. However, to improve the CO<sub>2</sub> capture performance, the biomass needs further thermal treatment or chemical functionalization to attract more CO<sub>2</sub> molecules under the post-combustion scenario.

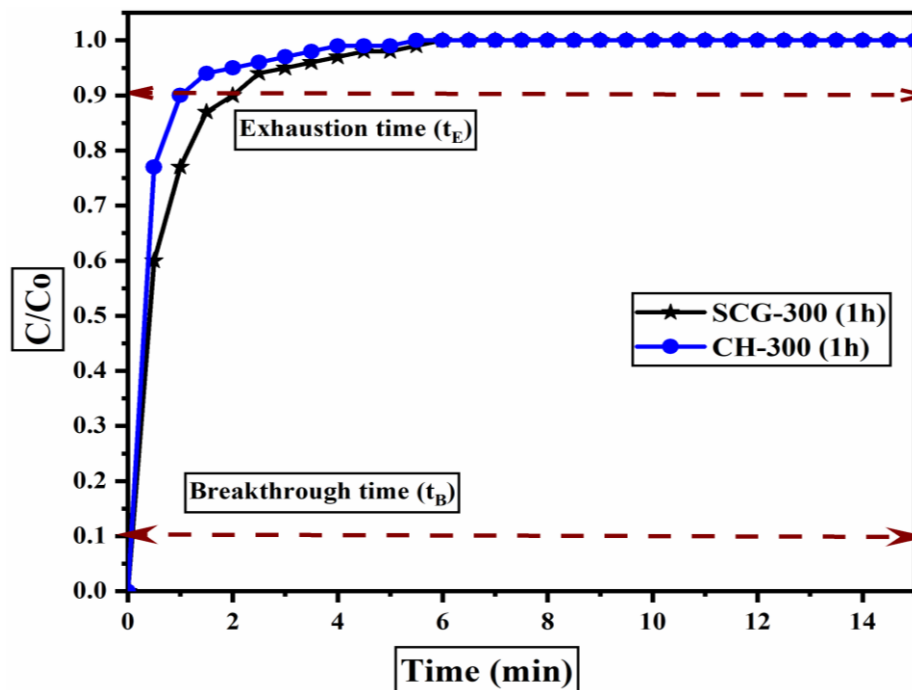


**Figure 4.12:** Breakthrough CO<sub>2</sub> capture performance of torrefied biomass samples.

#### 4.7 Conclusions

The study examined the impact of torrefaction temperature and residence time on the yield and physicochemical properties of torrefied biomass samples derived from SCG and CH. Furthermore, the performance of the torrefied biomass for post-combustion CO<sub>2</sub> capture was evaluated. An increase in torrefaction of SCG and CH led to a rise in the carbon content of the torrefied solids. On the contrary, the torrefied solids' hydrogen, sulphur, and oxygen contents decrease with an increase in torrefaction temperature for both precursors. The decline in hydrogen content with elevating torrefaction temperature could be attributed to the release of lighter hydrocarbons during torrefaction. The experimental mass yields and HHV values were compared with model results obtained from the Aspen Plus simulation. The experimental mass

yield and HHV values correlates with the model predictions at lower torrefaction temperature (200 °C). However, regarding the solid yield (wt.%) the model predictions are slightly higher than the experimental results for both precursors at temperatures above 200 °C compared to the model values of the HHV. Overall, this study shows that torrefaction influences the physicochemical properties of biomass by increasing the carbon content, high heating value, extended the specific surface area and thermal stability. In addition, XPS and FTIR results proved that the conversion from " $-C-O/-C=O$ " to "aromatic  $-C-C/=C$ " was the key point for improving phenol and aromatic content in the torrefied biomass sample prepared at the severe torrefaction conditions. The influence of the nature of precursors and are assessed in a fixed-bed reactor at 25 °C and atmospheric pressure for  $CO_2/N_2$  feed stream. The surface chemistry and developed pore structure facilitated the  $CO_2$  capture for SCG (0.38 mmol/g) than CH (0.23 mmol/g) at the similar capture condition (25 °C and 30 vol% of  $CO_2$  in  $N_2$ ). However, further thermal treatment or functionalization of SCG under more severe conditions or functionalization with nitrogenated species are imperative to develop the porous structure, morphology, and tailor the surface of the carbonaceous adsorbent to improve the  $CO_2$  capture performance in terms of enhanced  $CO_2$  adsorption capacity, selectivity of  $CO_2$  over  $N_2$ , and stability under a typical post-combustion scenario.

## **Chapter 5 Pyrolysis kinetics and activation thermodynamic parameters of spent coffee grounds and coffee husk using thermogravimetric analysis**

Most of the content of this chapter has been published as a research article in the Canadian Journal of Chemical Engineering. The Wiley publication holds the copyright and the permission to use the aforementioned article in this thesis has been obtained from Wiley as presented in Appendix G.

### **Citation:**

**Mukherjee, A**, Okolie, J. A, Tyagi, R, Niu, C, Dalai, A.K., (2021). Pyrolysis kinetics and activation thermodynamic parameters of exhausted coffee residue and coffee husk using thermogravimetric analysis, *The Canadian Journal of Chemical Engineering*, 99(8), pp. 1683-1695.

### **Contribution of the Ph.D. Candidate:**

Alivia Mukherjee did the following: (1) performing the experiments and analysing the physicochemical properties of the precursor; (2) interpretation and validating the experimental findings including modeling in Matlab and (5) writing the manuscript. Dr. Jude A. Okolie and Ramani Tyagi helped with developing the model in Matlab. Dr. Ajay K. Dalai and Dr. Catherine Niu supervised to draft the manuscript through discussions during this time.

### **Contribution of this chapter to the overall PhD research**

The second objective and the subsequent sub-objective of the research is addressed in this section of the thesis. This chapter provides the kinetic studies of slow pyrolysis of lignocellulosic biomass precursors (SCG and CH). Evaluating the kinetic and thermodynamics parameter were imperative to optimize the thermochemical conversion technique, slow pyrolysis in this regard. The result provides basic understanding of the degradation pathway and the effect of temperatures and heating rate on the mass loss during pyrolysis of biomass feedstock, kinetics, and thermodynamics parameters.

## 5.1 Abstract

Spent coffee grounds (SCG) and coffee husk (CH) are potential feedstock for energy production through thermochemical and biochemical conversion processes. The Kinetics study of SCG and CH is essential for the design and optimization of different thermochemical conversion processes and can provide useful insights for the design of pyrolysis reactors. In this study, four different iso-conversional methods were employed in the estimation of the activation energy ( $E_A$ ) and pre-exponential factor ( $A$ ). The method used includes three integral methods such as Flynn–Wall–Ozawa (FWO), Kissinger–Akahira–Sunose (KAS), Kissinger and one differential method; Friedman model. Data from the thermogravimetric/differential thermogravimetric analysis (TGA/DTG) at varying heating rates of 5–20 °C/min in an inert atmosphere were used in this study. It was observed that the heating rate influences the pyrolysis parameters such as peak temperature, maximum degradation rate and initial decomposition temperature. The activation energy for SCG using the FWO method was in the range of 62.3–102.4 kJmol<sup>-1</sup>. Likewise, the KAS and Friedman methods yielded activation energy between 51.3–93.3 kJmol<sup>-1</sup> and 10.6–122.7 kJmol<sup>-1</sup>, respectively. In addition, the activation energy calculated for CH using FWO, KAS and Friedman methods were shown to be ranged from 39.1–140.6 kJmol<sup>-1</sup>, 27.7–131.6 kJmol<sup>-1</sup> and 24.9–111.2 kJmol<sup>-1</sup>, respectively. The activation energy calculated using the Kissinger model was higher for both the precursors and ranged from 141.7–162.1 kJmol<sup>-1</sup> for SCG and CH, respectively. The fluctuation of activation energy with fractional conversion could be attributed to the interactions between the lignocellulosic component's degradation of the feedstock and complex reaction pathway during pyrolysis. Combining the kinetic study and thermodynamic parameters evaluation with the physicochemical properties, we concluded that both SCG and CH have considerable bioenergy potential for thermochemical conversion. However, SCG is a superior precursor in terms of higher activity, energy requirement during the conversion and the physicochemical characteristics than CH.

## 5.2 Introduction

With rapid industrialization and urbanization because of population growth, coupled with decreasing fossil fuels reserve, there is an urgent demand to develop alternative and sustainable energy sources. Renewable energy resources such as wind, biomass, and solar energy have some advantages over fossil fuels in terms of their environmentally friendly nature. Unlike other renewable energy resources, biomass can produce liquid and gaseous transportation fuels (Okolie et al., 2019). Furthermore, biomass is widely available and a cheap source of renewable energy. Coffee residues are examples of waste biomass that can be utilized to produce liquid transportation fuels to minimize waste disposal issues and the environmental challenges associated with fossil fuel consumption. For instance, Coffee husk (CH) is the dried coffee skin that is left behind during coffee roasting, while coffee pulp (CP) is obtained during the wet coffee processing (Aristizábal-Marulanda et al., 2017). On the other hand, spent coffee grounds (SCG) is generated from the coffee brewing process through the production of instant coffee with hot water. For every tonne (t) of fresh coffee consumed annually, about 0.18 t of CH is generated. Additionally, the annual production of SCG was estimated at six million tonnes worldwide (Mussatto et al., 2011). Reducing coffee by-products presents a severe environmental challenge. On the other hand, the residues generated from the coffee industry could be utilized as a potential feedstock for diverse applications. For instance, coffee residues can be used as feedstock for biofuels and biochemical production, as a fertilizer and to produce bioactive compounds (Janissen and Huynh, 2018).

Biomass can be transformed into biofuels and green chemicals through the thermochemical conversions (e.g. torrefaction, slow-pyrolysis and gasification) and biochemical pathways (e.g. anaerobic digestion and fermentation) (Okolie et al., 2020a). The thermochemical pathway uses heat and chemical energy to decompose biomass compounds and organic waste into sustainable fuels. Alternatively, microorganisms and enzymes are used to decompose biomass into green fuels during the biochemical conversion pathways (Cai et al., 2017). Thermochemical conversion routes have several advantages such as short residence time, high conversion efficiency and the ability to use several feedstock (Patel et al., 2019). Compared to all other thermochemical pathways, pyrolysis is of interest for the following reasons. First, it can produce solid-residue (char), tar, aqueous phase (aerosols or vapour) and non-condensable gas (syngas) from biomass feedstock. Secondly, the process is usually carried out in an inert environment (Nitrogen or Argon), and it is mostly influenced by different operating factors such as temperature, heating rate, type of feedstock, residence time, gas flow rate, moisture

content in the feedstock and particle-size of the precursor (Mishra and Mohanty, 2018). Finally, the products obtained from pyrolysis can be readily stored, transported and used as a substitute for fossil-based energy sources, which makes them highly attractive, especially when concerning environmental-related issues especially global warming (Hu et al., 2016).

Since pyrolysis product yield and composition is highly dependent on the type and composition of feedstock used together with the experimental conditions used in the degradation process, it is imperative to understand the reaction pathway and degradation mechanisms. Kinetic studies of biomass provide information about the reaction mechanisms and pathways. Moreover, an in-depth understanding of the pyrolysis kinetics of biomass is essential for the design and optimization of thermochemical conversion reactors (Mishra and Mohanty, 2018). Furthermore, kinetic analysis is useful for mathematical modelling and the optimization of reaction conditions (El-Sayed and Mostafa, 2014). On the other hand, thermodynamic parameter estimation provides valuable information for energy calculations and process feasibility studies mainly from the engineering perspective.

Thermogravimetric analysis (TGA) and derivative thermogravimetric analysis (DTG) is a widely used tool to investigate the thermochemical degradation of different biomass samples and events during the combustion of biomass, gasification and pyrolysis processes. TGA is well known as the most straightforward analytical tool to evaluate the kinetic parameters of biomass feedstock. The thermogravimetric (TG) data provides measurements in terms of the substrate mass and rate of devolatilization of biomass as a function of temperature and time in a controlled non-isothermal environment (Zhang et al., 2016). A comprehensive weight-loss profile during the thermal decomposition of biomass feedstock can be determined from TGA analysis. Data from TGA analysis also provides useful information for the estimation of kinetic parameters, which is critical for the modelling and understanding of different thermochemical conversion systems (Cruz and Crnkovic, 2016).

To estimate kinetics parameters (e.g. pre- exponential factor and activation energy) using the TGA analysis two methods are inherent: the non - isothermal and isothermal methods (Biagini et al., 2017). The former method provides more accurate results in terms of activation energy and pre – exponential factors. The non – isothermal method can be divided into two groups the model-free methods and the model fitting method (Patel et al., 2019). The model – free methods are easy to apply and more reliable with few errors during the evaluation of kinetic parameters compared to the model-fitting method. Furthermore, they do not involve any model assumption; instead, they apply different types of heating rate curves to evaluate the kinetic parameters (Mishra and Mohanty, 2018). Some kinetic models based on the iso-conversional

methods include; Kissinger-Akahira-Sunose (KAS), Flynn-Wall-Ozawa (FWO), Kissinger and Friedman methods. The iso-conversional methods have been utilized by several researchers to study the kinetics of waste biomass (Huang et al., 2019; Cai et al., 2018; Kaur et al., 2018; Mishra and Mohanty, 2018; Cruz and Crnkovic, 2016; El-Sayed and Mostafa, 2014; Hu et al., 2016; Zhang et al., 2016).

Although several studies have reported the pyrolysis kinetics of different agricultural residues to the best of the authors' knowledge (Ashraf et al., 2019; Biagini et al., 2019; Ahmad et al., 2017), there are limited data available for the kinetics of SCG and CH. With that, the objective of this study is to investigate the thermal degradation and pyrolysis kinetics of SCG and CH by using thermogravimetric/derivative thermogravimetric analysis (TGA/DTG) analysis performed in an inert atmosphere. The iso-conversional methods of the Kissinger-Akahira-Sunose (KAS), Flynn-Wall-Ozawa (FWO) and Friedman method were used to estimate the kinetics parameters. In addition, the activation thermodynamic parameters, including the change in enthalpy ( $\Delta H$ ), Gibbs free energy ( $\Delta G$ ), and entropy ( $\Delta S$ ), were also evaluated. To the best of the author's knowledge, there are minimal studies available that comprehensively evaluate the pyrolysis kinetics, thermal behaviour, and thermodynamic analysis of SCG and CH. This study provides a basis for future optimization of pyrolysis reactors and operating parameters.

### 5.3 Materials and Method

#### 5.3.1 Biomass collection and pre-treatment

The details regarding the biomass collection and pre-treatment are provided in Chapter 3 (section 3.1). Also, the methodology adapted to execute this research objective is schematically shown in Figure 5.1

#### 5.3.2 Proximate and ultimate analyses of biomass samples

The details regarding the proximate and ultimate analysis of the precursors are provided in Chapter 3.

#### 5.3.3 Calorific value

The theoretical higher heating value (HHV) of SCG and CH were determined following Friedl's formula as shown in Eq. (5.1) (Friedl et al., 2005).

$$\text{HHV (kJ/kg)} = (3.55 \times C^2) - (232 \times C) - (2230 \times H) + (51.2 \times C \times H) + (131 \times N) + 20600 \dots \dots \dots (5.1)$$

Where, the elemental compositions of C, H, and N are in wt. %.



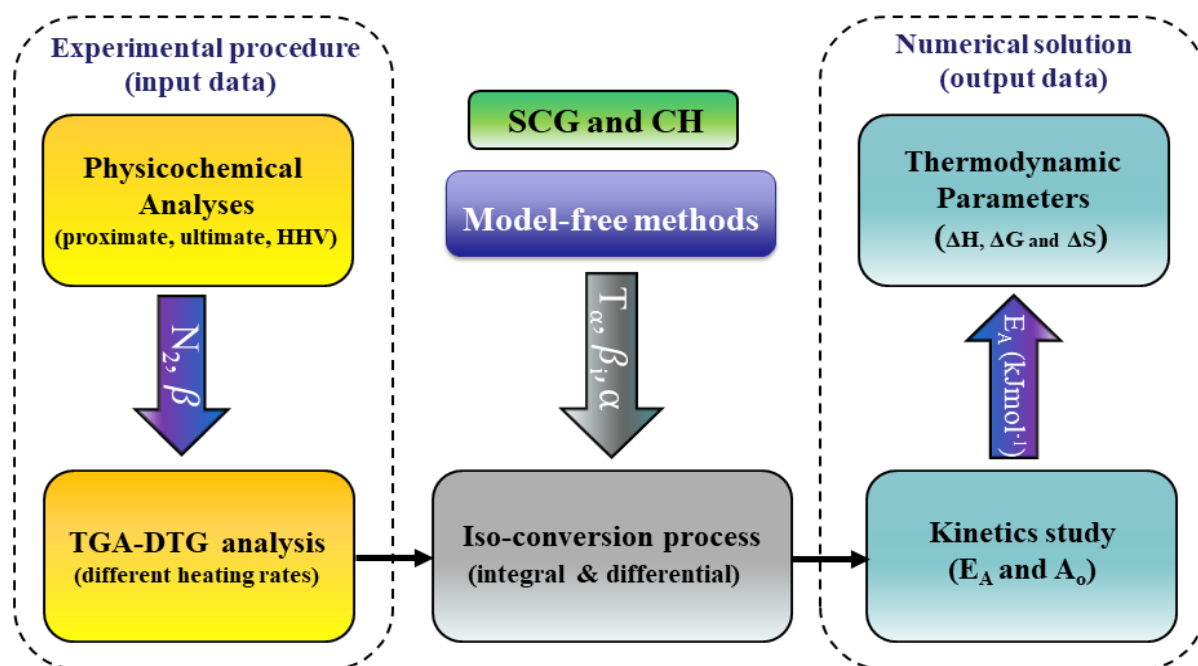


**Figure 5.1:** Schematic representation of the methodology adapted for research-objective 2.

### 5.3.4 Thermogravimetric analysis (TGA) of the precursors

The TGA-DTG analysis of the precursors are provided in detail in Chapter 3.

### 5.3.5 Sample Preparation for Fourier transform mid-infrared spectroscopy analysis

To prepare the homogenized SCG and CH samples for FT-MIR analysis, the samples were diluted with potassium bromide (KBr) to attain about 1.1 – 1.3% of the overall weight of the samples. The procedure is performed by adding a mixture of biomass samples (5.0 – 6.5 mg) and KBr (488.5 – 493.5 mg) to a polycarbonate vial (5 ml capacity). The vial contains eight grinding balls of 2.6mm diameter and made with stainless steel. The vials were distributed evenly into two Spex Sample Prep 2662 cryo-block which are cooled with liquid nitrogen for 10 min. This helps to attain the optimum sample brittleness for grinding. The Cryo-blocks were then transferred to a Spex Sample Prep Geno/Grinder 2010 for grinding. Grinding was carried out at 1250 rpm for 4 min. After grinding, the vials were transferred to a desiccator and left there until the samples attained room temperature. The cooled samples were weighted to 98.5– 99.5 mg and transferred to a 13 mm die set. The samples placed on the top die were spread evenly and flatted with the die set anvil. With a second 13 mm die placed over the first one, another sample aliquot was spread on it. The prepared samples were pressed with an automated hydraulic press for 3 s at 1.5, 4.0, and 5.5 tonnes. The final samples were placed into a sample wheel for analysis.

## ❖ FT-MIR Data collection and analysis

Agilent Technologies (Cary 670 series, Agilent Technologies Inc., CA, USA) microscope was used to collect the FT – MIR data (Karunakaran et al., 2020). The microscope which is located at the mid-IR beamline at the Canadian Light Source, Saskatoon, Canada was equipped with a TriGlycine Sulphate (DLaTGS) detector and a bulk analysis accessory. To reduce interference from CO<sub>2</sub> and water vapor absorption bands the sample chamber was purged with dry nitrogen. The MIR data were logged with a mean of 32 scans for each sample at a spectral range and resolution of 4,000 to 600 cm<sup>-1</sup> wavenumbers and 2 cm<sup>-1</sup> respectively. Orange (version 3.13) and OriginPro (Origin Lab Corporation, 2018) software were used in the spectral analysis and plotting respectively. The FT–MIR spectral analysis using orange software was carried out sequentially as follows: First, background correction was performed using the KBr spectrum followed by 3-point smoothing.

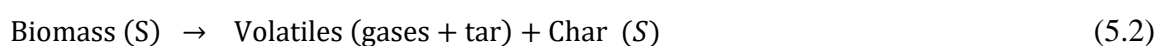
After which normalization with the sample weights was performed. Following data normalization, baseline correction was performed with rubber band (64 points) correction algorithm. Partial least square regression (PLSR) method was used in the quantification and prediction of structural sugars and lignin. The spectra information is compared with that of the component's concentration obtained from the reference methods.

The PSLR is a multivariate approach that is used to develop predictive models for highly collinear factors. Since the number of samples evaluated by the reference methods for different constituent differs, the PSLR models for each individual constituent were developed distinctly. To determine the optimum number of PLSR factors, the singular value decomposition (SVD) and full cross-validation were employed by the model. The calibration and validation sets were selected randomly and repeated thrice to ensure the accuracy of the model.

### 5.4 Kinetic study

Devolatilization behaviour of lignocellulosic biomass is a complex process involving a series of intermediate chemical reactions co-occurring at different phases. On the other hand, the pyrolytic characteristic of biomass is proposed as a single conversion step in which the biomass decomposes into volatiles and char as represented in Eq. (5.2).

$$k(T)$$



Where,  $k(T)$  is temperature-dependent rate constant.

For decomposition reactions such as combustion, pyrolysis or gasification, the reaction progress can be measured by comparing the heat or mass deviations observed from the reacting species. The conversion ( $\alpha$ ) can be represented in terms of their mass variation (thermogravimetry) of reactant, as expressed in Eq. (5.3). Mass or heat variations can be measured precisely using thermal analysis techniques such as the differential thermal analysis (DTA), thermogravimetric analysis (TGA), and differential scanning calorimetry (DSC). The TGA often estimates the weight loss of a sample with elevating temperature. On the contrary, DTG analysis measures the temperature variation between the samples and some reference materials. Differential Scanning Calorimetry (DSC), on the other hand, is like DTA except that it requires extensive measurement of heat flow into the sample.

$$\alpha = \frac{m_0 - m_T}{m_0 - m_f} \quad (5.3)$$

Where,  $m_0$  denotes the initial mass of the reacting sample in mg and  $m_f$  represent the final mass of the reactant in mg and  $m_T$  is the mass of the reactant at any temperature T.

The rate constant k (dependent on temperature, T) is usually defined in terms of activation energy using the Arrhenius equation as follows in Eq. (5.4):

$$k(T) = A_0 \exp \left( -\frac{E_A}{RT} \right) \quad (5.4)$$

Where,  $A_0$  and  $E_A$  denote the frequency/pre-exponential factor ( $\text{min}^{-1}$ ) and activation energy ( $\text{kJmol}^{-1}$ ), respectively, R and T stands for universal gas constant ( $\text{Jmol}^{-1}\text{K}^{-1}$ ) and absolute temperature (K), respectively. Similarly, the rate of chemical reaction is defined as the extent of the thermal decomposition of the biomass as represented in Eq. (5.5). It should be noted that Eq. (5.5) is a function of the conversion rate ( $\alpha$ ), temperature (T, K) and pressure (P,  $\text{Nm}^{-2}$ ).

$$\frac{d\alpha}{dt} = k(T) f(\alpha) h(P) \quad (5.5)$$

From Eq. (5.5), the pressure term  $h(P)$  could be neglected. This is attributed to the insignificant effect of pressure on most thermal decomposition processes (Vyazovkin et al., 2011). Thus, Eq. (5.5) can be expressed in terms of the conversion rate and temperature as presented in Eq. (5.6):

$$\frac{d\alpha}{dt} = k(T) f(\alpha) \quad (5.6)$$

Combining Eq. (5.6) and Eq. (5.4) produces Eq. (5.7).

$$\frac{d\alpha}{dt} = A_0 \exp \left( -\frac{E_A}{RT} \right) f(\alpha) \quad (5.7)$$

where,  $f(\alpha)$  can also be referred to as the reaction model since it describes the rate of conversion on the process itself. Assuming that the solid lignocellulosic biomass is found to

obey the  $n^{\text{th}}$ -order kinetics during thermal degradation then  $f(\alpha)$  can be expressed as presented in Eq. (5.8):

$$f(\alpha) = (1 - \alpha)^n \quad (5.8)$$

Where, 'n' represents the order of the reaction. Combining Eq. (5.7) and Eq. (5.8) gives a basis for differential kinetic equation that can be used for both non-isothermal and isothermal temperature conditions that produce Eq. (5.9):

$$\frac{d\alpha}{dt} = A_0 \exp\left(-\frac{E_A}{RT}\right) (1 - \alpha)^n \quad (5.9)$$

However, for non-isothermal conditions with heating rate ' $\beta$ ' in  $\text{Kmin}^{-1}$  also known as  $\frac{dT}{dt}$  can be expressed as Eq. in (5.10):

$$\beta = \frac{d\alpha}{dt} \times \frac{dT}{d\alpha} \quad (5.10)$$

Combining Eq. (5.9) and Eq. (5.10) yields Eq. (5.11) as follows:

$$\frac{d\alpha}{dt} = \frac{A_0}{\beta} \exp\left(-\frac{E_A}{RT}\right) (1 - \alpha)^n \quad (5.11)$$

Equation 5.11 can be rearranged and expressed in the integral forms as shown below in Eq. (5.12):

$$g(\alpha) = \int_0^\alpha \frac{d\alpha}{f(\alpha)} = \int_{T_0}^T \frac{A_0}{\beta} \exp\left(-\frac{E_A}{RT}\right) dT = \frac{A_0}{\beta} \int_{T_0}^T \exp\left(-\frac{E_A}{RT}\right) dT = \frac{A_0 E_A}{\beta R} P(x) \quad (5.12)$$

Where,  $g(\alpha)$  and  $P(x)$  represent the integral conversion and temperature integral, respectively and  $x = E_A/RT$ . The temperature integral ' $P(x)$ ' does not have an explicit solution; however, the numerical approximation method proposed by various authors can be used to evaluate  $P(x)$ . It is noteworthy to mention that the value of  $P(x)$  in Eq. (5.12) varies with the type of approximation used.

In this study, four different iso-conversional models (Kissinger–Akahira–Sunose (KAS) method, Flynn-Wall-Ozawa (FWO) method, Kissinger's method and Friedman method) were used to determine the kinetic parameters  $E_A$  ( $\text{kJmol}^{-1}$ ) and  $A_0$  ( $\text{s}^{-1}$ ) using the data derived from the experimental data of TGA/DTG thermograms. Additionally, the iso-conversion methods used in this study do not require a prior determination of reaction mechanism to estimate the kinetic parameters of biomass decomposition.

## 5.5 Iso-conversional models

The iso-conversional methods are widely used in the evaluation of the activation energies. For a given conversion of " $\alpha$ ," the iso – conversional method can evaluate the activation energy

with the assumption that the kinetics of the reactions does not depend on the heating rate. Besides, the conversion of biomass into the required products is considered as a single-step process (Damartzis et al., 2011).

### 5.5.1 Kissenger–Akahira-Sunose (KAS) equation

The Kissenger–Akahira-Sunose (KAS) method applies the Murray and White approximation (Dhyani and Bhaskar, 2018) and  $P(x)$  is expressed as stated in Eq. (5.13).

$$P(x) \approx x^{-2} e^{-x} \quad (5.13)$$

Substituting Eq. (5.13) into Eq. (5.12) gives a final form of the relationship between heating rate and temperature as presented in Eq. (5.14):

$$\ln \left( \frac{\beta}{T^2} \right) = \ln \left( \frac{A_0 E_A}{Rg(\alpha)} \right) - \frac{E_A}{RT} \quad (5.14)$$

The activation energy ( $E_A$ ) can be determined by the slope of  $\ln \left( \frac{\beta}{T^2} \right)$  against  $(1/T)$  for the specified value of conversion ( $\alpha$ ).

### 5.5.2 Flynn–Wall- Ozawa (FWO) equation

The FWO iso-conversional model is one of the most accepted methods used to estimate the kinetic parameters. This method is based on Doyle's approximation (Doyle, 1965) (Dhyani and Bhaskar, 2018) which can be expressed as shown in Eq. (5.15):

$$P(x) \approx \exp (-2.315 - 0.4567x) \quad (5.15)$$

Substituting the value of  $P(x)$  derived from Eq. (5.15) into Eq. (5.12) and rearranging results gives the equation for the FWO model, as shown below in Eq. (5.16) and Eq. (5.17):

$$\ln (\beta) = \ln \left( \frac{A_0 E_A}{Rg(\alpha)} \right) - 5.331 - 1.052 \frac{E_A}{RT} \quad (5.16)$$

$$\ln (\beta) = \text{constant} - 1.052 \frac{E_A}{RT} \quad (5.17)$$

From equation (5.17), a linear plot of  $\ln (\beta)$  against  $1/T$  would produce a slope of  $-1.052 E_A/R$  from which the activation energy ( $E_A$ ) value can be obtained for the corresponding conversion value ( $\alpha$ ).

### 5.5.3 Kissinger's Method

Since most iso-conversional methods are unable to accurately predict the frequency factor ( $A_0$ ) the Kissinger method was used to estimate the frequency factor. Although Kissinger's method uses multiple heating rates, a single value of activation energy is obtained (Kumar et al., 2019).

Kissinger's method is easy to apply and has been used extensively in the determination of frequency factor ( $A_0$ ) and activation energy ( $E_A$ ) by several researchers. The Kissinger equation can be derived from Eq. (5.7), assuming that the maximum reaction rate condition is  $d\alpha^2/dt^2 = 0$ .

Therefore, the equation is reduced to:

$$\ln \left[ \frac{\beta}{Tm^2} \right] = \ln \left[ \frac{A_0 R}{E_A} \right] - \frac{E_A}{RTm} \quad (5.18)$$

Where,  $T_m$  refers to the peak temperature obtained from the DTG curve.

From Eq. (5.18), a curve of the left-hand side of the equation versus the inverse of the peak temperature ( $1/T_m$ ) gives a slope of  $-E_A/R$  from which the activation energy ( $E_A$ ) can be evaluated. Similarly, the frequency factor,  $A_0$ , can be calculated from the intercept of the same curve.

#### 5.5.4 Friedman method

The method of Friedman is widely used for the determination of activation energy due to its simplicity and accuracy compared to other iso-conversional methods (Huang et al., 2019). The Friedman approach is sensitive to data noise therefore advanced data smoothing has been used to improve the accuracy of the results. The locally weighted scatterplot smoothing (LOWESS) method was employed to process the DTG curves of the pyrolysis of coffee residues. An in-depth description of the smoothing procedure can be obtained from the work of Simonoff et al. (1998)

The Friedman equation can be derived by taking the natural logarithm of Eq. (5.6) as follows

$$\ln \left[ \frac{d\alpha}{dt} \right] = \ln [A_0 f(\alpha)] - \frac{E_A}{RT} \quad (5.19)$$

Using Eq. (5.10), this equation reduces to:

$$\ln \left[ \beta \frac{d\alpha}{dT} \right] = \ln [A_0 f(\alpha)] - \frac{E_A}{RT} \quad (5.20)$$

From Eq. (5.20), with a specified conversion and series of TGA measurements at different heating rates the values of activation energy  $E_A$ , and  $\ln [A_0 f(\alpha)]$  can be estimated. Kinetic plots of  $\ln \left[ \beta \frac{d\alpha}{dT} \right]$  versus  $1/T$  provides a slope and intercept of  $-E_A/R$  and  $\ln [A_0 f(\alpha)]$ , respectively.

To apply the Friedman conversion method, the derivative conversion " $\frac{d\alpha}{dT}$ " data is required. The derivative conversion is estimated by performing a numerical differentiation of the conversion data with the central difference method (Cai et al., 2018).

## 5.6 Evaluation of the thermodynamic parameters

The thermodynamic parameters evaluated in this study include the Enthalpy ( $\Delta H$ ), Entropy ( $\Delta S$ ) and Gibbs free energy ( $\Delta G$ ). The thermodynamic parameters were calculated from the following Eqs. (5.21-5.23) (Kaur et al., 2018).

$$\Delta H = E_A - RT \quad (5.21)$$

$$\Delta G = E_A + \ln\left(\frac{T_p K_B}{A_0 h}\right) \cdot RT \quad (5.22)$$

$$-\Delta S = \left(\frac{\Delta G - \Delta H}{T_p}\right) \quad (5.23)$$

From the Eqs. (5.21) -(5.23) above,

$K_B$  = Boltzmann constant ( $1.381 \times 10^{-23} \text{JK}^{-1}$ );  $T_p$  = Peak temperature (K) derived from the DTG curve;  $h$  = Plank constant ( $6.626 \times 10^{-34} \text{J.s}$ ).

## 5.7 Results and discussions

### 5.7.1 Physicochemical properties of biomass samples

The proximate analysis of SCG and CH studied is presented in Table 5.1. It should be noted that the results of the proximate analysis were presented on an as-received basis for both the samples as well as the dried basis for SCG. Among the two coffee residues, SCG showed a relatively high moisture content (47.1 wt %) and volatile matter (40.4 wt %). In contrast, the ash content of CH is higher at 1.7 wt. % and volatile matter (77.7 wt. %). The fixed carbon contents of SCG and CH are 11.6 wt. % and 17.9 wt. %, respectively. The data shown in Table 5.1 confirm that SCG contain very large amounts of moisture content at more than 40%. On the other hand, both samples also contain low ash content which is desirable for thermochemical conversion processes. High ash content in samples may cause fouling and disposal problems. However, after the pre-treatment of SCG (oven drying) the moisture content reduced to less than 5 wt% and eventually the volatile matter content and fixed carbon content improved as shown in Table 5.1. High volatile matter content in both the precursors mainly SCG is convenient for valorization through thermochemical conversion processes such as pyrolysis, combustion and gasification (Kumar et al., 2019).

The ultimate analysis for both SCG and CH showed a relatively high carbon content of 50 wt. % and 48.5 wt. %, and a considerable amount of hydrogen of 5.9 wt% (CH) and 6.7 wt % (SCG), respectively. The findings on C and H content reveal the potential of coffee residues to generate energy and fuels. Moreover, the low nitrogen and sulphur contents (< 3%) found in

both coffee residues indicates that there will be relatively low production of toxic gases such as NO<sub>x</sub> and SO<sub>x</sub> during pyrolysis.

The experimental HHV of SCG and CH were reported as 22.3 MJkg<sup>-1</sup> and 18.3MJ kg<sup>-1</sup>, respectively. The high calorific values of both coffee residues are attributable to their lower ash and higher volatile matter content. The calorific values of SCG and CH were estimated to be higher when compared to the calorific values of agriculture waste such as rice husk (12.9 MJ kg<sup>-1</sup>), wheat straw (14.7 MJ kg<sup>-1</sup>), rice straw (14.9 MJ kg<sup>-1</sup>), and corn cob (16 MJ kg<sup>-1</sup>) (Biswas et al., 2017). The estimated HHV of SCG and CH also illustrates their suitability as feedstock for green fuels and chemicals production through the thermochemical conversion processes. Lignin content of SCG and CH is reported as 32.6±0.3 wt. % and 19.6±0.1 wt. %, respectively. On the other hand, the structural sugar contents of CH (39.2±0.1 wt. %) is lower than that of SCG (43.3±0.4 wt. %).

**Table 5.1:** Proximate, ultimate, and high heating value of spent coffee grounds and coffee husk.

Analysis	SCG (as-received basis)	SCG (dried basis)	CH (as received)
<b>Proximate analysis (dry basis, wt. %)</b>			
Moisture content	47.1±0.4	3.3±0.1	2.7±0.05
Volatile matter	40.4±0.13	81.2±0.1	77.7±0.23
Ash content	0.9±0.01	0.9±0.1	1.7±0.01
Fixed Carbon*	11.6±0.01	14.6±0.01	17.9±0.02
<b>Ultimate analysis (dry basis, wt. %)</b>			
C	50.0±0.01		48.5±0.02
H	6.7±0.05		5.9±0.01
N	2.5±0.03		2.8±0.01
S	0.9±0.001		0.6±0.03
O**	39.0±0.10		40.6±0.01
<b>Chemical structure/composition</b>			
Structural Sugar	43.3±0.4		39.2±0.1
Total Lignin	32.6±0.3		19.6±0.1
<b>Higher heating value (HHV) (MJ/kg)</b>			
Experimental HHV	22.3		18.3
Theoretical HHV***	20.4		19.6

\*Fixed carbon (wt %) is calculated from the equation: FC wt. % = 100 - (M + VM + Ash)

\*\*Oxygen (O, wt %) is calculated from the equation: O wt. % = 100 - (C + H + N + S + Ash)

\*\*\* The Theoretical HHV value was computed by Friedl's formula.



### 5.7.2 Thermogravimetric analysis of biomass samples

The thermogravimetric analysis includes the change in weight of the sample with respect to the reaction temperature and time during the pyrolysis process. The curves ascertained the change in the physical and chemical structure in feedstock occurring during the thermal degradation of biomass. The thermal decomposition behaviour of SCG and CH were studied with thermogravimetry (weight loss, TGA) and derivative thermogravimetry (rate of weight loss, DTG) analyzer at a constant heating rate of 10 °C/min in an inert atmosphere of N<sub>2</sub> under non-isothermal condition. Figure 5.2 shows the weight-loss behaviour of the biomasses with respect to the pyrolysis temperature (TGA) and the subsequent derivatives of the TGA curves (DTG) for SCG and CH, respectively. The TGA and DTG curves were analyzed to elucidate the pyrolytic and thermal decomposition behaviour of SCG and CH. As can be seen in Figure 5.2 (a), the pyrolysis characteristics of SCG and CH is a similar but a complex process where three different pyrolytic stages are detected. As shown in Figures 5. 2 (a) & (b), SCG and CH exhibit a similar devolatilization pattern with initial thermal decomposition starting at 150°C. Additionally, three different pyrolytic stages were observed. The first stage, which occurs at a temperature up to 230°C, could be attributed to the loss of moisture, decomposition of minerals, and degradation of low molecular weight compounds due to the hygroscopic nature of SCG and CH (Mallick et al., 2018). Weight loss of approximately 4 wt.% and 3 wt.% were observed during the first stage of the dehydration of SCG and CH, respectively. Lower retained moisture content (<10%) both in SCG and CH makes them potential feedstock for combustion.

The second stage of weight loss occurs at a higher temperature of 240-460 °C for SCG and 220-450 °C for CH. This stage is also known as the active pyrolytic stage. In the active pyrolytic zone, most of the thermal transformation happens with the fragmentation of higher molecular weight compounds into smaller molecular compounds and the evolution of the highest amounts of gaseous compounds such as CO, CO<sub>2</sub>, H<sub>2</sub>, and CH<sub>4</sub>. With the increment of the pyrolysis temperature from 240 – 460 °C, the yield of residual solid has a declining trend. This stage is equivalent to the loss of hemicellulose, cellulose, and a small amount of lignin in biomass samples.

Among the two coffee residues, the highest weight loss was recorded for SCG (66%), compared to CH (59%). Owing to high volatile matter, hemicellulose, and cellulose content in SCG (dried), which undergoes thermal degradation in the active pyrolytic zone, the percent mass loss is higher compared to that of CH.

The last stage of thermal decomposition occurs at temperatures of 560–800°C for SCG and CH. This stage corresponds to the endothermic thermal degradation of the crystalline part of cellulose and lignin. However, the degradation rate at this stage is much slower compared to other stages and could be attributed to the recalcitrant nature of lignin, indicating that no appreciable mass conversion reactions took place in the passive pyrolytic zone. Total mass loss of 14% and 19 % of the original weight was found for SCG and CH, respectively, in the passive pyrolysis zone. Lignin is a complex polymeric substance consisting of phenylpropane molecules and highly branched C-H groups. As a result of its complex structure and recalcitrant nature, lignin is tough to degrade. From the thermogravimetric curves it is evident that most of the thermal conversion happened at the active pyrolytic zone and at the temperature range of 230-460 °C for both coffee residue.

The DTG curves of SCG and CH are illustrated in Figure 5. 2 (b). The DTG thermographs of the two coffee residues differ in height and peak positions. This indicates that the difference in physicochemical properties (ultimate, proximate, and chemical composition) of the two coffee residues. Moreover, the distribution of the inorganic and organic components could also affect their thermal decomposition behaviour. From the DTG curves, a two-step degradation is evident for both coffee residues. The first shoulder peaks observed from the DTG curves at 220°C for SCG and 215 °C for CH correspond to the decomposition of hemicellulose. It is linked with the loss of hemicellulose as it decomposes in the temperature range of 220-315 °C (Biswas et al., 2017). On the other hand, the maximum peaks at around 355 °C and 351°C for SCG and CH, respectively, correspond to cellulose decomposition. Cellulose undergoes thermal decomposition at temperature range of 315-450 °C (Soysa et al., 2016). Finally, lignin decomposition has a broad temperature range from 200-500°C and is indicated by the peak at the flat tailing section of the DTG curves.

DTG thermographs peaks confirm the results from TGA analysis indicating that hemicellulose decomposes at lower temperature ranges, followed by cellulose decomposition, lignin decomposes at a higher temperature above 400 °C with char (solid-residue) formation which might undergo aromatization at this range of temperature (Mishra and Mohanty, 2018). Furthermore, the height of the DTG curves is different for the precursors which reflect that it is influenced by the lignocellulosic composition and their thermal decomposition.

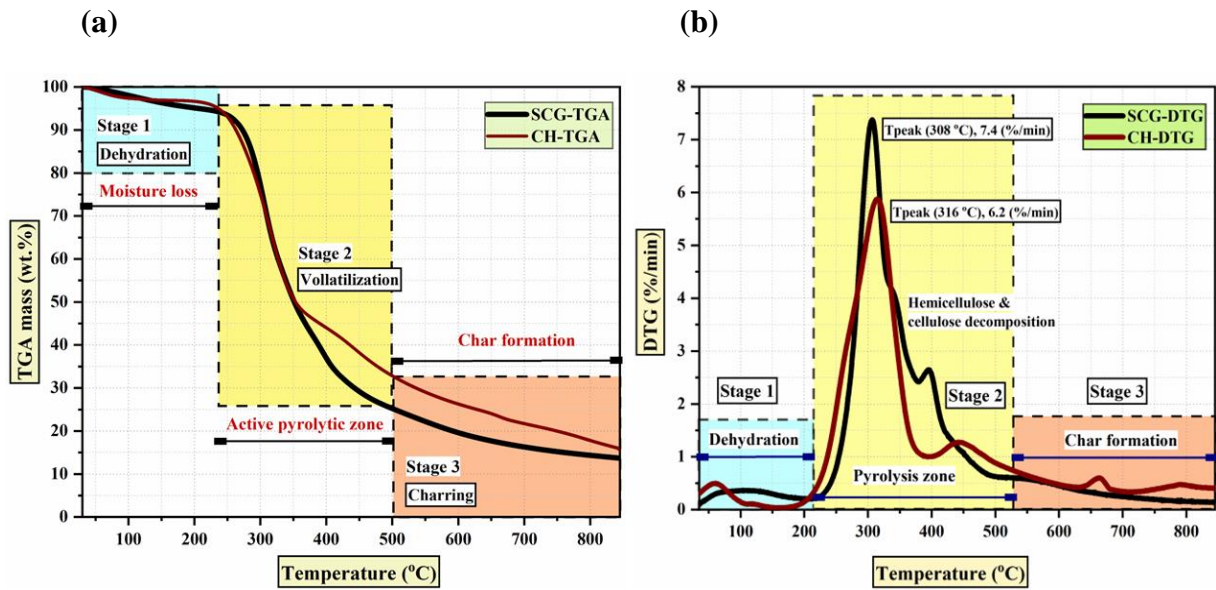


**Figure 5.2:** (a) TGA profiles of spent coffee grounds (SCG) and coffee husk (CH) at a constant heating rate of 10 °C/min, (b) DTG profiles of spent coffee grounds (SCG) and coffee husk (CH) at a constant heating rate of 10 °C/min.

### 5.7.3 Effect of heating rate on the thermal decomposition of biomass samples

The effect of heating rate ( $\beta$ ) on the pyrolytic behaviour and the thermal degradation pattern of SCG and CH were analyzed in a non-isothermal condition under varying heating rates and inert atmosphere ( $N_2$ ) are depicted in the TGA-DTG profiles in Figures 5.3 (a) & (b) and Figures 5.4 (c) & (d). Four different heating rates of 5, 10, 15 and 20 °C/min were comprehensively studied with their TGA and DTG results presented. As revealed in Figures 5.3 (a) & (b) and Figures 5.4 (c) & (d), the heating rate influences the maximum peak temperature ( $T_{peak}$ ), decomposition rate, and the maximum weight loss of the samples. The Figures 5.3 and 5.4 demonstrates that with the increasing heating rates the initial and final temperature in the pyrolysis region increases to the higher range. However, the thermal decomposition profiles of SCG and CH at all heating rates remains the same. This shows a similar degradation pattern and reaction mechanism for all heating rates. Furthermore, with elevating heating rate, the thermal decomposition is observed to approach the higher temperature zone as observed in Figures 5.3 (b) & 5.4 (d), respectively.

The DTG curves in Figures 5.3 (b) & 5.4 (d) indicate that the pyrolysis characteristics temperature of the active pyrolytic zone (second stage) rises with increasing heating rate for SCG and CH. Furthermore, from Figures 5. 5 (a) & (b), the temperature at which 5% of the

sample weight is converted ( $T_{5\%}$ ) and maximum weight loss temperature ( $T_{\text{peak}}$ ) increases with elevating heating rate. Similarly, the maximum decomposition rate rose from 3.7-15 wt %  $\text{min}^{-1}$  for SCG (Figure 5.3 (b)) and 3.0 to 12.1 wt. %  $\text{min}^{-1}$  for CH (Figure 5.4 (d)). Kumar et al., (2019) observed similar results during the pyrolysis kinetic studies of Ru/Fe impregnated banana pseudo stem. At elevated heating rate of 20 °C/min, the authors observed a shorter residence time for the Ru/Fe impregnated banana pseudo stem samples. Furthermore, there was an increase in the temperature required for organic matter decomposition. The authors attributed this behaviour to the low heat conductivity of biomass samples. As a result of the low heat conductivity of biomass samples, longer time is required for heat conduction of the particle from the external surface to the interior; therefore, a temperature gradient could be formed throughout the biomass cross-section during heating (Kumar et al., 2019). This leads to a slow heat transfer and reduction in heat transfer efficiency at elevated heating rate. Several researchers described that a lower heating rate is suitable for improved heat transfer in biomass samples. During the pyrolytic degradation of biomass at low heating rates, secondary reactions like re-condensation, re-polymerization along with cracking reactions generates char/tar formation resulting in less weight loss (Kumar et al., 2019).

However, this is not the case in our study. Pyrolysis process is controlled by kinetics together with heat and mass transfer. In the present study, we evaluated the pyrolysis kinetics using data from TGA, where a small mass (about 12 mg) of the sample were heated in a TGA analyzer. The residual mass of the samples as well as the surrounding fluid temperature were measured over time, with the surrounding fluid temperature assumed to be the same as the surface temperature of the sample (negligible inter-particle mass transfer). However, in evaluating the pyrolysis kinetics, we assume that the mass of the sample is so small that heat transfer limitations are negligible. As a result, heat transfer limitations are not included in the model. Therefore, degradation of the biomass samples is controlled by the kinetics. Regardless, it is important to note that in most practical applications, heat transfer limitations could still play a major role and will need to be considered. A higher heating rate also promotes the formation of gases and lower char during thermal degradation of SCG and CH due to the low heat transfer and temperature gradient.

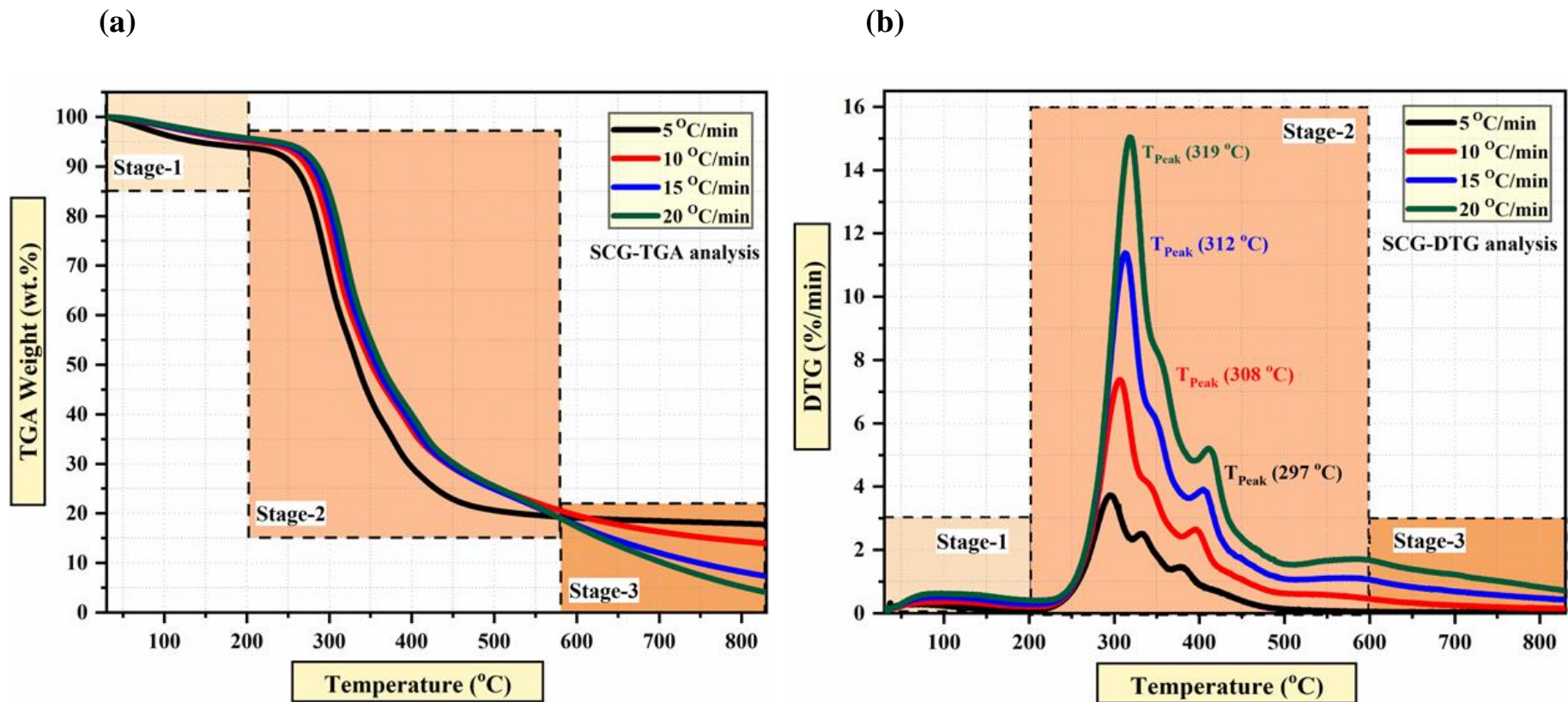


**Figure 5.3:** TGA and DTG profiles of spent coffee grounds (SCG) at different heating rates 5–20 °C/min: (a) TGA profiles of SCG (b) DTG profiles of SCG.

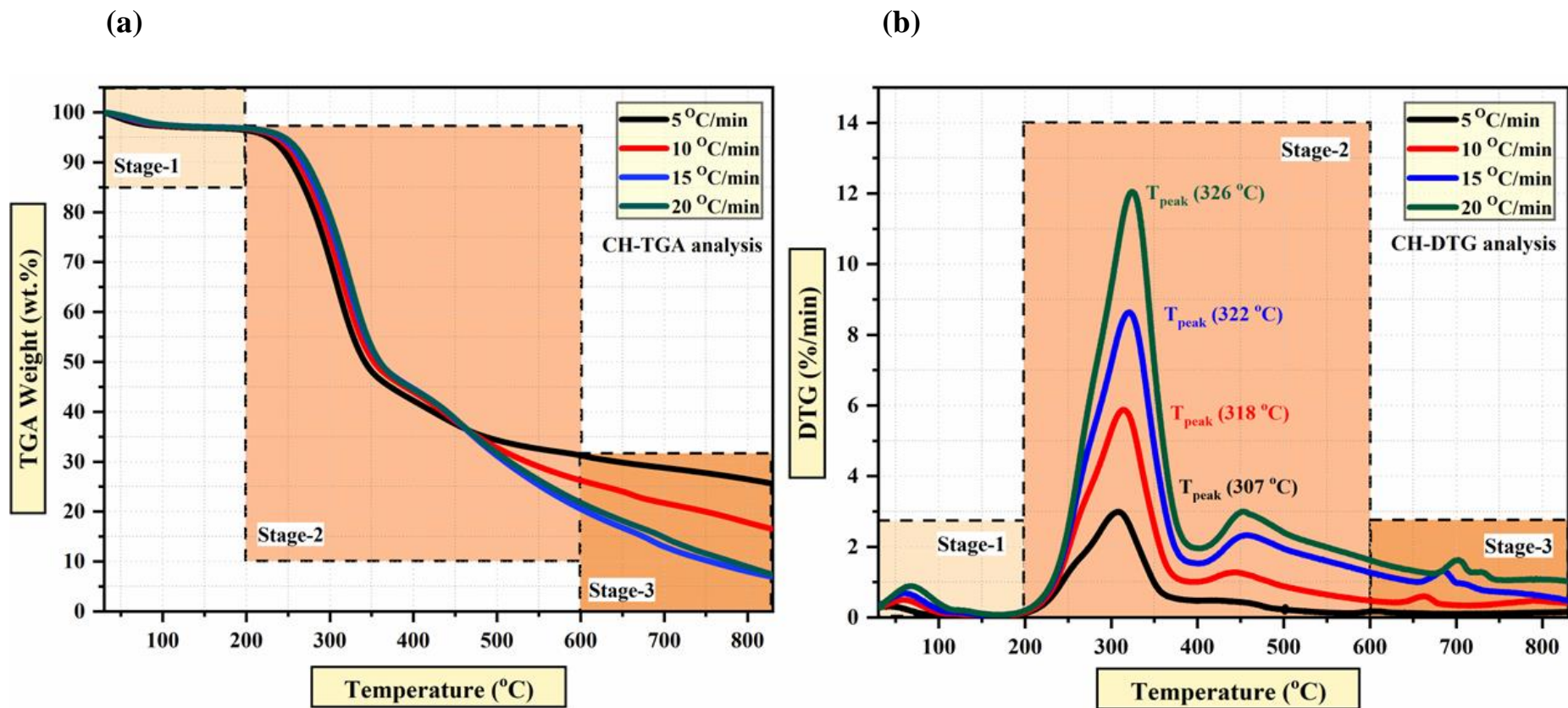


**Figure 5.4:** TGA and DTG profiles of Coffee husk (CH) at different heating rates 5–20 °C/min: (c) TGA profiles of CH (d) DTG profiles of CH.

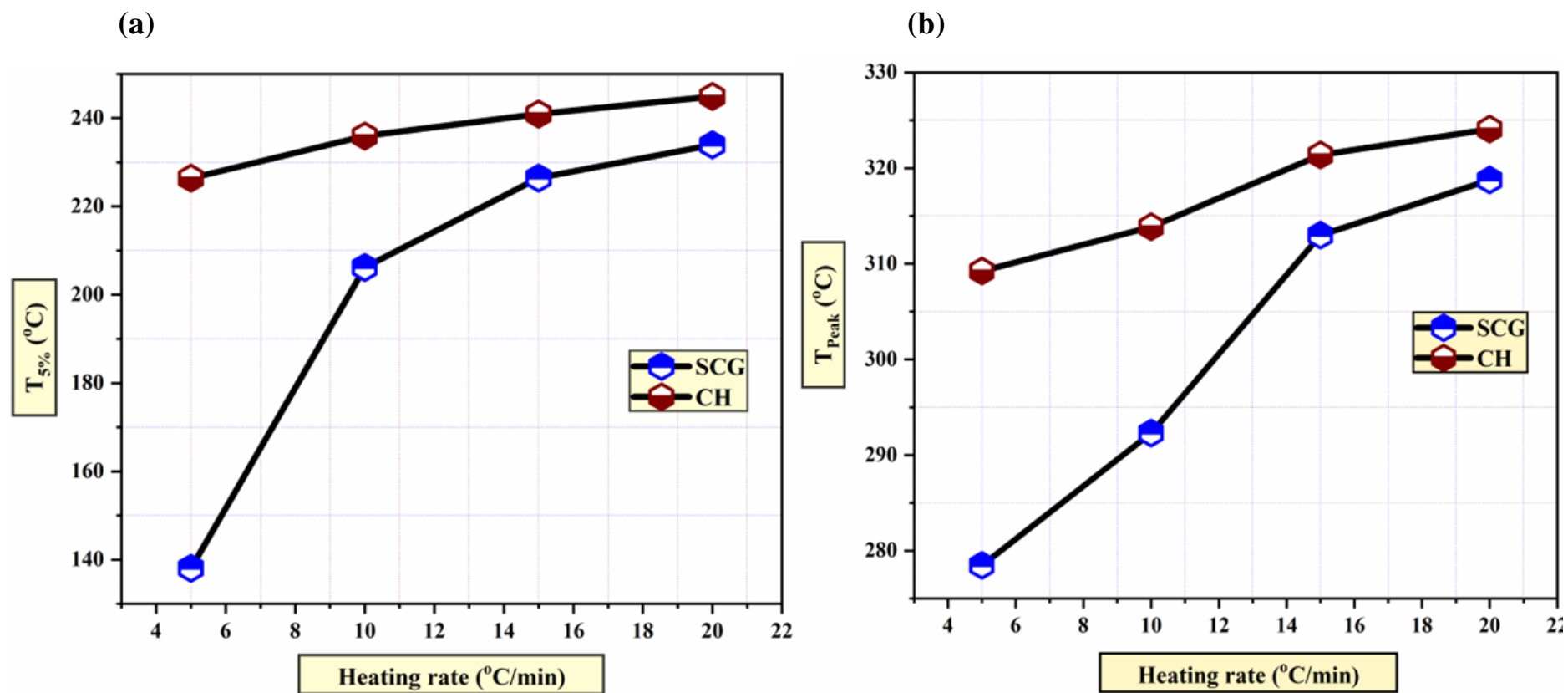


**Figure 5.5:** (a) Effects of heating rate on the kinetics for an initial conversion of 5% for SCG and CH (b) Effects of heating rate on the temperature at which the maximum weight loss is attained ( $T_{\text{peak}}$ ) for SCG and CH.

#### 5.7.4 Kinetic Analysis

Understanding of the reaction kinetics of the biomass pyrolysis is an essential parameter to design a system effective for the thermochemical conversion of biomass. In this study, the kinetics parameters, including apparent activation energies ( $E_A$ ,  $\text{kJmol}^{-1}$ ) and frequency factors ( $A_0$ ,  $\text{s}^{-1}$ ) were estimated through the model-free methods such as FWO, Friedman, KAS and Kissinger's method. Three different iso-conversional methods (FWO, Friedman and KAS) were used to evaluate the activation energies from the straight-line slopes, while the intercept obtained from the Kissinger method provided a basis for the determination of the frequency factor. The thermogravimetric curves (TGA) obtained at varying heating rates of  $5\text{--}20\text{ }^\circ\text{Cmin}^{-1}$  for SCG and CH were used together with Eqs. (5.14), (5.17), (5.18) and (5.20) to calculate the kinetic parameters against each fractional conversion starting from 0.1 to 0.7. The model-free methods were also used to study the relationship between the activation energy ( $E_A$ ), conversion ( $\alpha$ ) and frequency factor ( $A_0$ ) for both SCG and CH.

Figure 5.6 and Figure 5.7 shows the linear least square regression plots for FWO, KAS and Friedman model at progressing conversion rates. The plots of FWO and KAS models for both coffee residues show a similar trend while that of Friedman is slightly different. For both coffee residues (SCG and CH), the conversion used ranges from 0.1–0.7. It should be noted that the conversion rate lower than 0.1 and higher than 0.7 was not used in this study as a result of their non-linear characteristics and lower value of the correlation coefficient ( $R^2$ ).

Moreover, all the model used in the present study showed a very good fit with the experimental data. This is verified with the value of the correlation coefficient ( $R^2$ ), which is above 0.9 at all the conversion range studied except for the Friedman method at 0.7 conversion. The high value of the correlation coefficient also shows the accurate prediction of the activation energy in this study. Compared to the KAS and Friedman iso-conversional method, the FWO exhibited superior  $R^2$  for both SCG and CH leading to a better fit for pyrolytic reactions.



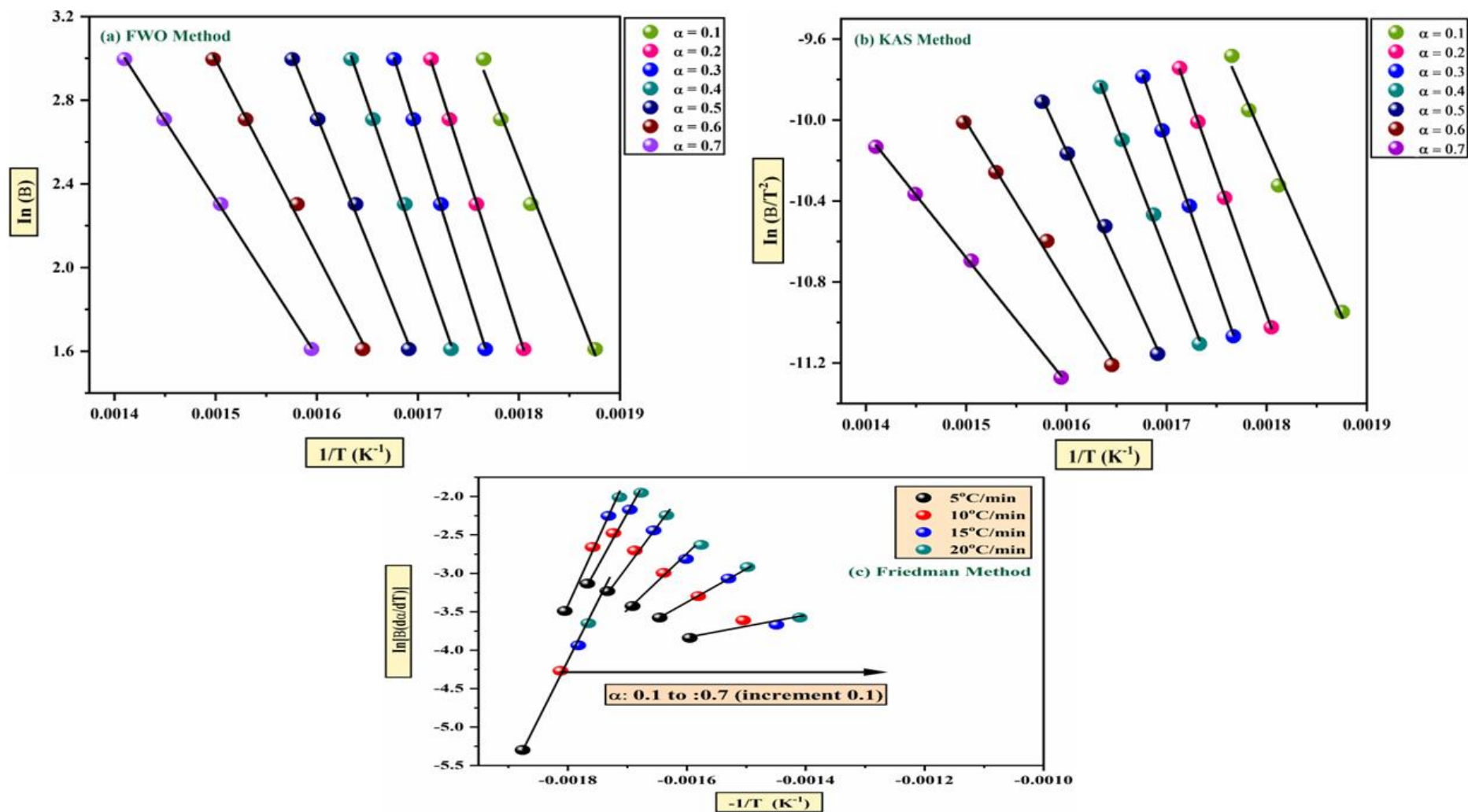


**Figure 5.6:** Linear least square regression plot for spent coffee grounds (SCG) at different conversions ( $\alpha$ ) used for the determination of activation energy by (a) FWO; (b) KAS and (c) Friedman. The lines in figure (c) reflects the values of  $\alpha$  ranging from 0.1 to 0.7 starting from left to right.

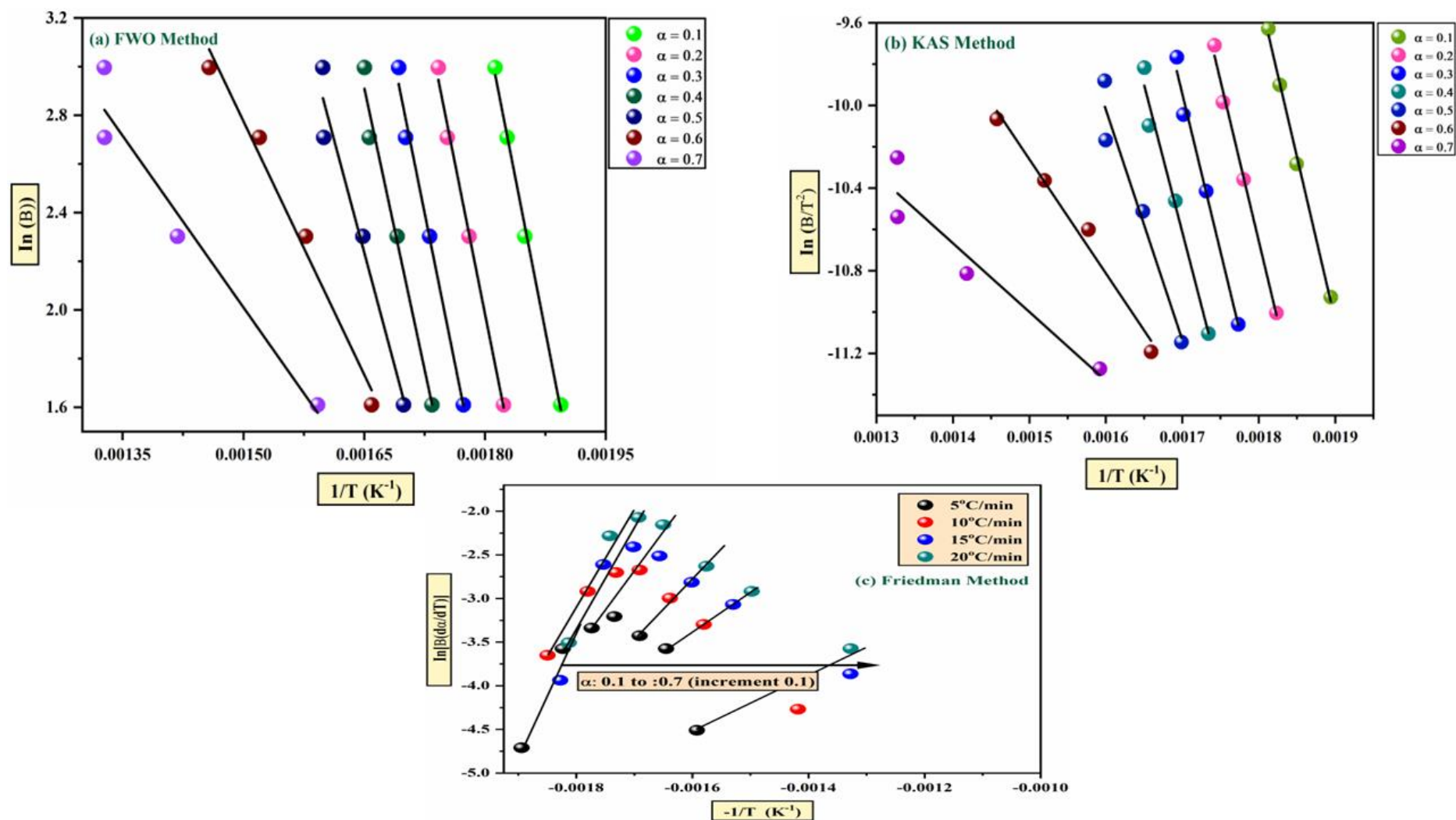


**Figure 5.7:** Linear least square regression plot for coffee husk (CH) at different conversions ( $\alpha$ ) used for the determination of activation energy by (a) FWO; (b) KAS and (c) Friedman. The lines in figure (c) reflects the values of  $\alpha$  ranging from 0.1 to 0.7 starting from left to right.

Tables 5.2 and 5.3 show the estimated kinetics parameters ( $E_A$  and  $A_0$ ) for SCG and CH, respectively, at different conversion range from 0.1–0.7. As shown in Table 5.2, the activation energy for SCG using the FWO method was in the range of 62.3 – 102.4 kJmol<sup>-1</sup>. Likewise, the KAS and Friedman method yielded activation energy between 51.3–93.3 kJ mol<sup>-1</sup> and 10.6–122.7 kJ mol<sup>-1</sup>, respectively. Moreover, as shown in Table 5.3, the activation energy for CH using FWO, KAS, and Friedman method are reported as 39.1–140.6 kJ mol<sup>-1</sup>, 27.7–131.6 kJ mol<sup>-1</sup> and 24.9–111.2 kJ mol<sup>-1</sup>, respectively. However, the activation energy evaluated using the Kissinger method was in the range of 141.7-162.1 kJmol<sup>-1</sup> for SCG and CH, respectively. An increasing trend in the activation energies for both SCG and CH was observed during the initial stages of pyrolysis. With the increasing conversion, the activation energy falls. The rise and fall of activation energy is attributable to the endothermic and exothermic nature of complex reactions under inert atmosphere. The variation in activation energies with respect to conversion of SCG and CH could also be attributed to the different pyrolysis kinetic behaviours and percentage of cellulose and hemicellulose and lignin present in each compound, together with their collective interactions (Kaur et al., 2018).

Low volatile matter and high fixed carbon content in biomass samples contributes to low reactivity thereby increasing the activation energy. Volatile matter can be defined as the quantity of condensable vapor and permanent gases that is evolved when biomass is heated (Cai et al., 2018) Increase in volatile matter indicates improved reactivity while a low volatile matter requires more activation energy. On the other hand, the amount of fixed carbon in biomass samples represents the solid combustible residues left behind after heating the samples and removing volatile matter. Therefore, biomass samples with high fixed carbon contents would also require high activation energy for the formation of products during pyrolysis. Kaur et al., (2018), have reported similar observations in the case of Castor oil. In another study by Ashraf et al., (2019) the authors reported the activation energies of two coals Dukki Coal (DC) and Chamalang Coal (CC) and four different agricultural residues Corn Husk (CH), Falsa Stick (FS), Rice Husk (RH) and Sunflower Disc (SD). The activation energies ( $E_A$ ) were in the order of CC < DC < SD < RH < FS < CH. The superior activation energy ( $E_A$ ) of CH was attributed to its low volatile matter and high fixed carbon contents compared to coal and other agricultural residues.

**Table 5.2:** The kinetic parameters obtained from the iso-conversional method using the fitted equation for spent coffee grounds (SCG).

<b>Feedstock: SCG</b>									
$\alpha$	<b>FWO method</b>			<b>KAS method</b>			<b>Friedman method</b>		
	$E_A$ (kJmol <sup>-1</sup> )	$A_o$ (s <sup>-1</sup> )	$R^2$	$E_A$ (kJmol <sup>-1</sup> )	$A_o$ (s <sup>-1</sup> )	$R^2$	$E_A$ (kJmol <sup>-1</sup> )	$A_o$ (s <sup>-1</sup> )	$R^2$
<b>0.1</b>	102.4	1.1 x 10 <sup>9</sup>	0.9924	93.3	1.5 x 10 <sup>8</sup>	0.9911	122.7	1.1 x 10 <sup>11</sup>	0.9957
<b>0.2</b>	125.2	1.8 x 10 <sup>11</sup>	0.9998	115.8	2.2 x 10 <sup>10</sup>	0.9998	134.9	1.5 x 10 <sup>12</sup>	0.9967
<b>0.3</b>	127.7	3.1 x 10 <sup>11</sup>	0.9998	118.1	3.6 x 10 <sup>10</sup>	0.9997	109.1	4.9 x 10 <sup>9</sup>	0.9942
<b>0.4</b>	116.1	2.3 x 10 <sup>10</sup>	0.9983	106.1	2.6 x 10 <sup>9</sup>	0.9979	82.4	1.3 x 10 <sup>7</sup>	0.9937
<b>0.5</b>	99.7	6.1 x 10 <sup>8</sup>	0.9976	89.5	6.3 x 10 <sup>7</sup>	0.9969	56.3	3.4 x 10 <sup>4</sup>	0.9893
<b>0.6</b>	77.4	4.1 x 10 <sup>6</sup>	0.9956	66.8	3.7 x 10 <sup>5</sup>	0.9938	36.9	3.6 x 10 <sup>2</sup>	0.9997
<b>0.7</b>	62.3	1.3 x 10 <sup>5</sup>	0.9998	51.3	1.1 x 10 <sup>4</sup>	0.9995	10.6	3.8 x 10 <sup>1</sup>	0.7596
<b>Average</b>	<b>101.6</b>	<b>7.2 x 10<sup>10</sup></b>	-	<b>91.6</b>	<b>8.7 x 10<sup>9</sup></b>	-	<b>90.4</b>	<b>2.3 x 10<sup>11</sup></b>	-
<b>Kissinger</b>	<b>141.7</b>	5.4x 10 <sup>12</sup>	0.9643						

**Table 5.3:** The kinetic parameters obtained from the iso-conversional method using the fitted equation for coffee husk (CH).

<b>Feedstock: CH</b>									
$\alpha$	<b>FWO method</b>			<b>KAS method</b>			<b>Friedman method</b>		
	$E_A$ (kJmol <sup>-1</sup> )	$A_o$ (s <sup>-1</sup> )	$R^2$	$E_A$ (kJmol <sup>-1</sup> )	$A_o$ (s <sup>-1</sup> )	$R^2$	$E_A$ (kJmol <sup>-1</sup> )	$A_o$ (s <sup>-1</sup> )	$R^2$
<b>0.1</b>	140.6	1.6 x 10 <sup>12</sup>	0.997	131.6	2.4 x 10 <sup>11</sup>	0.9966	111.2	3.1 x 10 <sup>9</sup>	0.7814
<b>0.2</b>	138.0	9.3 x 10 <sup>11</sup>	0.995	128.7	1.3 x 10 <sup>11</sup>	0.9943	125.9	7.0 x 10 <sup>10</sup>	0.9858
<b>0.3</b>	136.7	6.9 x 10 <sup>11</sup>	0.9899	127.1	9.1 x 10 <sup>10</sup>	0.9884	121.3	2.6 x 10 <sup>10</sup>	0.9713
<b>0.4</b>	128.4	1.2 x 10 <sup>11</sup>	0.9826	118.6	1.5 x 10 <sup>10</sup>	0.9797	90.4	3.1 x 10 <sup>7</sup>	0.9205
<b>0.5</b>	102.7	4.9 x 10 <sup>8</sup>	0.9626	92.6	5.7 x 10 <sup>7</sup>	0.9543	80.0	3.7 x 10 <sup>6</sup>	0.9124
<b>0.6</b>	57.7	2.8 x 10 <sup>4</sup>	0.9829	45.9	1.9 x 10 <sup>3</sup>	0.9823	77.0	1.9 x 10 <sup>6</sup>	0.97154
<b>0.7</b>	39.1	4.1 x 10 <sup>2</sup>	0.9517	27.7	2.8 x 10 <sup>1</sup>	0.9102	24.9	1.4 x 10 <sup>1</sup>	0.8087
<b>Average</b>	<b>106.2</b>	<b>4.8 x 10<sup>11</sup></b>	-	<b>96.0</b>	<b>6.7 x 10<sup>10</sup></b>	-	<b>100.9</b>	<b>1.4 x 10<sup>10</sup></b>	-
<b>Kissinger</b>	<b>162.1</b>	3.6 x 10 <sup>14</sup>	0.9488						

The apparent kinetic parameters for SCG and CH are evaluated from the average of the kinetic parameters (activation energy and frequency factor) for four different heating rates. In the present study, the apparent activation energy obtained for SCG is 101.55 kJ mol<sup>-1</sup> (FWO method), 91.56 kJmol<sup>-1</sup> (KAS method) and 90.4 kJmol<sup>-1</sup> (Friedman method). On the other hand, the apparent activation energy evaluated for CH is slightly higher at 106.2 kJmol<sup>-1</sup> (FWO method), 96.0 kJmol<sup>-1</sup> (KAS method) and 100.1 kJmol<sup>-1</sup> (Friedman method). The average activation energies for both coffee residue were found to be lower compared to the apparent activation energies of Para grass (189.54 kJmol<sup>-1</sup>) (Ahmad et al., 2017) tobacco waste (118-257 kJmol<sup>-1</sup>) (Wu et al., 2015) and rice husk (221-229 kJmol<sup>-1</sup>) (Braga et al., 2014). Activation energy defined as the minimum amount of energy that is required for a reaction to proceed or to produce an activated complex. Activation energy is also an essential criterion for the determination of a fuel reactivity (Gai et al., 2013). Since fuel reactivity plays a significant role in gasification and pyrolysis, it is crucial to understand the extent and relationship between activation energy and conversion during pyrolysis. It is almost impossible to start reactions with high activation energy as increased value demonstrates that the rate of reaction is slow. However, the lower activation energy of the biomass is desirable for co-firing with various other biomasses having either very lower or higher E<sub>A</sub>-values to enhance the energy efficiency of the process. Therefore, SCG is seen as a superior fuel compared to CH. Furthermore, since the activation energy of biomass is strongly dependent on the pyrolysis mechanism, it could be stated that both SCG and CH has a different reaction mechanism during pyrolysis.

For both SCG and CH, the apparent activation energy calculated using the Friedman method is lower than that of the FWO and KAS method. Friedman's way is a more efficient approach to estimate the activation energy because the technique does not require any assumptions or approximations. Furthermore, Friedman approach uses a relatively straightforward differential form of kinetic law. Although, the method has some limitations such as baseline error and the sensitivity of instantaneous heat to experimental noise.

The relationship between conversion and activation energy estimated from the Friedman, KAS and FWO method is illustrated in Figure 5.8. The trend in the variation of activation energy with conversion is similar for KAS and FWO methods for SCG and CH (it increased from 0.1-0.3 and started declining). On the contrary, the Friedman method showed a slight deviation because the activation energy using this method for both coffee residues started declining from 0.3 conversion. It should be noted that the activation energy versus conversion plot could be useful towards the prediction of the nature of the reaction (e.g., reversible, independent,

competing or consecutive reactions). The process is likely to contain a rate-controlling or single dominant reaction when there is a slight deviation of activation energy with conversion (Ma et al., 2015). However, if the activation energy is strongly dependent on the conversion as in the case of this study, then the reaction could be an independent, consecutive, or competing reaction (Kumar et al., 2019). Moreover, a decrease of activation energy with conversion is an indication that the reaction is endothermic, followed by an irreversible step. On the other hand, a rise in activation energy with conversion is an indication of an exothermic reaction (Kaur et al., 2018).

As shown in Figure 5.8 (a), the apparent activation energy for SCG rises at conversion value of 0.1 – 0.2, following by a decrease with increasing conversion for Friedman method. For the KAS and FWO method, the activation energy rises to a maximum value at the conversion of 0.3 before decreasing gradually until conversion of 0.7. In Figure 5.8 (b), for CH feedstock, there is no increase in activation energy for KAS and FWO methods; instead, the maximum value was at the lowest conversion of 0.1. Moreover, the Friedman method displayed a similar trend as that of SCG. The initial increase in activation energy shows the presence of endothermic reactions. The fluctuation of activation energy with conversion by the KAS, FWO and Friedman method reported in the study was similar to that of palm kernel (Ma et al., 2015) hazelnut husk (Ceylan and Topçu, 2014) and castor (Kaur et al., 2018). The average activation energy obtained from SCG, and CH is compared with the existing literature values ( $E_A$  evaluated using the FWO method), as shown in Table 5.4. The values of  $E_A$  as  $102.4 \text{ kJmol}^{-1}$  (SCG) and  $140.6 \text{ kJmol}^{-1}$  (CH) are relatively lower than that of the listed lignocellulosic biomass.

Furthermore, the presence of multiple peaks and convolutions in the plots in Figure 5.8 (a) and (b) could be attributed to the difference in the thermal characteristics of components (e.g. cellulose, hemicellulose, lignin and extractives) present in SCG and CH. Each individual component decomposes at different thermal conditions and varying conversion steps (Ma et al., 2015). The fluctuation of activation energy with conversion by the KAS, FWO and Friedman method reported in the study was similar to that of palm kernel (Ma et al., 2015), hazelnut husk (Ceylan and Topçu, 2014) and castor (Kaur et al., 2018). ). The average activation energy obtained from SCG, and CH is compared with the existing literature values ( $E_A$ ) evaluated using the isoconversional methods, as shown in Table 5.4. Referring to the Table 5.4, the  $E_A$  as derived from the isoconversional methods (FWO, KAS and Friedman

methods) were in the range of 90.4-101.6 kJmol<sup>-1</sup> for SCG and 96.0-106.2 kJmol<sup>-1</sup> for CH and were relatively lower than that of the listed lignocellulosic biomass samples.

The frequency (pre-exponential factor, A) factor determined with SCG in this study ranges from 1.1 x 10<sup>04</sup>-8.7 x 10<sup>09</sup> s<sup>-1</sup> (KAS method), 1.3 x 10<sup>03</sup>-3.1 x 10<sup>11</sup> s<sup>-1</sup> (FWO method) and 3.8 x 10<sup>01</sup>-1.5x 10<sup>12</sup> s<sup>-1</sup> (Friedman method) presented in Table 2. Similarly, CH yields a relatively higher frequency factor in the range of 2.8 x10<sup>01</sup>-2.4 x 10<sup>11</sup> s<sup>-1</sup> (KAS method), 2.8 x 10<sup>04</sup>-1.6 x 10<sup>12</sup> s<sup>-1</sup> (FWO method), and 1.4x 10<sup>01</sup>-7.0 x 10<sup>10</sup> s<sup>-1</sup> (Friedman method) presented in Table 5.3. Pre-exponential factor (A) is an essential factor that describes the solid phase reaction chemistry, and its evaluation is required to optimize the biomass pyrolysis reaction. Lower value of exponential factor less than (<10<sup>09</sup> s<sup>-1</sup>) is an indication of a solid phase surface reaction. Moreover, a relatively high value of frequency factor illustrates a complex reaction (Kaur et al., 2018). Analogous to the activation energy, the variation of the frequency factor against conversion could also be attributed to the varying biomass composition and series of complex reactions occurring during biomass pyrolysis attributable to the complex structure of the biomass.

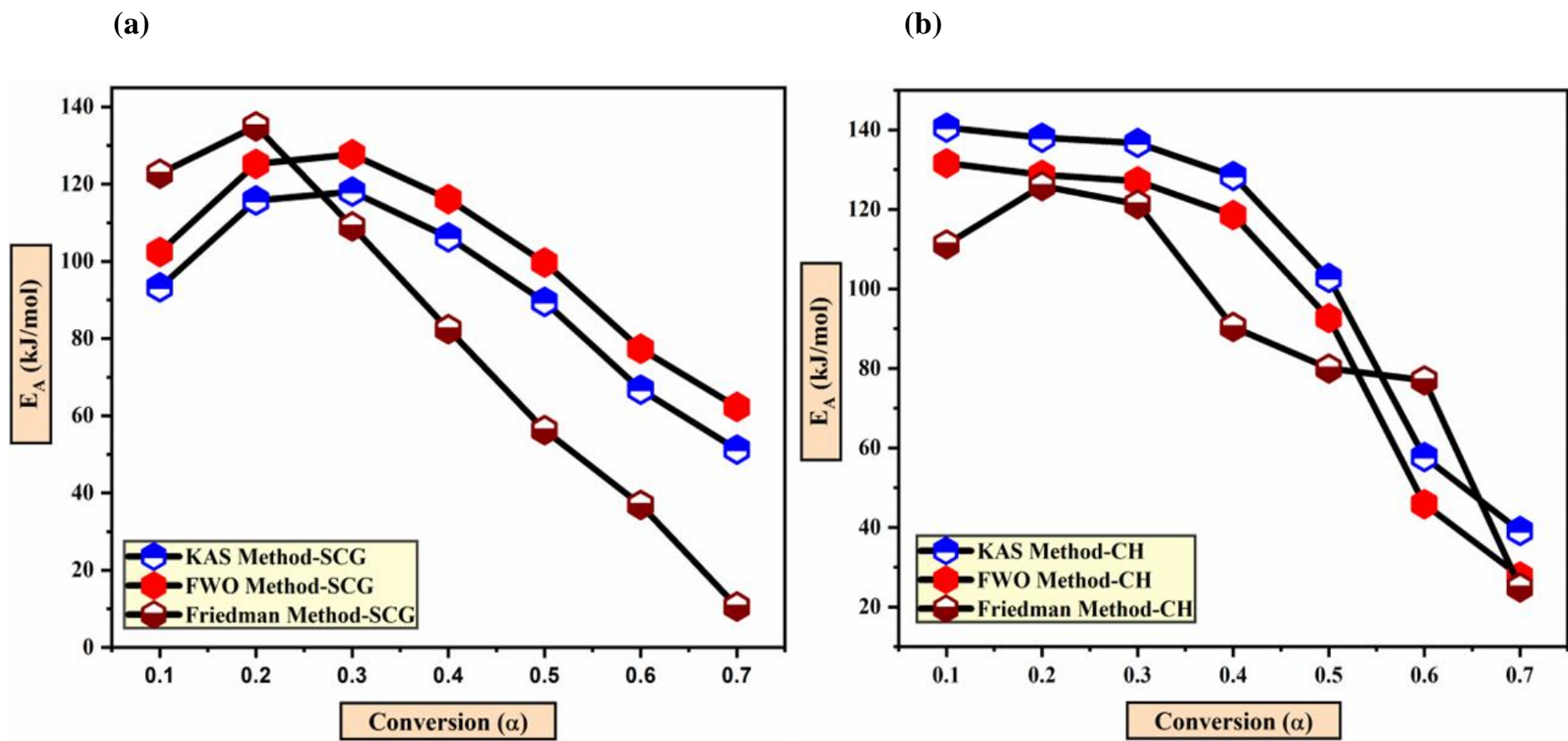


**Figure 5.8:** Change in activation energy with conversion for different the iso-conversional methods for (a) spent coffee grounds (SCG) (b) coffee husk (CH).



**Table 5.4:** Comparison activation energies (average  $E_A$ ) of coffee residue calculated using different iso-conversional methods with data reported in the literature.

Biomass samples	Activation energy (average, $E_A$ , kJ mol <sup>-1</sup> )			Reference	
	FWO method	KAS method	Friedman method		
Spent coffee grounds (SCG)	102.4	91.6	90.4	Present study	
Coffee husk (CH)	140.6	96.0	100.9	Present study	
Coffee grounds (CGR)	241	244	-N/A-	(Fermoso, 2018)	
Rice Husk (RH)	-N/A-			109.4	(Ashraf et al., 2019)
Corn husk (CH)				98.2	
Sunflower disc (SD)				113.3	
Falsa Sticks (FS)				103.6	
Ducky coal (DC)				129.8	
Banana pseudo-stem (BS, raw sample)	116.2	113.4	-N/A-	(Kumar et al., 2019)	
Banana pseudo-stem (Bs-Ru) impregnated	73.3	68.2			
Banana pseudo-stem (Bs-Fe) impregnated	86.8	82.3			
Pine sawdust	179.3	171.7	168.6	(Mishra and Mohanty, 2018)	
Sal sawdust	156.6	148.4	181.5		
Areca nut husk	179.5	171.2	184.6		
Castor ( <i>Ricinus Communis</i> )	167.1	165.9	-N/A-	(Kaur et al., 2018)	
<i>Prosopis juli-flora</i>	203	204	-N/A-	(Chandrasekaran et al., 2017)	
Hazelnut husk	131.0	127.8	-N/A-	(Ceylan and Topcu, 2014)	

### 5.7.5 Thermodynamic Parameters estimation

Besides the estimation of kinetic parameters, the determination of the thermodynamic parameters is also essential for energy calculations and process feasibility studies of pyrolysis process. The evaluation of the thermodynamic parameters of SCG and CH are also necessary for a well-designed large-scale reactor for Coffee residue-based pyrolysis process. Thermodynamic estimation provides information on the variation of enthalpy ( $\Delta H$ ,  $\text{kJmol}^{-1}$ ), entropy ( $\Delta S$ ,  $\text{Jmol}^{-1}$ ), and Gibbs energy ( $\Delta G$ ,  $\text{kJmol}^{-1}$ ) with conversion.

Enthalpy ( $\Delta H$ ) changes a measurement of the variance in energy among the reagents and the stimulated intricate substance. It is referred to as the energy needed to dissociate reactants bonds. Enthalpy also represents the total heat content of a system. For thermochemical conversion reactions such as pyrolysis, enthalpy can be defined as the overall amount of energy consumed by the biomass during its transformation to different products such as biochar, bio-oil and syn-gas. The lower difference between the enthalpies ( $\Delta H$ ) and apparent activation energies ( $E_A$ ) is desirable as it favours to overcome the potential energy barrier with ease which is essential to produce intermediate products (activated complex) followed by the final product (Ahmad et al., 2017). The changes in enthalpy ( $\Delta H$ ) with conversion for SCG and CH at each conversional fraction are presented in Tables 5.5 and 5.6. For all the three iso-conversional methods (KAS, FWO and Friedman), a slight deviation in enthalpy values with increasing conversion could be attributed to the difference in energy between the reagent and activated complex. The lesser the energy difference, the more tendency is to form the activated complex. The average enthalpy obtained using the KAS, FWO and Friedman method were reported as  $91.1 \text{ kJ mol}^{-1}$ ,  $101.3 \text{ kJmol}^{-1}$  and  $85.2 \text{ kJmol}^{-1}$  respectively for CH. On the contrary, SCG has a lower average enthalpy value of  $86.9 \text{ kJmol}^{-1}$  (KAS),  $99.1 \text{ kJmol}^{-1}$  (FWO) and  $76.6 \text{ kJmol}^{-1}$  (Friedman). The highest value of  $\Delta H$  is obtained at conversion ranges of 0.1 – 0.3 for both the feedstocks as shown in Figures 5.9 (a) and (b). This implies that increased heat is needed for the pyrolysis of SCG and CH at values of conversion ranging from 0.1–0.3. The value of enthalpy ( $\Delta H$ ) is almost  $\sim 4\text{-}5 \text{ kJmol}^{-1}$  lower for both SCG and CH when compared to the apparent activation energies at each conversion using the FWO, KAS and Friedman methods, respectively. This smaller difference reflects that the pyrolysis reaction was occurring, disintegration of biomass was easier, and the product formation was feasible in an energy-efficient ambience.

**Table 5.5:** The thermodynamic parameters as a function of temperature for spent coffee grounds (SCG).

<b>KAS Model</b>			
<b>Conversion</b>	<b><math>\Delta H</math> (kJmol<sup>-1</sup>)</b>	<b>*<math>\Delta G</math> (kJmol<sup>-1</sup>)</b>	<b>*<math>\Delta S</math> (Jmol<sup>-1</sup>)</b>
<b>0.1</b>	88.6	146.4	-102.3
<b>0.2</b>	111.1	145.4	-60.7
<b>0.3</b>	113.4	145.3	-56.4
<b>0.4</b>	101.5	145.8	-78.2
<b>0.5</b>	84.8	146.6	-109.2
<b>0.6</b>	62.1	148.0	-151.9
<b>0.7</b>	46.6	149.2	-181.6
<b>Average</b>	<b>86.9</b>	<b>146.6</b>	<b>-105.8</b>
<b>FWO model</b>			
<b>Conversion</b>	<b><math>\Delta H</math> (kJmol<sup>-1</sup>)</b>	<b>*<math>\Delta G</math> (kJmol<sup>-1</sup>)</b>	<b>*<math>\Delta S</math> (Jmol<sup>-1</sup>)</b>
<b>0.1</b>	100.0	146.0	-81.3
<b>0.2</b>	122.8	145.0	-39.3
<b>0.3</b>	125.3	144.9	-34.7
<b>0.4</b>	113.7	145.4	-56.0
<b>0.5</b>	97.3	146.1	-86.3
<b>0.6</b>	74.9	147.3	-128.0
<b>0.7</b>	59.9	148.3	-156.4
<b>Average</b>	<b>99.1</b>	<b>146.1</b>	<b>-83.1</b>
<b>Freidman model</b>			
<b>Conversion</b>	<b><math>\Delta H</math> (kJmol<sup>-1</sup>)</b>	<b>*<math>\Delta G</math> (kJmol<sup>-1</sup>)</b>	<b>*<math>\Delta S</math> (Jmol<sup>-1</sup>)</b>
<b>0.1</b>	120.3	145.1	-43.9
<b>0.2</b>	132.6	144.6	-21.4
<b>0.3</b>	106.6	145.6	-69.1
<b>0.4</b>	80.0	147.0	-118.5
<b>0.5</b>	53.9	148.8	-167.9
<b>0.6</b>	34.5	150.7	-205.6
<b>0.7</b>	8.14	156.6	-262.7
<b>Average</b>	<b>76.6</b>	<b>148.4</b>	<b>-127.0</b>
<b>*Values are calculated using <math>T_{mp}</math> at heating rate of 10 °C/min</b>			

**Table 5.6:** The thermodynamic parameters as a function of temperature for coffee husk (CH).

<b>KAS Model</b>			
<b>Conversion</b>	<b><math>\Delta H</math> (kJmol<sup>-1</sup>)</b>	<b>*<math>\Delta G</math> (kJmol<sup>-1</sup>)</b>	<b>*<math>\Delta S</math> (Jmol<sup>-1</sup>)</b>
<b>0.1</b>	126.7	150.83	-40.75
<b>0.2</b>	123.8	150.94	-45.84
<b>0.3</b>	122.2	151.00	-48.67
<b>0.4</b>	113.7	151.34	-63.62
<b>0.5</b>	87.8	152.54	-109.54
<b>0.6</b>	41.0	155.97	-194.38
<b>0.7</b>	22.8	158.44	-229.33
<b>Average</b>	<b>91.1</b>	<b>153.01</b>	<b>-104.59</b>
<b>FWO Model</b>			
<b>Conversion</b>	<b><math>\Delta H</math> (kJmol<sup>-1</sup>)</b>	<b>*<math>\Delta G</math> (kJmol<sup>-1</sup>)</b>	<b>*<math>\Delta S</math> (Jmol<sup>-1</sup>)</b>
<b>0.1</b>	135.7	150.5	-25.1
<b>0.2</b>	133.1	150.6	-29.5
<b>0.3</b>	131.8	150.6	-31.9
<b>0.4</b>	123.5	151.0	-46.4
<b>0.5</b>	97.8	152.1	-91.6
<b>0.6</b>	52.8	154.9	-172.5
<b>0.7</b>	34.2	156.8	-207.2
<b>Average</b>	<b>101.3</b>	<b>152.3</b>	<b>-86.3</b>
<b>Freidman Model</b>			
<b>Conversion</b>	<b><math>\Delta H</math> (kJmol<sup>-1</sup>)</b>	<b>*<math>\Delta G</math> (kJmol<sup>-1</sup>)</b>	<b>*<math>\Delta S</math> (Jmol<sup>-1</sup>)</b>
<b>0.1</b>	106.3	151.7	-76.7
<b>0.2</b>	121.0	151.1	-50.8
<b>0.3</b>	116.4	151.2	-58.9
<b>0.4</b>	85.6	152.7	-113.5
<b>0.5</b>	75.1	153.3	-132.1
<b>0.6</b>	72.1	153.4	-137.5
<b>0.7</b>	20.1	159.0	-234.8
<b>Average</b>	<b>85.2</b>	<b>153.2</b>	<b>-114.9</b>
<b>*Values are calculated using <math>T_{mp}</math> at heating rate of 10 °C/min</b>			

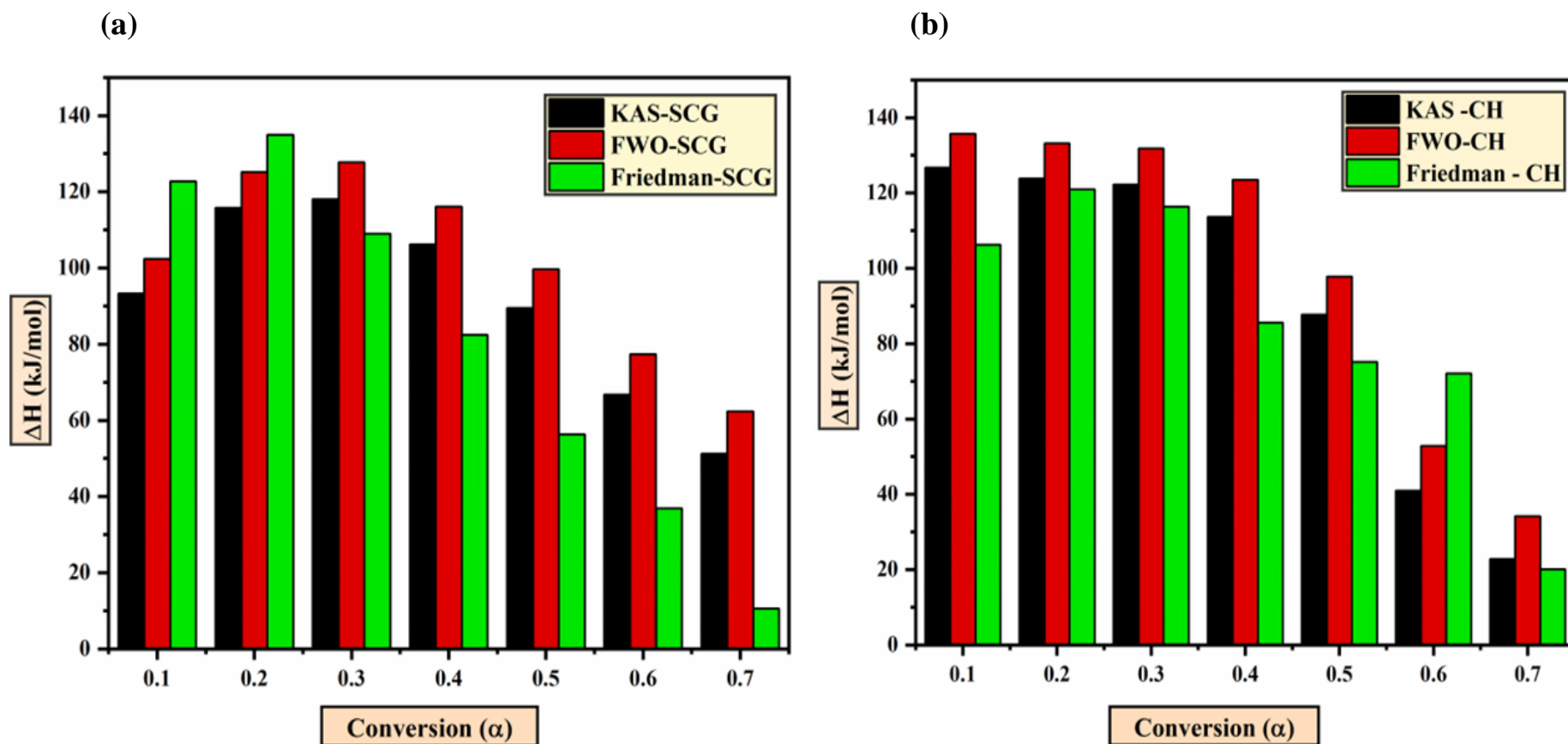


**Figure 5.9:** Change in enthalpy with conversion for different iso-conversional methods: (a) spent coffee grounds (SCG) (b) coffee husk (CH).

Gibbs free energy ( $\Delta G$ ) represents the overall rise in the system energy for the formation of activated complex (Sheng et al., 2014; Kim et al., 2010). Where, higher  $\Delta G$  values indicate that the system requires more energy to undergo the thermal transformation and lower value of  $\Delta G$  implies that at lower energy supply, the product formation will be favored. The average  $\Delta G$  values for SCG calculated by KAS, FWO and Friedman models are 146.64, 146.11 and 148.35  $\text{kJmol}^{-1}$ , respectively (Table 5.5). On the other hand, CH has an estimated average  $\Delta G$  values of 153.01  $\text{kJmol}^{-1}$  (KAS), 152.33  $\text{kJmol}^{-1}$  (FWO) and 153.18  $\text{kJmol}^{-1}$  (Friedman method). It should be noted that the difference in the average  $\Delta G$  values for SCG and CH were not very significant. The average  $\Delta G$  for both SCG and CH is lower compared to Para grass (170  $\text{kJmol}^{-1}$ ), rice straw (164.6  $\text{kJmol}^{-1}$ ) and rice bran (167.17  $\text{kJmol}^{-1}$ ) (Ahmad et al., 2017). This finding reflects the bioenergy potential of SCG. The entropy of a system measures the degree of randomness or disorderliness of the reacting system. The array of carbon layers formed in the biochar is explained through the entropy ( $\Delta S$ ) of the pyrolysis of biomass. It was observed from Tables 5.5 and 5.6 that the entropy values for both SCG and CH are negative for all the fractional conversion from 0.1-0.7. This implies that the degree of randomness of the products from bond dissociation is less than that of the starting reactants and indicates that the thermal equilibrium was achieved. Moreover, the low value of entropy could be because of the material passing through some chemical or physical changes to approach thermodynamic equilibrium. The positive values of Gibbs free energy ( $\Delta G$ ) and negative values of entropy ( $\Delta S$ ) at each conversion implies that the thermal degradation of SCG and CH is a non-spontaneous process.

## 5.8 Conclusions

The pyrolysis kinetics of spent coffee grounds (SCG) and coffee husk (CH) were comprehensively studied using TGA data. Model-free iso-conversional approach such as Kissinger, KAS, FWO and Friedman method were used to calculate the apparent activation energies and pre-exponential factors. The TGA analysis of the two samples shows that the degradation pattern of SCG and CH exists in three different stages of weight loss. The first stage is attributed to the loss of moisture and volatile components. The second stage of weight loss, also known as the active pyrolytic zone, occurs at a temperature of 240 – 460 °C for SCG and 220–450 °C for CH. This stage corresponds to the loss of cellulose and hemicellulose. The last stage at higher temperatures is attributed to the lignin decomposition. Higher content of lignin in SCG led to a slower degradation thermal decomposition observed as two significant mass-loss peaks in the DTG curve that distinguished from CH attributed to the lower content of lignin. The effect of heating rate was significant mainly at higher heating rate (20 °C/min)

where the thermal decomposition approached higher temperature irrespective of the nature of the precursors. The difference in the pyrolysis characteristics of SCG and CH can be attributed to the difference in molecular weight, varying composition and structure of the inherited hemicellulose and cellulose and lignin in the feedstock. The average activation energy calculated for SCG were 101.6 kJmol<sup>-1</sup> (FWO method), 91.56 kJmol<sup>-1</sup> (KAS method) and 90.4 kJmol<sup>-1</sup> (Friedman method). On the other, the activation energy evaluated for CH is slightly higher at 106.2 kJmol<sup>-1</sup> (FWO method), 96.0 kJmol<sup>-1</sup> (KAS method) and 101 kJmol<sup>-1</sup> (Friedman method). However, the activation energy value derived from the Kissinger's method was in the range of 141.7-162.1 kJmol<sup>-1</sup> for SCG and CH, respectively. This fluctuation in the activation energy comes from the interaction hemicellulose, cellulose and lignin. Lower values of activation energy at each fractional conversion of SCG implies that the thermal conversion can take place in an energy-efficient ambience reflecting their feasibility of valorization through pyrolysis than CH. Thermodynamic estimation shows that the degree of randomness of the products from bond dissociation is less than that of the starting reactants. From a thermodynamic parameter perspective, the findings showed a small difference between the activation energies and enthalpy at each conversion using all the model free iso-conversional models. This reflect that the pyrolysis reaction of the coffee residues is endothermic in nature. The correlation coefficient ( $R^2$ ) for each output showed a good agreement between the experimental and predicted values ( $R^2=0.99$ ). With higher volatile content, high heating value (22.3 MJ/kg), activation energy (90.4-101.6 kJmol<sup>-1</sup>), Gibbs free energy (146.11-148.35 kJmol<sup>-1</sup>), entropy (-127 Jmol<sup>-1</sup>), lower content of N (2.3 wt%) and S (0.6 wt%) of SCG compared to CH have shown that it has higher potential for adsorbent production than CH and can also be exploited as a feedstock for the production of biochar, bio-oil or other gaseous products, cost-effectively and in an energy-efficient manner.

## **Chapter 6 Carbon dioxide capture from flue gas in biochar produced from spent coffee grounds: Effect of surface chemistry and porous structure**

Most of this chapter's content has been published as a research article in the Journal of Environmental Chemical Engineering. Elsevier holds the copyright, and the permission to use the article mentioned above in this thesis has been obtained from Elsevier (see Appendix G).

### **Citation:**

**Mukherjee, A.**, Borugadda, V. B., Dynes, J. J., Niu, C., & Dalai, A.K. (2021). Carbon dioxide capture from flue gas in biochar produced from spent coffee grounds: Effects of surface chemistry and porous structure, *Journal of Environmental Chemical Engineering*, 5(9), p. 106049.

In addition, some portions of this chapter were presented at the following conferences, poster presentations and 3 Minutes Thesis Competitions (3MT) (presented in Appendix A).

### **Conference Presentations:**

**Mukherjee, A.**, Borugadda, V.B., Niu C., & Dalai, A.K., "Preparation of exhausted coffee residue derived biochar for breakthrough carbon dioxide adsorption at different temperatures: Effects of surface chemistry and porous structure on the sorption performance," oral presentation at American Chemical Society-Spring: ACS 2021, virtual conference, April 5-30<sup>th</sup>, 2021.

**Mukherjee, A.**, Niu C., & Dalai, A.K., "Preparation and optimization of biochar obtained from exhausted coffee residue for post-combustion carbon dioxide capture in a temperature swing adsorption unit: Effects of surface chemistry and textural properties," oral presentation at Molecules to Materials–MTM 2020, virtual conference, Department of Applied Chemistry, SVNIT, Surat, Gujarat, India, December 17-18<sup>th</sup>, 2020.

### **Poster Presentations:**

**Mukherjee, A.**, Borugadda, V.B., Niu C., & Dalai, A.K., "Valorization of exhausted coffee residue for post-combustion carbon dioxide capture" poster presentation at Canadian Light Synchrotron, Annual Users' Meeting (CLS-AUM 2020), Saskatoon, Saskatchewan, Canada, October 7-8<sup>th</sup>, 2020.



**Mukherjee, A.,** Niu C., & Dalai, A.K., "Spent coffee grounds for carbon dioxide capture: A holistic approach to tackle climate change" poster presentation at 1st Engineering Graduate Research Conference (1<sup>st</sup> EGR), Saskatoon, Saskatchewan, Canada, September 23<sup>rd</sup>, 2019.

### **Contribution of the Ph.D. Candidate**

Alivia Mukherjee did the following: (1) planning, performing experiments and conducting analyses of precursor and biochar samples; (2) analyzed the experimental findings and related data; (4) calibrated the bench-scale CO<sub>2</sub> adsorption set-up (5) interpretation and validated the breakthrough CO<sub>2</sub> capture performance (5) writing the manuscript. Dr. Venu B. Borugadda helped with the NEXAFS measurements performed at the Canadian Light Source (CLS, Saskatoon) and reviewed the manuscript mainly with the NEXAFS section. Dr. James J. Dynes helped validate the NEXAFS analysis's experimental findings. Dr. Ajay K. Dalai and Dr. Catherine Niu assisted in planning the work, coordinated the manuscript preparation through supervision and discussions.

### **Contribution of this chapter to the overall Ph.D. research**

The third objective of the research is addressed in this chapter (Chapter 6). Evaluating the influence of pyrolysis temperature on the physicochemical characteristics of biochar are imperative to comprehend its effect on the development of porosity, formation of surface functional groups, aromatic structure, and its candidacy towards CO<sub>2</sub> capture performance. The study intended to provide an understanding of the impact of pyrolysis temperature on the product yield and physicochemical characteristics during pyrolysis of SCG in an inert environment. Furthermore, the results helped comprehend the role of textural properties, surface chemistry and aromatic structure of the corresponding biochar samples on CO<sub>2</sub> capture performance in the CO<sub>2</sub>/N<sub>2</sub> feed stream and CO<sub>2</sub> adsorption mechanism.

## 6.1 Abstract

Coffee is a relevant agricultural product and one of the most consumed hot beverages globally. To assess the impact of pyrolysis temperatures (400–600 °C) and heating rates (5 to 20 °C/min) on the biochar yield and textural characteristics, spent coffee grounds (SCG) was subjected to slow-pyrolysis in a pilot-scale fixed-bed reactor set-up. Further, complementary spectroscopic and textural analyses were executed to evaluate the impact of pyrolysis temperatures on the corresponding biochar surface properties, including textural characteristics, reactivity, and surface functionalities. The correlation of pyrolysis temperature with change in biochar's surface properties and CO<sub>2</sub> mitigation efficiency is examined. The ultimate analysis, FTIR spectroscopy, <sup>13</sup>C-NMR spectroscopy and Raman scattering measurements confirmed an increment in the degree of aromaticity or decomposition of organic complexes in biochar. The development of basic surface functionalities after the thermal treatment was ascertained by XPS and NEXAFS analyses. Based on the surface composition and textural properties, the CO<sub>2</sub> adsorption capacity of biochar synthesized at 600 °C was assessed under varying adsorption temperatures and at ambient pressure employing a fixed-bed reactor. SCG-600 showed a large CO<sub>2</sub> uptake of 2.8 mmol/g under a typical post-combustion scenario in this investigation. CO<sub>2</sub> adsorption mechanism followed the pseudo-first-order kinetics and lower activation energy over varying investigated temperatures reveals the binding process is physical in nature. SCG-600 could be proposed as a promising biochar with a combination of higher surface area, well-developed microporous structure, and heterogeneous and basic surface functional moieties to meet the specific requirements in dynamic CO<sub>2</sub> adsorption.

## 6.2 Introduction

The enormous population growth is coupled directly with economic development, rapid urbanization, and industrialization. Conventional energy sources, such as fossil fuels, are predominantly used to quench and serve almost 81.7% of world energy needs (Afolabi et al., 2020). The consumption is predicted to increase monotonically to approximately 112.2 million barrels per day in a decade (Mohanty et al., 2013). Growing concerns about shrinking fossil fuels to fulfil the world's increasing energy consumption have led to increased fuel costs (Shalini, 2018). Additionally, the global environmental issue is triggered by harnessing excessive fossil fuels and the release of greenhouse gases (GHGs), mainly CO<sub>2</sub>, owing to anthropogenic activities that have gained massive public attention due to their potential environmental threat. There are many pieces of evidence to explain that the surplus of atmospheric CO<sub>2</sub> (< 410 ppm) has become a critical issue in recent times due to global warming and climatic consequences that cannot be over-emphasized (Mukherjee et al., 2019). The progressive rise in the worldwide energy demand and environmental concerns is predicted to thrive significantly and in close quarters with the increased global population (Fakayode et al., 2020). Therefore, with the looming predicted future exhaustion of these conventional energy sources and the worldwide interest shifted to unconventional eco-friendly energy strategies to reduce over-reliance on fossil fuels. To abate adverse environmental impacts and quest for a cleaner environment to offset GHGs emissions simultaneously triggered the scientific and researcher community with post-combustion carbon capture as one of the promising techniques in the scenario of the least-cost effort and maximum efficiency (Chiodo et al., 2016). The primary facility of building a post-combustion CO<sub>2</sub> capture technology is that it could be easily retrofitted to any existing gigantic technologies with a lower risk of implementation and compromise (Ismail et al., 2020; Yadavalli et al., 2017).

Biomass feedstock derived from the organic or living origin is the world's most promising, clean, carbon-neutral, sustainable energy resource and inexhaustible carbon source. Lignocellulose-based biomass could be a promising substitute for conventional fossil fuels attributed to their low sulphur and nitrogen contents that reduce the emission of acidic pollutants and air toxics, followed by uniform distribution, abundant availability and CO<sub>2</sub> neutrality (Biswas et al., 2017). The agro-industrial waste and forest residue are the most common biomasses. They are of interest because of their advantages such as high availability, no competition with arable lands, renewable nature, engineering reusability, and cost-effectiveness. Pyrolysis is one of the most alluring fuel processing techniques conducted under

an inert atmosphere (N<sub>2</sub>) at high temperatures (400–700 °C), exploiting complex organic compounds (long polysaccharides) (Wang et al., 2018; Cai et al., 2017). It is an emerging time-saving technology for the proper management of biomass. One of the main aspects of pyrolysis is the conversion of carbonaceous feedstock into three main pyrogenic products; biochar, bio-oil and light hydrocarbon gases that could be further valorized (directly or indirectly) into a higher energy-dense product. Biochar production from biomass feedstock is possibly a reasonable approach to climate change mitigation of greenhouse gases and waste management (Wang et al., 2018).

After petroleum products, coffee (commercially explored species: *Coffea arabica* L./*Coffea canephora*) is one of the largest commodities traded globally and the most widely consumed brewed beverages prepared from the roasted bean in the world (Yen et al., 2005). One instance of residual biomass (3rd-generation) with adverse impacts on the environment is the spent coffee grounds (denoted as SCG), which is the residue/by-product obtained after the brewing process of the coffee beans. Due to the current production and consumption pattern, substantial quantities of SCG have been generated annually (which retains around half of the total mass of coffee feedstock) in a commercial or domestic context and present a significant disposal challenge (Hernández Rodríguez et al., 2018). SCG, an agro-waste material is typically discarded in landfills or incinerated, causes severe environmental problems due to the disintegration and potential release of toxic and residual caffeine, tannin, lipids, and methane contaminants, thus contributing to adverse impact on the environment and climatic change. Owing to its high organic content and availability, the thermochemical conversion of such ecologically and economically efficient biomass is in the hierarchy of proper waste management that could reduce its environmental impact (Edathil et al., 2018). Regarding the challenges posed by SCG, it could be a renewable source of biochar production that could be further explored for post-combustion CO<sub>2</sub> capture, generation of biofuels or as catalyst support.

Pyrolysis of SCG for biochar preparation has been proved as a useful way of agricultural management and has remarkable environmental benefits owing to its unique physicochemical characteristics that could be further utilized for CO<sub>2</sub> sequestration. However, pristine biochar can generally perform better under high initial feed CO<sub>2</sub> concentration/ partial pressures limiting its usage under a typical post-combustion scenario. To improve the CO<sub>2</sub> capture performance under post-combustion conditions, it is proposed to tailor the surface functionalities by nitrogen-containing compounds or oxygen functional moieties. In this regard, Xu et al. (2019) investigated the impact of N-doped biochar synthesized from bagasse

(BG) and hickory chips (HC) on the sorption performance of CO<sub>2</sub>. In their investigation, they found that BMHC450-N (ball-milled hickory chips 450-N doped biochar sample) showed improvement in the CO<sub>2</sub> adsorption performance by 31.6–55.2% in comparison to pristine as well as ball-milled biochar. The enhancement in CO<sub>2</sub> sorption performance is attributed to the presence of N-related groups (amine and nitrile groups) on the surface of BMHC450-N, favouring the interaction between Lewis acid (CO<sub>2</sub>) and the basic surface species.

Additionally, Nguyen and Lee (2016) synthesized N-doped biochar beads from chicken manure (AMBC) by ionic gelation technique and studied the effect of HNO<sub>3</sub> and sodium  $\alpha$ -L-gulopyranuronate on CO<sub>2</sub> removal. They reported the maximum removal of 10.2 mmol/g using the as-prepared AMBC beads at 20°C and 20 vol% of CO<sub>2</sub> concentration. The presence of nitrogenated or oxygenated basic functional species in the parent material or functionalized biochar could substantially affect the CO<sub>2</sub> removal efficiency owing to the Lewis acid and basic interaction.

The literature on pyrolysis of SCG as the organic substrate to capture CO<sub>2</sub> under post-combustion scenarios is scarce. Therefore, in the present investigation, the specific aim was to propose a strategy to utilize SCG as the model organic substrate to synthesize biochar through the slow-pyrolysis technique and systematically study the impact of pyrolysis temperatures (400–600 °C) and heating rates (5–20 °C/min) to tune biochar yield and textural properties. To further elucidate the impact of pyrolysis temperature, biochar samples were further subjected to characterizations using complementary analytical techniques for envisaging the role of surface functionalities, reactivity (proximate, ultimate, TGA, FTIR, <sup>13</sup>C-NMR, XPS and NEXAFS analyses), structural properties (XRD analysis) and textural characteristics (specific surface area, pore-volume and pore-size distribution). Additionally, the CO<sub>2</sub> capture performances of biochar synthesized at 600 °C (SCG-600) were thoroughly conducted under varying adsorption temperatures (30–90°C) at a fixed initial CO<sub>2</sub> concentration (30 vol% of inlet CO<sub>2</sub> balanced by N<sub>2</sub>) under ambient pressure in a fixed-bed bench-scale reactor set-up. Also, to explore the impact of thermal treatment on the CO<sub>2</sub> mitigation efficiency, a series of CO<sub>2</sub> adsorption was performed using the as-synthesized adsorbents under similar dynamic post-combustion conditions (30 °C and 30 vol% of inlet CO<sub>2</sub> balanced by N<sub>2</sub>). Additionally, the kinetic parameters and activation energy were assessed to examine the nature of the CO<sub>2</sub> adsorption mechanism and the strength of the interaction between the promising adsorbent (SCG-600) and CO<sub>2</sub> molecules.

## 6.3 Materials and Methods

### 6.3.1 Biomass collection and pre-treatment

The details regarding biomass collection and pre-treatment of SCG are provided in detail in chapter 3 (section 3.1). The methodology adapted to execute this research objective is schematically represented in Figure 6.1.

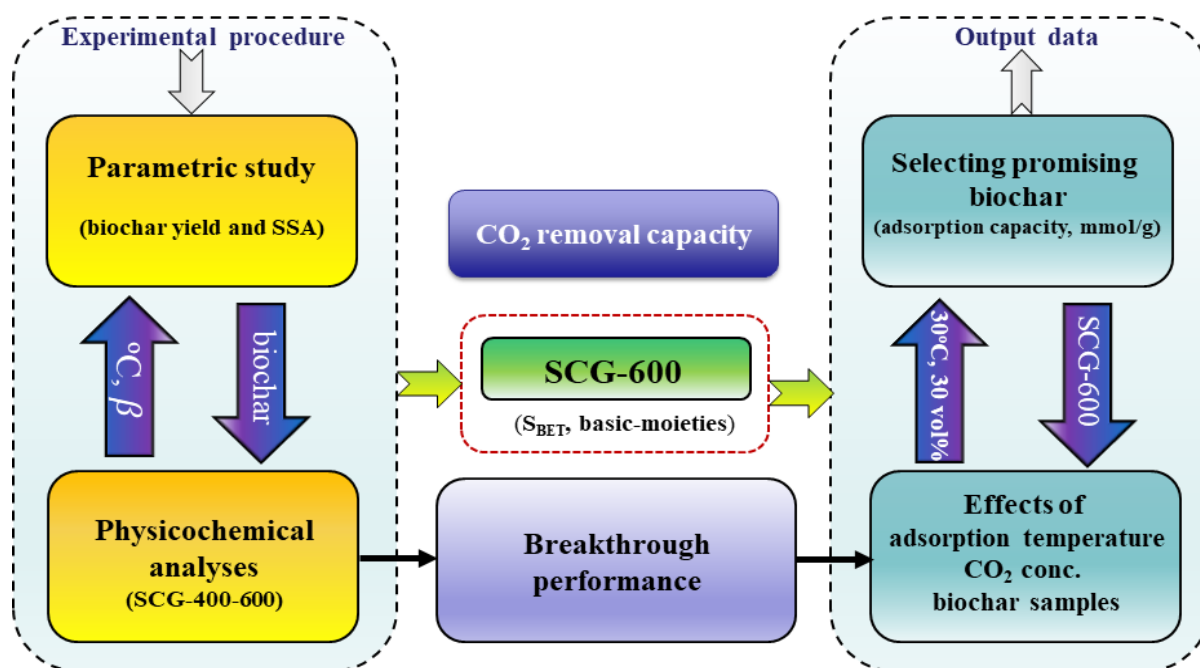


**Figure 6.1:** Schematic representation of the methodology adapted for research-objective 3.

### 6.3.2 Slow pyrolysis set-up and biochar production

The specification of the fixed bed reactor for slow pyrolysis is presented in table 3.1 and the schematics is presented in Figure 3.1. In this regard, per batch of an experiment,  $10 \pm 0.5$  g of dried SCG with medium sized particle fraction ( $d_{50} = 522 \mu\text{m}$ ) was used and was held on a supported glass-wool. The thermal treatment was conducted under a constant inert atmosphere of  $\text{N}_2$  flow protection purged at 100 mL/min, controlled, and monitored by using a mass-flow controller (MFC). Once stabilized at the predetermined temperature (400–600 °C) maintaining the final temperature for 1 h, then the reactor was cooled down in presence of  $\text{N}_2$  and the exhausted gases were cooled by circulating cold water. The resultant biochar samples were cooled naturally to ambient temperature ( $25 \pm 5$  °C) inside the furnace and were stored in a glass container to avoid any contamination or absorption of moisture for further analyses and  $\text{CO}_2$  adsorption experiments. The corresponding pyrolysis biochar samples were labelled

according to the peak pyrolysis temperature: SCG-400, SCG-500, and SCG-600. The biochar yield is calculated using the following Eq. 6.1 (Cheng et al., 2020):

$$\text{Biochar Yield (\%)} = (M_{\text{biochar}}/M_{\text{SCG}}) * 100 \% \dots\dots\dots(6.1)$$

where,  $M_{\text{biochar}}$  and  $M_{\text{SCG}}$  are the mass of corresponding biochar and dried SCG, respectively.

### 6.3.3 Characterization of the precursor and biochar samples

Diverse complimentary analytical techniques were used to analyse the physicochemical properties of the precursor and the corresponding biochar samples as presented in detail in section 3.6 of the previous chapter (chapter 3).

#### ❖ C1s Near-edge X-ray Absorption Fine Structure Spectroscopy (NEXAFS)

NEXAFS analysis was done to better comprehend the chemical composition and characteristics of biomass and the biochar samples (SGM, CLS, Saskatchewan, Canada) (Shahkarami et al., 2015). For sample analysis, average values were calculated from triplicate measurement with a standard deviation of less than  $\pm 5\%$ .

#### • Samples preparation on gold-coated Si wafers for NEXAFS analysis

C K near-edge X-ray absorption fine structure for SCG and pyrolyzed SCG at 400, 500, and 600 °C were obtained on an 11ID-1 beamline at the Canadian Light Source (CLS) located at the University of Saskatchewan. SCG and pyrolyzed SCG at 400, 500, and 600 °C were mixed with deionized water (1-2 mg/mL) in 1.5 mL Eppendorf vials to acquire a slurry. Further, the vortex mixer was used to uniformly disperse the fine solid particles and wet the slurry. After ensuring the complete mixing, using a pipette an aliquot of 4 - 6  $\mu\text{L}$  was deposited on gold (Au) coated silica (Si) wafers that were fixed to the sample plate using double-sided carbon tape and vacuum dried at room temperature to remove the water.

#### • Sample measurement for NEXAFS analysis

C (1s) NEXAFS spectra were acquired for SCG and pyrolyzed SCG via slew scanning mode on spherical grating monochromator (SGM) beamline at CLS that was designed for high-resolution soft X-ray spectroscopy. The prepared sample plate was loaded into a high vacuum chamber ( $1e^{-7}$  torr); while recording the spectra the ring current was filled to 250 mA for every 8 h. The beamline was configured for a resolving power of ca. 7500 at the C K-edge and the photon energy was scanned from 270 to 300 eV with 0.1 eV resolution and a dwell time of 0.5 s. Ten different spots were measured (60s per spot) on each sample to ensure that the resulting

spectra were identical. Total electron yield (TEY) was collected by monitoring the drain current for all the samples at beam spot size  $100 \mu\text{m}^2$ . Background measurements were collected at the photon energy range of 270 to 300 eV for gold (Au) mesh for normalization. The processed data were averaged for ten scans and divided with Au data to plot against photon energy. C (1s) fine structures were characterized according to the peak assignments in Table 6.1. Cody et.al. (1998) reported that C (1s) NEXAFS region beyond 290 eV transitions incline to be broad and overlay with each other; therefore, the main transitions ( $1s-\pi^*$ ) and transitions after 290 eV ( $1s-\sigma^*$ ) were also used to interpret the outcomes of the fine structures.

**Table 6.1:** C 1s NEXAFS assignment of peak energies, bond types, and transitions of SCG and SCG derived biochar samples.

Nature of the C	Bond Type	Transition	Peak energy (eV)	Fit position (eV)
Aromatic Quinone	C=C	$1 s-\pi^*$	283 – 284.5	284.3
Aromatic C with substituent	C=C-OH C=O R-(C=O)-R'	$1 s-\pi^*$	286 – 287.4	286.6
Carboxylic	R-COOH COO C=O	$1 s-3p/ \sigma^*$	288 – 288.7	288.4

### 6.3.4 Breakthrough CO<sub>2</sub> adsorption measurements

To assess the CO<sub>2</sub> capture performance, a series of adsorption experiments were conducted in a fixed Inconel tubular reactor (one inch) under isothermal conditions. The schematic representation of the breakthrough CO<sub>2</sub> adsorption set-up is shown in Figure 3.3. The details regarding the experimental set-up and breakthrough adsorption experiments are provided in section 3.7 of chapter 3. To assess the CO<sub>2</sub> capture performance, a series of adsorption experiments were conducted in a fixed Inconel tubular reactor under isothermal conditions. For conducting each run of experiments, the reactor was loaded with  $2 \pm 0.2$  g of adsorbents. Before conducting each adsorption experiment the loaded reactor was further preheated to  $160 \pm 10$  °C for 2 h under N<sub>2</sub> protection at 50 mL/min to remove the presence of excess moisture or pre-sorbed gases on the biochar. Following the dehydration process, the loaded-reactor was cooled down to the investigated adsorption temperatures (30–90 °C) and the binary mixture of pure CO<sub>2</sub> and N<sub>2</sub> was purged through the bed of adsorbents. All the experiments were repeated



thrice, and the average values of the breakthrough adsorption capacities were presented in this study.

#### 6.4 Kinetic study and activation energy evaluation

To investigate the CO<sub>2</sub> adsorption mechanism, the experimental data was subsequently modelled using well-established kinetic models (pseudo-first-order, pseudo-second-order and intra-particle diffusion models) (Singh et al., 2019; Edathil et al., 2018). The linear form of the kinetic models (pseudo-first order, pseudo-second order and intra-particle diffusion models) are presented in Eqs. 6.2-6.4.

$$\ln(q_e - q_t) = \ln q_e - K_1 t \quad (6.2)$$

$$\frac{t}{q_t} = \frac{1}{K_2 q_e^2} + \frac{t}{q_e} \quad (6.3)$$

$$q_t = K_{id} t^{\frac{1}{2}} + C \quad (6.4)$$

The activation energy of the CO<sub>2</sub> adsorption process was determined using the following Eq. 6.5.

$$\ln K_{id} = \ln k_0 - \frac{E_a}{RT} \quad (6.5)$$

### 6.5 Results and discussions

#### 6.5.1 Effect of pyrolysis operating parameters on biochar yield

The characterization of the resulting biochar depends on several pyrolysis operating parameters, but pyrolysis temperature and heating rate are expected to be the significant parameters influencing the biochar yield from lignocellulosic biomass. To ensure that the least stable biomass components (hemicellulose and cellulose) are decomposed, 400 °C was selected as the lowest temperature, while 600 °C was the upper limit of pyrolysis temperature. Also, the energy consumption will be high for pyrolysis experiments conducted above 600 °C. It was observed for SCG that with increasing the severity of pyrolysis temperature at a constant heating rate (5 °C/min) and at a constant reaction time of 60 min, the biochar yield declines. It is worth highlighting that the maximum conversion yield in the biochar is obtained at the temperature of 400 °C (31.3 ± 0.7 wt. %) with a lower at 600 °C (25.4 ± 1.1 wt. %), respectively. The declining biochar yield at the higher pyrolysis temperature could be attributed to the further cracking of pyrolysis tar (Wang et al., 2018). A similar finding of the declining yield of biochar substrate with the rise in pyrolysis temperatures was observed for waste coffee

grounds (38.6–26.6 wt. %) as reported by Tsai and Liu, (2013). Correspondingly, the biochar yield declined from  $25.4 \pm 1.1$  wt. % to  $21.8 \pm 1.5$  wt. % with increasing the heating rate from 5 to 20 °C/min. During the thermal cracking of biomass at higher heating rate, rapid quenching of volatile vapours causes a decrease in biochar yield as evident from the Table 6.2 (Patra et al., 2021). In this regard, the relationship between the pyrolysis operating parameters (pyrolysis temperature and heating rate) and biochar yield is negatively associated owing to the occurrence of series of decomposition and volatilization reactions during the pyrolysis process as can be seen from the Table 6.2.

**Table 6.2:** Effects of Process conditions on biochar yield from spent coffee grounds.

<b>Biochar yield at a constant reaction time (60 min) and heating rate (5 °C/min)</b>		
<b>Sample</b>	<b>Temperature (°C)</b>	<b>Biochar yield (wt. %)</b>
<b>SCG-400</b>	400	$31.3 \pm 0.7$
<b>SCG-500</b>	500	$27.1 \pm 1.2$
<b>SCG-600</b>	600	$25.4 \pm 1.1$
<b>Biochar yield at a constant pyrolysis temperature (600 °C) and reaction time (60 min)</b>		
<b>Sample</b>	<b>Heating rate (°C/min)</b>	<b>Biochar yield (wt %)</b>
<b>SCG-600-10</b>	10	$24.3 \pm 1.3$
<b>SCG-600-15</b>	15	$23.7 \pm 0.8$
<b>SCG-600-20</b>	20	$21.8 \pm 1.5$

### 6.5.2 Effects of pyrolysis operating parameters on specific surface area

With increasing the pyrolysis temperature at a constant heating rate (5 °C/min), the surface area ( $S_{BET}$ ) of the corresponding biochar improved sharply from  $179 \text{ m}^2/\text{g}$  (400 °C, SCG-400) to  $539 \text{ m}^2/\text{g}$  (600 °C, SCG-600). This enhancement in the specific surface area could be attributed to the escape of more volatile matters and water due to the possible devolatilization and dehydration reactions, making space within the network of pores and carbon matrix (D. Xu et al., 2019). Contrary, on increasing the heating rate at a fixed temperature (600 °C), the surface area reduced from  $539 \text{ m}^2/\text{g}$  (5 °C/min) to  $416 \text{ m}^2/\text{g}$  (20 °C/min), as schematically shown in Figure 6.2. At lower heating rates, the diffusion of pyrolysis products/volatile compounds occurs with ease as it gets enough time to diffuse through the network of pores. Though, with considerably increasing the heating rate, the time for the volatile compounds to escape from the polymeric backbone is significantly reduced along with mass transfer limitations. Consequently, the pace of the diffusion is impacted at higher heating rates, as a result, volatile compounds, and condensable hydrocarbons (tar) accumulated between and within the network of pores. This could increase the chance of carbon deposition, blockage of the pore entrances,

and could also cause fusion of pores which negatively affects the specific surface area in pyrolysis biochar.

Owing to this finding, the pyrolysis heating rate was fixed at 5 °C/min and reaction time at 60 min but the effects of pyrolysis temperature (400–600 °C) were further assessed owing to its significant influence on the physicochemical transformation and their candidacy towards dynamic CO<sub>2</sub> capture performance under the post-combustion scenario.

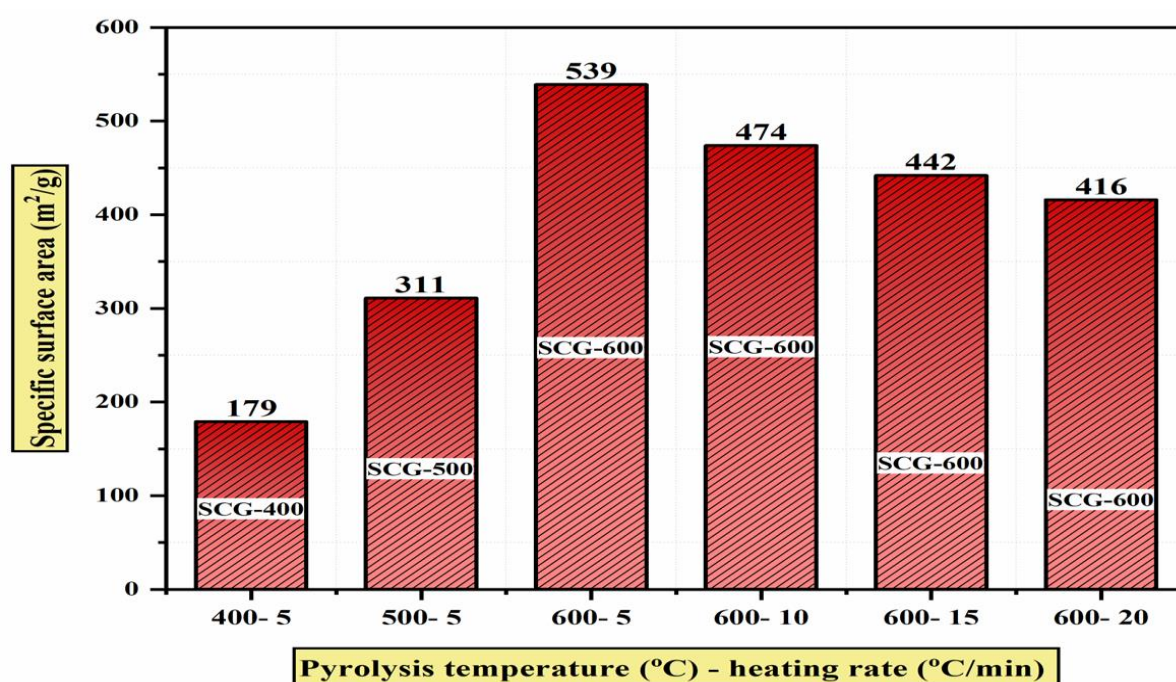


**Figure 6.2:** Effects of pyrolysis temperatures and heating rate on specific surface area of biochar samples.

### 6.5.3 Proximate analysis of biomass and biochar samples

The physicochemical properties of SCG and the corresponding biochar samples are summarized and presented in Table 6.3. The findings of the proximate analysis demonstrate that the moisture, ash, volatile matter, and fixed carbon content in SCG were 3.3, 0.9, 81.2 and 14.6 wt. % (dry basis), respectively and the findings are also according to the ones obtained for typical lignocellulose biomasses. As evident, the ash content in SCG is quite low and volatile matter content is high, which makes SCG a suitable candidate for thermochemical valorization like slow pyrolysis. Biomass with lower alkali content like SCG is preferable as it could reduce

the issues like fouling and slagging inside the furnace and also the high volatile content makes the starting precursor a highly reactive fuel (Shariff et al., 2016).

Although the biochar's ash content increased at more severe conditions as can be seen in Table 6.3, which ranged from 3.5 to 9.2 wt. % for SCG-400 to SCG-600 and is attributed to the relative enrichment of inorganic components and more mineral matter forming ashes in the pyrolysis biochar. The corresponding biochar showed a declining trend in the volatile matter and moisture content from 81.2 to 24.6 wt. % and 3.3–1.9 wt. %, respectively owing to the occurrence of series of devolatilization, dehydration reactions and cracking at higher pyrolysis temperature. However, the fixed carbon content increased, and the highest amount was reported for SCG-600 at 64.3 wt. %. The chemical composition of SCG and SCG derived biochar samples were studied by measuring the content of C, H, N, S, and O (percentages by weight), and the observed data are reported in Table 6.3.

**Table 6.3:** Proximate analysis of biomass and biochar samples derived at different pyrolysis temperatures.

Sample	Moisture <sup>db</sup> (wt. %)	volatile matter <sup>db</sup> (wt. %)	Ash <sup>db</sup> (wt. %)	Fixed carbon* (wt. %)
SCG	3.3±0.1	81.2±0.1	0.9±0.1	14.6±0.01
SCG-400	2.5±0.2	42.7±0.6	3.5±0.4	51.3±0.3
SCG-500	2.3±0.2	31.4±0.4	7.3±0.2	59±0.3
SCG-600	1.9±0.3	24.6±0.6	9.2±0.5	64.3±0.3

db: dry basis; \*Fixed carbon: 100- (Moisture + Ash + Volatile matter) wt. %

#### 6.5.4 Ultimate analysis and atomic ratios of biomass and biochar samples

Table 6.4 shows the elemental composition in the biomass and the corresponding biochar samples. Overall, the elemental composition of the tested biochar varied significantly, and it shows that with increasing temperature, the biochar gets richer in C, but H and O content decreased owing to the release of respective functional groups and volatile compounds from SCG during the series of decomposition and volatilization reactions. Indeed, the C content increased from about 50-81.5 wt. % at 600 °C from the starting precursor. In this study, SCG-600 was the most carbonized biochar with a significant fraction of C retained in it (81.5 wt. %). The high C content of SCG-600 suggests the complete conversion of the biomass constituents, i.e. hemicellulose, cellulose, and lignin into volatiles and aromatic carbon during volatilization, at 1 h of holding time (Kong et al., 2019). Referring to table 6.4, the relatively larger O and H contents evident in SCG are attributed to the lower degree of aromaticity. However, a fall in H

(6.7–2.9 wt. %) and O (39.0-2.4 wt. %) content is evident for the biochar samples with the increasing temperature, owing to the breaking of oxygenated functional moieties from the organic matrix and formation of more stable carbonaceous and aromatic structure. Although there was no obvious pattern of N content in biochar samples, it increased (2.5–4.01 wt %) with increasing the severity of pyrolysis temperature.

**Table 6.4:** Ultimate (CHNS) analysis (on a dried basis) and atomic ratios of biomass and biochar samples.

Sample	SCG	SCG-400	SCG-500	SCG-600
<b>Elemental composition (wt. %)</b>				
<b>C</b>	50±0.01	78±0.02	79.7±0.01	81.5±0.01
<b>H</b>	6.7±0.1	4.1±0.03	3.4±0.05	2.9±0.05
<b>N</b>	2.5±0.03	4.4±0.02	4.2±0.03	4.01±0.01
<b>S</b>	0.9±0.01	0.05±0.02	0.04±0.02	0.04±0.01
<b>O*</b>	39.0±0.1	10±0.2	5.4±0.2	2.4±0.1
<b>Atomic ratios</b>				
<b>H/C**</b>	1.6	0.63	0.51	0.43
<b>O/C***</b>	0.60	0.10	0.06	0.02

\*Difference O (wt %): 100 - (C + H + N + S + Ash) wt. %

\*\* Calculated using average values of H and C, \*\*\* Calculated using average values of O and C

$H/C = (H/1.008)/(C/12.011)$ ;  $O/C = (O/15.999)/(C/12.011)$

The calculated atomic ratios and the empirical formula of SCG and the tested biochar are also summarized in Table 6.4. The atomic ratios provide indications of the degree of biomass carbonization and improvement of surface chemistry in biochar. The results indicated that the atomic ratios H/C (1.6–0.43) and O/C (0.60-0.02) tend to decline with the increasing pyrolysis temperature. This behaviour could be attributed to the series of dehydration and decarboxylation reactions during pyrolysis and also an indication of improved carbonization as well as the formation of stable aromatic compounds and graphitic structure (Namkung et al., 2017). The lowest atomic ratios suggest that SCG-600 is highly carbonized. Also, reduced polarity would favour the CO<sub>2</sub> adsorption performance under a typical post-combustion scenario.

### 6.5.5 pH analysis of biomass and biochar samples

To ascertain the basicity of the corresponding biochar samples, pH was measured further in aqueous solution (de-ionized water). Table 6.5 summarizes the pH values measured in an aqueous solution for SCG and the corresponding pyrolysis biochar. As it could be observed

from Table 6.5, that the measured pH of the corresponding biochar samples increased from 5.5 to 8.2 for starting precursor to SCG-600. Indeed, these values rose from acidic pH (5.5) to an alkaline one (8.2), which are generally typical with increasing the severity of pyrolysis temperature. The increase in pH further established the augmentation of basic functional species and could be attributed to the accumulated ash content (alkali and alkaline earth metals) in the tested biochar, removal of acidic oxygenated-functional moieties from the biochar surface and formation of nitrogenated functional species (pyrrolic and /or pyridonic-N and quaternary/graphitic-N) on biochar surface. This trend in enhancement of pH also depicts the formation of  $K_2CO_3$  during pyrolysis of SCG resulting in the intercalation of  $K^+$  into the carbon-matrix of the samples. This would lead to widening of the space between the carbon layers and enhance the specific surface area of the biochar samples as evident from the data of specific surface area analysis ( $S_{BET}$ , Section 6.6.7). Azargohar et al., (2013) reported a similar finding on the rise in pH of wheat straw-derived biochar to bases following pyrolysis process at higher pyrolysis temperature.

**Table 6.5:** pH analysis of biomass and biochar samples.

Sample	pH* (water)	Ash (%, w/w)
SCG	5.5	0.9
SCG 400	6.8	3.5
SCG 500	7.6	7.3
SCG 600	8.2	9.2

\*Error margins for the pH measurements were  $\pm 0.05$

### 6.5.6 Thermal stability analysis of biomass and biochar samples

Thermogravimetric (TGA) and differential thermogravimetric (DTG) analysis of SCG and biochar show the decomposition profile and the transformations that have occurred (in dried basis) when exposed to heating until 800 °C at the heating rate of 10 °C/min under purified  $N_2$  protection of 100 mL/min and a comparison of the decomposition is schematically shown in Figure 6.32 (a & b). The TGA curves as shown in Figure 6.3 (a), present three defined degradation steps, which are typical for the lignocellulose-based biomass and bio-char pyrolysis process. The first stage starts at approximately 30 °C to around 200 °C and corresponds to soft weight losses as a result of the adsorbed water evaporation (dehydration stage) and low volatile compounds from micropores and meso-pores of around 8 (SCG) to 2.1% (SCG 600) (Gascó et al., 2018) . The most significant transformation occurs during the second stage called the devolatilization phase, starting at 200 and terminated at about 600 °C

corroborating to substantial weight losses, corresponding to the two-step thermochemical conversion process of biopolymer fractions (hemicellulose, cellulose, and lignin) as also evident from the DTG profile (Figure 6.2 (b)) (Lee et al., 2013).

As shown in the Figure 6.3 (b), the first peak corresponds to the combustion of hemicellulose (320 °C) followed by cellulose decomposition (360 °C), corresponding to the maximum mass loss rate of 7.2 wt. % min<sup>-1</sup> for SCG (Ibn Ferjani et al., 2019). In contrast, the second peak could be related to combustion of aromatic structure with higher molecular weight, triglycerides and their derivatives at a higher temperature of 400 °C (Batista et al., 2020). Alternatively, lignin, undergoes degradation for a wider range of temperature from 200 to 800 °C, with a sharp peak at 400 °C, as evident from the DTG curve (Figure 6.2 (b)).

Above 600 °C, the weight loss becomes very slow and a flat region is reached, termed as carbonization/stabilization phase (Figure 6.2 (a)), leaving pyrolysis biochar with condensed aromatic carbons and reduced functional moieties (Shalini, 2018). The TGA curve also shows that with increasing pyrolysis temperature the biochar samples attain more thermal stability or more resistance to decompose. In this regard, SCG-600 exhibited the greatest thermal stability with an overall mass loss in the range of around 28 wt.%. The release of main constituents of biomass viz., hemicellulose, cellulose, and lignin from carbohydrate-rich precursor-like SCG with the increasing severity of temperature predominantly leads to the formation of a microporous structure with increased surface area as evident from the Table 6.6. The improved textural properties are desirable for enhanced CO<sub>2</sub> adsorption performance under the post-combustion scenario.

#### **6.5.7 BET surface area of biomass and biochar samples**

The specific surface area ( $S_{\text{BET}}$ , m<sup>2</sup>/g) and porosity of the corresponding biochar are one of the crucial parameters that govern the potential of CO<sub>2</sub> adsorption capacity under a typical post-combustion scenario. An overview of the textural properties of SCG and the tested biochar is provided by the results summarized in Table 6.6. Indeed, pyrolysis temperature has a significant impact on the specific surface area and pore volume of the corresponding biochar that increased drastically from 2.5 m<sup>2</sup>/g (SCG) to 539 m<sup>2</sup>/g (SCG-600) and 0.005 cm<sup>3</sup>/g (SCG) to 0.32 cm<sup>3</sup>/g (SCG-600), respectively owing to the inherent porous structure and development of microporosity.

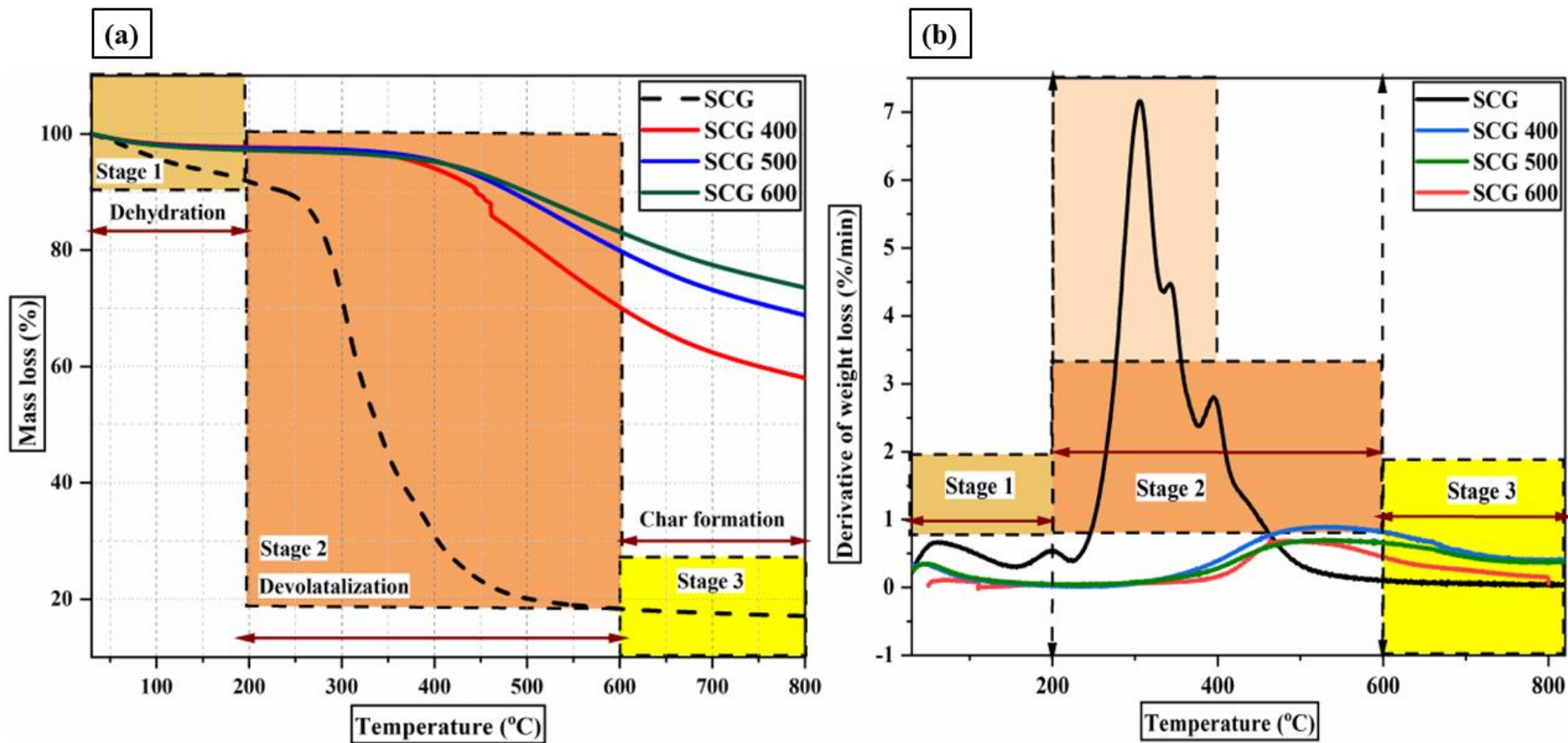


Figure 6.3: (a) TGA and (b) DTG analysis of SCG and SCG derived biochar samples.



This noticeable enhancement in the specific surface area could be attributed to the generation of micropores and characteristics of microporous structure. This improvement in biochar textural properties at higher pyrolysis temperature is likely related to significant devolatilization, removal of oxygenated functional moieties and condensed hydrocarbon (tar). Consequently, the decomposition of amorphous organic content contributed to the formation of porous biochar with a network of empty spaces into the carbon matrix suitable for CO<sub>2</sub> sorption. Ferjani et al, (2019) reported that increasing pyrolysis temperature (300–600 °C) has a positive correlation with the specific surface area of the produced biochar from grape marc. They reported that the surface area of the tested biochar increased to 253 m<sup>2</sup>/g at the highest temperature. It is worth highlighting that high surface area, along with microporous structure (availability of micropores) makes SCG-600 a superior candidate for effective dynamic CO<sub>2</sub> adsorption performance under the post-combustion scenario.

**Table 6.6:** Textural properties of biomass and biochar samples produced at different pyrolysis temperatures.

Sample	Specific surface area (m <sup>2</sup> /g)	Micro-pore surface area (m <sup>2</sup> /g)	Total pore volume (cm <sup>3</sup> /g)	Average pore width (nm)
SCG	2.5	--	0.005	10.0
SCG-400	179	125	0.13	7.7
SCG-500	311	234	0.24	5.4
SCG-600	539	421	0.32	3.2

### 6.5.8 XRD analysis of biomass and biochar samples

The wide-angle stacked powder XRD pattern of SCG and the biochar samples was studied in the range of  $2\theta = 10\text{--}80^\circ$  as schematically shown in Figure 6.4. The thermal conversion process may modify both the physicochemical properties of the crystalline material in biochar with a notable structural alteration. In diffractograms of SCG show, a major diffraction peak depicted approximately at  $2\theta = 21\text{--}23^\circ$ . The peak was found to be compatible with the presence of an aromatic layer possessing a stacking structure of native cellulose amorphous-crystalline I and can be indexed as diffuse ( $I_{002}$ ) (Ngaosuwan et al., 2016). A broad hump at  $2\theta = 43^\circ$  in the corresponding biochar samples, attributed to the diffraction peaks of the graphitic and disordered graphitic plane ( $I_{100}$ ), due to the progressive stacking of graphene sheets and aromatic groups. Increasing the severity of pyrolysis temperature, broad-band at  $2\theta = 43^\circ$  indicates the formation of carbon-rich amorphous cellulose II structure perpendicular to

aromatic crystallites that show the destruction of lignocelluloses in the carbon matrix and change in textural properties (Saikia et al., 2019).

Disordered/amorphous structure, low crystallinity with aromatic characteristics was evident from the reduced intensity and sharpness of the hump in the XRD pattern of the biochar samples (Kaur et al., 2019). Additionally, the FT-IR and  $^{13}\text{C}$ -NMR spectrum of the SCG derived biochar samples (FTIR analysis and solid-state nuclear magnetic resonance of SCG and biochar samples) confirmed a similar observation of the development of aromatic characteristics in biochar as seen from the XRD pattern.

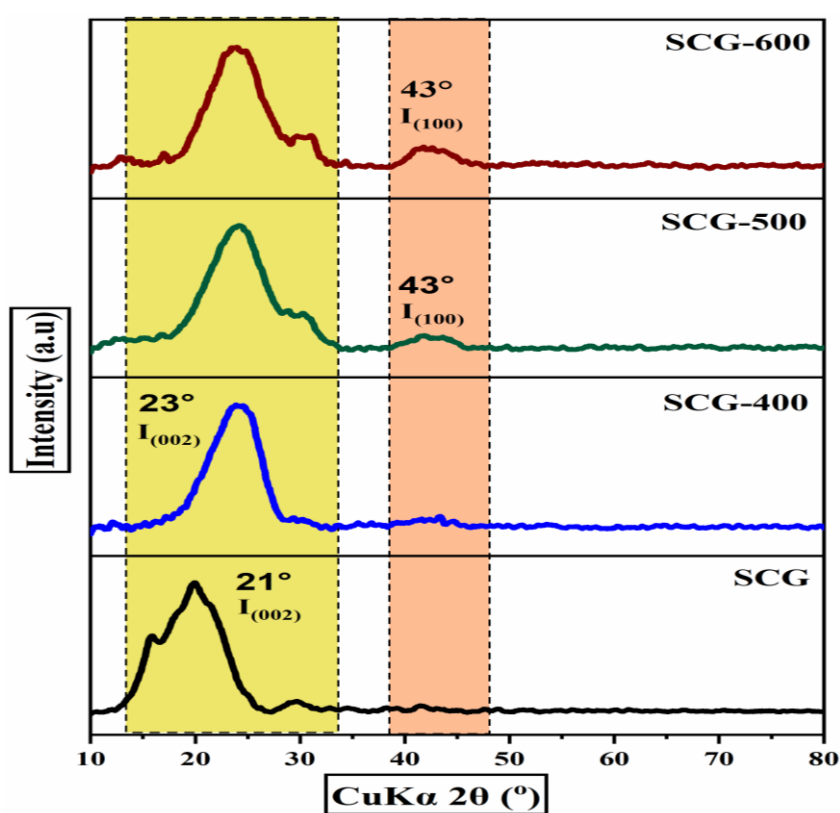


**Figure 6.4:** Wide-angle XRD patterns of SCG and SCG derived biochar samples.

### 6.5.9 FTIR analysis of biomass and biochar samples

To determine the structural evolution of SCG under slow pyrolysis conditions, the FT-IR technique was employed in the range from  $500$  to  $4000\text{ cm}^{-1}$ . Figure 6.5 shows the FT-IR transmission spectral peaks with diverse intensities (strong, broad, and weak) of absorption of the vast majority of functional groups present in SCG and biochar samples. With increasing the severity of pyrolysis temperature, SCG-derived biochar showed a resulting shift of FT-IR

spectral peaks that slowly lost their intensities in different degrees and disappeared in the corresponding biochar samples unlike the spectrum evident in the starting material (SCG) (Kim et al., 2017). For effective CO<sub>2</sub> adsorption performance under the post-combustion scenario, biochar's surface should possess basic characteristics as the active site along with high specific surface area and uniform distribution of micropores (Promraksa and Rakmak, 2020). Based on the visual interpretation, the prominent and broad spectroscopic assignments visible between 3200 and 3600 cm<sup>-1</sup> wavenumbers with a maximum at around 3300 cm<sup>-1</sup> indicates the presence of O-H and N-H stretching vibrations owing to alcohol, phenols, or carboxyl functional groups present in SCG. The existence of O-H and a minor contribution of N-H functional groups reveal the strong intra- and intermolecular hydrogen bonding and characteristic peak of crystalline cellulose in SCG (Taskin et al., 2019). However, with the rise in pyrolysis temperature the dehydration reaction and the generation of a large number of volatile compounds accelerated, so the intensity of this broad absorbance spectrum had a significant decrease in SCG and diminish sharply at 600 °C. The two sharp peaks observed between 2920 and 2850 cm<sup>-1</sup> and at 1465 cm<sup>-1</sup> are assigned to long linear aliphatic groups of -CH<sub>3</sub> and -CH<sub>2</sub> asymmetric and symmetric stretching vibrations which also diminished sharply for SCG-500 and SCG-600. The reduced vibrational intensities in the corresponding biochar are attributed to the loss of unstable aliphatic compounds (C-CH<sub>x</sub>) of cellulose-based materials at higher temperatures resulting in the occurrence of dehydration and demethylation reactions. The loss of -OH and C-H functional groups with increasing the severity of pyrolysis temperature identifies that they are not stable in SCG but contribute towards increasing surface area and favourable pore formation owing to the concurrent development of fused-ring aromatic structures in the biochar samples. The vibrations of C=C (aromatic ring) and -CH<sub>2</sub>- bands (C-H of alkene group) were confirmed by the presence of the peaks at around 1620 and 1455 cm<sup>-1</sup> and the presence of these bands in the corresponding biochar indicates the stability of the aromatic linkage (Lahijani et al., 2018). These findings are consistent with the data of atomic ratios (H/C and O/C) for SCG-600 as shown in Table 6.4, indicating the formation aromaticity, pH and depreciation in chemical structure and polarity.

The surface functional groups in biochar have been dominantly regulated by the pyrolysis temperatures, causing a gradual reduction and even disappearance of specific peaks and synthesis of the aromatic structure. The increase of basic and reduction of acidic functional moieties during the pyrolysis process at severe temperatures could be attributed to the reduction of oxygenated functional species and formation of N-containing functional groups on biochar

surface via series of possible decarboxylation and dehydration reactions that could favour the CO<sub>2</sub> adsorption (Franciski et al., 2018).

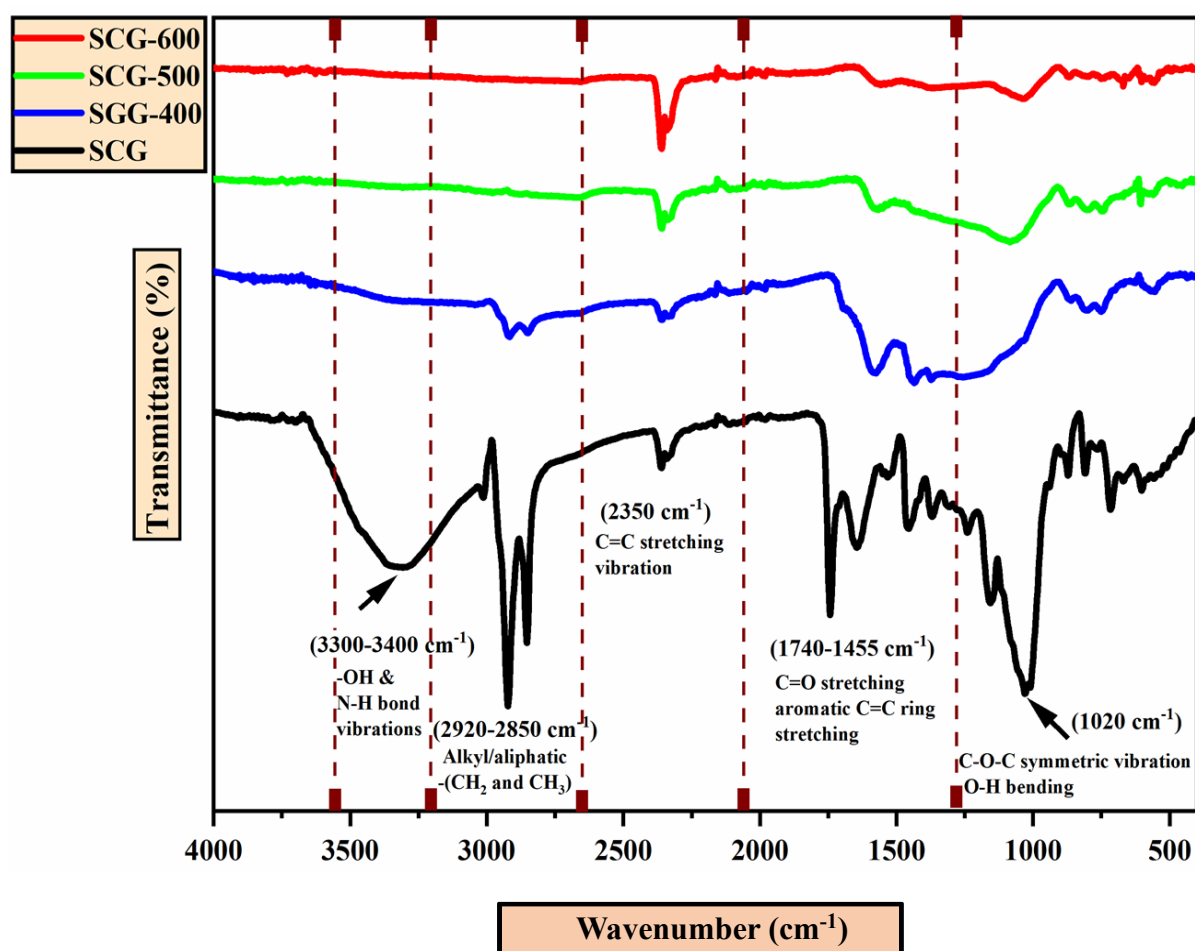


**Figure 6.5:** FTIR spectra of SCG and the corresponding biochar samples.

### 6.5.10 Solid-state Nuclear Magnetic Resonance (<sup>13</sup>C-NMR) Spectroscopy

SCG and the bio-chars generated from pyrolysis in 400 and 500 °C temperature ranges were examined by <sup>13</sup>C CP/TOSS solid-state <sup>13</sup>C-NMR spectroscopy. The chemical bands identified from the <sup>13</sup>C NMR spectra were dominated by a peak of aromatic carbons as schematically shown in Figure 6.6. The Table 6.7 gives the relative composition of aliphatic and aromatic moieties with probable assignments for the bands in the range of 25–225 ppm. The change in chemical shift is used as the qualitative indication to identify the alteration in structural components in the biochar samples after thermal treatment (Chand et al., 2019). Upon charring, the relative intensity of fused-ring aromatic C-H characters increased in SCG-500 as evident from the characteristic dominant broadband centered at <sup>13</sup>C-NMR chemical shifts between 120 and 150 ppm. This shift in the aromatic configuration is another complementary indication that

SCG-500 is comparatively highly rich in aromatic sp<sup>2</sup> carbon fraction (Rutherford et al., 2012). The increase in aromatic character and loss of aliphatic bands at higher temperatures suggests that biochar produced at higher temperatures would be aromatic or poly-aromatic in structure, favourable for trapping recalcitrant CO<sub>2</sub> owing to the increasing Vander Waals force in biochar matrix (Igalavithana et al., 2020).

**Table 6.7:** Quantitative percentages of various functional groups present in biomass and biochar samples based on <sup>13</sup>C-NMR spectra.

Sample	Total integrated peak area, %			
	Aliphatic (6-105 ppm)	Aromatic (120-145 ppm)	Carboxylic acid (170-180 ppm)	Ester (205-225 ppm)
SCG	84.1	1.3	14.4	0.2
SCG-400	7.5	89.4	1.9	1.2
SCG-500	5.5	92	0.9	1.6

#### 6.5.11 XPS analysis of biomass and biochar samples

XPS spectra were used to investigate the chemical bonding/states and the nature of the various oxygenated and nitrogenated species present on the surface of biochar. The quantification of the surface elemental compositions (atom ratio %) of SCG and the corresponding biochar is summarized in Table 6.8. Similar, to the findings of the bulk composition of biochar (Table 6.4), the O content on the surface of the biochar declined from 45.3% to 11.4% and the C content increased from 53.2% to 68.5% indicating the carbonaceous nature of the samples synthesized after the thermochemical conversion. The presence of nitrogen moieties is attributed to the protein and caffeine in SCG along with carbon and oxygen have been reported as advantageous for CO<sub>2</sub> adsorption as it enhances the surface active sites and basicity of the biochar (Ismail et al., 2020).

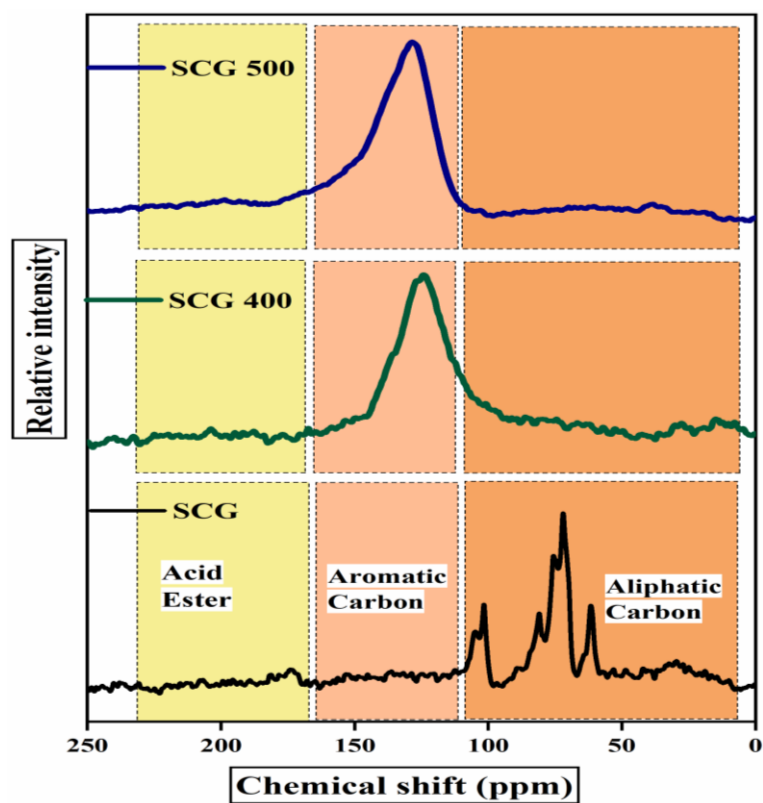


**Figure 6.6:**  $^{13}\text{C}$  Nuclear Magnetic Resonance spectra of SCG and SCG derived biochar samples.

Additionally, to recognize the complete bonding configurations of the heteroatoms (N1s and O1s), the high-resolution spectra were de-convoluted into different components with different binding energies (B. E's) representing various nitrogen and oxygen containing-moieties on the biochar sample's surface as displayed in Figures 6.7 and 6.8. The relative area percentage (A %) for N1s and O1s deconvoluted peaks of the XPS spectra is illustrated in Table 6.9. The high-resolution N1s spectrum with binding energies (B.E's) comprises three nitrogen species revealed at 398.1 eV (N-6) assigned to pyridinic-N, 400.3 eV (N-5) for pyrrolic and /or pyridonic-N and 401.6 (N-Q) eV for quaternary/graphitic-N and pyridine-N-oxide (N-X), respectively (Han et al., 2019). For both SCG-400 and SCG-600, N-5 (55.5–51.9 wt %) is the dominant species on the surface than N-6 and N-Q. For SCG-600, the area % of N-6 increased while N-5 and N-Q species showed an opposite trend as shown in Table 6.8. The decreasing trend of N-5 and N-Q could be attributed to the complete conversion of pyridonic and/or pyrrolic-N and quaternary-N into a more stable form of N-6 nitrogen species. All the three forms of nitrogenated species are beneficial for  $\text{CO}_2$  capture. It has been reported that pyridinic-N (N-6) and pyrrolic and /or pyridonic-N (N-5) species have the strongest impacts on the extent

of CO<sub>2</sub> adsorption as they could effectually ameliorate the polarity of carbon favourable for CO<sub>2</sub> adsorption (Wang et al., 2020; Singh et al., 2019). N-5 and N-6 functional moieties have electron-donating capability to  $\Pi$ -system and can strongly interact with Lewis's acid-like CO<sub>2</sub> molecules by  $\pi$ - $\pi$  interaction and electrostatics signifying their Lewis basicity.

O1s spectra deconvoluted into three peaks assigned at 531.2–531.5 eV (O1) corresponds to the ketone, carbonyl or lactone functional groups followed by ether and alcohol groups at 532.3–532.5 eV (O2) and ether oxygen atoms in anhydrides and esters at 533.3–533.6 eV (O3), respectively. The increase in atom area % (A %) for O1 and O2 (Table 6.9), indicates an enhancement in surface basicity of SCG-600 which could be favourable for CO<sub>2</sub> adsorption performance. This finding signifies that biochar prepared at 600 °C exhibits high Lewis's basicity as compared to SCG-400 and beneficial for the capture of Lewis acidic CO<sub>2</sub> molecule. A similar finding on improved CO<sub>2</sub> adsorption performance with increased Lewis basicity owing to acid-base interaction and selectivity had been investigated and reported by Tiwari et al., (2018).

**Table 6.8:** XPS derived surface elemental composition (atom ratio %) of SCG and SCG-derived biochar samples.

Sample	C (1s) %	O (1s) %	N (1s) %	O/C
SCG	53.2	45.3	1.5	0.64
SCG-400	63.4	15.7	1.8	0.14
SCG-500	67.7	13.2	2.4	0.12
SCG-600	68.5	11.4	3.1	0.10

**Table 6.9:** Deconvolution results of N1s and O1s spectra of SCG derived biochar samples (relative area percentage %).

Sample	XPS (at. % of total N and O)					
	N-6	N-5	N-Q	O1	O2	O3
SCG-400	22.5	55.5	19.9	47.9	17.1	5.9
SCG-600	39.4	51.3	9.5	51.2	20.9	7.1

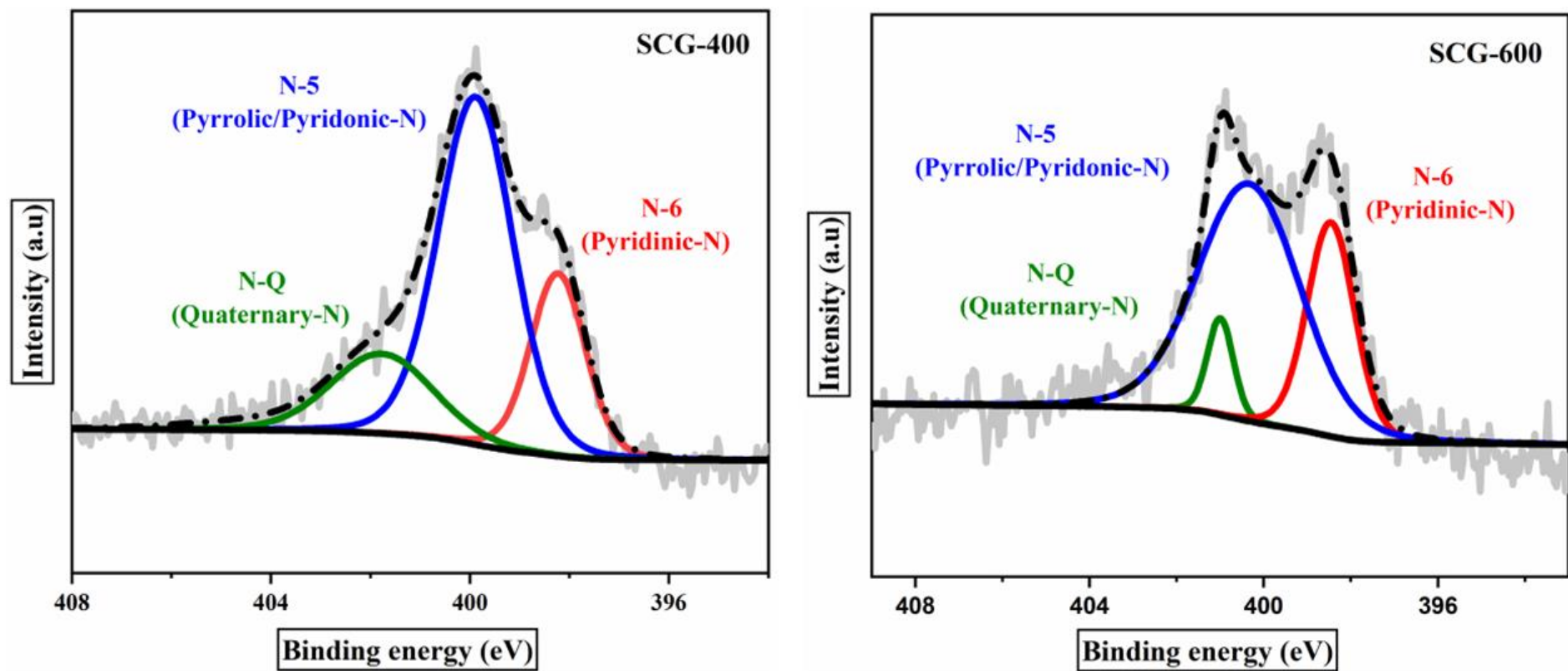
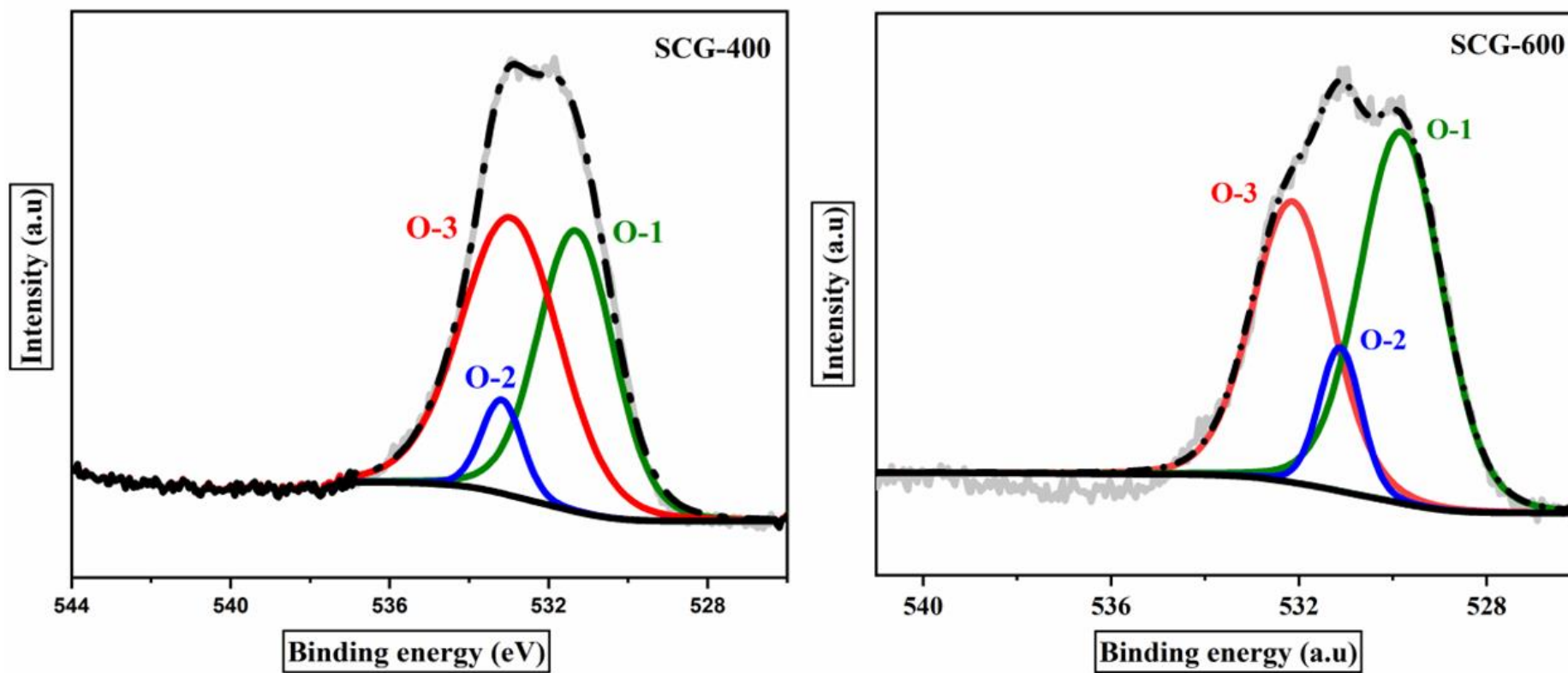


Figure 6.7: Deconvoluted N1s spectra of SCG-400 and SCG-600.





**Figure 6.8:** Deconvoluted O1s spectra of SCG-400 and SCG-600.

### 6.5.12 NEXAFS analysis of biomass and biochar samples

Stacked spectra of C 1s near-edge X-ray absorption fine structure (NEXAFS) of the spent coffee grounds and pyrolyzed spent coffee grounds at 400 °C, 500 °C, and 600 °C are shown in Figure 6.9; similarly, assignment of bond types, peak energies and transitions are reported in Table 6.1. C 1s fine structures exposed the carbon bonding environments in the SCG and pyrolyzed SCGs at different temperatures. From Figure 6.8, it can be noticed that the significant broad characteristic peak was noticed at 285.3 eV for SCG represents C1s→ $\pi^*$  C=C transitions related to the carbon bonded to the aromatic carbon, alkylated and protonated carbonyl substituted aryl-C ascribed to the inherent lignin content in the SCG (Coffey et al., 2002). Heymann et al., (2011) reported that owing to the wide breadth of each peak/s, it could be attributed to the multiple resonances rather than a single type of absorption bands. Further, the wideness of the aromatic transition recommended a complex chemical structure of the SCG and pyrolyzed SCG (di Stasio and Braun, 2006). The second peak with its maxima at 287.9 eV corresponds to C1s→ $\pi^*$  CO, C=C-OH transitions representing phenolic, carbonyl, and ester C, respectively (Latham et al., 2018; Keiluweit et al., 2010). At higher energies i.e., 289.5 eV, carboxylic acids (COOH) of hemicellulose and lignin are found which represents C1s→ $\pi^*$  C=O, R-COOH transitions (Heymann et al., 2011; Keiluweit et al., 2010). Besides this spectral analysis, a similar observation was received by Heymann et al. (2011) during their study on grass char and wood char; Latham et al. (2018) studied hydrothermal carbons treated at high temperatures (400, 600, and 800 °C) originated from sucrose; heat treatment of wood and grass samples by Keiluweit et al. (2010). Identical transitions and carbon types were observed for the SCG's that were pyrolyzed at 400, 500, and 600 °C (Figure 6.8). However, along with pyrolysis temperature, a 0.1–0.3 eV systematic shift in the peak positions was detected in comparison to SCG (untreated) which is a common trend noticed for heat-treated samples (Latham et al., 2018; Heymann et al., 2011; Keiluweit et al., 2010). Pyrolysis of SCG at higher temperatures (400, 500, and 600 °C) resulted in the increment in the aromaticity (Figure 6.8, 285.3 eV, C1s→ $\pi^*$  C=C graphitic transitions) and loss of the other functional groups which are associated with aliphatic and oxygen-containing groups that are present in the 287.9 and 289.5 eV photon energy regions. The same outcomes in loss of aliphatic and oxygen-containing groups and shifts in the peaks with temperature were observed from the FTIR and XPS data (FTIR and XPS analyses of SCG and SCG derived biochar samples). Along with the increase in the pyrolysis temperature, comparative fluctuations in the functional groups were noticed on each fine structure. Furthermore, at high temperatures, a sharp peak was observed at 292.6 –

292.9 eV (Figure 6.8) that resembles the highly oriented pyrolytic lignin from SCG that represents the  $C1s \rightarrow \sigma^* C=C$ ,  $C-C$  alkyl transitions (Bernard et al., 2010). In conclusion, the  $C1s$  K-edge fine structures of SCG and pyrolyzed SCG's chemical composition is in line with FTIR,  $^{13}C$ -NMR, XPS and the data from these spectral techniques are complementing the NEXAFS data.

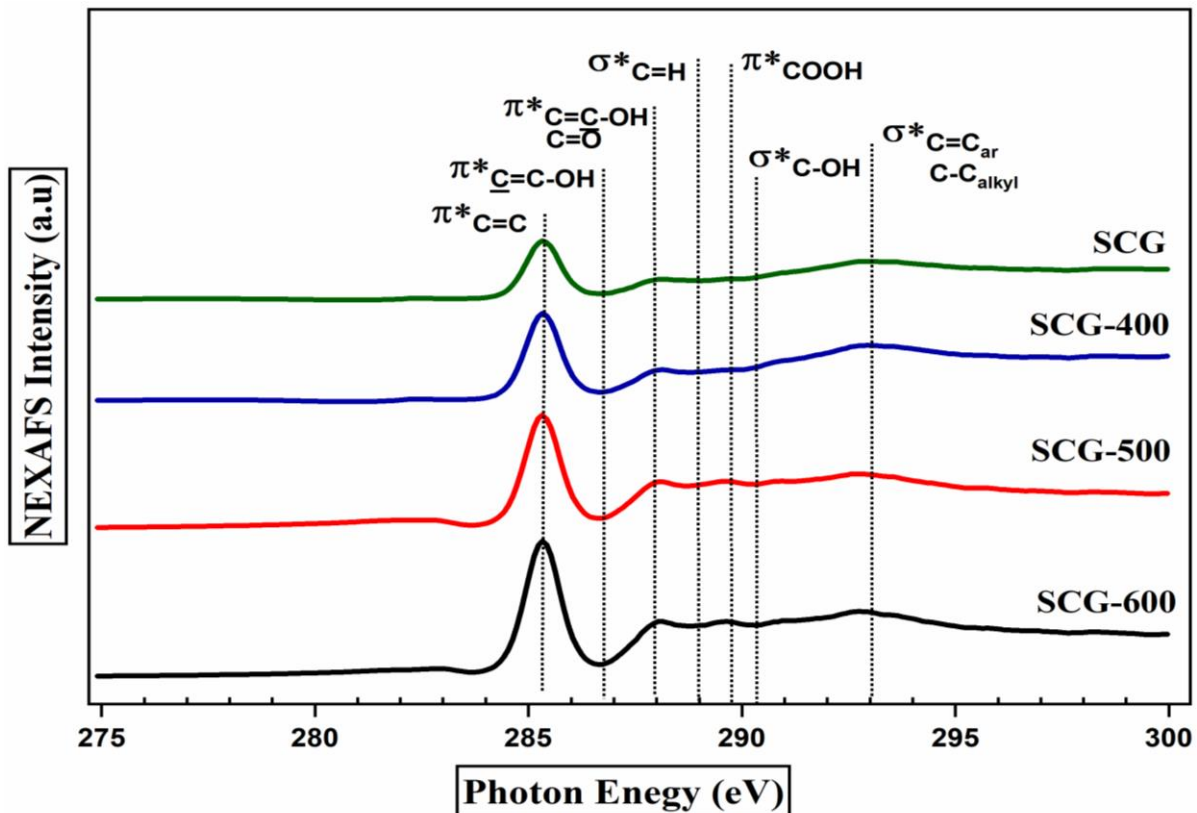


**Figure 6.9:** Stacked  $C1s$  NEXAFS spectra of SCG and SCG derived biochar samples.

### 6.6 Breakthrough $CO_2$ adsorption performance of SCG derived biochar samples

Typical S-shaped breakthrough curves seen are a graphical representation of the relationship between the ratio of outlet/inlet concentration ( $C_{CO_2}(\text{out})/C_{CO_2}(\text{in})$ ) in the mixed-gas stream and the contact time (min) with the subsequent occupation of the adsorbent's active sites until saturation (Al Mesfer and Danish, 2018). The rate of  $CO_2$  adsorption was rapid at the beginning, and gradually the rate reduced after the breakthrough time ( $t_B$ ) and came to a plateau after saturation of the adsorbent bed at exhaustion ( $t_E$ ), representing it was at equilibrium. The breakthrough ( $t_B$ ) and exhaustion time ( $t_E$ ) are the two crucial parameters studied when investigating the impacts of the adsorption conditions on the  $CO_2$  sorption capacity of the adsorbents. The time when the ratio of  $CO_2$  in the outlet to the initial concentration reaches 0.1

is termed as the breakthrough time and when the ratio of CO<sub>2</sub> outlet to the initial increases and reaches 0.9 is called the exhaustion time, both expressed in minutes in this regard. Initially, the outlet concentration of CO<sub>2</sub> was not detected, attributed to the complete adsorption (100%) by the available active sites and favourable pores on the surface but after the breakthrough, the concentration of CO<sub>2</sub> in the outlet stream gradually increases and becomes equal to the inlet. No further CO<sub>2</sub> adsorption takes place at the point of saturation attaining equilibrium.

### **6.6.1 Effects of adsorption conditions on CO<sub>2</sub> adsorption capacity**

A set of adsorption experiments were performed using SCG-600 as a representative sample to ascertain the effects of varying adsorption temperatures from 30 to 90 °C on the breakthrough curves at a constant CO<sub>2</sub> concentration (CO<sub>2</sub> feed= 30 vol%) balanced by N<sub>2</sub> as represented in Figure 6.10 (a). The initial feed concentration of CO<sub>2</sub> kept constant at 30 vol% and the rest balanced by N<sub>2</sub> was based on the previous lab experience (Shahkarami et al., 2015) and the results obtained from the adsorption capacities at varying CO<sub>2</sub> concentrations as shown in Table 6.10. Also, after investigating the effects of feed concentration on the CO<sub>2</sub> adsorption performance, it was found that at a lower concentration of CO<sub>2</sub> (10 vol%) the adsorption capacity (0.7 mmol/g) is low, but the exhaustion time ( $t_E$ , min) is longer owing to the availability of adsorption sites for a prolonged period. However, the performance enhanced with increasing the initial concentration to 30 vol% due to the increase in the partial pressure of CO<sub>2</sub> in the feed stream. It was observed that the CO<sub>2</sub> binding capacity of SCG-600 (mmol/g) decreases significantly with increasing the investigating temperatures from 30 to 90 °C accompanied by a declining trend of breakthrough time as evident from Figure 6.9 (a). The average results of equilibrium adsorption capacity obtained at varying temperatures were in the range of 2.8 (30 °C) to 0.5 (90 °C) mmol/g at a fixed feed concentration is presented and summarised in Table 6.10. The fall in CO<sub>2</sub> adsorption capacity at higher temperatures indicates that the adsorption mechanism is predominantly physical in nature and the reaction is exothermic (Latham et al., 2018). The governing mechanism of adsorption could be physical in nature owing to the loss in functional groups after the severe thermal treatment (Ismail et al., 2020).

In this study, the highest adsorption capacity of 2.8 mmol/g was obtained at 30 vol% of C<sub>CO2</sub> and at 30 °C. Also, the breakthrough time was reduced from 5.5 min to < 1 min by increasing the adsorption temperature for SCG-600 as summarised in Table 6.10. The lower affinity and instability among the CO<sub>2</sub> molecules at higher temperatures could be attributed to the increased

molecular diffusion rate generating instability on the surface and exothermicity of the adsorption process. A similar finding on declining adsorption capacity with increasing adsorption-temperatures using N-enriched carbon sorbent prepared from Urea-formaldehyde resin was reported by Tiwari et al., (2018) and yellow-mombin derived activated carbon samples by (Fiuza-jr et al., 2016). Also, experimental findings suggest that CO<sub>2</sub> is weakly bound to the biochar surface (SCG-600) through physisorption, so surface area was a significant determinant of CO<sub>2</sub> adsorption; however, the presence of nitrogenous species (N-6 & N-5 species) also played a significant role in CO<sub>2</sub> adsorption.

Pyrolysis of SCG at higher temperature endowed SCG-600 with hydrophobic, non-polar characteristics, higher specific surface area and basic functionalities (oxygenated and nitrogenated moieties) preferable for CO<sub>2</sub> adsorption performance. Correspondingly, the formation of stable aromatic structures in SCG-600 was corroborated by the reduced O/C atomic ratio, also facilitated the CO<sub>2</sub> adsorption.

**Table 6.10:** Breakthrough adsorption performance of SCG-600 under varying column temperatures and initial feed concentration of CO<sub>2</sub>.

<b>SCG-600, constant CO<sub>2</sub> concentration: 30 vol % balanced by N<sub>2</sub> (dynamic conditions)</b>			
<b>Adsorption temperature (°C)</b>	<b>Breakthrough time (min)</b>	<b>Adsorption capacity (mmol/g)</b>	<b>Standard Deviation</b>
<b>30</b>	5.5	2.8	0.37
<b>45</b>	3.5	1.5	0.14
<b>60</b>	2.4	1.2	0.22
<b>75</b>	1.1	0.9	0.17
<b>90</b>	0.8	0.5	0.16
<b>Sample: SCG-600, constant column temperature: 30 °C, feed concentration: CO<sub>2</sub> in N<sub>2</sub></b>			
<b>CO<sub>2</sub> (10 vol % in N<sub>2</sub>)</b>	6.8	0.7	0.21
<b>CO<sub>2</sub> (20 vol % in N<sub>2</sub>)</b>	6.2	1.6	0.15
<b>CO<sub>2</sub> (30 vol % in N<sub>2</sub>)</b>	5.5	2.8	0.37

### 6.6.2 Breakthrough adsorption capacity of biochar samples

The effect of pyrolysis temperature on the adsorption capacity was ascertained by the performance of the corresponding biochar under the fixed operating conditions of adsorption temperature at (30 °C) and initial CO<sub>2</sub> concentration of 30 vol% balanced by N<sub>2</sub> as graphically represented in Figure 6.10 (b) and the average adsorption capacity of the biochar samples are summarised in Table 6.11.

The adsorption breakthrough occurs early for SCG-400 compared to SCG-600 at the same initial CO<sub>2</sub> concentration of 30 vol% of CO<sub>2</sub> in feed (balanced by N<sub>2</sub>) and adsorption temperature at 30 °C. The adsorption capacity of SCG-600 was the maximum among all the series of adsorbents investigated and was reduced from 2.8 to 0.7 mmol/g under a similar capture scenario. The adsorption capacity of SCG-600 was comparatively the highest, owing to its superior surface characteristics and remarkable surface functionalities (availability of N-6, N-5 species, and basic-O species), enhancement of basicity and the formation of higher aromatic rings forming stable graphite-like structures during the thermal treatment.

**Table 6.11** Breakthrough adsorption performance of biochar samples derived from SCG.

<b>Constant temperature: 30 °C and CO<sub>2</sub> concentration: 30 vol % balanced by N<sub>2</sub></b>			
<b>Sample</b>	<b>Breakthrough time (min)</b>	<b>Adsorption capacity (mmol/g)</b>	<b>Standard Deviation</b>
<b>SCG-600</b>	5.5	2.8	0.37
<b>SCG-500</b>	3.0	1.3	0.19
<b>SCG-400</b>	1.2	0.7	0.22

From Table 6.12, it is evident that SCG-600 is a promising carbon-based solid adsorbent synthesized from slow-pyrolysis of SCG that exhibited compatible CO<sub>2</sub> adsorption capacity under a typical post-combustion condition compared to biochar, biomass derived activated carbon and other carbon-based adsorbents. This superior performance of SCG-600 could be attributed to the trade-off between textural characteristics and surface composition that is favourable for interaction between the basic functional moieties with Lewis-acid CO<sub>2</sub> molecules in the flue gas stream.

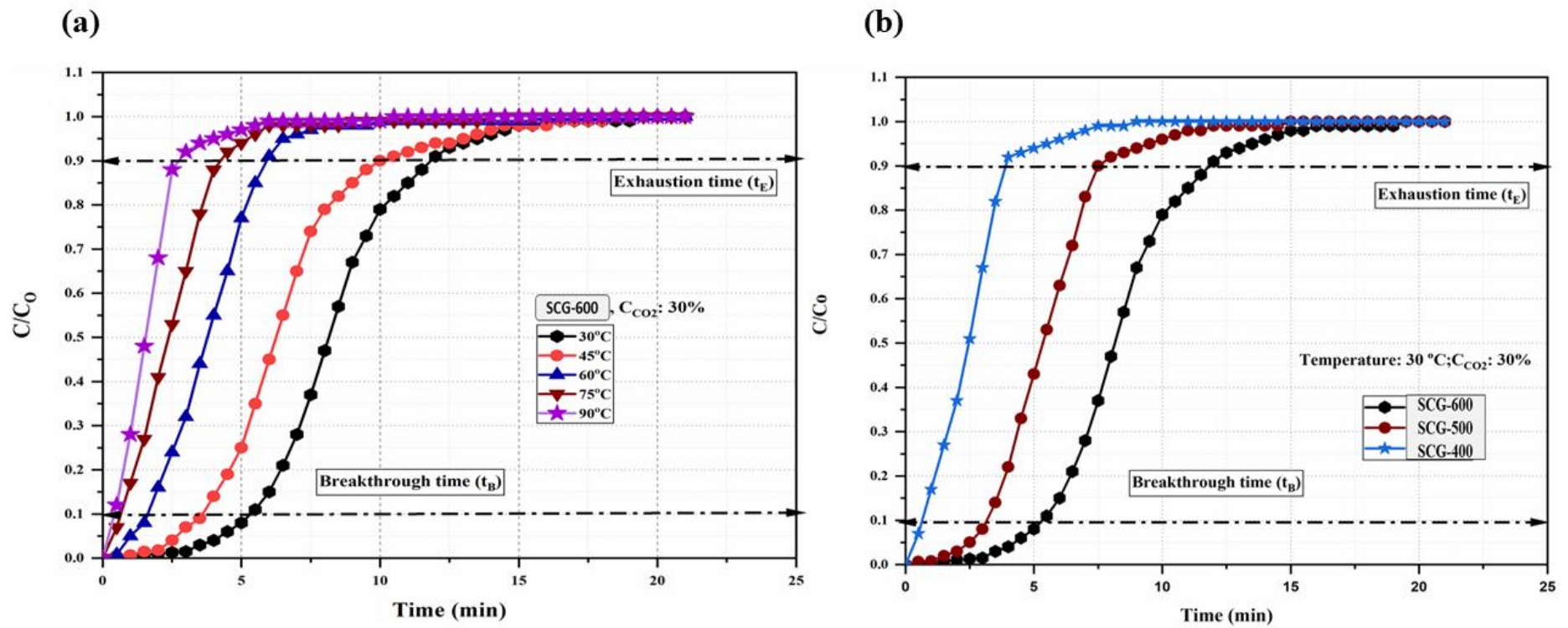


**Figure 6.10:** (a) Breakthrough adsorption curve of SCG-600 at varying column temperatures, (b) Breakthrough adsorption curve of biochar samples derived from SCG.

**Table 6.12:** CO<sub>2</sub> adsorption performance of carbon-based adsorbents under the post-combustion conditions (binary mixture of CO<sub>2</sub>/N<sub>2</sub>).

Carbon sorbents	Specific surface area, $S_{BET}$ (m <sup>2</sup> /g)	Adsorption capacity of CO <sub>2</sub> at 1 bar (mmol/g)	Reference
SCG-600 (biochar)	539	2.8 (30 °C)	This study
SCG-500 (biochar)	311	1.3 (30 °C)	
SCG-400 (biochar)	179	0.7 (30 °C)	
Urea Bagasse (KOH activated)	4546.9	1.40 (30 °C)	(Tiwari et al., 2018)
MF-700 (Melamine-formaldehyde-700 °C)	266	0.83 (30 °C)	(Goel et al., 2015)
AC derived from Eucalyptus wood (NH <sub>3</sub> treatment)	1637	1.1 (30 °C)	(Heidari et al., 2014)
Optimised activated carbon (agriculture residues)	371	2.46 (25 °C)	(Rashidi et al., 2014)
Commercial activated carbon	717	3.15 (25 °C)	
Waste tobacco derived AC	1104	2.5	(Sha et al., 2015)
PS550 (pine sawdust derived at 550 °C)	315.6	0.67	(Igalavithana et al., 2020)
PSS550(pine sawdust derived AC)	581.7	0.73	
BMHC600-N (N-doped ball milled hickory chips)	548	52.5 mg/g (1.2 mmol/g)	(X. Xu et al., 2019)
BMBG600-N (N-doped ball milled bagasse)	473	48.2 mg/g (1.09 mmol/g)	
BMBG450 (Ball milled sugarcane bagasse)	430	46.8 mg/g (1.06 mmol/g)	(Creamer et al., 2014)
BG450 (pristine sugarcane bagasse)	370	47.9 mg/g (1.1 mmol/g)	
AC derived from bamboo	787	2.52 (25 °C)	(Dilokekunakul et al., 2020)
AC-UK	532	2.63 (25 °C)	
AC-Air	811	2.26 (25 °C)	
Zeolite seeds crystals	1254	2.39 (30 °C)	(Gunawan et al., 2018)
Titanium granules	71	2.55 (30 °C)	(Song et al., 2013)
Cotton stalk derived AC (NH <sub>3</sub> treatment)	435	1.80 (20 °C)	(Xiong et al., 2013)



## 6.7 Adsorption kinetic study and activation energy

Adsorption kinetics and activation energy are significant characteristics that determine the extent of interaction between carbon-based solid adsorbents and CO<sub>2</sub> in the mixed gas stream. The adsorption process proceeds in three main steps; (i) external diffusion of CO<sub>2</sub> followed by (ii) internal diffusion and (iii) CO<sub>2</sub> adsorption through interacting with active and basic sites of the adsorbent available within the network of pores (Raganati et al., 2019). Adsorption kinetic performs a crucial role for a better understanding of the interaction between adsorbate-adsorbent but predicting kinetic parameters involves generally involves complexity. The adsorption kinetics were studied by fitting the CO<sub>2</sub> adsorption data obtained at varying column temperatures to the well-established pseudo-first, second order and intra-particle diffusion models, owing to their simplicity to depict the nature of adsorbate-adsorbent interactions. The assumptions for the kinetic models are based on the correlation between the rate of adsorption, the number of available adsorption sites and the strength of the interaction between adsorbate-adsorbent. The rate of adsorption and the availability of active sites are directly correlated to the pseudo-first-order model and the latter depicts a strong interaction owing to some chemical reactions between the adsorbate and adsorbent. In this study, the pseudo-first-order kinetic model fitted well with the experimental data obtained at varying investigating temperatures with the highest value of correlation coefficient  $R^2 = 0.96$  and sum of square error less than 10% (Table 6.13). The pseudo-first-order model better described the CO<sub>2</sub> adsorption mechanism that involves weak adsorbate-adsorbent interaction at a typical post-combustion scenario. Table 6.13 summarizes the related parameters of different kinetic models examined for SCG-600 at 30 °C of adsorption temperature and 30 vol% of initial CO<sub>2</sub> concentration balanced by N<sub>2</sub>.

The kinetic rate constants (K) at different temperatures (30–90 °C) were determined by fitting the Arrhenius equation to the data obtained from the pseudo-first-order model. Table 6.13 showed the values of the rate constants (K) at different adsorption temperatures. Figure 6.11 showed the Arrhenius plot from which the activation energy obtained was 21.20 kJ/mol. The lower value of activation energy (<25 kJ/mol) shows the adsorption was predominantly physical in nature owing to the moderately weak interaction between the adsorbate-adsorbent (CO<sub>2</sub>-biochar surface) (Rashidi et al., 2014)

**Table 6.13:** Values of adsorption kinetic parameters of SCG-600 at varying adsorption temperatures.

Isotherm model	Parameters	Value	R <sup>2</sup>
Pseudo-first-order	K <sub>1</sub> (min <sup>-1</sup> )	1.5	0.96
	q <sub>e</sub> (experimental, mmol/g)	2.8	
	q <sub>e</sub> (predicted, mmol/g)	3.3	
Pseudo-second-order	K <sub>2</sub> (g/mmol*min)	1.2	0.94
	q <sub>e</sub> (experimental, mmol/g)	2.8	
	q <sub>e</sub> (predicted, mmol/g)	4.5	
Intra-particle diffusion	K <sub>id</sub> (mmol/g*min <sup>0.5</sup> )	1.3	0.93
	C (mmol/g)	-0.5	

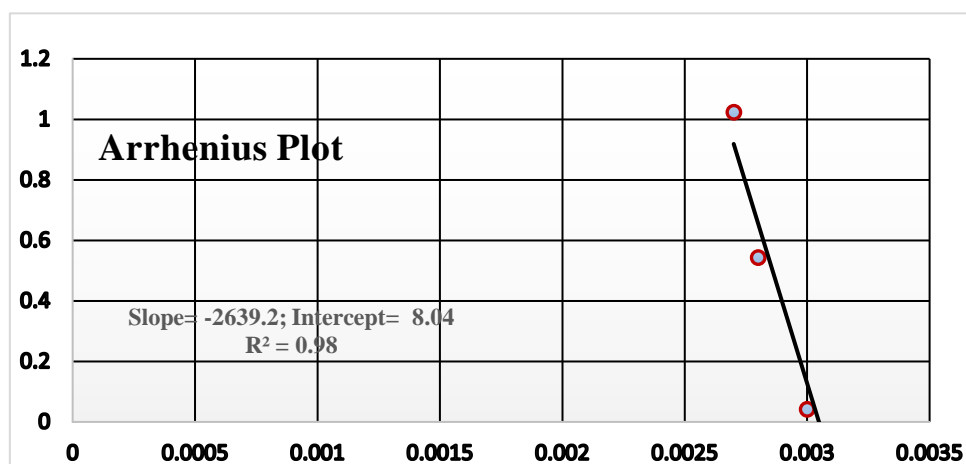


**Figure 6.11:** Arrhenius plot.

## 6.8 Conclusions

Biochar is environmentally friendly and a cheaper alternative than other common carbonaceous samples available for post-combustion CO<sub>2</sub> capture. It is because it can be synthesized from waste biomass residues available in large quantities, through one-step slow pyrolysis technique at a relatively low temperature without exploiting sophisticated equipment or adding extra chemicals. Regarding supply, biochar can be generated from sustainable and inexpensive source like spent coffee grounds, so the source is abundant to explore further for slow pyrolysis. In recent years, the spent coffee grounds have received significant attention as a potential source of biomass for valorization. In this study, it was upgraded to produce pyrolysis biochar for mitigating anthropogenic CO<sub>2</sub> emissions at relatively low technology risk. The effects of pyrolysis operating parameters (temperature and heating rate) on biochar yield and textural

properties were evaluated. It was observed that increasing the severity of pyrolysis temperature and heating rate demonstrated a declining biochar yield. Also, increasing heating rate had a detrimental impact on the textural properties but with the rise in pyrolysis temperature the specific surface area was enhanced. In this regard, the physiochemical changes of the biochar samples prepared at varying pyrolysis temperatures and at a constant heating rate were analyzed by series of complementary analyses to ascertain their candidacy towards CO<sub>2</sub> capture performance. Adsorption studies for CO<sub>2</sub> were carried out to investigate the sensitivity of SCG-600 to varying adsorption temperatures (30–90 °C) at ambient pressure with the CO<sub>2</sub>/N<sub>2</sub> feed stream. Both adsorption temperatures and the type of adsorbents impacted the shape and breakthrough time of the CO<sub>2</sub> adsorption. With the rise in adsorption temperature to 90 °C, SCG-600 lost more adsorbed amounts of CO<sub>2</sub> owing to the physical and exothermic nature of the adsorption process. Comparatively the presence of high surface area and well-developed porous structure of SCG-600 are found to be the governing parameters for significantly high CO<sub>2</sub> adsorption under a typical post-combustion scenario. Additionally, the availability of basic functionalities and high aromaticity of SCG-600 might have enhanced the CO<sub>2</sub> adsorption process. For SCG-600 basic functionalities facilitated the Lewis-acid-to-base interaction and high aromaticity enhances the Van der Waals force between the biochar matrix and CO<sub>2</sub> molecule. The maximum removal capacity of SCG 600 obtained was 2.8 mmol/g under the investigated adsorption conditions (adsorption temperature at 30 °C and inlet CO<sub>2</sub> concentration of 30 vol% balanced by N<sub>2</sub>). The Adsorptive kinetic of SCG-600 followed the pseudo-first-order kinetic model with low activation energy (> 25 kJ/mol), which indicated that the adsorption was physical in nature. Overall, the relevance of high specific surface area, well-developed microporous structure, non-polar characteristics, aromaticity, availability of N-6 and N-5 nitrogenated species and basic oxygenated groups make SCG-600 a potential candidate for a typical dynamic breakthrough-CO<sub>2</sub> capture adsorbent at industrial sites. Therefore, slow pyrolysis compared to torrefaction can be proposed as an efficient thermochemical conversion technique to produce biochar. Additionally, investigations are required to ascertain the transformation of AC samples derived from further valorization of SCG-600 through physical activation and surface functionalization in terms of textural properties and surface functionalities to enhance the CO<sub>2</sub> removal performance under post-combustion condition.

## **Chapter 7 Preparation of activated carbon from spent coffee grounds and functionalization by deep eutectic solvent: Effect of textural properties and surface chemistry on CO<sub>2</sub> capture performance**

A version of this section of the thesis is submitted for publication in a peer-reviewed journal.

In addition, some portions of this chapter were presented at the following conferences, poster presentations and 3 Minutes Thesis Competitions (3MT) (presented in Appendix A).

### **Conference Presentation:**

**Mukherjee, A.**, Niu C., & Dalai, A.K., "Carbon dioxide capture exploiting novel activated carbon from spent coffee grounds", oral presentation at Research for a Better World - A Holistic Approach, Graduate Student Association (2019), Saskatoon, Canada, February 27<sup>th</sup> & 28<sup>th</sup>, 2019.

**Mukherjee, A.**, Niu C., & Dalai, A.K., " Novel Activated Carbon from Spent Coffee Grounds for CO<sub>2</sub> Capture: Effects of Textural Properties and Surface Properties", oral presentation at Advances in Carbon Dioxide Capture & Utilization for Sustainable Climate (ACCUSC-2022), Department of Chemical Engineering, National Institute of Technology, Rourkela, 4<sup>th</sup>-10<sup>th</sup> July 2022.

### **Poster Presentation:**

**Mukherjee, A.**, Niu C., & Dalai, A.K., "Activated carbon synthesized from spent coffee grounds for carbon dioxide capture" poster presentation at 2nd Engineering Graduate Research Conference (2<sup>nd</sup> EGR), Saskatoon, Canada, September 13<sup>th</sup>, 2021.

### **Contribution of the Ph.D. Candidate**

In consultation with supervisors, the bench-scale adsorption set-up re-installed and calibrated by Alivia Mukherjee. All the activated carbon samples were prepared by Alivia Mukherjee. All the experiments were planned and conducted by Alivia Mukherjee. All the sample characterizations were performed, and the related data were analyzed by Alivia Mukherjee. The data analyses and interpretations were conducted by Alivia Mukherjee. Dr. Biswajit Saha helped with the preparation of DES and functionalization of activated carbon samples and reviewing the manuscript. All the written text was prepared by Alivia Mukherjee and all the experiments were discussed with Drs. Ajay K. Dalai and Dr. Catherine Niu.

### **Contribution of this chapter to the overall study**

In Chapter 7, the importance of the influence of the activation parameters on specific surface and AC yield were discussed. Furthermore, the role of surface chemistry along with the textural characteristics on CO<sub>2</sub> capture performance had been evaluated. The activation parameters and the functionalization agent are important factors in porosity and formation of the surface functional groups on the surface of the produced activated carbons. To develop an activated carbon adsorbent with tailored properties, the effects of the precursor and carbonization techniques on CO<sub>2</sub> adsorption capacity and selectivity of activated carbons were studied. In this chapter, the impacts of the activation conditions (temperature, holding time and CO<sub>2</sub> flow rate) and functionalization using natural deep eutectic solvent (DES) on the textural properties and surface chemistry of the prepared activated carbon samples are discussed and the performances of the samples in CO<sub>2</sub>/N<sub>2</sub> feed stream is evaluated.

## 7.1 Abstract

In this research, spent coffee grounds (SCG) have been selected as a potential feedstock to synthesize activated carbon (AC) through a two-step physical activation technique. The activation parameters were optimized by employing the Response Surface Methodology (RSM) combined with the Box-Behnken design (BBD) method. The impact of input activation parameters included the activation temperature (600-800 °C), activation time (60-120 min) and CO<sub>2</sub> flow rate (150-250 mL/min) were investigated extensively using BBD methodology. The second-order quadratic model developed by ANOVA and lack-of-fit test well described each response and the significant parameters. Accordingly, at the optimum conditions obtained at 800 °C, 90 min and 150 mL/min, the predicted response of specific surface area (1202.1 m<sup>2</sup>/g) was in good agreement with the actual response of specific surface area (1224 m<sup>2</sup>/g). Natural deep eutectic solvent (DES) has been used to tailor the surface functionalities of the optimized AC (pristine) to alleviate the CO<sub>2</sub> capture performance. The change in textural characteristics, surface chemistry and morphology of the pristine and DES-AC samples were characterized and compared by using complementary analytical techniques, including ultimate analysis, ash content, TGA, S<sub>BET</sub>, XRD, XPS and SEM analyses. The studies highlighted that the surface area of the functionalized AC was reduced to 1033 m<sup>2</sup>/g, but more basic functional moieties developed on the surface compared to pristine AC. The DES functionalized AC has shown adequate CO<sub>2</sub> capture performance of 5.5 mmol/g compared to pristine AC (4.34 mmol/g) at 25 °C and 15 vol % of CO<sub>2</sub> (in N<sub>2</sub>). Furthermore, DES functionalized AC has shown excellent cyclic stability and facile regeneration after multiple adsorption and desorption runs. Hence, preparing activated carbon from SCG via two-step physical activation and DES impregnation could be proposed as a promising valorization strategy to alleviate the CO<sub>2</sub> emission problem from a large-point stationary source.

## 7.2 Introduction

In the last few decades, anthropogenic emission of greenhouse gases, mainly carbon dioxide (CO<sub>2</sub>) in the ambient air, has been considered one of the primary driving forces due to the assertion that it triggers global warming (Nasri et al., 2014). The abnormal change in weather patterns along with the noticeable rise in temperature is defined as global warming. The emission of CO<sub>2</sub> accounts for about three-quarters of total greenhouse gas emissions and is one of the critical factors in the worldwide climate change scenario and ocean acidification. Owing to the mass combustion of the most utilized energy source such as fossil fuel resources (petroleum or coal) to sate the global energy demand due to the abundant availability and economic efficiencies, the emission of CO<sub>2</sub> and the global warming issue have triggered (Pu et al., 2021). Presently, the atmospheric concentration of CO<sub>2</sub> has approached a level of approximately 415 ppm from the pre-industrial time, which is already beyond the earth's total capacity (Rahman et al., 2020). Foreseen detrimental consequences of this phenomenon can be observed globally, such as extreme forest fires and heatwaves, melting of ice sheets and glaciers in the Antarctic, rising sea levels, damage to crops and health issues. The rise in global average temperature by more than 2°C would lead to serious environmental consequences. It can be attributed to the increased atmospheric concentration of CO<sub>2</sub> to approximately 570 ppm in 2100 (Han et al., 2019b). The scientific community and policymakers of developed and developing nations should put joint effort to alleviate the massive consequences on the global ecosystem and tackle the tremendous impacts on the terrestrial environment in future.

Carbon capture and storage (CCS) technologies would help to evade the disastrous impacts on the eco-system strategically, combat carbon dioxide emissions and simultaneously allow the usage and combustion of fossil fuels (Shewchuk et al., 2021). Among all the available CO<sub>2</sub> capture technologies, the post-combustion CO<sub>2</sub> capture technique has comparatively gained popularity owing to its low technological risk. It can be easily retrofitted to the existing emission sources without excessive disturbance to their operational structure. CO<sub>2</sub> is trapped from the flue gas streams emitted after fossil fuel combustion in the post-combustion capture technique to combat global warming (Kumar et al., 2020). Commonly used post-combustion CO<sub>2</sub> capture techniques include amine-based or ionic-liquid-based absorption, cryogenic distillation technique, membrane separation and adsorption with solid adsorbents (Chao et al., 2021). Although adsorption on solid adsorbent has been proposed as a mature and promising capture technique instead of chemical absorption using amine-based solvents. The process

challenges of amine-based absorption often encountered include high heat of absorption, high energy demand for regeneration, solvent losses, corrosivity of the reaction medium and expensive economics (Ogungbenro et al., 2017). Recently, intensive research interests have been paid to developing carbon-based adsorbents with higher adsorption capacity, affinity, renewability, and faster kinetics, such as zeolites (Lu et al., 2008) and metal-organic frameworks (Wu et al., 2010), and engineered carbonaceous porous materials (biochar or activated carbons) (Mukherjee et al., 2021a, Mukherjee et al., 2019). A strategy to promote a bio-based and sustainable economy could be achieved by undergoing valorization of lignocellulosic biomass to produce value-added products like biochar or activated carbons (ACs) that could eventually minimize the accumulation of waste.

In Canada, biomass-derived from coffee industries mainly spent coffee grounds (SCG) are underutilized and are arbitrarily disposed of in open landfills, escalating severe environmental issues like methane ( $\text{CH}_4$ ) generation. However, SCG has displayed interesting inherent physicochemical properties that could be valorized to produce value-added products (Mukherjee et al., 2021a). Valorising spent coffee grounds to synthesize AC brings two-fold benefits from the commercial perspective. Firstly, the volume of SCG generated can be reduced and secondly, its outstanding physicochemical properties can be utilized to produce carbonaceous adsorbent that can trap recalcitrant  $\text{CO}_2$ . Our previous study investigated the  $\text{CO}_2$  adsorption potential of biochar derived from SCG from torrefaction (Mukherjee et al., 2022) and slow pyrolysis (Mukherjee et al., 2021a). In that study, we examined the physicochemical properties of SCG-derived biochar synthesized and used for  $\text{CO}_2$  capture performance. The torrefied biochar synthesized using SCG at the extreme torrefaction conditions (300 °C) removed 0.38 mmol/g of  $\text{CO}_2$  from the flue gas stream at 25°C and in presence of 30 vol% of  $\text{CO}_2$  in  $\text{N}_2$ . Similarly, under a typical post-combustion capture scenario, the highest  $\text{CO}_2$  removal obtained using biochar derived from SCG at 600 °C was 2.8 mmol/g at 30 °C and 30 vol% of  $\text{CO}_2$ . However, further thermal treatment at elevated temperature or surface functionalization is necessary to enhance the  $\text{CO}_2$  adsorption performance. However, very few studies have compared the potential of torrefaction and slow pyrolysis as the thermal treatment technique before undergoing the two-stage physical activation to synthesize AC. The synthesis of AC has grabbed immense attention owing to its ease of synthesis from various low-cost precursors such as SCG, well-organized internal porous structure, higher specific surface area, a wide range of surface functionalities and ease of regeneration (Zhu et al., 2014). Furthermore, the synthesis of AC utilizing lignocellulosic biomass can be proposed as a potential strategy to



promote a bio-based economy owing to its abundant availability at a low price with prospective to compete with commercial AC, which is mainly synthesized from non-renewable sources and are generally expensive (Rashidi and Yusup, 2019).

Conversion of SCG to AC could be executed through two activation pathways: physical and chemical activation techniques. Amongst the two activation techniques, the physical activation technique is preferable owing to the absence of harsh chemical treatment. It doesn't involve any additional corrosion problems and washing stage. Contrary in the chemical activation technique, both carbonization and activation steps proceed simultaneously as a single step but in the presence of harsh chemical activating agents. Potassium hydroxide (KOH) has been widely applied as one of the popular chemical activating agents but has high susceptibility to human health and the ecosystem.

Synthesis of ACs via physical activation involves a twofold process of pyrolysis and subsequent activation in the presence of suitable oxidizing agents for instance air, steam (H<sub>2</sub>O) or CO<sub>2</sub> (Mukherjee et al., 2019). The preparation of ACs for gas-phase applications such as CO<sub>2</sub> adsorption and the selection of a suitable oxidizing agent is imperative. Preparing activated carbon using air is not preferred owing to its high surface burn-off and low carbon yield. Amongst the oxidizing agents, steam and CO<sub>2</sub> are widely applied as the activating agents that undergo endothermic reaction with adequate temperature controllability during the activation process. The steam activation process involves generating steam using a steam generator and a metering pump and is more energy-intensive than CO<sub>2</sub> activation. In CO<sub>2</sub> activation, the activating agent can be consumed directly from the gas tank. Also, the CO<sub>2</sub> activation process permits tailoring of the pore structure and generates narrow microporosity compared to steam activation (Heo and Park, 2015). This behaviour of developing different porosity by the activating agents (H<sub>2</sub>O and CO<sub>2</sub>) could be attributed to the way of interacting with the active sites of the carbonaceous material located at the pore-centre and pore-wall (Smets et al., 2016). The CO<sub>2</sub> penetrates the internal structure of the biochar during activation and reacts with the unstable carbon and unreachable pores by eliminating carbon monoxide (CO) and generating narrow microporosity. Hence, the CO<sub>2</sub> activation process is an economical and more convenient pathway to synthesize ACs for CO<sub>2</sub> capture than steam activation (Rashidi and Yusup, 2019). Accordingly, in this regard, physical activation using CO<sub>2</sub> has been explored as a more straightforward strategy. It has the potential to synthesize porous carbon-based adsorbents with well-developed textural properties and surface functionalities.

Owing to the weak Lewis acidic nature, CO<sub>2</sub> can be trapped well onto a basic surface or surface containing N-functional moieties, resulting in a superior adsorption behaviour, and attributed to the acid-base interaction. Extensive research is still required to replace harsh chemical activating agents with a green and environmentally friendly solvent. Several research initiatives have been going on to modify the surface functionalities of activated carbon using ecologically friendly chemicals to trap CO<sub>2</sub> molecules from flue gas streams. Natural deep eutectic solvents (DES) with many unique characteristics such as thermal stability, non-toxicity, biodegradable components, ease of synthesis and application can be referred to as the environmentally friendly green solvent. DES can be considered a suitable solvent owing to its abundant availability, biodegradability, performance, and price, which can enhance the surface functionalities by adding more basicity for superior CO<sub>2</sub> capture performance that can be replaced with any harsh chemical solvents. Few pieces of literature available have shown the comparative performance of raw and functionalized activated carbon with DES derived from two-step physical activation using SCG as the precursor. Recently, Hussin et al., (2021) have studied and compared the CO<sub>2</sub> capture performance of raw and functionalized AC derived from palm shells. They explored the usage of deep eutectic solvent (DES) synthesized using different molar ratios of choline hydroxide, glycerol, and urea to tailor the surface functionalities of the raw AC sample with more N-containing functional moieties. They reported that DES synthesized using choline hydroxide and urea has shown superior CO<sub>2</sub> capture performance than other functionalized (choline hydroxide: glycerol) and raw AC samples has shown superior stability performed under a similar capture scenario and.

Furthermore, manipulating the activation pathway is crucial to synthesizing activated carbon with a higher specific surface area well-organized pore structure with a wealth of diverse functional groups. In this regard, the one-parameter factor at a time methodology has been studied extensively and mainly reported to determine the optimum activation conditions. However, with many process parameters, these single-dimensional searches become time-consuming and uneconomical as it overlooks the interaction between independent input parameters. In recent response surface methodology (RSM) has been employed to study optimizing the process parameters and their interaction between different process parameters. The RSM, coupled with the Box Behnken Design (BBD), has become an efficient statistical tool to synthesize optimized AC. Among all other statistical design tools, the RSM has shown the potential to be an efficient statistical tool for optimizing the activation conditions. It is a well-established design methodology that uses the least number of experiments but also

analyses the interaction between different process parameters towards the output response. Furthermore, it can avoid treatment combinations at an extreme range and can efficiently estimate if the points are at the centre or at the mid-points of the edges of the process (Lim et al., 2021).

This study aimed to synthesize AC from SCG-derived biochar (SCG-600) using CO<sub>2</sub>-induced physical activation to have desired elemental composition, well-developed textural properties, and availability of basic surface functional moieties. For this reason, activation parameters significantly influencing the physicochemical properties of AC were optimized using the RSM coupled with the BBD methodology. The influence and interaction of three activation input parameters, namely activation temperature (°C), holding time (min) and CO<sub>2</sub> flow rate (mL/min), were evaluated towards the specific surface area ( $S_{BET}$ ) and total AC yield (wt%). Furthermore, this study compares the specific surface area and CO<sub>2</sub> capture performance of torrefied and slow-pyrolysis derived AC samples synthesized under the optimized conditions. Consequently, the novelty of this study is that it involves DES functionalization of SCG-derived AC. The performance of optimized pristine and DES functionalized activated carbon were compared in terms of diverse and complimentary physicochemical analytical techniques such as ultimate analysis, ash content, textural characteristics ( $S_{BET}$ , pore-volume and pore-size distribution), TGA analysis, CO<sub>2</sub>-TPD analysis, XPS, XRD and SEM analyses. Moreover, the effects of adsorption temperature and CO<sub>2</sub> concentrations on the equilibrium CO<sub>2</sub> adsorption capacity were assessed to obtain a co-relationship between the adsorption capacity and the adsorption conditions under simulated feed conditions. The stability of AC samples was analysed through the multiple adsorption-desorption cycle technique. Finally, the as-synthesized optimum activated carbon and data from literature were compared and tabulated in terms of the CO<sub>2</sub> adsorption capacity.

### **7.3 Box-Behnken experimental design and statistical analysis**

Box-Behnken design (BBD) in Response surface methodology (RSM) is a strong mathematical and statistical tool, which is adopted to evaluate the relation between independent input process parameters and output responses for the determination of the optimum condition by reducing the number of experiments and thus the overall cost of experiment. Owing to its simplicity and feasibility, it provides meaningful conclusions with interactive effects of operating parameters on output responses (Das and Mishra, 2017). In this research, three independent factors and three level Box-Behnken design (BBD) method were utilized to investigate the correlation

between the combined and interaction effects of individual input process factors (activation temperature, holding time and CO<sub>2</sub> flow rate) to both responses (specific surface area and activated carbon yield). The factors and levels examined in this research to perform the CO<sub>2</sub> activation is shown in Table 7.1. The activation temperature, holding time and CO<sub>2</sub> flow rate were chosen as the crucial parameters to be optimized owing to their significant influence on the specific surface area ( $S_{BET}$ , m<sup>2</sup>/g) and AC yield (wt %). The input parameters were designated as A, B and C varied from low to high values and were coded as -1, 0 and +1 as summarised in Table 7.1. In this regard, A represented the activation temperature (600-800 °C), B the holding time (60–120 min) and C, the CO<sub>2</sub> flow rate (150–250 mL/min). The complete design matrix of in actual and coded values along with the responses (actual and predicted) is summarized in Table 7.2. The Three-factors-three level BBD model comprises a total of 17 runs among which 12 are factorial and 5 central runs. The responses chosen for this study were specific surface area ( $Y_1$ ) and AC yield ( $Y_2$ ) at atmospheric pressure and ambient temperature conditions.

**Table 7.1:** Factors and levels in CO<sub>2</sub> activation.

Factors	Name	Symbol	Unit	Coded levels		
				Low (-1)	Intermediate (0)	High (+1)
A	Activation temperature	X <sub>1</sub>	°C	600	700	800
B	Holding time	X <sub>2</sub>	min	60	90	120
C	CO <sub>2</sub> flow rate	X <sub>3</sub>	mL/min	150	200	250

## 7.4 Materials and Methodology

### 7.4.1 Biomass collection, slow pyrolysis, physical activation, and functionalization

The details regarding the biomass collection, pre-treatment, slow pyrolysis (chapter 6) and physical activation of SCG to synthesize physically activated AC, preparation of DES and functionalization using DES at different molar ratios are presented in detail in chapter 3. In this regard, the total yield of AC (wt.%) is calculated using Eq. 3.1, as stated in chapter 3. Also, the methodology adapted to execute this phase of the research is represented schematically in Figure 7.1.

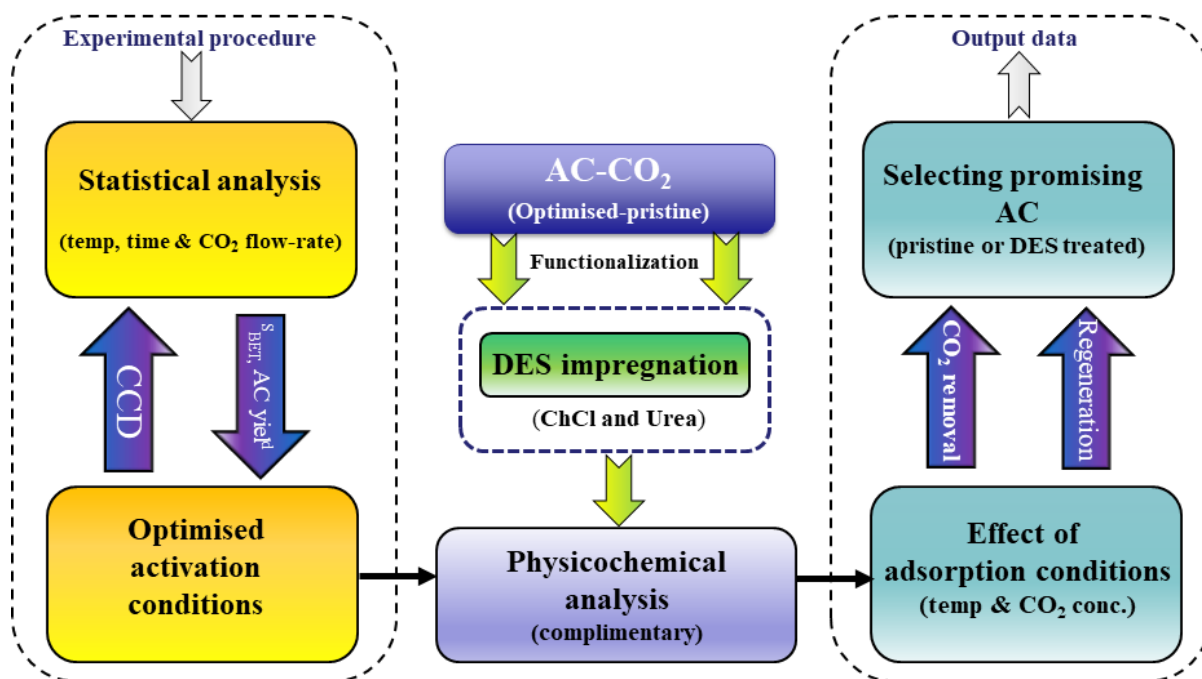


**Figure 7.1:** Methodology adapted to execute the research-objective 4.

#### 7.4.2 Breakthrough carbon dioxide adsorption performance

The details regarding the breakthrough CO<sub>2</sub> adsorption setup, breakthrough adsorption performance and selectivity are presented in chapter 3. Before assessing the breakthrough CO<sub>2</sub> capture performance, the fixed-bed reactor was loaded with 2±0.1 g of AC samples and pre-heated at 120 °C for 2 h under a nitrogen (N<sub>2</sub>) environment. This was followed by cooling down the reactor to the desired column temperatures (25-70 °C), and the feed gas was switched to a mixture of CO<sub>2</sub>/N<sub>2</sub> and the adsorption process continued until a point of saturation was reached when the CO<sub>2</sub> concentration in the outlet became equal to the CO<sub>2</sub> concentration in the inlet. CO<sub>2</sub> adsorption capacity in this study was determined using the equation stated in chapter 3 (Eq. 3.4). The adsorption process at 25 °C and desorption process at 120°C was repeated several times to assess their durability under multiple cycles. The AC samples were subjected to 15 consecutive cycles of adsorption and desorption to examine their ability to regenerate and stability.

### 7.5 Results and discussions

#### 7.5.1 Development of regression model equation

The complete three-factor-three-level design matrix for the activated carbon production with the respective experimental (actual) and predicted values of specific surface area (Y<sub>1</sub>) and AC

yield ( $Y_2$ ) are summarized in Table 7.2. The findings demonstrate that the specific surface area ( $Y_1$ ) ranges from 577-1224  $m^2/g$  while the AC yield ( $Y_2$ ) is found in the range of 55.3-64.8 wt. %. In this regard, the sequence of these experimental runs was randomly accomplished to avoid bias errors due to inessential factors. Also, the 5 central runs were performed to estimate the experimental errors and data reproducibility of the experimental runs (Das and Mishra, 2017). It can be observed from the Table 7.2, that the predicted values and the experimental findings are in proximity, demonstrating that the developed model could identify the co-relationship between the combined effect of the process parameters toward both the responses.

The sequential model sum of square formed the basis of selection of the appropriate model to predict the responses based on the highest order polynomial term in which the additional terms are not aliased but significant (Rashidi and Yusup, 2019). Accordingly, the findings revealed that quadratic models suitable to describe the responses to specific surface area ( $Y_1$ ) and AC yield ( $Y_2$ ) owing to the lower standard deviation and higher  $R^2$  value. The final empirical models for the responses  $Y_1$  (specific surface area) and  $Y_2$  (AC yield) are represented by the following Eqs. (7.1) and (7.2) in terms of coded factors.

$$Y_1 = 746.60 + 248.63A + 42.63B - 21.50C + 39.75AB - 51.50AC + 9.00BC + 75.33A^2 - 18.18B^2 + 40.58C^2 \dots\dots\dots(7.1)$$

$$Y_2 = 62.10 - 3.35A - 1.15B + 0.22C - 0.60AB - 5.4 \times 10^{-17}AC + 0.100BC - 1.23A^2 - 0.23B^2 - 0.17C^2 \dots\dots\dots(7.2)$$

Using the abovementioned equations, the predicted responses of the specific surface area ( $Y_1$ ) and AC yield ( $Y_2$ ) were evaluated. The type of effect each term has on the model is determined by observing the sign in front of each coefficient. Referred to the regression Eqs. (7.1) and (7.2), the plus sign in front of each coefficient revealed a synergistic or a positive impact, whereas the minus sign characterized the antagonistic or negative effect in the value of the responses ( $Y_1$  and  $Y_2$ ) (Das and Mishra, 2017). From the Eq. (7.1), it can be observed that the constant 746.60 was independent of any factors either independent or interactions. It can also be observed from Eq. (7.1) that the linear terms, A and B (except C), interactive terms AB and BC (except AC) and quadratic terms  $A^2$  and  $C^2$  (except  $B^2$ ) had a positive impact on the specific surface area (response:  $Y_1$ ) of the AC samples. The findings denote that with increasing the magnitude of the parameters with a positive sign would have a positive influence on the specific surface area of the AC samples. Similarly, from the Eq. (7.2) it was evident that the constant 62.10 was independent of any factors and the linear terms except C, interactive terms except

BC and the quadratic terms have negative influence in AC yield (response:  $Y_2$ ). Consequently, with increasing magnitude of the corresponding parameters with negative sign there will be a negative impact on the total AC yield (wt. %).

**Table 7.2:** Experimental and model predicted responses by varying the activation input parameters.

Std.	Run No.	Real Value			Coded Value			Specific surface area (m <sup>2</sup> /g)		Activated carbon yield (wt. %)	
		R1	R2	R3	C1	C2	C3	Actual	Predicted	Actual	Predicted
4	1	800	120	200	1	1	0	1146	1152.8	55.3	55.6
15	2	700	90	200	0	0	0	767	764.6	61.7	61.2
6	3	800	90	150	1	0	-1	1224	1202.1	57.4	57.1
17	4	700	90	200	0	0	0	747	752.3	62.5	63.1
5	5	600	90	150	-1	0	-1	611	602	63.5	63.8
1	6	600	60	200	-1	-1	1	577	570.3	64.8	64.5
2	7	800	60	200	1	-1	1	982	988	58.7	59.1
10	8	700	120	150	0	1	-1	827	842.1	60.2	60.3
14	9	700	90	200	0	0	1	757	764.6	61.8	62.1
3	10	600	120	200	-1	1	0	582	576	63.8	49.7
11	11	700	60	250	0	-1	1	729	714	63	62.9
12	12	700	120	250	0	1	1	833	817	60.8	60.9
16	13	700	90	200	0	0	0	768	762	62.5	62.1
9	14	700	60	150	0	-1	0	759	774.9	62.8	62.7
13	15	700	90	200	0	0	0	784	764.6	62	62.1
7	16	600	90	250	-1	-1	1	640	662	64	64.3
8	17	800	90	250	1	0	1	1047	1056.1	57.9	57.6

Note: (R: Real value) R1: Activation temperature; R2: Holding time; R3: CO<sub>2</sub> flowrate and (C: Coded value) C1: Activation temperature C2: Holding time and C3: CO<sub>2</sub> flow rate.



### 7.5.2 Statistical analysis

The model appropriateness and significance can be further validated through the analysis of variance (ANOVA) (Tang et al., 2013). In this regard, ANOVA was conducted to corroborate the stability of the quadratic model as suggested by the Design Expert® software (version 9.0.6) for both the responses specific surface area ( $Y_1$ ) and AC yield ( $Y_2$ ) and summarised in Tables (7.3) and (7.4), respectively. In ANOVA analysis, the statistical significance of the corresponding parameter can be evaluated from the model F value and p values. As can be observed in Table 7.3, for the response  $Y_1$ , the model F-value of 145.47 and  $\text{prob} > F = < 0.0001$  verified the sufficiency and appropriateness of the model suggested by the Design expert® software. In addition, there is 0.001% chance that an F value (145.47) this large could occur due to noise. Fundamentally, the significance of the model term is indicated by the p-value and the value indicates the probability in getting results closer to the actual data with a small difference. For instance, p-value of  $< 0.05$  indicates that the term is significant, otherwise the p-value higher than 0.1 means that the term is irrelevant. Thereby for  $Y_1$  it was observed from the Table 7.3, taking F and p values into consideration of the parameters for response  $Y_1$ , all linear parameters A (activation temperature), B (holding time) and C ( $\text{CO}_2$  flow rate), the two-level interactions of AB and AC (except BC) and quadratic interactions of  $A^2$  and  $C^2$  (except  $B^2$ ) are significant terms. The combined impact of activation temperature and holding time (AB) as well as the interactive effect of activation temperature and  $\text{CO}_2$  flow rate (AC) had a significant effect on the specific surface area ( $Y_1$ ). However, for response  $Y_1$ , the combined interaction between the holding time and gas flow rate (BC) were insignificant and had no significant impact on the response  $Y_1$ .

In addition, results of ANOVA in Table 7.4 (response  $Y_2$ , AC yield) confirm the sufficiency of the model with high F-value (64.10) and a very low probability value. The main effect of linear factors (A and B), double impact of the activation temperature and holding time (AB) and quadratic term ( $A^2$ ) are statistically significant terms for activated carbon yield ( $Y_2$ ). In addition, Lack-of-fit also determines the adequacy of the model and should be insignificant for the reliability of the model. As can be observed from the Tables 7.3 and 7.4, the F-value of lack-of-fit of 3.94 and 1.71 infers that the lack-of-fit is insignificant compared to the pure error. It also infers that there are 10.93% and 30.16% chance that lack of fit this large could occur due to noise for response  $Y_1$  and  $Y_2$ , respectively. Furthermore, based on the model F-value

(145.47), the ANOVA analysis of the response  $Y_1$  (specific surface area) is more significant over the model F-value (64.10) for response  $Y_2$  (total AC yield).

**Table 7.3:** Specific Surface area (response:  $Y_1$ ).

Source	Sum of squares	df	Mean square	F-value	p- value
<b>Model</b>	$5.629 \times 10^5$	9	62538.96	145.47	<0.0001 (Significant)
<b>A-Activation temperature</b>	$4.945 \times 10^5$	1	$4.945 \times 10^5$	1150.25	<0.0001
<b>B-Holding time</b>	14535.13	1	14535.13	33.81	0.0007
<b>C-Flow rate of CO<sub>2</sub></b>	3698	1	3698	8.61	0.0219
<b>AB</b>	6320.25	1	6320.25	14.70	0.064
<b>AC</b>	10609.00	1	10609.00	24.68	0.0016
<b>BC</b>	324	1	324	0.75	0.4141
<b>A<sup>2</sup></b>	23889.92	1	23889.92	55.75	0.0001
<b>B<sup>2</sup></b>	1390.87	1	1390.87	3.24	0.1151
<b>C<sup>2</sup></b>	6931.92	1	6931.92	16.12	0.0051
<b>Residual</b>	3009.45	7	429.92	-	-
<b>Lack of fit</b>	2248.25	3	749.42	3.94	0.1093 (Not significant)
<b>Pure error</b>	761.20	4	190.30		
<b>Cor Total</b>	$5.65 \times 10^5$	16			

Preferably, the large value of regression coefficient ( $R^2$ ), adjusted  $R^2$  (adj- $R^2$ ) and predicted  $R^2$  (pred- $R^2$ ) determines the model adequacy. The goodness of fit ( $R^2$  and adj- $R^2$ ) were evaluated further to validate the reliability of the model suggested by the software. Regression coefficient ( $R^2$ ) is a significant parameter that determines the extent of how well the model fits the observation data. Consequently, regression coefficient ( $R^2$ ) closer to unity is desirable to determine the goodness of fit. The model fit summaries presented in Table 7.5 demonstrates specifically the regression coefficient ( $R^2$ ) of the model for responses  $Y_1$  and  $Y_2$  were 0.995 and 0.988, respectively. The values of regression coefficient obtained for the responses ( $Y_1$ ) and ( $Y_2$ ) were very high to advocate for the significance of the model. The findings demonstrate the response variation of 99.5 % and 98.8% owing to the independent parameters. Although only 0.05% and 1.2% of the total response variation cannot be described by the fitted model. In this regard, the obtained  $R^2$  value indicates a good appropriateness of this model as it exceeds the minimum value of 0.8. In addition, the adj- $R^2$  of 0.9878 and 0.9726 were in reasonable agreement with the pred- $R^2$  of 0.9343 and 0.8839 for response of  $Y_1$  and  $Y_2$ . The findings also

confirm the good predictability of the model, owing to the difference between adj-R<sup>2</sup> and pred-R<sup>2</sup> is within 0.2.

**Table 7.4:** Activated carbon yield (response: Y<sub>2</sub>).

Source	Sum of squares	df	Mean square	F-value	p- value
<b>Model</b>	109.19	9	3.39	64.10	<0.0001 (Significant)
<b>A-Activation temperature</b>	89.78	1	10.65	474.31	<0.0001
<b>B-Activation time</b>	10.58	1	0.0004	55.89	0.0001
<b>C-Flow rate</b>	0.40	1	0.3267	2.14	0.1869
<b>AB</b>	1.44	1	0.0625	7.61	0.0282
<b>AC</b>	0.000	1	0.25	0.00	1.000
<b>BC</b>	0.040	1	0	0.21	0.6597
<b>A<sup>2</sup></b>	6.32	1	2.91	33.38	0.0007
<b>B<sup>2</sup></b>	0.21	1	0.0283	1.13	0.3238
<b>C<sup>2</sup></b>	0.13	1	0.9698	0.68	0.4364
<b>Residual</b>	1.32	5	0.0405		
<b>Lack of fit</b>	0.74	3	0.0608	1.71	0.3016 (Not significant)
<b>Pure error</b>	0.58	2	0.01		
<b>Cor Total</b>	110.52	14			

Furthermore, the reliability of the suggested model can be further assessed through the findings of additional influential parameters such as coefficient of variation (CV) and adequate precision (AP) as summarised in Table 7.5 for both the responses. Adequacy precision evaluates the ratio of signal to noise (S/N). For the suggested model to be adequate, AP should be equal to or above 4 is desirable (Mashhadimoslem and Izadpanah, 2022). AP responses for Y<sub>1</sub> and Y<sub>2</sub> noted were 39.73 and 26.97, respectively, which are far above the value of 4 which signifies an adequate signal, and the model could navigate the design space. Furthermore, the CV is also an influencing factor that determines the significance of the model suggested by the Design Expert® software. As can be seen from Table 7.5, the CV value of both responses (2.6 and 0.7) are less than 10%, and consequently, it recommends that this model is feasible and advocates the reproducibility of the experiment.

**Table 7.5:** The model fit summaries for the responses (specific surface area and activated carbon yield).

Model fit summaries	Specific surface area (Y <sub>1</sub> )	Activated carbon yield (Y <sub>2</sub> )
Standard Deviation (S.D)	20.7	0.4
Mean	810.6	61.3
Coefficient of variance (C.V %)	2.6	0.7
R-squared (R <sup>2</sup> )	0.9947	0.9880
Adj-R <sup>2</sup>	0.9878	0.9726
Pred-R <sup>2</sup>	0.9343	0.8839
Adequate Precision (AP)	39.73	26.97

### 7.5.3 Effects of process parameters on specific surface area

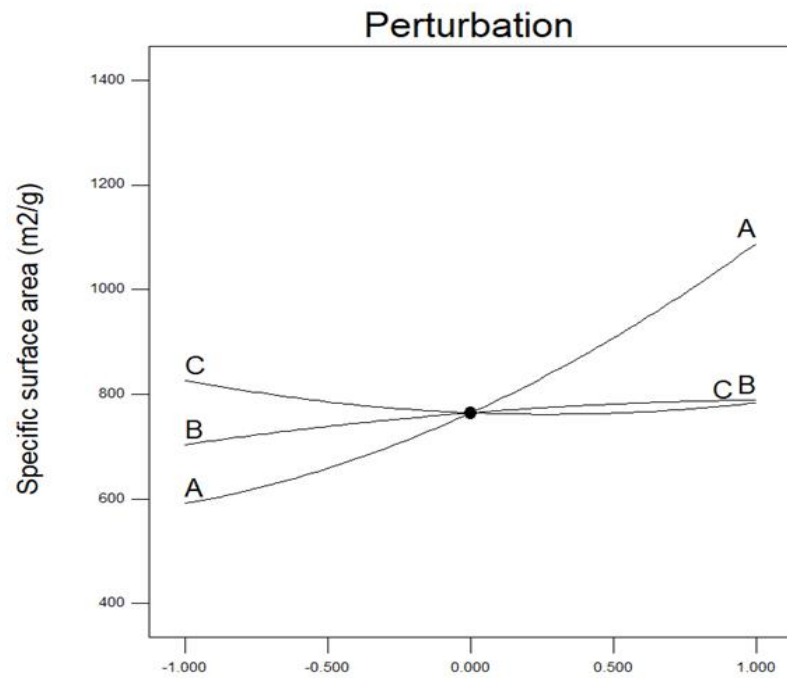
The effectiveness of activated carbon is determined by its specific surface area ( $S_{BET}$ , m<sup>2</sup>/g). Referring to ANOVA analysis for response specific surface area (Y<sub>1</sub>) in Table 7.3, the activation temperature is a significant parameter influencing the specific surface area with a p-value of <0.0001 and F-value of 1150.25 followed by holding time (F-value: 33.81) and CO<sub>2</sub> flow rate (F value: 8.61). The perturbation plot in Figure 7.2 (a) corroborates the findings and reveals the significant impact of activation temperature on specific surface area owing to the greatest slope. The specific surface area enhanced from 577 to 1224 m<sup>2</sup>/g with the increasing temperature from 600 to 800 °C. At higher activation temperature (800 °C) the endothermic reaction between the carbon-matrix and CO<sub>2</sub> intensifies. Hence, release of volatile matter, elimination reactions and dehydration reactions are accelerated leading to the pore development and higher specific surface area. Furthermore, the micropore development contributes to higher specific surface area is assisted by providing adequate holding time of around 70-90 min. A similar finding was also reported by Yuan et al., (2018), where they observed that with increasing the carbonization temperature to 900 °C, the specific surface area of the activated carbon sample increased in the range of 1003-1317 m<sup>2</sup>/g. On the other hand, extended holding time could cause widening of pores and results in reduced specific surface area. Similarly, intensifying the CO<sub>2</sub> flow rate to the highest point could negatively impact the specific surface area owing to the severe reaction between the carbon-skeleton and CO<sub>2</sub> resulting in pore shrinkage. In this regard, the maximum surface area of the AC sample in the

range of 982-1224 m<sup>2</sup>/g was obtained at the activation temperature of 800 °C and holding time of 60-120 min. The findings are further validated by the design matrix summarized in Table 7.2. In addition, referring to Table 7.3, the specific surface area was mostly impacted by the interactive interaction effect of activation temperature and holding time (AB). A 3-D response surface plot is presented in Figure 7.1 (b) that demonstrates the double effect of the significant factors activation temperature and holding time (A and B) on the response specific surface area (Y<sub>1</sub>).

#### **7.5.4 Effects of process parameters towards activated carbon yield**

The Figure 7.3 (a) displays the perturbation plot response plot of the AC yield (Y<sub>2</sub>) as a function of activation temperature (A), holding time (B) and CO<sub>2</sub> flow rate (C). From Figure 7.3 (a), it can be observed the activation temperature significantly influences the variation in AC yield owing to the steep curvature of the slope. On the other hand, hold-time and CO<sub>2</sub> flow rate are less sensitive towards the response Y<sub>2</sub> due to their moderate straight line. The AC yield (64.8 wt %) was maximum at the lowest temperature (600 °C) and reduces with the increasing temperature to 55.3 wt. % at 800 °C. Referring to Table 7.4, the findings can be further validated by the F-values (474.31) of the activation temperature which indicate that it is an influential parameter towards Y<sub>2</sub>. The decline in the product yield is a predictable observation and the plausible explanation of this could be accelerated dehydration and elimination reaction to kick off the volatile matter at higher temperature. Consequently, the amount of carbon yield is impacted and reduces. The carbon yield is also negative impacted by the extended holding time and intense CO<sub>2</sub> flow rate. Although, the influence is not as apparent as activation temperature as can be observed from the F-value of hold-time (55.89) and CO<sub>2</sub> flow rate (2.14) were not that apparent as can be seen from Table 7.4. This behaviour can be attributed to the excessive carbon burn-off and tar devolatilization with prolonged holding time and shrinkage in carbon matrix with intense CO<sub>2</sub> flow rate. A 3-D response surface plot is presented in Figure 7.2 (b) that demonstrates the interactive effect of the significant factors activation temperature (A) and holding time (B) on the response of AC yield (Y<sub>2</sub>). Rashidi and Yusup, (2021) has also reported a similar findings of declining product yield with increasing temperature, retention time and CO<sub>2</sub> flow rate.

(a)



(b)

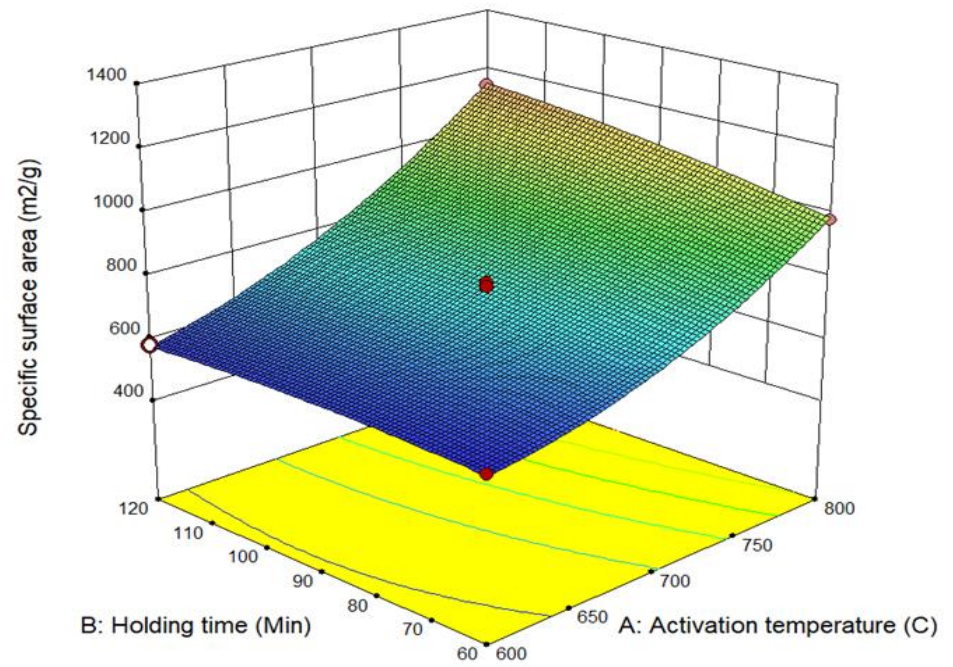
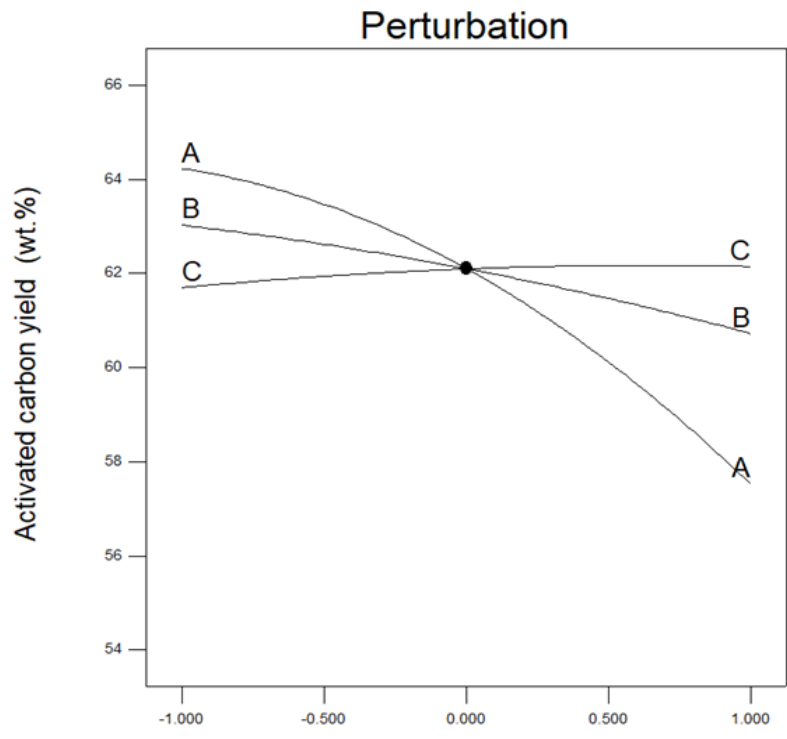


Figure 7.2 (a): Perturbation plot of specific surface area (response:  $Y_1$ ), (b): 3-D response of specific surface area ( $\text{CO}_2$  flowrate constant).

(a)



(b)

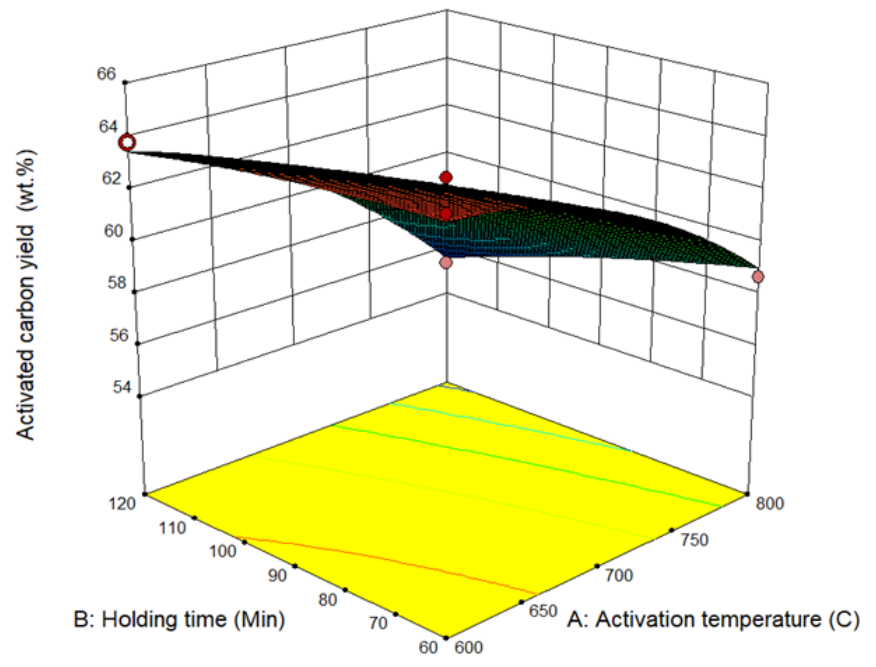


Figure 7.3 (a): Perturbation plot of activated carbon yield (response:  $Y_2$ ), (b): 3D response of AC yield ( $CO_2$  flowrate constant).

### 7.5.5 Process optimization and validation

Relatively excellent textural properties ( $S_{\text{BET}}$ ) and high AC yield are estimated to guarantee the effectiveness and economic feasibility of the mass activated carbon production process. Consequently, high specific surface area and high yield of AC is desirable from economic point of view. Optimizing the AC production condition is essential to determine the optimum process parameters to synthesize AC with larger specific surface area and high yield of AC. Although, optimizing the responses by applying the same conditions could be challenging owing to the difference in the region of interest of the process parameters. Hence, to determine the optimum activated carbon production conditions, the desirability approach in the Design-Expert® software was applied to meet the initial objective to generate high specific surface area with adequate AC yield ( $Y_2$ ). Further, a confirmatory experiment was performed to validate the reproducibility of the responses generated from the software. In this regard, the optimization criteria were set to maximize in the response values within the actual domain for specific surface area (577-1224  $\text{m}^2/\text{g}$ ) and AC yield in the range of (55.3-64.8 wt. %). Based on the analysis the following conditions were obtained as the optimised process conditions with the maximum value of the desirability function (0.95): activation temperature (800°C), holding time (90 min) and  $\text{CO}_2$  flow rate (150 mL/min). The validation runs at the optimum levels were performed and the findings are summarized in the Table 7.6. At the optimal condition, the predicted response values for surface area and AC yield were 1202.1  $\text{m}^2/\text{g}$  and 57.1 wt. %, respectively. It can be observed from Table 7.6, that the experimental findings are in closer proximity to the predicted values with relatively small differences of  $\pm 3.3$  and  $\pm 0.4$  for both the response  $Y_1$  and  $Y_2$ , respectively. Also, the errors associated with the AC yield ( $Y_2$ ) is less than the errors associated with the specific surface area ( $Y_1$ ). In this regard, Rashidi and Yusup, (2021) and Abioye et al., (2020) have reported a similar findings and have confirmed that to substantiate the model the difference between experimental findings and predicted value should not exceed 10%.

**Table 7.6:** Validation of actual data evaluated at the optimum activation conditions.

Response	Predicted value	Actual value	Standard deviation
Specific surface area ( $S_{\text{BET}}$ , $Y_1$ )	1202.1 $\text{m}^2/\text{g}$	1224 $\text{m}^2/\text{g}$	3.3
Activated carbon yield (AC, $Y_2$ )	57.1 wt. %	57.4 wt. %	0.4



### 7.5.6 CO<sub>2</sub> adsorption screening

Adsorption is a transitory phenomenon, and the extent of adsorption capacity of an adsorbent is dependent on the breakthrough adsorption time. The CO<sub>2</sub> adsorption test was performed to determine the breakthrough time and CO<sub>2</sub> adsorption capacity of DES functionalised AC samples. The breakthrough time along with the adsorption capacity are summarised the findings in Table 7.7.

**Table 7.7:** CO<sub>2</sub> adsorption performance of DES-treated AC samples.

Sample	Breakthrough time (min)	Adsorption capacity (mmol/g)
AC-DES-0.1	9	3.8
AC-DES-0.2	12	4.2
AC-DES-0.3	15	4.8
AC-DES-0.4	23	5.5

The findings from Table 7.7 depicts that the type of adsorbent influences the breakthrough adsorption time and adsorption capacity. As can be seen in Table 7.7, the longest breakthrough of 23 min was observed in DES-AC-0.4. The identified breakthrough time for other DES treated samples increased in the following order: AC-DES-0.1 (9 min), AC-DES-0.2 (12 min) and AC-DES-0.3 (15 min). The highest adsorption capacity of AC-DES-0.4 can be attributed to the availability of higher elemental N and active sites on the surface of the sample that significantly influences the CO<sub>2</sub> adsorption performance. Based on its longest breakthrough time and highest CO<sub>2</sub> adsorption capacity, AC-DES-0.4 was selected as the basis of functionalised AC sample for further comparative physicochemical analyses and CO<sub>2</sub> capture performance with pristine AC (AC-CO<sub>2</sub>) synthesized under the optimum activation conditions.

### 7.5.7 Evaluation between torrefied biomass and biochar derived activated carbon

This study assessed the impact of pre-thermal treatment conditions torrefaction (Mukherjee et al., 2022) and slow pyrolysis (Mukherjee et al., 2021a) before undergoing the two-stage physical activation technique. In this regard the textural characteristics and breakthrough CO<sub>2</sub> capture performance of the AC samples derived from the torrefied biomass (SCG-300-1) and biochar (SCG-600) samples were assessed. The specific surface area of the AC samples synthesized under the optimised activated conditions of 800 °C held for 90 min under CO<sub>2</sub> at 150 mL/min were 552 and 1224 m<sup>2</sup>/g from SCG-300-1 and SCG-600, respectively as the starting material. The surface area obtained using SCG-600 is almost twice the one synthesized

using SCG-300-1 and this behaviour could be attributed to the already well-developed microporous structure and surface area of SCG-600 and removal of volatiles after CO<sub>2</sub> activation. Furthermore, the breakthrough CO<sub>2</sub> adsorption capacity of the AC samples were examined at 25 °C and 1 atmospheric pressure in the presence of 15 vol% of CO<sub>2</sub> balanced by N<sub>2</sub>. The highest equilibrium adsorption capacities obtained were 2.87 and 4.34 mmol/g for TAC-CO<sub>2</sub> and AC-CO<sub>2</sub>, respectively. The difference in performance could be attributed to the well-developed porous structure and availability of high specific surface area of AC-CO<sub>2</sub>. Therefore, for further analyses, functionalization, and breakthrough CO<sub>2</sub> adsorption experiments, AC-CO<sub>2</sub> was selected as the promising AC sample prepared from slow pyrolysis of SCG compared to TAC-CO<sub>2</sub>.

### 7.5.8 Ultimate analysis and ash content

The ultimate analysis was performed to estimate the value of elemental carbon, hydrogen, nitrogen, and sulphur in AC samples derived from SCG using CHNS/O analyser that is summarised in Table 7.8. In this regard, the oxygen is calculated by the difference. The results of the analysis demonstrate that the hydrogen (H) and oxygen (O) content decreased in both the AC samples owing to the release of the hetero atoms in the form of gas at the high activation temperature and the findings are consistent with the findings reported by Hussin et al., (2021). Accordingly, an enhancement in carbon (C) and nitrogen (N) content and declining trend of H and O content has been detected upon CO<sub>2</sub> activation and DES impregnation process in the sample. Improved N content in DES treated sample would also indicate successful doping of N atoms in the carbon matrix. Enriched C and N content in AC-DES-0.4 sample would promote the CO<sub>2</sub> adsorption owing to the improved Vander Waals force and acid-base interactions (Hussin et al., 2021). Minimal ash content of the precursor as reported in the previous chapter (chapter 6) is favourable for optimal yield of AC production as depicted in Table 7.2. From Table 7.8, it is observed that the C and N content enriched in the range of 92.0 wt% to 92.5 Wt % and 2.8 wt% to 4.1 wt% for pristine and DES impregnated AC samples.

**Table 7.8:** Ultimate analysis and ash content of pristine and DES-treated AC samples.

Sample	Elemental analysis* (wt. %)					Ash content (wt. %)
	C	H	N	S	O*	
AC-DES-0.4	92.5	0.8	4.1	-N/A-	1.5	1.1
AC-CO <sub>2</sub>	92.0	1.2	2.8	-N/A-	2.3	1.7

\*O content: 100- (C +H +N +S+ Ash) wt. %

### 7.5.9 XRD analysis

X-ray diffraction (XRD) pattern of the AC samples from SCG is illustrated in Figure 7.4. The XRD-patterns have a substantial intensity in low-angle scatter, indicating the presence of pores in the AC samples as also evident from the SEM analysis presented in 7.5.14. The XRD pattern exhibited two broad diffraction peaks at about  $2\theta = 26^\circ$  and  $43^\circ$  as illustrated in Figure 7.4, which correspond to the (002) and (100) planes interlayer reflection of graphitic carbon in the AC samples (Mashhadimoslem and Izadpanah, 2022). Broad diffraction peak at  $26^\circ$  indicate that the AC samples have a semi-crystalline form structure in the local region and stacked aromatic layer form structure of carbon matrix and formation of graphitic carbon in the AC samples (Serafin et al., 2021). However, after the impregnation, the intensity of the diffraction pattern of DES treated AC samples reduced and gets weaker. Although, no significant difference could be observed in the XRD-diffraction pattern (Figure 7.4). The findings reveal the appearance of typical amorphous graphitic carbonaceous structure which could be due to the presence of stacked-disordered carbon rings in the carbon samples. It is favourable for  $\text{CO}_2$  adsorption owing to the development of well-defined porous structure as also evident from the textural characteristics. Hussin et al., (2021) also reported a similar finding on the development of amorphous and porous structure after the activation process and reduced peak-intensity after the DES modification of the AC samples.

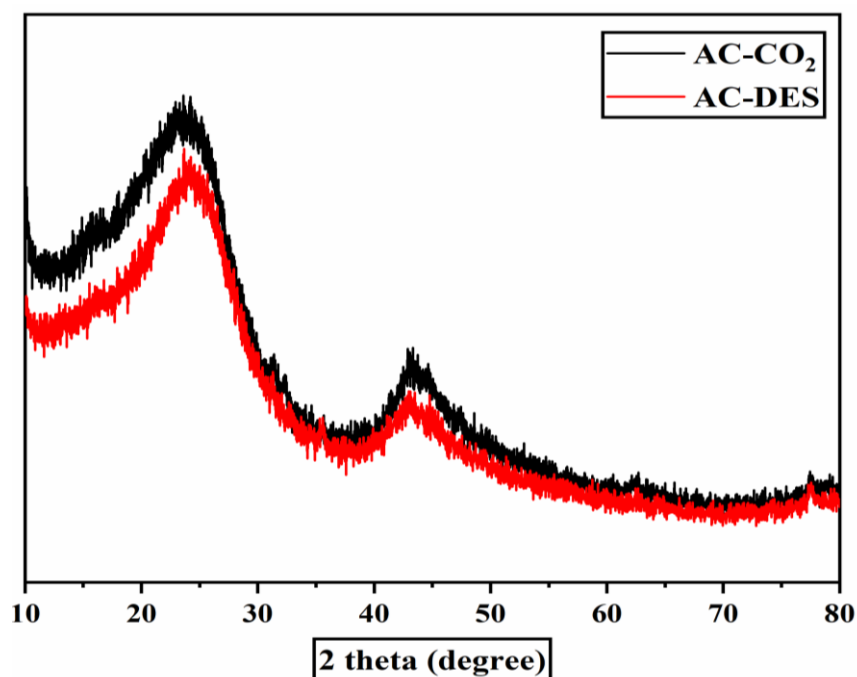


**Figure 7.4:** XRD analysis of pristine (AC-CO<sub>2</sub>) and DES treated AC sample.

### 7.5.10 Thermogravimetric analysis

The thermal degradation pattern of the selected AC samples was studied under the N<sub>2</sub> atmosphere, and the result is illustrated in Figure 7.5. The TGA analysis was conducted between 25 to 600 °C to identify the mass reduction of each carbonaceous samples. The TGA results of the AC samples indicated that activation occurs via a series of processes including removal of surface-bonded moisture and volatile matter, formation of carbon backbone and development of the porous network in the carbon matrix. Accordingly, the temperature profile of the samples is divided in three phases: (i) 25-100 °C, (ii) 100-400 °C and (iii) 400-600 °C. The first phase refers to the removal of moisture content from the carbonaceous samples. Minimal moisture content (1.3-3.4 wt %) for pristine and DES treated AC samples could be beneficial for CO<sub>2</sub> adsorption. Referring to Figure 7.5, onset temperature of both the AC samples were between 400 and 500 °C. An appreciable shift in the onset temperature in both pristine and DES treated AC samples compared to the precursor could be attributed to an accomplishment in de-volatilisation of the volatile components throughout the CO<sub>2</sub> activation process. It can be observed that after the CO<sub>2</sub> activation process at higher activation temperature and functionalization the thermal stability of the AC samples improved dramatically compared to raw SCG as reported in the previous chapter (chapter 6). As can be observed from Figure 7.5, the stability of the carbonaceous adsorbents can be clearly observed mainly in the phases (ii) and (iii). After CO<sub>2</sub> activation, both the AC samples exhibited negligible mass loss of 3.4 wt% and 4.3 wt% in the range of 100-400 °C and gradual mass loss of 8.9 wt. % and 12 wt.% at 400-600 °C for pristine and DES functionalised carbon samples. However, the AC-CO<sub>2</sub> displayed higher thermal stability compared to AC-DES-0.4 and that could be due to the evolution of vapour after the impregnation process. A similar finding was reported by Jawad et al., (2019), where they reported that compared to raw Malaysian Selantik-low rank coal the activated Selantik coal (SC) displayed higher thermal stability after the KOH activation than the starting precursor.

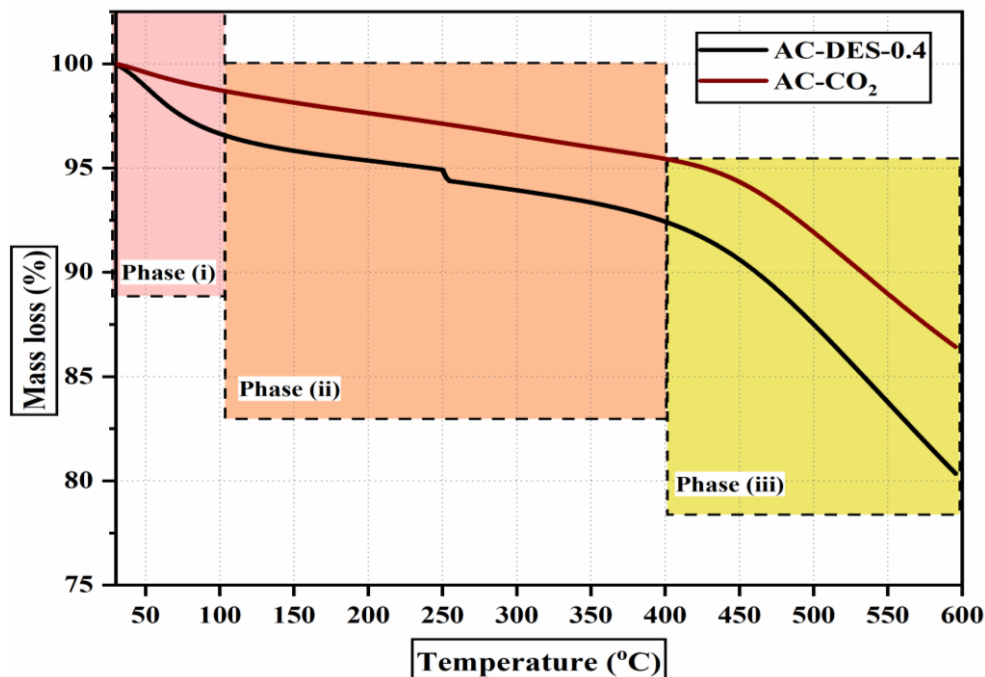


**Figure 7.5:** Thermogravimetric analysis of AC samples.

### 7.5.11 Temperature-programmed desorption (TPD)

Temperature programmed desorption (TPD) technique using CO<sub>2</sub> as the probe gas is constantly performed to investigate the surface basicity of carbonaceous materials. The temperature within which the programmed desorption by temperature of the AC samples performed were within the range of 30-800 °C. The temperature range was selected to avoid collapse of the structure of the carbonaceous samples. Figure 7.6 demonstrates the CO<sub>2</sub>-TPD evolution profiles the studied AC samples (pristine and DES functionalized samples). Following the guidelines reported by Wang et al., (2022) and Jiang et al., (2008) the distribution of basic sites in different strength of the AC samples were estimated and summarized in Table 7.9. Both the AC samples have demonstrated medium to strong basic sites as can be observed from the Figure 7.6.

**Table 7.9:** Distribution of basic sites and temperature range.

Strength	Temperature range (°C)
Weak basicity	50-132
Medium-strong basicity	177-500

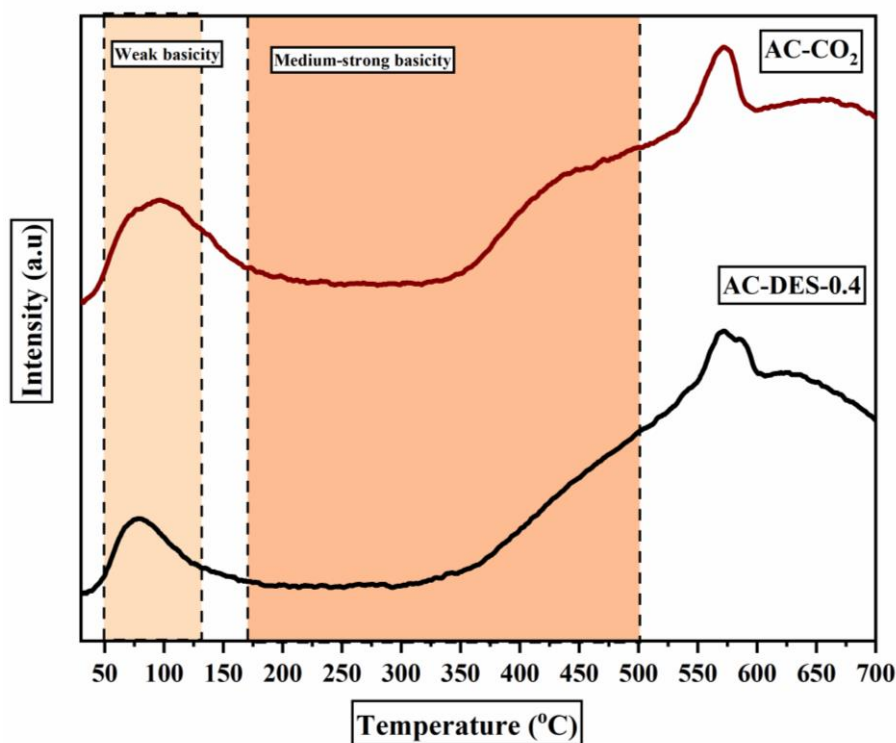


**Figure 7.6:** CO<sub>2</sub>-TPD profile of pristine and DES treated AC samples.

Furthermore, in the CO<sub>2</sub> spectra, multiple peaks were detected for both the carbonaceous samples. A peak at low range of temperature (200-400 °C) correspond to the decomposition of carboxylic groups and the intensity is less in both the samples. Peaks between the temperature ranges 450-650 °C correspond to the carboxylic anhydride and decomposition of lactones as previously reported by Wang et al., (2022). The amount of surface basicity in the corresponding carbonaceous samples were calculated based on the area of the CO<sub>2</sub>-TPD profiles. In this regard, the amount the total amount of CO<sub>2</sub> evolved during the desorption for DES treated AC (AC-DES-0.4) was 39 mmol/g and for pristine AC (AC-CO<sub>2</sub>) was 29.9 mmol/g. As expected, the surface basicity of DES treated AC sample improved considerably than pristine AC owing to the functionalization with the mixture of choline chloride and urea. The higher surface basicity is prioritized for the removal of CO<sub>2</sub> from flue gas stream owing to the enhanced Lewis acid to base interactions and is explained further through the adsorption performances.

### 7.5.12 Textural properties of the activated carbon samples

Nitrogen adsorption-desorption isotherm carried out at 77 K reveals the textural properties such as  $S_{\text{BET}}$ , pore volume, and average pore diameter of the ACs (pristine and DES impregnated) derived from SCG. The shape of the  $\text{N}_2$  adsorption-desorption isotherm could reveal the preliminary qualitative information of  $\text{N}_2$  adsorption on the porous structure and surface area of the AC samples. Figure 7.7 shows full  $\text{N}_2$  adsorption-desorption isotherm of the AC samples. The textural characteristics of the AC samples ( $S_{\text{BET}}$ , micropore area, total pore-volume, micropore-volume) and summarised in Table 7.10.

In accordance with the IUPAC classification, the  $\text{N}_2$  adsorption-desorption isotherm of the pristine AC sample (AC- $\text{CO}_2$ ) followed type IV isotherm with an H4 hysteresis loop, with closed fitting and it demonstrates the dominance of slit-shaped micropores over mesopores, formed by layered structure of slit-shaped micropores over mesopores, formed by layered structure (Shahkarami et al., 2016). In this regard, the hysteresis loop of the pristine AC sample is categorised as type H4 hysteresis loop that are associated with the presence of slit-pores in the micro-pore region and is reported for numerous AC samples (Dilokekunakul et al., 2020; Jawad et al., 2019). The findings reveal that the pristine AC investigated, exhibit microporous structure, pore size distribution mostly in the micropore range and improved pore-volume as also evident from the Table 7.10. Additionally, for the DES impregnated AC sample, the adsorption-desorption isotherm at a low relative pressure between 0.4 and 0.9 corresponded to type IV isotherm with a prominent but displayed considerably wide H4 hysteresis loop than pristine AC indicating the formation of mesopores along with micropores. Referring to the Figure 7.7, isotherm of AC- $\text{CO}_2$ , exhibit very narrow hysteresis loops, which is a trait of the presence of micropores mostly and AC-DES-0.4 has a pronounced hysteresis loop, indicating a higher number of mesopores.

It can be observed from Figure 7.7 that  $\text{N}_2$  adsorption increased significantly for both the AC samples, which indicated an increase in both the surface area and pore-volume as evident from the Table 7.10. As evident from the sharp  $\text{N}_2$  adsorption-desorption isotherm, AC- $\text{CO}_2$  has shown the highest surface area and pore volume with a  $S_{\text{BET}}$  of  $1224 \text{ m}^2/\text{g}$  and pore volume of  $0.63 \text{ cm}^3/\text{g}$ . The change in porous structure and formation of pores in the micro-pore range, mostly takes place during the activation process as it induces surface release of heteroatoms and volatiles to form more pores in the structure. However, the surface area of DES impregnated AC reduced significantly to  $1033 \text{ m}^2/\text{g}$  and pore-volume reduced to  $0.52 \text{ cm}^3/\text{g}$ .

The finding agrees with the result reported by Hussin et al., (2021). The decline in BET surface area and pore-volume of the DES treated AC sample could be attributed to the DES impregnation process followed by DES particles absorbed in the most internal part of the pores, thereby, blocking the fine pores of the impregnated AC sample as also observed in the SEM image (Figure 7.10). Although, many active sites were created on the functionalised AC surface which could accelerate the CO<sub>2</sub> capture performance under the post-combustion conditions. At this moment, adsorption of CO<sub>2</sub> is influenced by both the textural properties of the AC sample as well as on the reaction occurred between adsorbate (CO<sub>2</sub>) and the adsorbent surface (AC-DES-0.4).

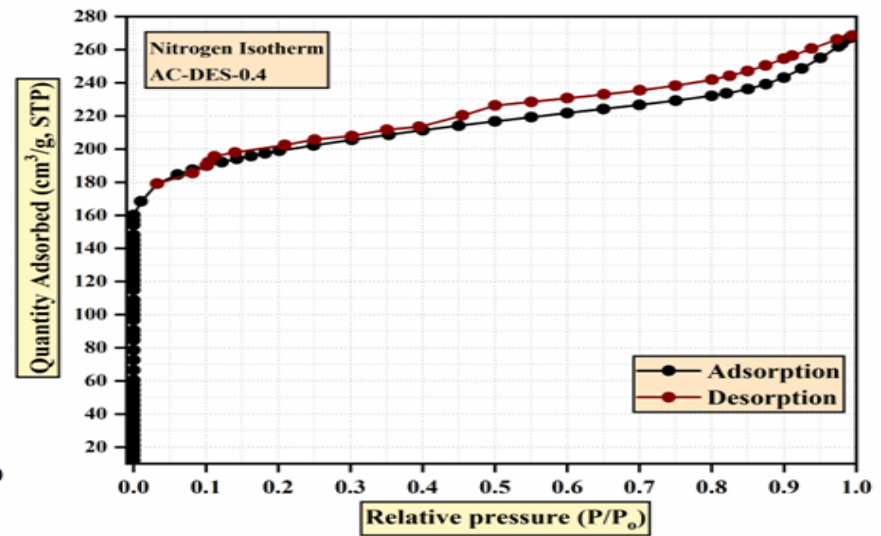
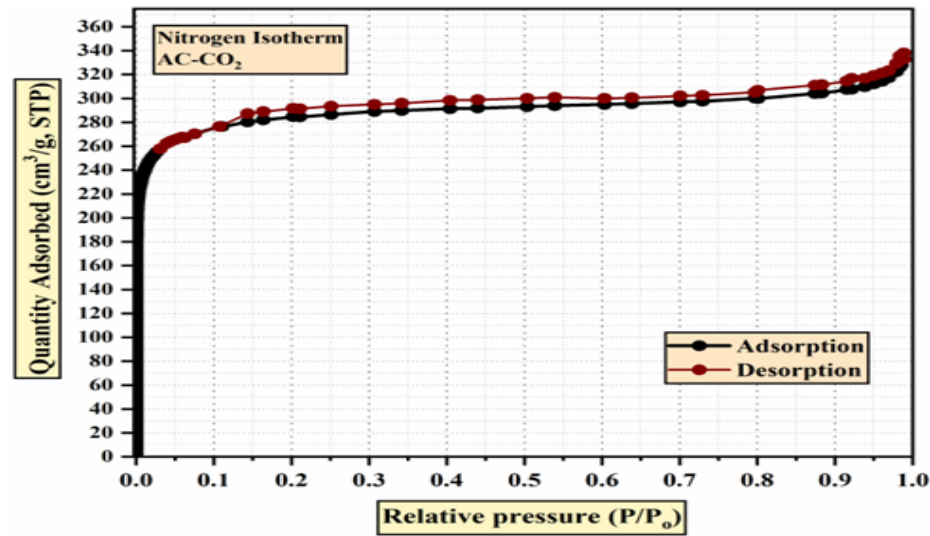
The pore-size distribution is one of the main characteristics of the AC when explored for gas separation process. The pores of activated carbon are divided into three major categories: micropores (diameters >2 nm), mesopores (diameters 2-50 nm) and macropores (diameters <50 nm) (Shahkharami et al., 2015). The average pore-size of pristine AC and DES treated AC were 1.70 and 2.14, respectively. Owing to the significant enlargement of the pore-space, the average pore-diameter in DES treated AC sample was higher and was in the mesoporous range compared to pristine AC sample. Furthermore, using nonlinear density functional theory (NLDFT) assuming slit pores, the pore-size distribution of the AC samples were obtained and is displayed in Figure 7.8 (a) and (b). The microporous nature of the pristine AC sample is further confirmed from the characters of pore-size distribution as shown in the Figures 7.8 (a). It can be observed that the main peak is centered at around the region of fine micropores (0.7 nm) with pore volume of 0.34 cm<sup>3</sup>/g while the rest of the pores were within the range of micropores 0.8-2.0 nm. Therefore, to obtain an adsorbent with desired textural characteristics in terms of S<sub>BET</sub> and pore-diameter, for gas separation process needs crucial monitoring while impregnating it with functionalizing agent.

**Table 7.10:** Textural properties of the activated carbon samples.

Sample	Specific surface area (S <sub>BET</sub> , m <sup>2</sup> /g)	Micro-pore surface area (m <sup>2</sup> /g)	Total pore volume (V <sub>T</sub> , cm <sup>3</sup> /g)	Average pore width (nm)
AC-CO <sub>2</sub>	1224	1055	0.63	1.70
AC-DES-0.4	1033	880	0.52	2.14

S<sub>BET</sub>; Specific surface area calculated by the BET method; V<sub>T</sub>; Total pore volume at P/P<sub>0</sub> of ~0.99; micro-pore surface area: t-plot method.





Sample	Specific surface area (m <sup>2</sup> /g)	t-plot micropore area (m <sup>2</sup> /g)	External surface area (m <sup>2</sup> /g)
AC-CO <sub>2</sub>	1224	1055	169
	Total pore volume (cm <sup>3</sup> /g)	t-plot micropore volume (cm <sup>3</sup> /g)	Pore-size (nm)
	0.63	0.54	1.7
Sample	Specific surface area (m <sup>2</sup> /g)	t-plot micropore area (m <sup>2</sup> /g)	External surface area (m <sup>2</sup> /g)
AC-DES	1033	868	165
	Total pore volume (cm <sup>3</sup> /g)	t-plot micropore volume (cm <sup>3</sup> /g)	Pore-size (nm)
	0.52	0.37	2.1

Figure 7.7: N<sub>2</sub> adsorption isotherms of AC samples: AC-CO<sub>2</sub> and AC-DES-0.4

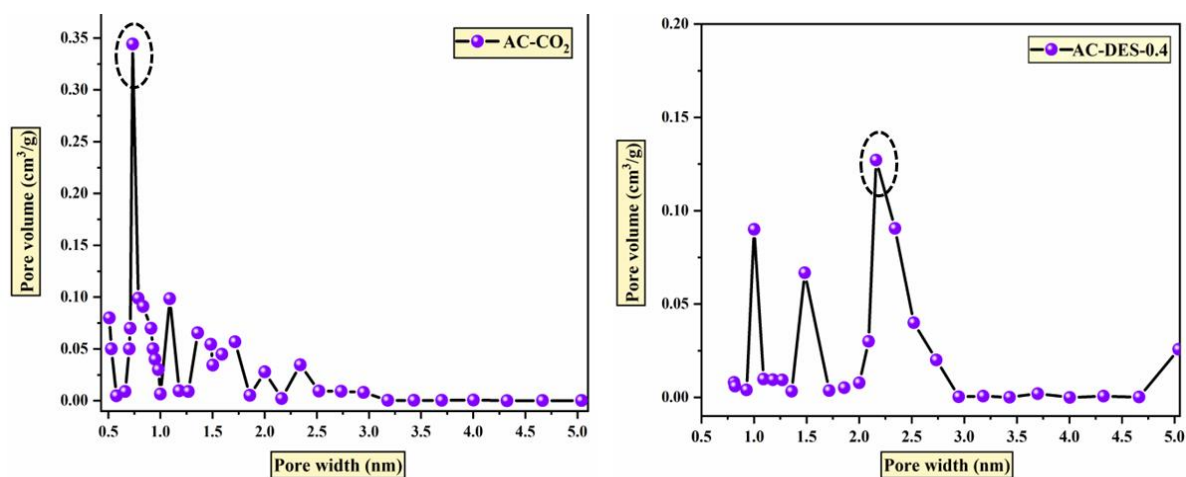


**Figure 7.8** (a): Pore size distribution of the AC-CO<sub>2</sub> sample and (b) Pore size distribution of AC-DES-0.4 obtained using N<sub>2</sub> at 77K

### 7.5.13 XPS analysis

N1s spectra of the AC samples were deconvoluted into three main peaks of different binding energies as shown Figures 7.9 (a) and (b) and are summarised in Table 7.10. The peak at 398.1-398.4 eV is assigned to pyridinic-type nitrogen (N-6), peak at 400.1-400.4 eV is assigned to Pyrrolic/pyridonic type nitrogen (N-5) and quaternary (N-Q) at 400.7-401.5 eV nitrogen, respectively (Wang et al., 2020). It can be seen from Table 7.11, that N-5 and N-6 are higher for the DES functionalised AC sample. Upon activation, the contribution of N-Q reduced for both the samples as evident from the Table 7.11 (Tiwari et al., 2017). Both pyridinic (N-5) and Pyrrolic (N-6) contributes to the basicity of the carbonaceous surface, but N-5 has more pronounced impact towards CO<sub>2</sub> capture owing to the lower binding energy and the ability to ameliorate the polarity of the carbon owing to its electron donation ability (Lim et al., 2016). The carbon's basicity is enhanced from the improved N-5 content and is prioritized as it provides more active surface sites for its Lewis basic nature to interact with CO<sub>2</sub> which Lewis acidic in nature (Tiwari et al., 2017). The Table 7.11 shows O1s spectra of samples (deconvoluted into three peaks). In this regard, the O1s spectra after deconvolution generated three peaks at 531.5 eV (O1), 532.5 eV (O2) and 533.6 eV for (O3) (Singh et al., 2019a). It is observed that O-1 which is assigned to carbonyl, ketone or lactone groups and O-2 which represents the ether or alcohol groups (C-OH) are maximum in AC-DES-0.4 compared to the pristine AC sample (Table 7.9). For enhanced CO<sub>2</sub> removal, presence of basic oxygenated species (O-1) and (O-3) are necessary and hence O-1 and O-3 could favour the CO<sub>2</sub> removal owing to the improved surface basicity of the DES treated AC sample. Therefore, it can be

observed that with improved basic nitrogenated species and oxygenated species AC-DES-0.4 is more basic in nature than AC-CO<sub>2</sub>.

**Table 7.11:** N1s and O1s Deconvoluted spectra of pristine and DES treated AC samples.

XPS (at. % of total O)			
Elements	Binding energy (eV)	AC-CO <sub>2</sub> (at. %)	AC-DES-0.4 (at. %)
O-1	531.2-531.5	44.9	63.3
O-2	532.3-532.5	49.8	52.4
O-3	533.3-533.6	-N/D-	6.3
XPS (at. % of total N)			
Elements	Binding energy (eV)	AC-CO <sub>2</sub> (at. %)	AC-DES-0.4 (at. %)
N-6	398-398.8	16.8	26.5
N-5	400.2-400.7	65.3	73.7
N-Q	401-401.5	15.5	9.4

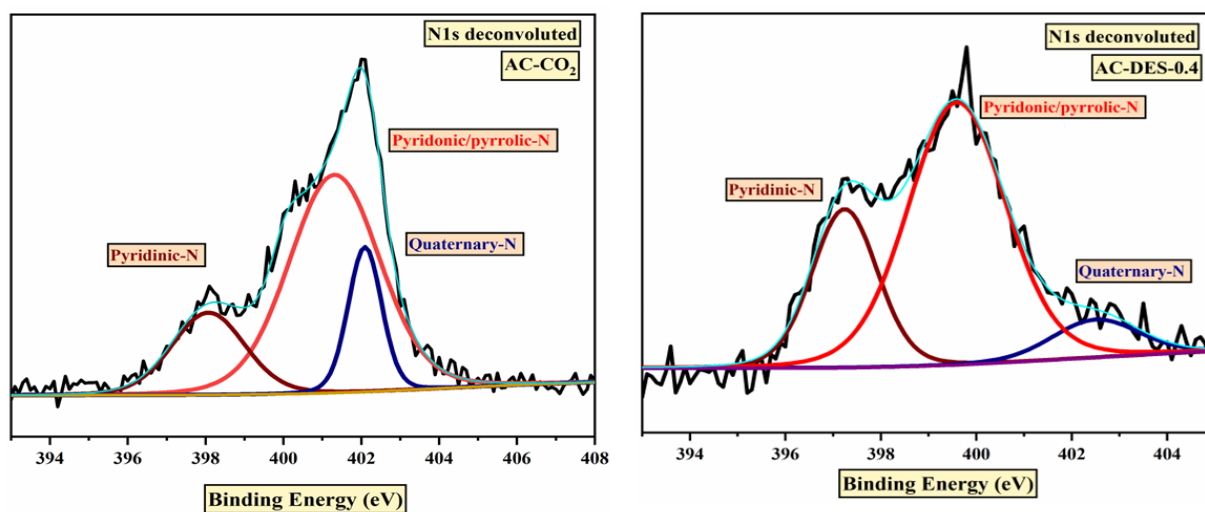


**Figure 7.9:** Deconvoluted N1s spectra of (a) pristine AC (AC-CO<sub>2</sub>) and (b) DES treated AC sample (AC-DES-0.4)

### 7.5.14 Surface Morphology

SEM analysis is mainly performed to investigate the sample's surface morphology and it also provides high-resolution image for estimating the surface fractures, flaws, pores shape and size. Figures 7.10 (a) & (b) shows SEM micrographs of pristine and DES treated AC samples, to examine and compare the change in surface morphology after the impregnation process. The SEM micrographs corresponding to pristine AC (Figure 7.10 (a)) and DES treated AC (Figure 7.10 (b)), showed a considerable difference with respect to their surface morphology and external surface texture pores. The surface morphology altered significantly and exhibited remarkable change on the surface after undergoing CO<sub>2</sub> activation. The SEM image for pristine AC in Figure 7.10 (a), clearly displays the irregular-shaped surface along with presence of many small fragments, cracks, and crevices. In Figure 7.10 (a), rough surface and high porous structure indicate the evolution of pores owing to the release of volatile-organic components and reaction between CO<sub>2</sub> and the carbon-matrix also assists in the ore-formation. Accordingly, presence of abundant pores of different size implies the enhancement in surface area and accounting for better porous characteristics in pristine AC, which eventually may have a significant impact on the CO<sub>2</sub> capture performance. On the contrary, after impregnating the carbon sample with DES, the external surface seems to be eroded and pores have been clogged owing to the agglomeration of DES on its external surface (Figure 7.10 (b)).

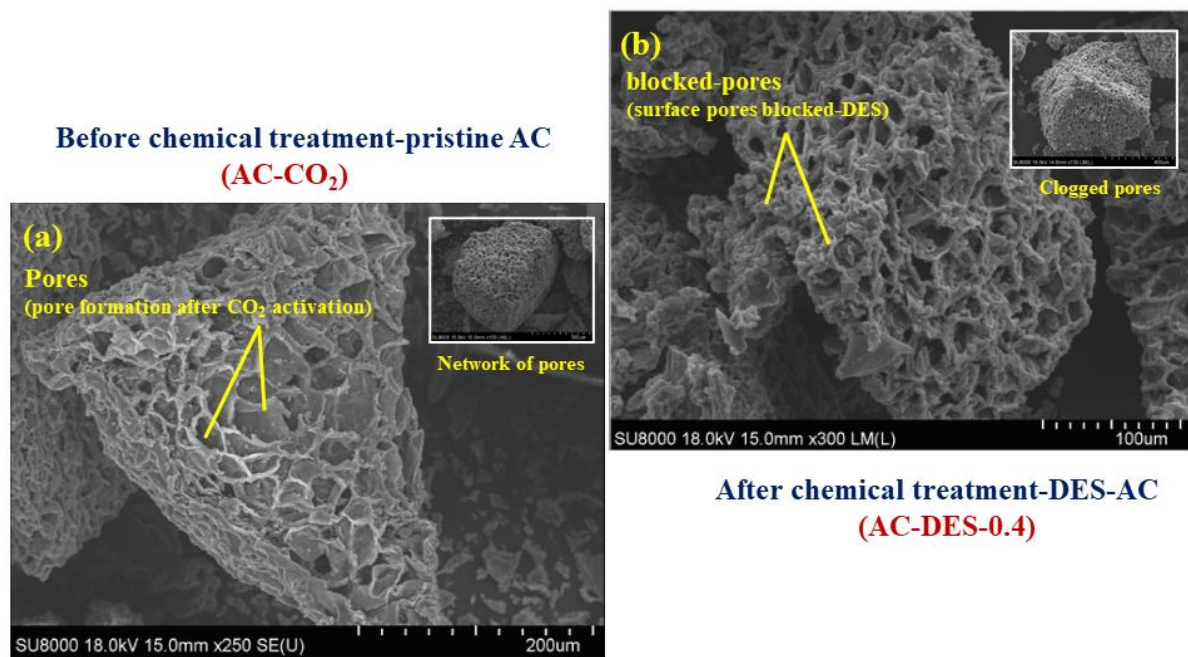


**Figure 7.10:** SEM analysis of (a) AC-CO<sub>2</sub> (before DES impregnation) and (b) AC-DES-0.4

Consequently, there is a fall in the pore-volume as evident from the findings of BET surface area analysis (7.5.12). The difference in SEM images of pristine and DES impregnated AC samples with respect to their surface morphology and arrangement of pores suggests the effectiveness of activation process and confirms the change in surface morphology after the DES impregnation.

## **7.6 Breakthrough CO<sub>2</sub> adsorption performance**

In general, breakthrough curve that appears as an S shaped curve is evaluated to determine the efficacy of a carbonaceous adsorbent in terms of the CO<sub>2</sub> removal capacity in a fixed bed reactor system under dynamic adsorption conditions. The breakthrough curve displays the breakthrough adsorption performance which depicts the co-relationship between the ratio of outlet to inlet CO<sub>2</sub> concentrations and the contact time. The breakthrough time ( $t_b$ ) and exhaustion time ( $t_E$ ) is defined as the contact time when the ratio of outlet to inlet CO<sub>2</sub> concentration reaches to 0.1 and 0.9, respectively.

### **7.6.1 Effects of column temperature on CO<sub>2</sub> capture performance**

To study the influence of adsorption temperature on breakthrough adsorption performance, the column temperature was varied inside a fixed bed reactor under the dynamic adsorption condition. The adsorption temperature was varied from 25 to 70 °C for both pristine and DES functionalised samples. All the breakthrough experiments were conducted under a fixed inlet CO<sub>2</sub> concentration (15 vol% in N<sub>2</sub>) and standard atmospheric pressure. The breakthrough CO<sub>2</sub> adsorption performance of the AC samples are summarised in Table 7.12. Furthermore, the breakthrough curves of pristine and DES functionalised AC samples as a function of varying column temperatures are displayed in Figure 7.11 (a) and (b), respectively. From Figure 7.11 (a) and (b) it can be observed that all samples have displayed the ability to capture CO<sub>2</sub> under all column temperatures. The initial outlet of CO<sub>2</sub> was not detected in the effluent stream mainly owing to the complete adsorption by the adsorbents. However, CO<sub>2</sub> was detected gradually with the progress of contact time and reached saturation where the adsorbent surface is saturated with adsorbate and the mass transfer zone (MTZ) reached the bed outlet (Singh et al., 2019a). As can be observed from Figure 7.11 (a) and (b), the breakthrough curve is broad at 25 °C for both the samples and show substantial CO<sub>2</sub> uptake but slope varied and becomes steeper with increasing column temperature to 70 °C due to faster adsorption rate along with reduced saturation time and adsorption capacity. Although the trend is similar for both the samples but adsorption capacity of pristine AC reduces drastically to 2.9 mmol/g in compared

to DES treated AC (3.7 mmol/g). The plausible explanation could be that at higher adsorption temperature (70 °C), the adsorption capacity drops drastically for pristine AC from 4.34 to 2.9 mmol/g because the influence of physisorption towards CO<sub>2</sub> adsorption reduces substantially. On the other hand, for the DES treated carbon the presence of basic nitrogenated functionalities is helpful in retaining the CO<sub>2</sub> adsorption capacity through chemisorption even under higher column temperature. Increase in column temperature also causes shift of breakthrough point towards lower saturation time indicating exothermic nature of the capture process. Even though, pristine AC displayed considerably higher S<sub>BET</sub>, but AC-DES-0.4 showed a substantial difference in CO<sub>2</sub> capture performance. In this regard, AC-DES-0.4 displayed superior breakthrough performance in terms of breakthrough adsorption time improved from 18.4 min to 23 min and equilibrium adsorption capacity from 4.34 to 5.5 mmol/g at 25 °C in a binary mixture of 15 vol % of CO<sub>2</sub> in N<sub>2</sub>. Multiple factors influenced the enhanced CO<sub>2</sub> capture performance of DES impregnated sample that includes developed textural characteristics, presence of elemental C and N, higher surface basicity due to the presence of N-5, N-6 functional species and basic-O functional groups (carbonyl/hydroxyl) that have promoted the interaction among CO<sub>2</sub> molecules (Lewis acid) through acid-base interactions or Vander Waals force of attractions. Similar observations were also reported by Hussin et al., (2021). The data of CO<sub>2</sub> adsorption performance of different biomass derived carbon materials were compared with the adsorbents prepared in this study as summarized in Table 7.13. Referring to Table 7.13, the adsorption capacities of both pristine and DES treated samples are comparable with the findings stated in the literature. From Table 7.13, it is evident that DES treated AC sample is a potential carbonaceous adsorbent synthesized from two-step physical activation and DES-impregnation technique that displayed a compatible CO<sub>2</sub> removal performance owing to the contribution of the well-developed textural characteristics and surface composition under a typical post-combustion scenario.

**Table 7.12:** Breakthrough CO<sub>2</sub> adsorption performance at varying column temperatures.

Sample	Temperature (°C)	Breakthrough time (min)	Exhaustion time (min)	Adsorption capacity (mmol/g)
<b>Temperature: varying column temperatures; CO<sub>2</sub> conc: fixed at 15 vol % in N<sub>2</sub></b>				
<b>AC-CO<sub>2</sub></b>	25	18.4	23	4.34±0.37
	35	13.8	20.9	4.2±0.42
	45	10.9	16.7	3.8±0.51
	55	8.3	11.8	3.1±0.63
	70	5.5	10.4	2.9±0.11
<b>Temperature: varying column temperatures; CO<sub>2</sub> conc: fixed at 15 vol % in N<sub>2</sub></b>				
<b>AC-DES-0.4</b>	25	23	30.3	5.5±0.13
	35	17.2	22.4	5.3±0.73
	45	12.8	19.3	4.9±0.55
	55	9.7	16.4	4.2±0.25
	70	6.1	12.5	3.7±0.66

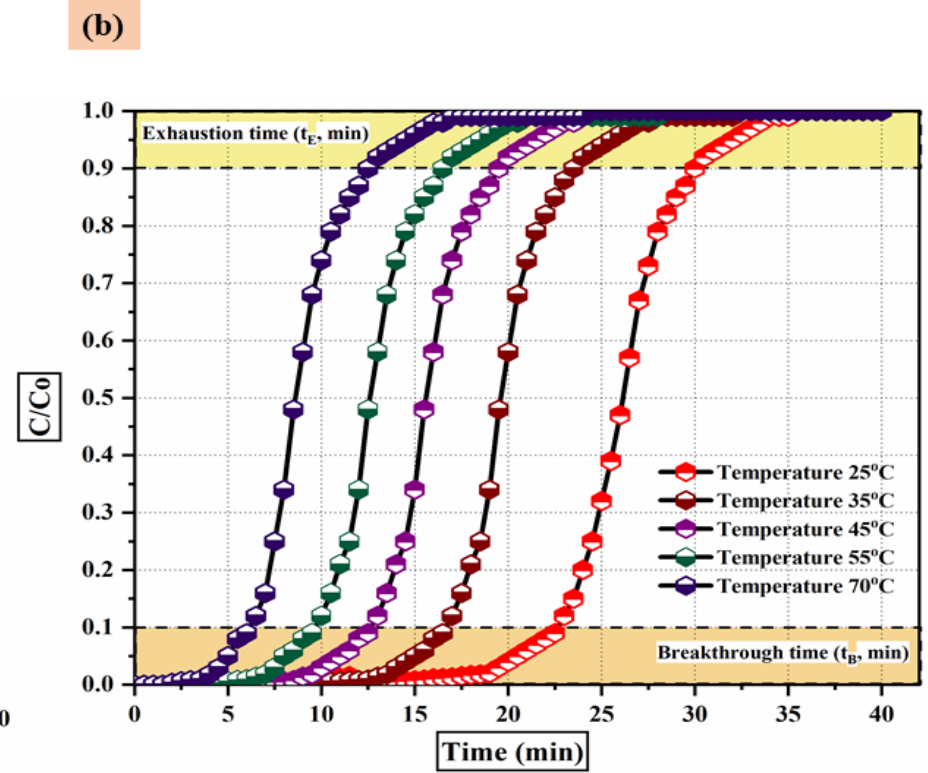
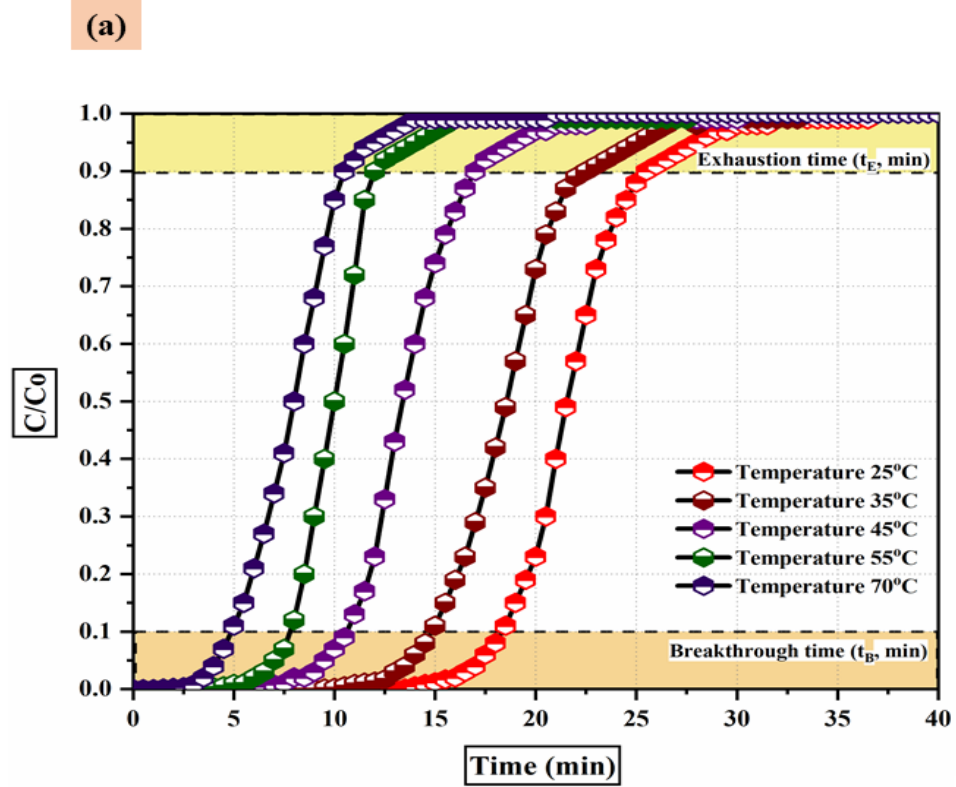


Figure 7.11: Effect of adsorption temperature on CO<sub>2</sub> capture performance (a) AC-CO<sub>2</sub> and (b) AC-DES-0.4.



**Table 7.13:** CO<sub>2</sub> removal performance of various carbon-based adsorbents reported in the existing literatures (under dynamic conditions).

Carbon sorbents	Activating/functionalizing agents	Adsorption capacity at 25 °C and 1 bar (mmol/g)	Reference
<b>SCG-600 (biochar)</b>	N <sub>2</sub>	2.8 (30 °C)	This study
<b>TAC</b>	CO <sub>2</sub>	2.87	
<b>AC-CO<sub>2</sub></b>	CO <sub>2</sub>	4.34	
<b>AC-DES-0.4</b>	Choline chloride and urea (DES-1:0.4)	5.5	
<b>Palm kernel based activated carbon</b>	CO <sub>2</sub>	2.3	(Rashidi and Yusup, 2019)
<b>Coffee grounds</b>	Ammoxidation (melamine) + KOH	2.67	(Liu and Huang, 2018)
<b>Date fruits (seeds)</b>	CO <sub>2</sub>	3.3	(Ogungbenro et al., 2017)
<b>Coconut shell</b>	CO <sub>2</sub>	1.8	(Rashidi et al., 2014)
<b>Paper mill sludge derived biochar (PMS)</b>	N <sub>2</sub>	0.67	Igalavithana et al., (2020)
<b>Pine sawdust (PSS) derived activated carbon</b>	Steam	0.73	
<b>Bamboo</b>	CO <sub>2</sub>	2.52	(Dilokekunakul et al., 2020)
	Urea	2.63	
<b>Activated carbon</b>	Nitrogen doped	5.4	(Sethia and Sayari, 2015)
<b>Birch activated carbon</b>	Steam	4.06	(Kishibayev et al., 2021)
<b>CACs-2-800 (AC derived from coffee grounds at 800 °C)</b>	KOH	3.8	(Wang et al., 2020)
<b>Petroleum coke and palm shell</b>	K <sub>2</sub> CO <sub>3</sub>	2.4	(Rashidi and Yusup, 2021)
<b>Activated carbon from whitewood</b>	Steam and MgO	49 mg/g (1.1 mmol/g)	(Shahkarami et al., 2016)
<b>Palm shell activated carbon</b>	Choline hydroxide and urea	37.2 mg/g (0.9 mmol/g)	(Hussin et al., 2021)
<b>Coconut shell-based AC</b>	Char + urea, and KOH	4.8	(J. Chen et al., 2016)

<b>WDC-01 (packaging waste derived AC)</b>	KOH (varying ratios)	2.4	(Idrees et al., 2018)
<b>WDC-02 (packaging waste derived AC)</b>		3.1	
<b>WDC-03 (packaging waste derived AC)</b>		4.2	
<b>WDC-04 (packaging waste derived AC)</b>		3.9	
<b>Pine nut-shell derived AC</b>	KOH	5.0	(Deng et al., 2014)
<b>Urea formaldehyde resin</b>	N-doped	3.2	(Liu et al., 2014)

### 7.6.2 Effects of inlet CO<sub>2</sub> concentration on CO<sub>2</sub> capture performance

The Figure 7.12 (a) and (b) displays the effect of initial CO<sub>2</sub> concentrations in the range of 10-20 vol% on the breakthrough adsorption performance carried under a fixed column temperature of 25 °C and at standard atmospheric pressure conditions. It can be observed from Table 7.14, that with increasing the CO<sub>2</sub> volume fraction from 10 to 20 vol%, the breakthrough point appears earlier owing to the faster bed saturation. Although, the adsorption capacity improves with the increasing CO<sub>2</sub> concentration. For instance, when the initial CO<sub>2</sub> concentration increased from 10 to 20 vol%, the adsorption capacity of AC-CO<sub>2</sub> increased from 4.17 mmol/g to 4.92 mmol/g and for AC-DES-0.4 it increased from 5.2 mmol/g to 6.03 mmol/g, respectively (Table 7.14). The plausible explanation of this enhancement in adsorption capacity and reduced breakthrough time with the increasing inlet CO<sub>2</sub> concentration to 20 vol% can be attributed to the fall in the diffusion coefficient in the system. Reduced CO<sub>2</sub> concentration significantly influences the CO<sub>2</sub> removal efficacy owing to the increased concentration gradient resulting in slower saturation of the system and increased exhaustion time. Also, at higher CO<sub>2</sub> concentration (20 vol %), large number of active sites on the surface of the adsorbent are participating, thus, limiting the adsorbent bed capacity, whereas lesser active sites are involved at lower CO<sub>2</sub> concentration. A similar finding was reported by Tan et al., (2014) who stated that with increasing the CO<sub>2</sub> concentration the breakthrough time is reduced producing the highest adsorption capacity.

**Table 7.14:** Breakthrough CO<sub>2</sub> adsorption performance at varying inlet concentrations of CO<sub>2</sub>.

Sample	Inlet conc. (CO <sub>2</sub> , % v/v)	Breakthrough time (min)	Adsorption capacity (mmol/g)	Exhaustion time (min)
AC-CO <sub>2</sub>	<b>Column temperature fixed at 25 °C (under dynamic conditions, CO<sub>2</sub>/N<sub>2</sub>)</b>			
	10	23.4	4.17±0.22	28.1
	15	18.4	4.34±0.37	23
	20	14.8	4.92±0.41	18.7
AC-DES-0.4	<b>Column temperature fixed at 25 °C (under dynamic conditions, CO<sub>2</sub>/N<sub>2</sub>)</b>			
	10	27.6	5.2±0.17	34.8
	15	23	5.5±0.13	30.3
	20	15.5	6.03±0.25	21.9

\*Standard deviation for AC-CO<sub>2</sub> were within ±0.5 and for AC-DES-0.4 were within ±0.30.

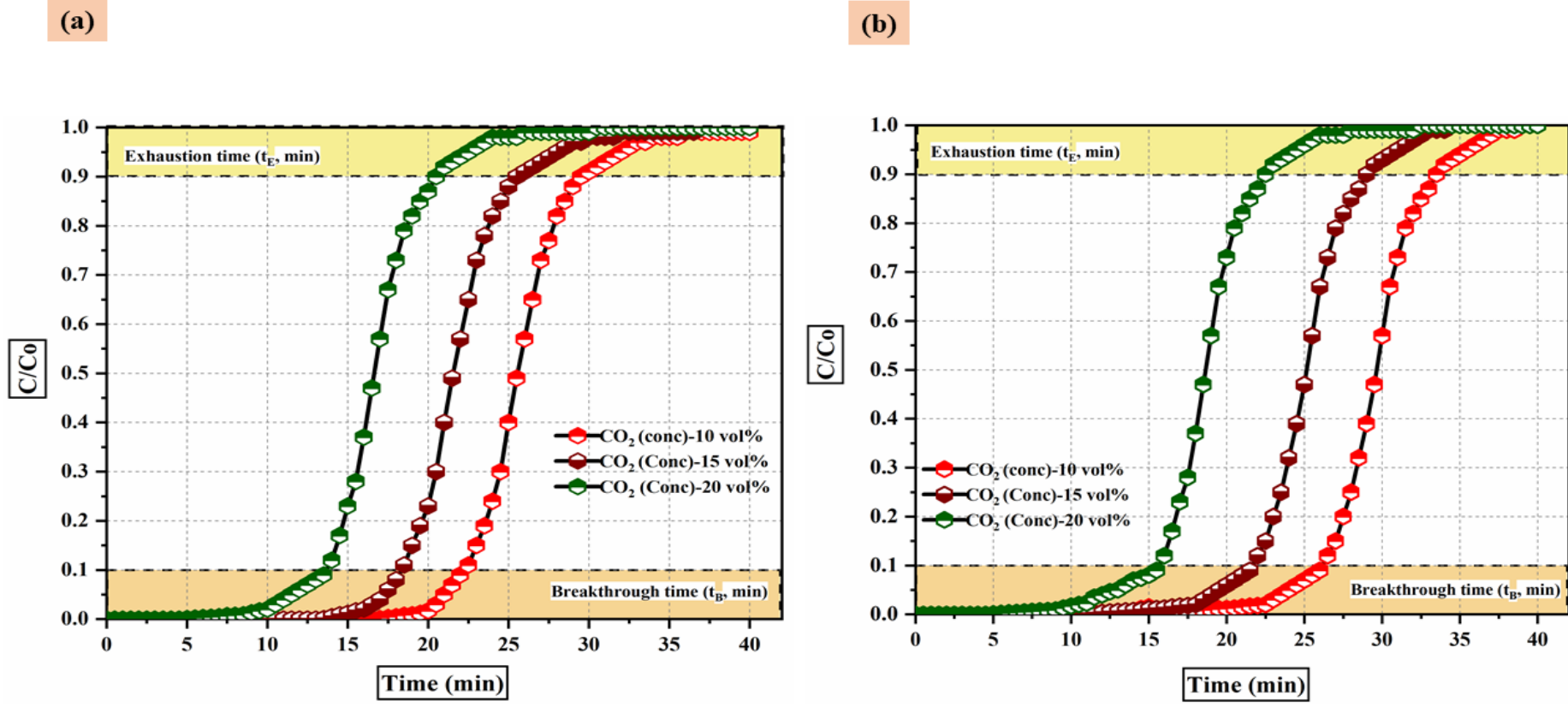


Figure 7.11: Effect of CO<sub>2</sub> concentration of adsorption performance (a) AC-CO<sub>2</sub> and (b) AC-DES-0.4.

### 7.6.3 Selectivity

The adsorption selectivity of binary component gas mixtures ( $\text{CO}_2/\text{N}_2$ ) of the pristine and DES AC samples were evaluated at 25 °C and 1 bar. The mixtures studied in this regard is 15 vol% of  $\text{CO}_2$  balanced in  $\text{N}_2$  (Sethia and Sayari, 2015). The adsorption selectivity calculated of the gas pair  $\text{CO}_2/\text{N}_2$  (mixture of 15 vol% of  $\text{CO}_2$  with 85 vol% of  $\text{N}_2$ ) were ( $S_{\text{CO}_2/\text{N}_2}$ ) 48.7 and ( $S_{\text{CO}_2/\text{N}_2}$ ) 60.2 for pristine and DES treated samples, respectively. Irrespective of the AC sample type, the  $\text{N}_2$  adsorption capacity was comparatively much smaller than  $\text{CO}_2$ . The findings revealed that DES treated AC sample showed very high selectivity and a substantial difference in the adsorbed amount of  $\text{CO}_2$  than  $\text{N}_2$  adsorption mainly owing to the presence of basic N functional moieties (pyridine or Pyrrolic) and oxygenated functional species (carbonyl or hydroxyl) as confirmed from the XPS analysis. The surface functionalities could improve the  $\text{CO}_2$  over  $\text{N}_2$  selectivity owing to the acid-base or stronger electrostatic interaction (Igalavithana et al., 2020). Consequently, by using DES treated sample,  $\text{CO}_2$  molecule can be selectively separated under the dynamic flow condition ( $\text{CO}_2/\text{N}_2$ ) under a typical post combustion condition.

### 7.6.4 Multiple adsorption-desorption study

Examining the regeneration ability of a saturated adsorbent is a significant aspect to stimulate the adsorption capacity and in determining economic feasibility. To exhibit superior regeneration ability, the adsorbent should display stability to  $\text{CO}_2$  adsorption in multiple adsorption-desorption cycles. In this regard, to study the regeneration stability of the AC samples (pristine and DES treated AC samples), 15 consecutive adsorption-desorption experiments were performed using a binary mixture of  $\text{CO}_2/\text{N}_2$  and the findings is displayed in Figure 7.13. Referring to Figure 7.13, the  $\text{CO}_2$  adsorption capacity of pristine and DES functionalised AC samples over 15 cycles. Figure demonstrates that the adsorption capacity for pristine AC at the first cycle was at and it reduced to at the second cycle. The adsorption capacity displayed a declining trend till the tenth cycle and remained stagnant at 3.8 mmol/g till the 15<sup>th</sup> cycle. Meanwhile, on the other hand, the DES impregnated AC displayed a good regeneration ability with insignificant decline in the adsorption capacities till the 15<sup>th</sup> cycle. In this regard, DES-AC showed a superior performance by retaining approximately 92% of the original adsorption capacity compared to pristine AC that displayed 89% retention in adsorption capacity after 15 cycles of consecutive adsorption-desorption. However, DES treated AC retained its adsorption capacity till six consecutive cycles but displayed fall in the

adsorption capacity and can be mainly owing to the presence of enriched nitrogen functional species, entire adsorbed CO<sub>2</sub> could not be desorbed from the surface. The maximum adsorption capacities of DES treated sample for the 1<sup>st</sup>, 2<sup>nd</sup> and 15<sup>th</sup> cycles were 5.5, 5.46, 5.06 mmol/g, respectively. However, both the samples displayed a declining trend in the adsorption capacities with the progress of multiple regeneration cycles which can be mainly attributed to the incomplete desorption, damage to pore structure in the carbon matrix to some extent or decomposition of the active sites.

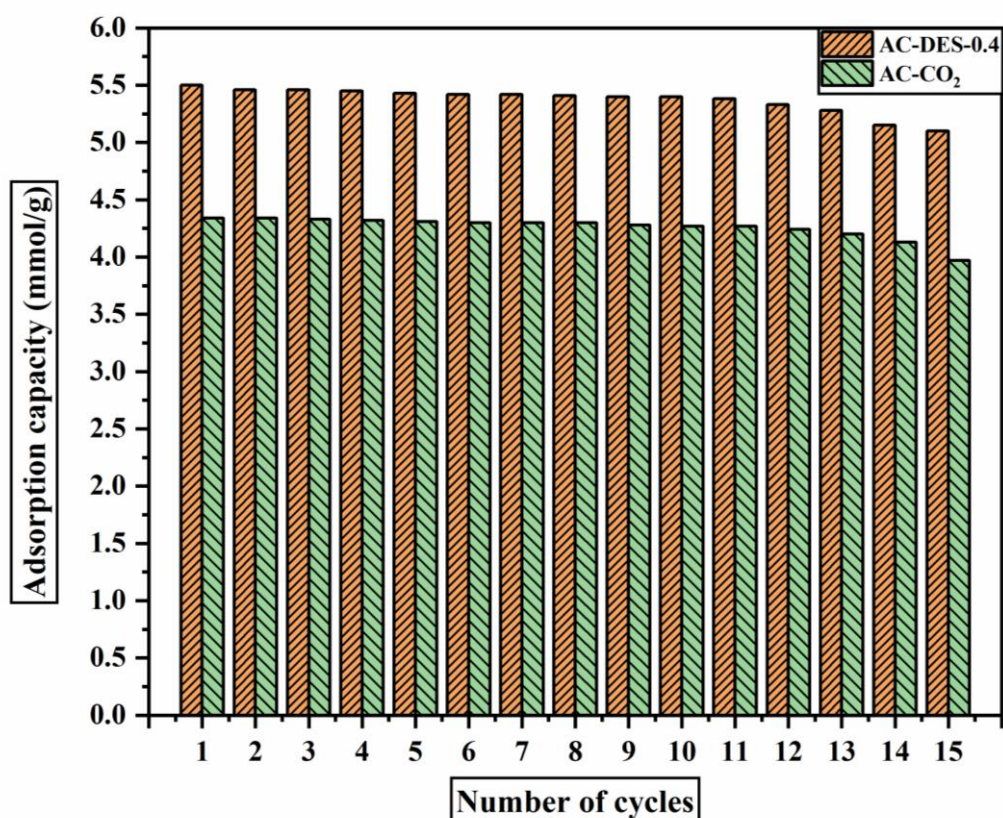


**Figure 7.13:** Multiple adsorption and desorption cycle of the AC samples.

## 7.7 Conclusions

In summary, pristine and DES treated AC samples prepared by CO<sub>2</sub> activation and DES impregnation is investigated in this study. Firstly, a series of SCG derived AC samples were prepared by undergoing two-stage physical activation using CO<sub>2</sub> as the activating agent. The activated carbon (AC) production conditions were optimized through the Box Behnken Design (BBD) technique in terms of specific surface area and AC yield. In this research, both the responses were evaluated based on the activation temperature (600-800 °C), holding time (60-

120 min) and CO<sub>2</sub> flow rate (150-250 mL/min). From the ANOVA analysis, it was evident based on the F-value and p-value that activation temperature significantly influenced both the responses. Based on the desirability function, the optimum activated carbon production condition was obtained at 800 °C, 90 min and 150 mL/min with desirability of 0.95. Maximum S<sub>BET</sub> of 1224 m<sup>2</sup>/g and yield of 57.4 % were obtained at the optimum conditions. Furthermore, the development of environmentally friendly and non-toxic activated carbon agent is imperative in terms of sustainability. Therefore, non-toxic, and biocompatible natural deep eutectic solvent was prepared by mixing choline chloride and urea at different molar ratios to functionalize the surface of pristine AC sample and incorporate basic functional groups on its surface. It was observed that, DES treated AC sample had comparatively the lower S<sub>BET</sub> (1033 m<sup>2</sup>/g), which is attributed to its recalcitrant chemical structure difficult to decompose even at lower-thermal treatment conditions as well as chemicals clogged the porous structure. The presence of nitrogenated functional species was confirmed using the ultimate and XPS analyses as the diagnostic analytical techniques. The presence of nitrogenated species mainly N-5 is favourable for high adsorption capacity of acidic CO<sub>2</sub> molecules under dynamic adsorption conditions. The superior performance of DES functionalised AC was attributed to the presence of basic oxygenated (carboxylates, lactones, and phenols) and nitrogenated functional groups (N-5/N-Q or N-6) on its surface as well as the porous structure and morphology available that accelerated the removal of acidic CO<sub>2</sub> molecules under dynamic adsorption conditions. The noticeably longer breakthrough time and higher CO<sub>2</sub> adsorption capacity (5.5 mmol/g) of DES treated AC sample can be attributed to the combination of developed textural properties, porous structure, morphology, and surface chemistry. Furthermore, the stability of DES treated samples displayed in multiple regeneration study represent it as a promising and potential carbonaceous adsorbent with an effective retention of approximately 92% after 15 cycles of consecutive adsorption and desorption performance. Compare to the conventional carbonaceous adsorbents' CO<sub>2</sub> removal performance reported in the literature and its functionalization broadly stated in the literature, DES impregnated AC sample prepared by using a mild and low-cost method retained high specific surface area (S<sub>BET</sub>) irrespective of maintaining its basic characteristics in the form of nitrogenated functional species and formation of active adsorption sites. Furthermore, DES treated AC sample has also demonstrated a superior adsorption capacity and stability rendering as an effective carbonaceous adsorbent for CO<sub>2</sub> adsorption from the flue gas stream.

## **Chapter 8 Techno-Economic analysis of activated carbon production from spent coffee grounds: Comparative evaluation of different production routes**

Most of this chapter's content has been published as a research article in the Energy Conversion and Management: X journal. Elsevier holds the copyright, and the permission to use the article mentioned above in this thesis has been obtained from Elsevier (see Appendix G).

### **Citation :**

Mukherjee, A., Okolie, J.A., Niu, C., & Dalai, A.K. (2022). Techno-Economic analysis of activated carbon production from spent coffee grounds: Comparative evaluation of different production routes, Energy Conversion and Management: X, volume (14), p. 100218.

A part of the work has also been presented as a conference presentation.

### **Conference Presentation:**

**Mukherjee, A.,** Niu C., & Dalai, A.K., " Novel Activated Carbon from Spent Coffee Grounds for CO<sub>2</sub> Capture: Effects of Textural Properties and Surface Properties", oral presentation at Advances in Carbon Dioxide Capture & Utilization for Sustainable Climate (ACCUSC-2022), Department of Chemical Engineering, National Institute of Technology, Rourkela, 4<sup>th</sup> to 10<sup>th</sup> July 2022.

### **Contribution of the Ph.D. Candidate**

Alivia: (1) performed the process of economic evaluation and sensitivity analysis studies, (2) Writing the manuscript, responded to the reviewer's comments. Dr. Jude A. Okolie helped to review the manuscript. Dr. Catherine Niu provided overall supervision of the research, and Dr. Ajay K. Dalai examined the research results, coordinated the manuscript preparation, and provided overall supervision of the study.

### **Contribution of this chapter to the overall Ph.D. research**

Before commercializing the activated carbon production technology from dried spent coffee grounds, a preliminary investigation is necessary. This chapter aims to evaluate and understand the overall economic feasibility and viability of the activated carbon production technology, examining different production routes and determining the sensitivity of activated carbon price to several parameters.



## 8.1 Abstract

Activated carbon (AC) has gained immense popularity due to its excellent physicochemical properties and ability to remove carbon dioxide (CO<sub>2</sub>) from the flue gas stream. This study examines the potential of spent coffee grounds (SCG) as a precursor to produce activated carbon (AC) via prominent thermochemical conversion technologies. Different production routes, such as slow pyrolysis, activation, and deep eutectic solvent (DES) functionalization, were compared in terms of their economic viability. In this study, three scenarios (Scenario 1–3) involving combinations of the technologies and production routes were evaluated and compared. Scenario 1 comprises slow pyrolysis, CO<sub>2</sub> activation and flue gas recycling for physical activation. Scenario 2 includes flue gas combustion, while the third scenario comprises flue gas combustion and DES impregnation. All processes were simulated with Aspen plus, while a detailed cash flow analysis was used to estimate the profitability parameters. The price of AC was found to be the most crucial determinant of an AC production plant's viability and feasibility. The minimum selling price (MSP) of AC samples produced from scenarios 1, 2 and 3 are U.S \$ 0.15/kg, \$ 0.21/kg, and \$ 0.28/kg, respectively. The price of pristine AC and DES-treated AC were lower than the commercially available activated carbon (U.S \$0.45/kg).

## 8.2 Introduction

Coffee is a promising agricultural product as well as a widely consumed beverage worldwide. It is often regarded as the second largest traded commodity after petroleum, with nearly 2 billion cups of coffee consumed each day globally (Du et al., 2020). Moreover, the processing of coffee beans involves a series of steps, including milling, roasting, grinding, and brewing. Coffee processing is accompanied by the production of a significant amount of by-product known as spent coffee grounds (SCG) (Karmee, 2018). For every kg of soluble coffee bean processed, about 2 kg of SCG is generated (Karmee, 2018). SCG is often dumped in landfills or incinerated, thereby creating environmental pollution. About 9 million tons of SCG are dumped in landfills annually (Murthy and Madhava Naidu, 2012).

SCG is a non-edible by-product from the coffee industry rich in carbohydrates, oil, carbon, nitrogen, proteins, and bioactive compounds. With the elevating coffee demand and consumption, it is imperative to balance the production with the proper valorization of the by-products, including SCG. The conversion of SCG to biofuels and green chemicals has gained momentum to foster sustainable waste management. As a result, several researchers have studied the production of biofuels and bioactive compounds from SCG (Jenkins et al. 2014; Al-Hamamre et al. 2012).

SCG could also be used to produce biochar and activated carbon (AC) for subsequent CO<sub>2</sub> capture under a post-combustion scenario. Biochar production from SCG has the potential to alleviate the challenges of climate change, greenhouse gas emissions and environmental pollution (Mukherjee et al., 2021a). Biochar can also be produced from other lignocellulosic biomasses such as sugarcane bagasse (Creamer et al., 2014), almond shells (Tiwari et al., 2017), and food waste (Patra et al., 2021). A recent study demonstrated that the biochar produced from SCG showed superior CO<sub>2</sub> adsorption capacity compared to biochar from other lignocellulosic materials (Mukherjee et al., 2021a). In another study, it has been demonstrated that the physical and chemical activation of biochar to AC could improve the surface properties and CO<sub>2</sub> adsorption capacity (Tiwari et al., 2017; Shahkarami et al., 2015a; Shahkarami et al., 2015b).

Moreover, the use of environmentally friendly deep eutectic solvents (DES) comprising a mixture of choline hydroxide and urea to functionalize the activated carbon has improved its CO<sub>2</sub> adsorption capacity (Hussin et al., 2021). In another study, the functionalization of AC with ionic liquids also increases the CO<sub>2</sub> adsorption capacity (Garip and Gizli, 2020). However, the preparation of DES is relatively simple compared to that of ionic liquids. In addition, DES

exhibits unique properties such as non-toxicity, high ionic conductivity, low cost, thermal stability, and biodegradability, which could favour CO<sub>2</sub> capture (Hussin et al., 2021).

Recently, Liu et al., (2021) performed the techno-economic analysis (TEA) of AC production from the spent mushroom substrate. However, a cash flow analysis and the MSP of AC were not determined. Another study estimated the TEA of an integrated process for producing biodiesel, glycerol, and AC from SCG (Tian et al., 2021). However, the method applies to China. In addition, a detailed cash flow analysis was not performed.

Furthermore, a comprehensive evaluation of the effects of process parameters on the MSP of AC is missing from the study. Although extensive research has been carried out on the techno-economic analysis (TEA) of different lignocellulosic biomass conversion processes, there is no available study on detailed TEA and sensitivity analysis of AC production from SCG. In Chapters 5 and 6, SCG was reported as a promising lignocellulosic biomass that could be utilized for valorization through thermochemical conversion techniques. Also, the preparation of pristine AC and DES-functionalization of pristine-AC from SCG for CO<sub>2</sub> capture is a promising strategy to minimize greenhouse emissions as reported in Chapter 7. However, the economic feasibility of the entire activation and DES-functionalization technique is scarcely reported. Therefore, this study proposes different AC production scenarios valorizing SCG as a potential lignocellulosic biomass. More importantly, a comparative evaluation of the process economics of AC production with and without functionalization is also missing in the literature. The present study presents a novel approach to assessing the economic viability of different production techniques by determining the minimum selling price (MSP) of AC coupled with sensitivity analysis. The study also compares the minimum selling price (MSP) of pristine and DES functionalized AC with the ones reported in the literature and provides a basis for the efficient valorization of SCG for AC production.

### **8.3 Research methodology**

#### **8.3.1 Design Basis**

This study developed the model by simulating spent coffee grounds (SCG). However, the proposed model to produce AC can also be used for other lignocellulosic biomass samples. The reason for selecting SCG as the base case to develop the model is its abundant availability in Canada and unique physicochemical properties (Mukherjee et al., 2021b). Also, SCG was used as a potential lignocellulosic precursor to generate biochar and AC with unique physicochemical characteristics, as mentioned in previous chapters 6 (Mukherjee et al., 2021a) and 7. Therefore, the simulations were performed by using the data extracted from the previously mentioned chapters and under the optimised process conditions. Furthermore,

compared to first-generation precursors, lignocellulose biomass does not impose a threat to food security versus fuel.

The overall process for all the three scenarios were simulated and implemented with Aspen Plus® v12.1 (AspenTech, Bedford, USA), licensed by the University of Saskatchewan. The plant was designed to process approximately 50,000 tons of SCG annually. This study's thermodynamics and energy calculations were executed using Aspen Plus®, which contains an in-built array of different physical properties databases. Figure 8.1 depicts the overall design procedure implemented to determine the economic feasibility and viability of the AC production using dried SCG.

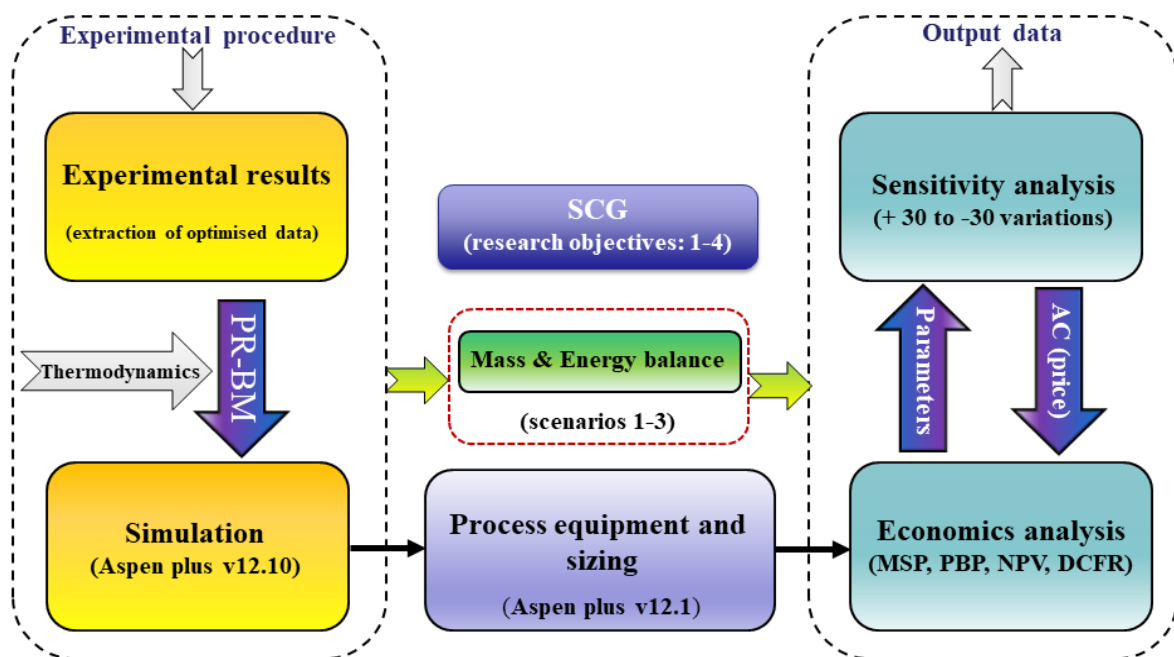


**Figure 8.1:** Schematics of the design procedure for the techno-economic analysis of activated carbon (AC) production using SCG.

### 8.3.2 Process design and simulation

Three different scenarios to produce AC routes were assessed in this study, as shown in Figure 8.2. Scenario 1 is a straightforward route and provides a foundation for further assessments. It consists of SCG drying, slow pyrolysis and CO<sub>2</sub> activation to generate AC. Furthermore, in scenario 1, the flue gas mainly consisting of CO<sub>2</sub> generated from the slow pyrolysis unit was sent back to the activation unit for the physical activation process. In scenario 2, the product gas from both the pyrolysis and activation processes were sent back to the combustion chamber unit. Combustion of the product gas in presence of air produces heat that was used for biomass

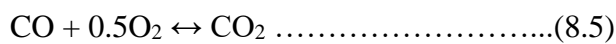
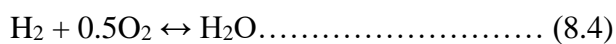
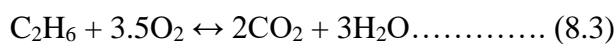
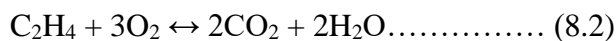
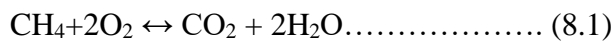
drying, thereby minimizing the energy requirement of the overall process. Scenario 3 comprises slow pyrolysis, CO<sub>2</sub> activation, a combustion unit, and a DES functionalization unit to tailor the surface chemistry of the pristine AC. Overall, the strategy compares different AC production routes from SCG regarding their economic viability.

The overall process for the three scenarios was simulated and implemented with Aspen Plus® v12.1 (AspenTech, Bedford, USA), licensed by the University of Saskatchewan. The process was designed to process approximately 50,000 tons/y of SCG. The plant capacity to process 50,000 tons/year of SCG was selected from the values reported in the existing literatures (Liu et al., 2021; Tian et al., 2021). However, the developed model could also be applied to other lignocellulose-based biomass materials. Aspen plus was used for the simulation because of the array of inbuilt physical properties databases useful for thermodynamics calculations and the mass and energy balance of the overall process. Aspen plus does not contain an inbuilt model for biomass pyrolysis; therefore, the entire process was simulated into different unit operations, as depicted in Figure 8.2. Moreover, SCG was defined as a non-conventional (NC) component whose components were determined based on the proximate analysis (dried-basis), ultimate analysis and requires characteristics of its properties such as enthalpy (HCOALGEN) and density (DCOALIGT). In our previous study, the moisture (3.3 wt. %), volatile matter (81.2 wt. %), fixed carbon (14.6 wt. %), and ash content (0.9 wt. %) of SCG were reported in chapter 6 (Table 6.3) (Mukherjee et al., 2021a). Additionally, the C, H, N, S and O are 50.0 wt. %, 6.7 wt. %, 2.5 wt. %, 0.9 wt. %, and 39.0 wt. %, respectively (Table 6.4). The RYield block was employed to decompose dried-SCG into its components (C, H<sub>2</sub>, N<sub>2</sub>, O<sub>2</sub>, H<sub>2</sub>O, ash, and S), while a calculator block was used to perform the decomposition through a FORTRAN subroutine statement. Details of the sub-routine statement and the calculator block methodology have been reported elsewhere (Okolie et al., 2020b).

As described in Figure 8.2 (scenario 1), wet SCG is sent to the air dryer operating at 100 °C and 0.1 MPa. The dryer reduces the moisture content of SCG that would facilitate the thermal treatment. A biomass dryer in Aspen plus was represented with a stoichiometric block. In contrast, a calculator block was used to determine the moisture content of SCG at the exit of the reactor. The dried SCG enters the RYield reactor at 600 °C and 0.1 MPa for decomposition into conventional components (DECOMP). According to the ultimate and proximate analysis, the reactors decompose SCG into biochar, CO, CO<sub>2</sub>, H<sub>2</sub>, N<sub>2</sub>, O<sub>2</sub>, and H<sub>2</sub>O. The product (biochar) exiting the yield reactor enters the RGibbs block for slow-pyrolysis process. The RGibbs block was used to simulate slow pyrolysis at 600 °C and atmospheric pressure conditions (0.1 MPa). In this regard, the data derived from the RGibbs block reactor was

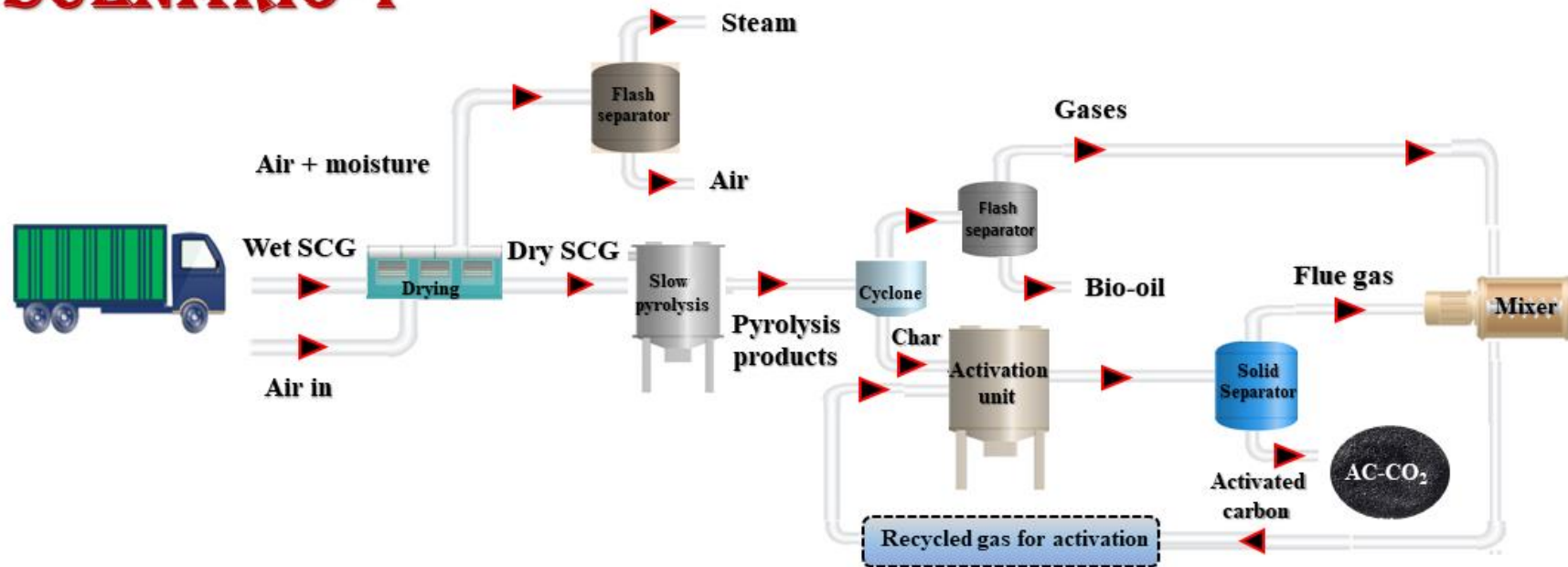
utilised to perform the thermodynamic calculations of the process. Moreover, a cyclone separator was used to remove the solid char (biochar) while the liquid, gases and volatiles were cooled before entering the flash separator for the removal of gases. It should be noted that the temperature and pressure of slow pyrolysis were selected based on the findings from chapter 6 and previously mentioned report (Mukherjee et al., 2021a).

The produced char (biochar) was physically activated with CO<sub>2</sub> at 800 °C and at atmospheric pressure (1-atm). The activation process was simulated with the RGibbs block, while the amount of CO<sub>2</sub> required to ensure that 57.4 wt. % yields of AC is produced was specified with design specs as mentioned in chapter 7. The optimum yield of 57.4 wt. % was chosen based on the optimized experimental outcome of AC yield derived using the Box- Behnken Design (BBD) of experiments as stated in chapter 7 (Tables 7.2 and 7.6). It should be mentioned that the ratio of adsorbent (AC) and the DES used in this regard is mixed at 1:2. The product gases emitted from the activation process and the pyrolysis units were sent to the combustion chamber (COMBCHAM) for burning to produce heat as stated for scenarios 2 and 3 (Figure 8.2). A stoichiometric reactor (Rstoic) operating at 1000 °C under 1.1 MPa pressure was used to represent the combustion unit. Rstoic reactor was modelled based on the five different equations (Eq. 8.1-8.5) based on the composition of the EXTFLG (Liu et al., 2021; Okolie et al., 2021c).

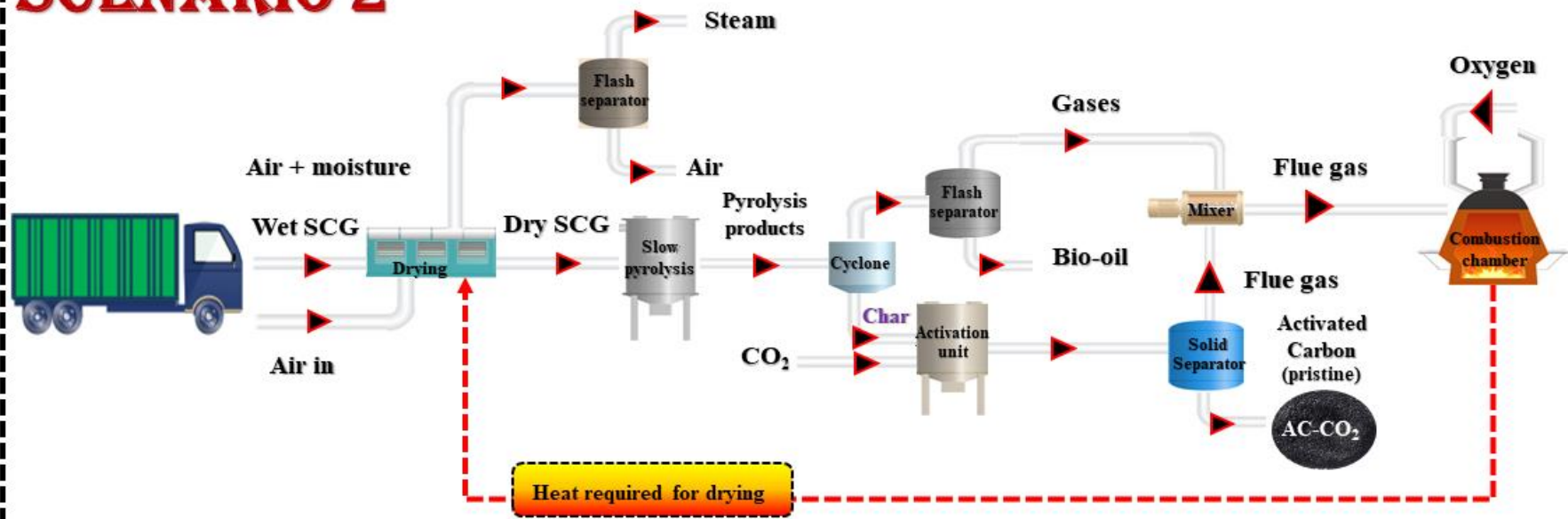


The thermodynamic methods of the entire process simulation uses the Peng-Robinson-Boston-Mathias (PR–BM) equation of state, which is suitable for low-pressure streams (Liu et al., 2021). Moreover, the operating conditions for the unit operations are obtained from the experimental studies reported in previous chapter 6 and 7, respectively. That way the model could be validated against the findings derived from the findings of the lab studies. All the assumptions used in the Aspen Plus® model and the economic model are summarised in Table 8.1.

# SCENARIO-1



# SCENARIO 2





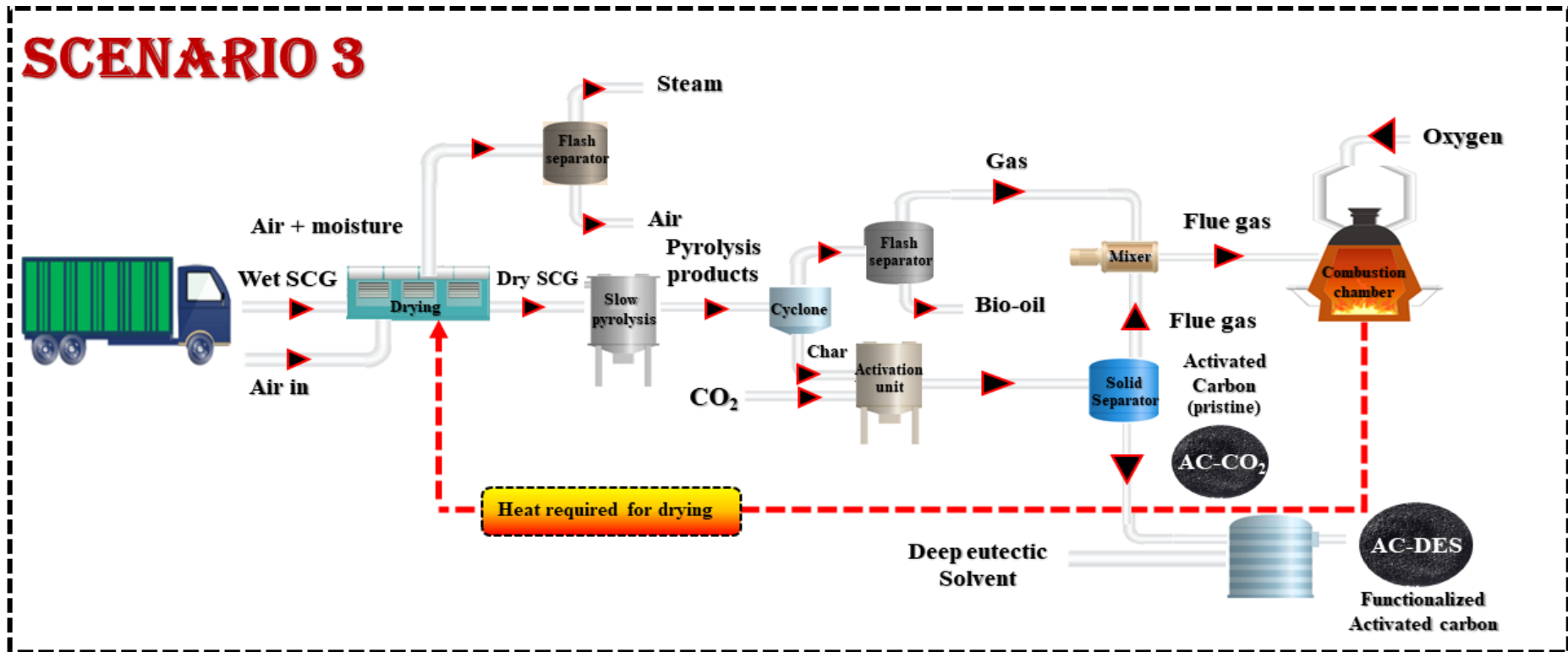


**Figure 8.2:** Flowsheet of the proposed design for AC production, (**scenario 1**): slow pyrolysis and physical activation, (**Scenario 2**): slow pyrolysis, physical activation, and flue gas combustion; (**scenario 3**): slow pyrolysis, physical activation, DES functionalization, and flue gas combustion.

### 8.3.3 Economic analysis

The economic analysis of AC production from SCG was estimated using the bottom-up approach. The method calculates the cost components as a part of the purchase cost of all equipment (COE), also known as the bare module cost (Brown, 2000). The capital expenditure (CAPEX) and operating expenditure (OPEX) were estimated based on Table 8.2.

**Table 8.1:** Assumptions used in the Aspen plus simulation and economic model (Okolie et al., 2021c).

Parameters	Assumptions
<b>Assumptions in process simulation</b>	
<b>Biomass decomposition products</b>	Biochar, CO, CO <sub>2</sub> , N <sub>2</sub> , H <sub>2</sub> , O <sub>2</sub> and H <sub>2</sub> O
<b>Ash</b>	Does not participate in the reactions
<b>Biochar decomposition products</b>	Carbon and Ash
<b>Equation of state</b>	PR–BM equation
<b>Assumptions in the economic model</b>	
<b>Currency used in economic model</b>	U.S \$
<b>Base year</b>	2021
<b>Cost of land</b>	2% of fixed capital investment
<b>Plant construction duration</b>	1 year
<b>Plant lifetime</b>	20 years
<b>Plant annual operation</b>	8000 h/y
<b>SCG capacity</b>	50,000 tons/y
<b>Annual salary of worker</b>	U. S. \$35,000/y
<b>Depreciation method</b>	Straight line method

The CAPEX includes the direct and indirect costs, while the OPEX comprises the fixed and variable operating costs (Okolie et al., 2021c). The labour cost was estimated as part of the fixed operating cost from equation (8.6). In Equation 8.6, P and N<sub>NP</sub> indicate the number of solid handling steps and on-particulate processing steps. The average annual salary of each worker was set at the U.S \$35,000 (Okolie et al., 2021c). Based on the expression of equation (8.6), the overall number of operators (N<sub>OL</sub>) required for scenarios 1, 2 and 3 are 6, 7 and 12, respectively Okolie et al., (2021c).

$$N_{OL} = \sqrt{31.7P^2 + 0.23N_{NP} + 6.29} \dots \dots \dots (8.6)$$

Discounted cash flow analysis (DCFA) was performed and used to determine the MSP of AC as well as the economic feasibility of different AC production routes. The process is economically viable if the MSP of AC is above the breakeven point. The economic viability of the process was also assessed with major parameters such as the net present value (NPV), payback period (PBP), net rate of return (NRR) and DCFA (Discounted cash flow analysis) of the project. A detailed description of each economic indicator as well as its advantages and limitations, has been reported by Ulrich and Vasudevan (2018).

The proposed plant is set up in Saskatchewan, Canada. However, a location factor (0.91) could be used to show the disparities in cost between Canada and Europe Pahrump (2021). The economic model was developed with currency in U.S \$. The cost of SCG was estimated to be U.S \$ 0.1/ dry ton based on the current market price of transportation and logistics (Liu et al., 2021). Moreover, the reference year was 2021, with the Chemical Engineering Plant Cost Index (CEPCI) used to adjust the equipment cost to the base year. All the assumptions used in the economic model and Aspen plus simulation are summarized in Table 8.1.

**Table 8.2:** CAPEX and OPEX estimation methodology.

<b>CAPEX Estimation</b>	
<b>Cost estimation</b>	Fraction of the purchase cost of all equipment
<b>Purchase cost of all equipment (COE) (a)</b>	COE
<b>Cost of equipment installation (b)</b>	0.4 of COE
<b>Controls and instrumentation cost (c)</b>	0.26 of COE
<b>Piping and electrical systems (d)</b>	0.41 of COE
<b>Building and services (e)</b>	0.1 of COE
<b>Direct cost (DC)</b>	$DC = (a) + (b) + (c) + (d) + (e)$
<b>Indirect cost (IC)</b>	$IC = 0.22 \text{ of } DC$
<b>Fixed capital investment (FCI)</b>	$FCI = DC + IC$
<b>Startup cost (SUC)</b>	0.05 of FCI
<b>Working capital (WC)</b>	0.15 of FCI
<b>CAPEX</b>	$CAPEX = FCI + SUC + WC$
<b>OPEX Estimation</b>	
<b>Cost of labor</b>	COL
<b>supervision and overhead cost (f)</b>	1.25 of COL
<b>Maintenance and miscellaneous expenses (g)</b>	0.04 of FCI
<b>Fixed operating cost (h)</b>	$(h) = COL + (f) + (g)$
<b>Spent coffee grounds cost (i)</b>	USD \$ 0.1/ dry ton
<b>Deep eutectic solvent (Choline chloride + Urea) (j)</b>	USD \$ 144 for Choline chloride (Sigmaaldrich, 2021) USD \$ 96.30 for Urea (SIGmaaldrich, 2021)
<b>Total raw material cost (k)</b>	$(k) = (i) + (j)$
<b>Electricity cost (m)</b>	USD \$0.069/KWh per unit (Okolie et al., 2021c)
<b>Cooling water cost (l)</b>	USD \$14.8/1000 m <sup>3</sup> (Okolie et al., 2021c)
<b>Variable operating cost (p)</b>	$(p) = (k) + (m) + (l)$
<b>OPEX</b>	$OPEX = (h) + (p)$

The COE was determined with the scaling method (Michailos et al., 2020). The approach calculates the cost of equipment with the base cost of similar equipment whose size is known using the Eq. 8.7.

$$C = C_o \left( \frac{S}{S_o} \right)^f \dots\dots\dots (8.7)$$

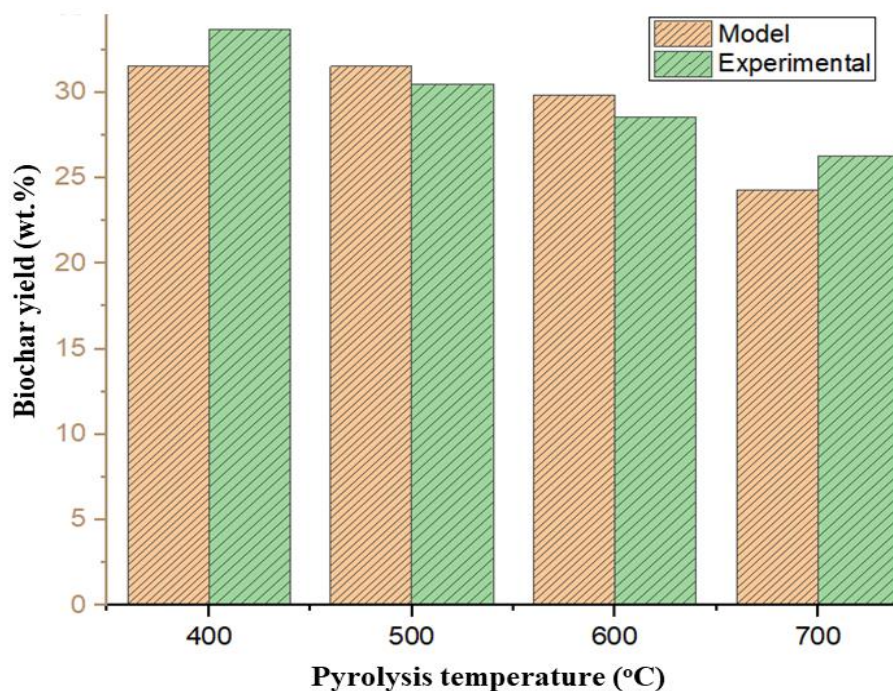
Where, S is the equipment capacity obtained from the Aspen Plus simulation, while So is the base capacity. C and Co are the actual and base equipment cost, respectively. In contrast, f represents the scaling factor.

Monte Carlo simulation was used to quantify the uncertainty and associated risk in the developed economic model. The Monte Carlo simulation was performed with Oracle Crystal Ball (OCB) software. OCB is a stochastic tool designed as a spreadsheet-based application suitable for uncertainty and risk analysis (Oke et al., 2021). The present study applies normal distribution with 30,000 trials to estimate the associated uncertainty in the economic model.

## **8.4 Results and discussions**

### **8.4.1 Model validation, mass, and energy analysis**

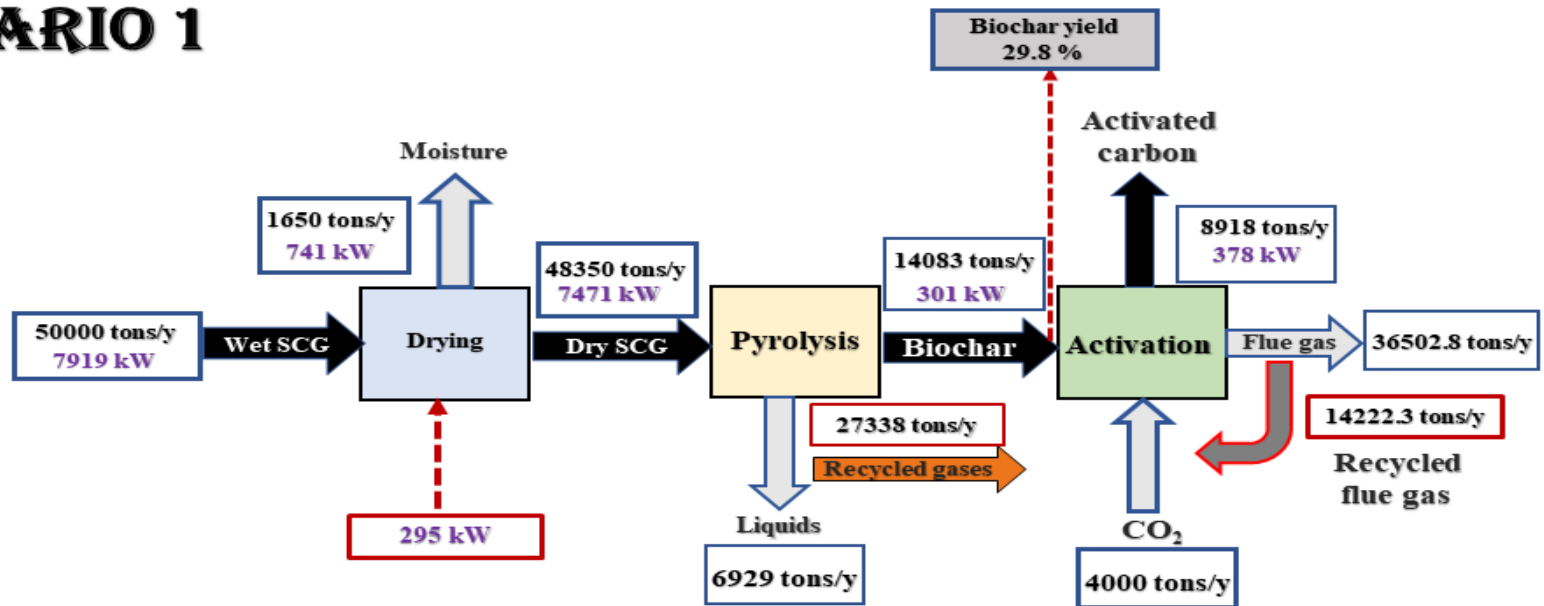
The experimental biochar yields from slow pyrolysis of SCG were compared with model results at temperatures range of 400–700 °C (Figure 8.3). The biochar's experimental yields were obtained from our previous findings reported in Chapter 6 (Table 6.2). The model predictions were obtained from the sensitivity analysis of RGibbs block in Aspen plus. The comparison of the model and experimental results is helpful in the validation of the model. It also helps to assess the proximity of the model predictions to reality. As shown in Figure 8.3, all the model results are close to the experimental values with minimum deviations (less than 10%). These findings indicate that the developed model effectively predicts biochar yields even at high temperatures.



**Figure 8.3:** Comparison of biochar yield from experimental and model results.

Figure 8.4 shows the mass and energy balance for the three proposed scenarios (scenario 1–3). For scenario 1, overall, 295 kW of energy was required for the drying process. However, the use of heat recycled from the flue gas combustion in scenarios 2 and 3 saves 95 kW of energy in the drying process compared to scenario 1. In scenario 1, 4000 tons/y of CO<sub>2</sub> was required for activation compared to 4831 tons/y as in the case of scenarios 2 and 3 (Figure 8.4) owing to the recycled flue gas stream used for physical activation as proposed in scenario 1. For every 50,000 tons/y of SCG, 8918 tons/y were produced for scenarios 1 and 2, respectively. Also, 12,172 tons/y of AC was derived from scenario 3 after DES functionalization. Overall, the biochar yield from slow pyrolysis for the three scenarios is 29.8 wt.%, which is close to the experimental yield at 600 °C (25.4wt. %). Scenarios 1 and 2 comprise two sequential steps for AC production (firstly slow pyrolysis of SCG for biochar production followed by physical activation using CO<sub>2</sub> as the activating agent).

# SCENARIO 1



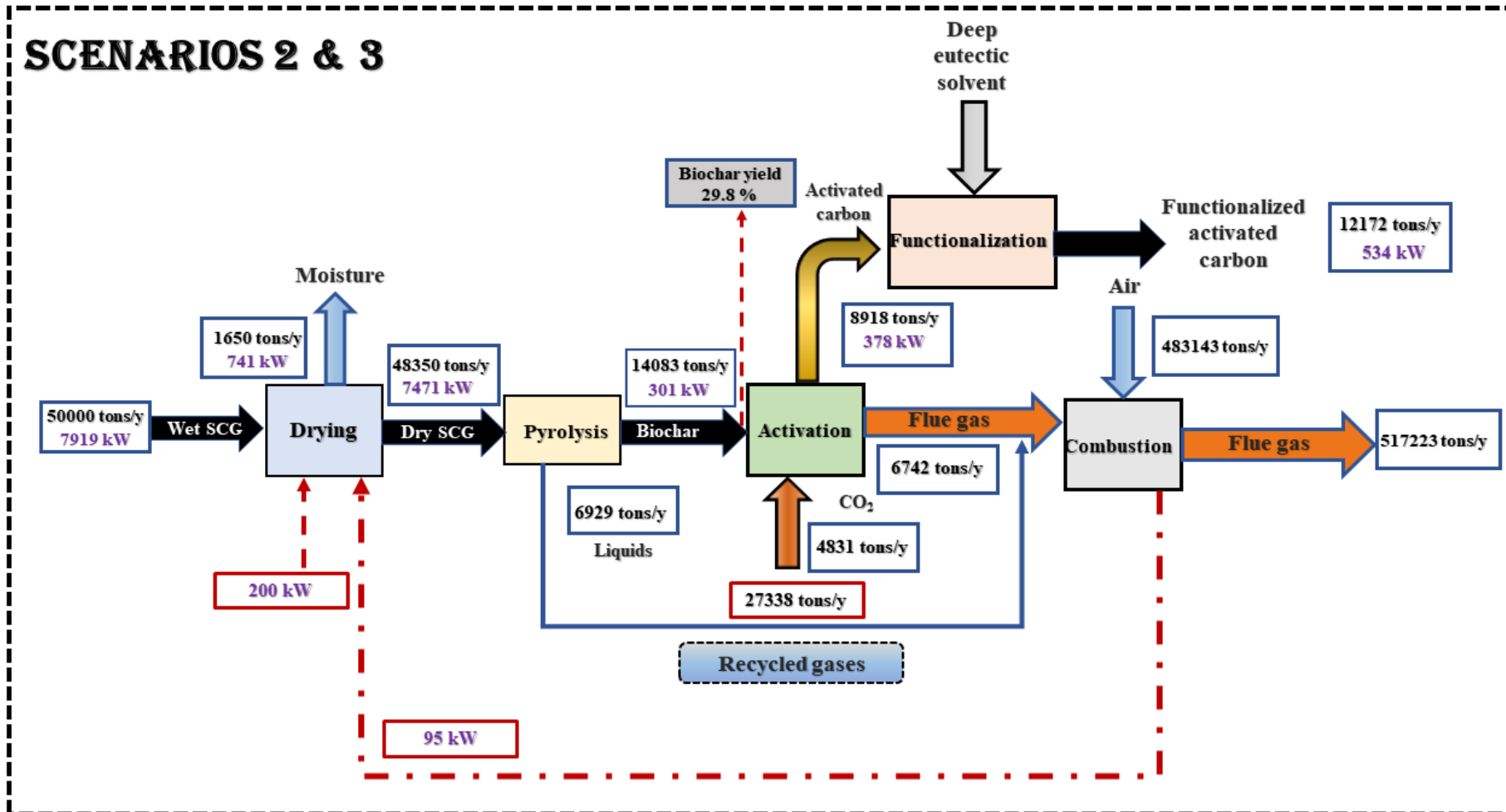


Figure 8.4: Overall mass and energy balance for scenarios 1-3.



However, scenario 3 comprises three sequential steps to produce AC production (slow pyrolysis for biochar production, physical activation followed by functionalization with DES). The physicochemical properties of biochar derived from slow pyrolysis of SCG for all three scenarios (1–3) have been documented in previous chapter 6 (section 6.5). Although, scenario 1 is a new concept modelled conceptually with Aspen plus® where the flue gas stream is recycled back to the activation unit for that physical activation.

#### **8.4.2 Economic analysis**

A detailed analysis of the COE for the three scenarios is demonstrated in Figure 8.5. The activation unit and pyrolysis reactor are the most expensive equipment for all three scenarios. The activation unit accounts for 49.1 %, 43.2 %, and 39% of the overall equipment costs for scenarios 1, 2 and 3. In contrast, the cost of a pyrolysis reactor accounts for 23.1%, 20.4% and 18.4% of the overall COE for scenarios 1, 2 and 3, respectively. The high costs of the activation unit could be attributed to the increased temperature requirement compared to the pyrolysis unit. Activation is performed at a higher temperature range of 800–1000 °C, which requires specialized reactor materials to withstand such temperatures. The total COE is illustrated in Figure 8.6. The cost declines in the following order: scenario 3 (4.7 million U.S \$) > Scenario 2 (4.2 million U.S \$) > Scenario 1 (3.7 U. S \$). The high cost of scenario 3 could be because of the additional functionalization and combustion units. Although the functionalization unit helps to improve the surface chemistry of AC, it contributes to an increase in the COE. The breakdown of the CAPEX and OPEX estimation is shown in Figure 8.7. The OPEX for the three scenarios increases as follows: scenario 1 (5.9 million U.S \$) < scenario 2 (8.3 million U.S \$) < scenario 3 (11.4 million U.S \$). The greater OPEX for scenario 3 could be because of the higher variable and fixed operating cost.

The variable operating cost includes the cost of SCG, DES chemicals (urea and choline chloride), Industrial grade CO<sub>2</sub> cost and utility cost (Michailos et al., 2019a). Additionally, the fixed operating cost (FOC) comprises overhead cost, maintenance cost, insurance, and labour, and they remain constant regardless of the production level.

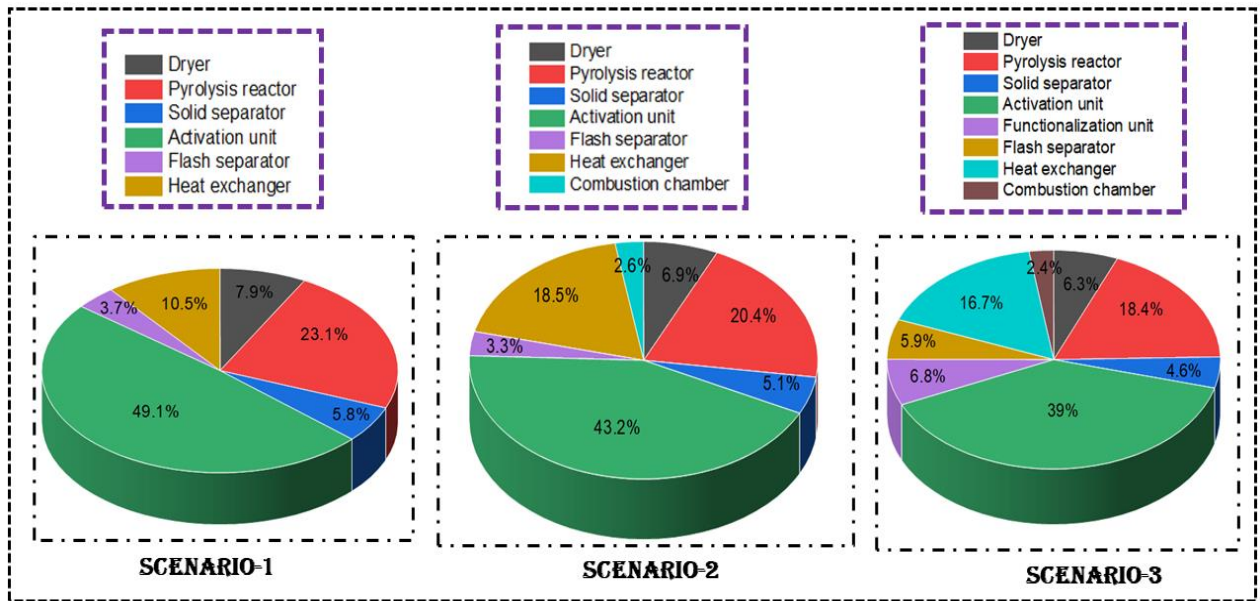


**Figure 8.5:** Breakdown of the equipment purchase costs for all the three scenarios.

The addition of combustion and functionalization units in scenarios 2 and 3 increases the number, cost of labour and raw materials. This could ultimately increase the OPEX of scenarios 2 and 3 compared to scenario 1. A breakdown of OPEX cost indicates that the utility and raw material cost accounts for most of the OPEX in all three scenarios (Figure 8.7). Raw material cost accounts for 60.8 % of the OPEX in scenario 3 due to the use of DES. Moreover, the electricity cost is higher for scenarios 2 and 3 than in scenario 1, owing to the addition of the combustion chamber unit. The contribution of the FOC was not substantial for all three scenarios. FOC contributed 17.2%, 15.1% and 12.2 % for scenarios 1, 2 and 3 respectively.

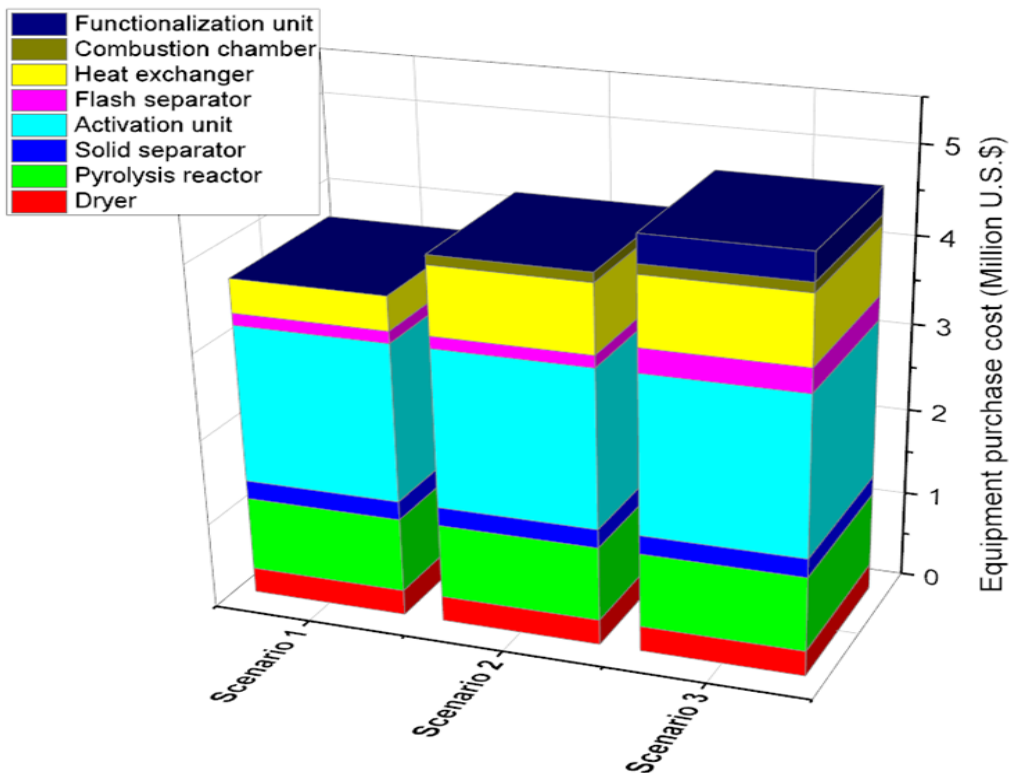


**Figure 8.6:** Overall cost of equipment for all the three scenarios.

The CAPEX for the three scenarios declines in the following order: scenario 3 (19.3 million U.S \$) > scenario 2 (17.4 million U.S \$) > scenario 1 (15.3 million U.S \$). The CAPEX includes the fixed capital investment (FCI), start-up cost and the working capital (WC), all of which are dependent on the COE. Therefore, the superior CAPEX of scenario 3 could be attributed to the increased COE. CAPEX and OPEX estimation provided the information needed for the discounted flow analysis (DCFA). The analysis was used to evaluate AC's MSP and calculate different profitability indexes (Michailos et al., 2019; León et al., 2020). The profitability of AC production from different routes was determined by comparing parameters such as payback period (PBP), net present value (NPV), and discounted cash flow rate of return (DCFR). A detailed explanation of the profitability index and its significance can be found elsewhere (Gutiérrez Ortiz, 2020).

Figure 8.8 shows the cash flow analysis for three different scenarios for AC production. As shown in Figure 8.8, negative cash flow was obtained for year zero due to the money used for land purchase and the total capital investment. Moreover, funds are recovered from sales and investments after complete construction and project initiation. These funds ensure that the cash flow becomes positive over the years.

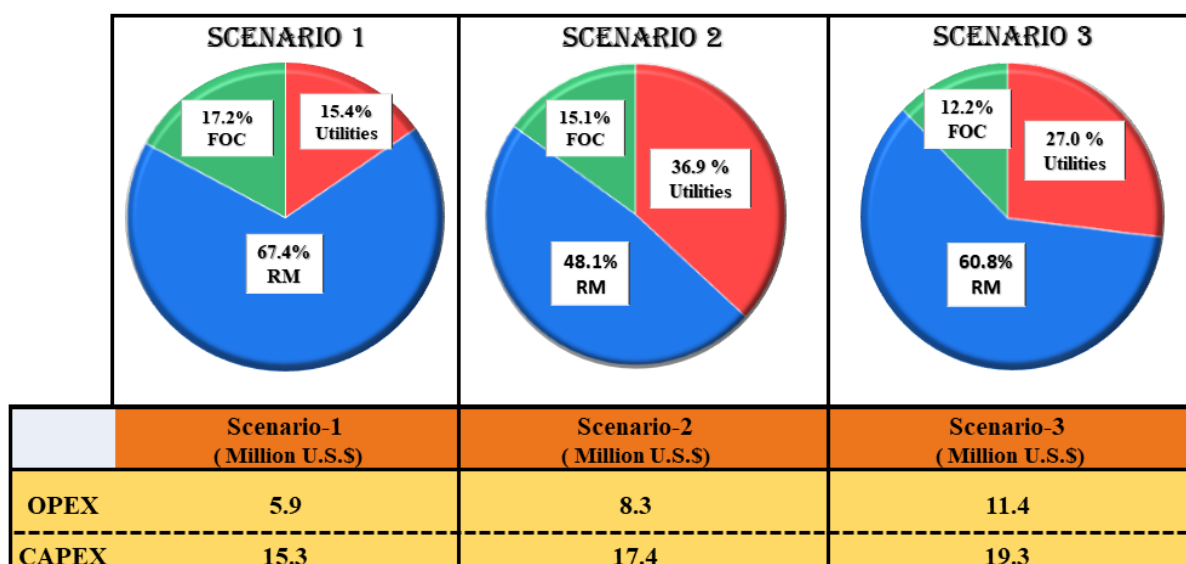


**Figure 8.7:** Total CAPEX and OPEX for the three scenarios and the OPEX breakdown.

The PBP estimated for the three scenarios for the undiscounted case decreases as follow: Scenario 3 (4.1 years) > scenario 2 (3.1 years) > scenario 1 (2.6 years). The PBP indicates the time it takes for the investment cash flow to equal the initial cost. The PBP should be less than the entire project life for an investment to be economically feasible. Based on the PBP, all three scenarios are profitable. Although promising, the PBP does not explain the performance of the project once the investment recovers its initial outlay. Therefore, the NPV and DCFR are also used as complimentary profitability index.

The MSP of the three production routes (the cost of AC that produces zero NPV) was assessed and compared with literature values and the price of commercial AC (Table 8.3). The AC produced from scenario 1 had the lowest MSP (0.15 U. S \$/kg). In contrast, scenarios 2 and 3 had MSP of AC as 0.21 U. S \$/kg and 0.28 U.S \$/kg respectively. This indicates that the AC production could become profitable from economic perspective if the price of AC is above this break-even point. The minimum selling price of AC for the three scenarios is comparable to that of commercial biochar and AC (Table 8.3). Struhs et al. (2020) developed a mobile pyrolysis unit and assessed the MSP of biochar produced from slow pyrolysis of the unit using cattle manure as feedstock. They obtained an MSP of 0.27 U.S \$/kg. In another study, Palm oil empty fruit bunches were used as feedstock to estimate the MSP of a slow pyrolysis plant in Selangor (Harsono et al., 2013). The produced biochar had an MSP of 0.53 U.S \$/kg. It should be mentioned that the cost estimation methods and MSP reported in the studies in Table 8.3

are different. Moreover, the price documented for different studies (Bora et al., 2020; Sahoo et al., 2019; Kung et al., 2013) is relevant to the publication date. Combining technologies such as slow pyrolysis and acid impregnation have the potential to improve the activated carbon properties for several industrial applications. Honeydew peels were used as feedstock for slow pyrolysis and acid impregnation (sulfuric and phosphoric acid) to produce activated carbon (Yunus et al., 2020). The integrated AC production process obtained an MSP value of 0.26. Moreover, the AC showed promising results in the removal of heavy metals from mining effluents. Advanced pyrolysis technologies such as microwave pyrolysis have also been used to produce biochar from different feedstock, including tree bark, palm date fronts and wood mix (Haeldermans et al., 2020). MSP values ranging from 0.49 to 0.88 U. S \$/kg were obtained using different feedstock. The MSP of the AC samples derived from three different scenarios are compatible as well as low compared to the values reported in the literatures. This could be attributed to multiple reasons that include equipment size mainly the drier size, less energy required for drying, recycled heat for the drying process, recycled flue gas stream for the activation process, and the usage of low cost and non-toxic deep eutectic solvent to tailor the surface chemistry of the modified AC samples. It is noteworthy to mention that although the MSP of AC reported in the present study is promising, several government policies schemes and study limitations should be considered. For instance, this study does not apply carbon pricing to specific countries. If applied, the MSP could decrease. However, the carbon pricing varies for different countries. Also, the produced activated carbon is intended to be used for several applications, including wastewater treatment, catalysts support, and energy applications, all of which require specific properties. These properties could be tailored to pyrolysis process conditions and activation routes, all of which have an impact on the MSP. The NPV of the undiscounted cash flow was 206.4M U. S.\$ (scenario-1) > 173.1 U. S.\$ (scenario-2) > 131.1 U. S.\$ (scenario-3) while the discounted cash flow (at  $i = 20\%$ ) has NPV was 31.9M U. S.\$ (scenario-1) > 23.6M U. S.\$ (scenario-2) > 13.6M U. S.\$ (scenario-3).

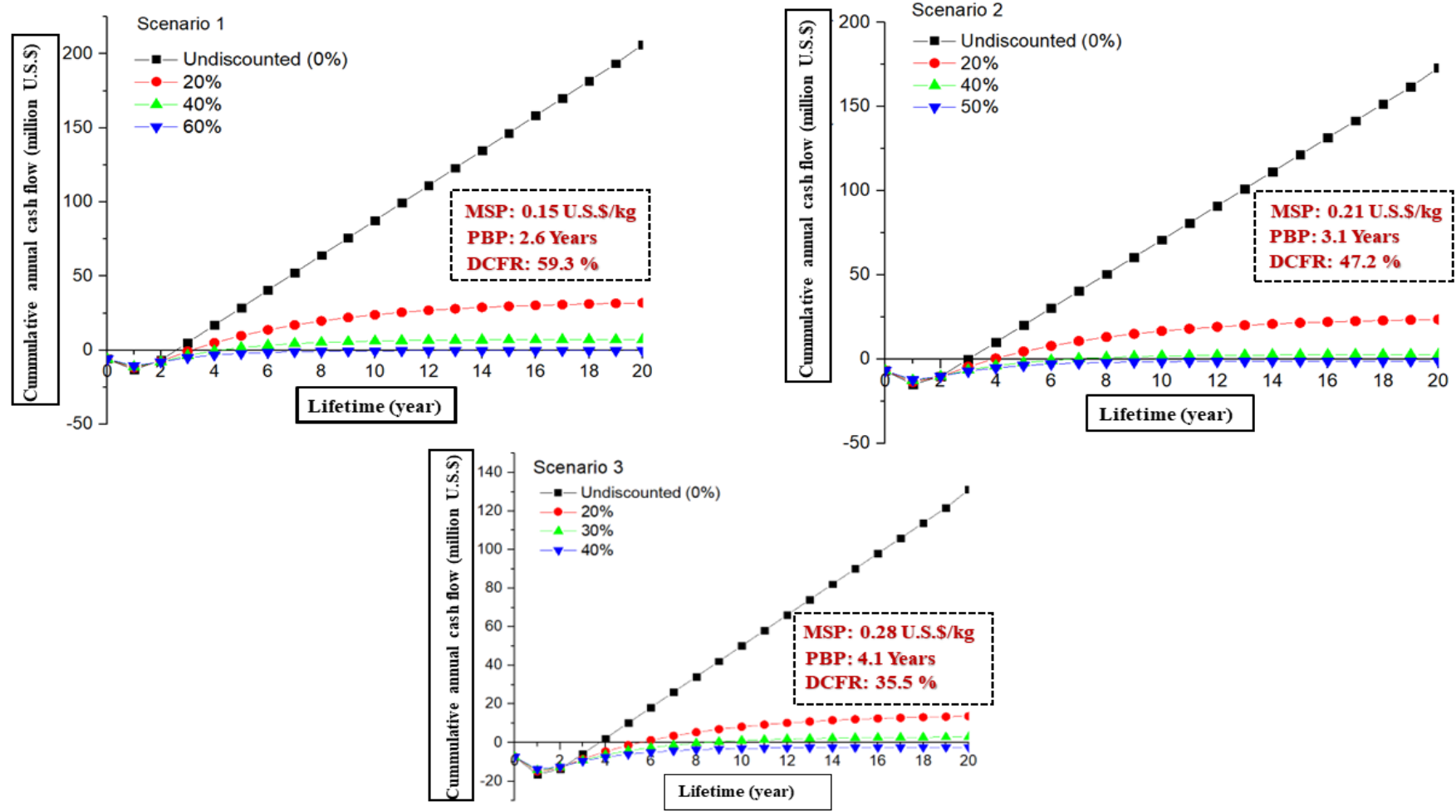


**Figure 8.8:** Discounted and undiscounted cash flow analysis for the three scenarios for AC production.

**Table 8.3:** Comparison of the minimum selling price of biochar and activated carbon from different studies.

Feedstock	Processing technology	Main product	MSP (U.S.\$/kg)	Ref.
<b>Palm oil empty fruit bunches</b>	Slow Pyrolysis	Biochar	0.53	(Harsono et al., 2013)
<b>Woodchips briquettes (WCB)</b>	Slow pyrolysis	Biochar	1.044	(Sahoo et al., 2019)
<b>Poplar</b>	Fast and Slow pyrolysis	Biochar	0.067 for fast pyrolysis derived biochar, and 0.074 for slow pyrolysis derived biochar	(Kung et al., 2013)
<b>Coffee husks (COF)</b>	Microwave slow pyrolysis	Biochar	0.49 (€ 0.43)	(Haeldermans et al., 2020)
<b>Medium-density fiberboard (MDF)</b>			0.64 (€ 0.57)	
<b>Palm date fronts (PDF)</b>			0.88 (€ 0.78)	
<b>Wood mix (AB)</b>			0.63 (€ 0.56)	
<b>Tree bark (TB)</b>			0.55 (€ 0.49)	
<b>Olives Stone kernels (OS)</b>			0.96 (€ 0.86)	
<b>Cattle manure</b>	Mobile slow pyrolysis unit	Biochar	0.27	(Struhs et al., 2020)
<b>Poultry litter</b>	Slow pyrolysis	Biochar	0.076-0.091	(Bora et al., 2020)
<b>Honeydew peels</b>	Slow pyrolysis and H <sub>2</sub> SO <sub>4</sub> impregnation	Activated carbon	0.26	(Yunus et al., 2020)
<b>Commercial activated carbon</b>	Not available	Activated carbon	0.45	("Charcoal, Activated, Norit®, Alkaline, Decolourizing   Canadawide," 2021)

<b>Spent coffee grounds</b>	Slow pyrolysis, CO <sub>2</sub> activation, flue gas combustion and DES impregnation	Activated carbon	0.28	This study
<b>Spent coffee grounds</b>	Slow pyrolysis, CO <sub>2</sub> activation and flue gas combustion	Activated carbon	0.21	This study
<b>Spent coffee grounds</b>	Slow pyrolysis and CO <sub>2</sub> activation.	Activated carbon	0.15	This study



### 8.4.3 Sensitivity analysis

A local sensitivity analysis was carried out to determine the effect of different parameters, including the CAPEX, interest rate, feedstock cost, and utility cost on the MSP. Sensitivity studies are performed by varying one input variable while maintaining the nominal values for the other variables (Michailos et al., 2019b). Figure 8.9 shows the sensitivity analysis results for the three scenarios.

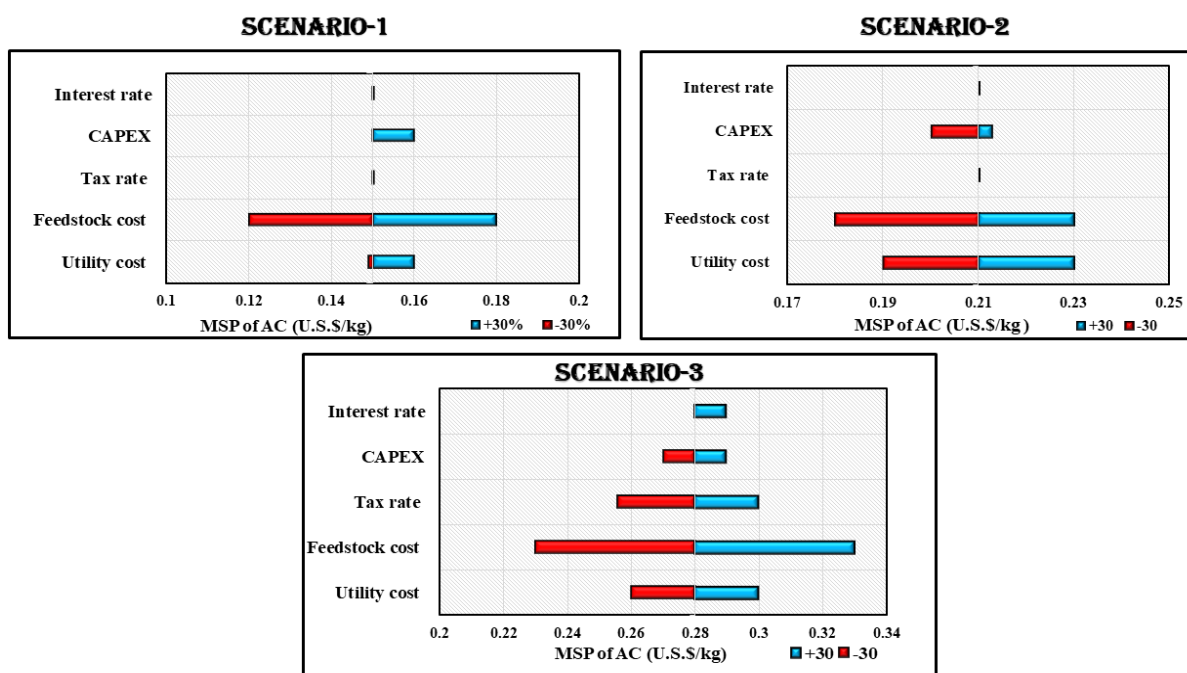


**Figure 8.9:** Sensitivity analysis showing the influence of several independent parameters on the MSP of AC for the three scenarios

Feedstock and utility costs greatly influenced the MSP for all scenarios. However, for scenario-3, elevation, or reduction in tax rate by 30% is also sensitive to the MSP of AC. A 30% elevation in the feedstock cost led to an increase in MSP from 0.15 to 0.18 U. S \$/kg for scenario 1. In contrast, the feedstock cost rose from 0.21 to 0.23 U. S \$/kg for scenario 2 and 0.28 – 0.33 U. S \$/kg for scenario 3. It should be mentioned that feedstock cost is dependent on the plant location and logistics. Therefore, these should be considered in future studies. Some studies have also proposed a mobile bio-refinery to minimize the cost of feedstock transportation and logistics (Struhs et al., 2020; Badger and Fransham, 2006). The feedstock cost also includes the cost of chemicals used in the DES and the CO<sub>2</sub> cost. Although, the CO<sub>2</sub> cost could be reduced by recycling the effluent CO<sub>2</sub> after activation.

The utility cost comprises electricity and cooling water and contributes significantly to the OPEX. A 30% increase in utility cost led to a rise in the MSP to 0.16 U. S \$/kg for scenario 1, 0.23 U.S \$/kg for scenario 2, and 0.3 U. S \$/kg for scenario 3. Moreover, a 30% decline in utility cost influenced the MSP positively. The MSP declined to 0.149 U.S.\$/kg for scenario 1, 0.19 U. S \$/kg for scenario 2 and 0.26 U. S \$/kg for scenario 3. The utility cost had a greater influence on scenarios 2 and 3 due to the additional combustion unit. Moreover, effective heat integration and pinch analysis can be used to reduce the utility cost.

Changing other factors such as CAPEX, tax rate, and interest rate had little influence on the MSP of AC produced from scenarios 1 and 2, respectively. The CAPEX has a medium effect on the MSP for all the scenarios. CAPEX accuracy depends on obtaining detailed cost data from a commercial plant, which is often challenging.

#### **8.4.4 Uncertainty analysis using Monte Carlo simulation**

The main limitation of excel for sensitivity analysis is that it provides a single outcome. However, probabilistic models can include the worst-case and best-case outcomes. A Monte Carlo simulation generates thousands of outcomes instead of one. Moreover, the local sensitivity analysis evaluates one variable at a time while other parameters are kept constant. Thus, the interactions among different variables and the influence on MSP are not considered (Michailos et al., 2019a). The probabilistic approach assigns distribution functions to several independent variables. These distributions are varied repetitively with the Monte Carlo simulation to produce a distribution function showing the probability of a specific outcome. Therefore, the same approach was used to study the effect of uncertainty or variability of the independent parameters on the MSP of AC.

The Oracle crystal ball used in the study is an excellent and straightforward tool for creating probabilistic models in Microsoft excel. A total of 30,000 outcomes trials were performed. In addition, the shape of the probability distribution for all the parameters was selected based on the understanding of different independent variables. For instance, the uniform distribution was chosen for the CAPEX. This kind of distribution requires that the user specify the minimum and maximum values and suggest that all the parameters have an equal chance of occurrence. The uniform distribution was selected for CAPEX because the capital costs were estimated based on information from academic literature, not industrial data. Other parameters such as the utility cost, interest rate, tax rate and feedstock cost were assigned the triangular distribution. The minimum, maximum and most likely values are specified in this kind of distribution.

**Figure 8.10:** Monte Carlo simulation results on the MSP of AC for the three scenarios

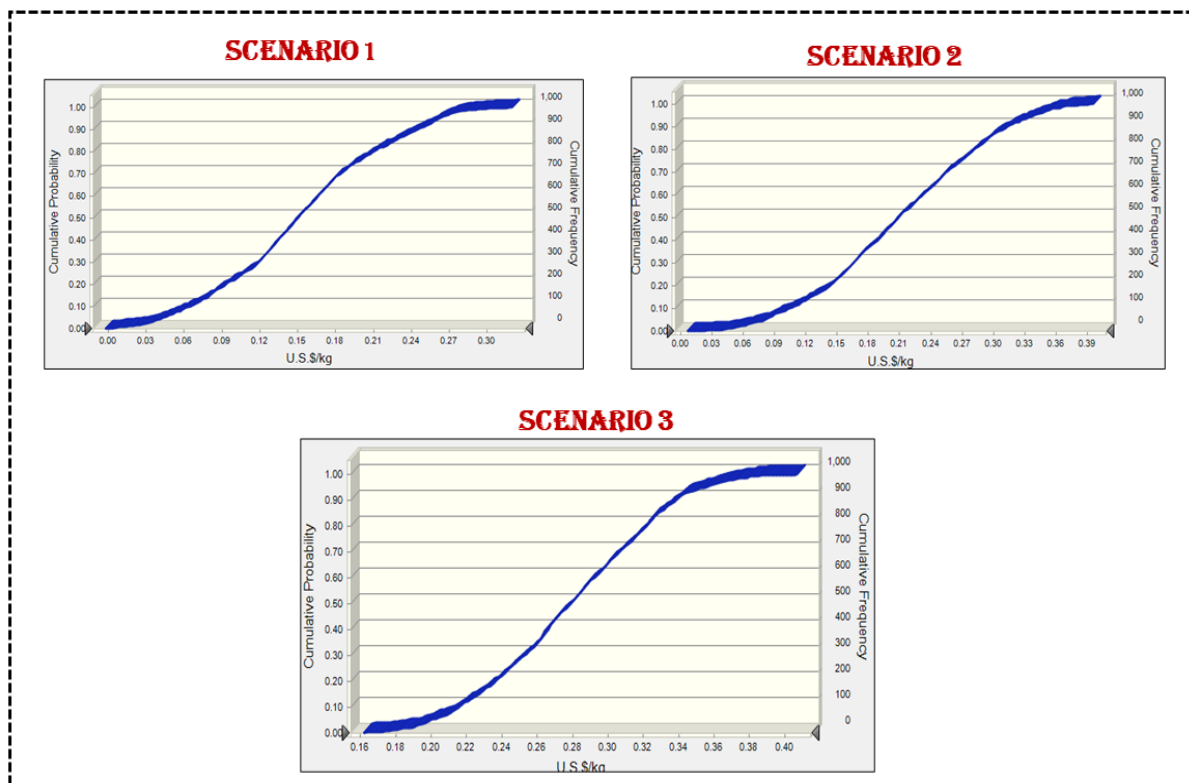


Figure 8.10 shows the cumulative probability function and cumulative frequency curve for 1000 trials. The mean MSP values (50 % probability) for scenarios 1, 2, 3 are 0.151 U.S \$/kg, 0.23 U.S \$/kg and 0.282 U.S \$/kg respectively. Moreover, scenario 1 has a 95% confidence interval for the MSP to be within 0.04 – 0.27 U.S \$/kg. In contrast, scenario 2 showed a 95 % confidence interval for the MSP of AC to be within 0.03 – 0.36 U.S \$/kg. Scenario 3 has MSP range of 0.18 – 0.39 U.S \$/kg at 95% confidence interval. There is a 70% probability for the MSP to be lower than the one computed for all three scenarios. Based on the sensitivity and uncertainty results, the project remains economically viable for all three scenarios considering future uncertainties, including tax rate, interest rate, feedstock, and utility cost. Although, a rigorous lifecycle assessment (LCA) should be performed, and the results combined with TEA before a commercialization decision can be made.

## 8.5 Conclusions

The present study assessed the economic viability of three scenarios for activated carbon production. Scenario 1 includes the slow pyrolysis and CO<sub>2</sub> activation unit. In addition, a flue gas recycling unit was implemented. Scenario 2 comprises flue gas combustion while the third scenario comprises flue gas combustion and deep eutectic solvent impregnation. All the scenarios are economically viable based on the NPV, PBP and MSP determined. The NPV of all the three scenarios is positive, indicating that they are all profitable. However, scenario 1 had the most superior undiscounted NPV of 206.4 million U.S.\$. On the other hand, scenario 3 had the lowest undiscounted NPV of 131.1 million U.S.\$. The AC produced from scenario 1 had the lowest MSP (0.15 U. S \$/kg). In contrast, scenarios 2 and 3 had MSP of AC as 0.21 U. S \$/kg and 0.28 U. S \$/kg respectively. In addition, a positive NPV and compatible MSP with the commercial AC makes the SCG conversion technology to generate AC an economically feasible technique. Furthermore, the sensitivity analysis shows that different factors such as feedstock cost, utility cost, tax rate, interest rate and CAPEX influenced the MSP of AC derived from different scenarios.

## Chapter 9 Summary, conclusions, significant contributions, and recommendations

### 9.1 Overall summary and conclusions

This research successfully developed and analyzed carbon-based adsorbents through different thermochemical conversion techniques for CO<sub>2</sub> removal performance. The overall objective of this thesis was to (1) compare and understand the influence of low (torrefaction) to mild (slow pyrolysis) thermal treatment techniques for the two-stage physical activation process, (2) evaluate the impact of precursors on synthesizing biochar and AC, (3) study the thermal decomposition pattern of the precursors, (4) understand the influence of activation parameters on the textural properties and product yield to optimize the activation conditions, (5) enhance CO<sub>2</sub> adsorption performance of DES functionalized AC samples, and (6) evaluate the economic feasibility of thermochemical conversion technology using SCG as the precursor to produce AC.

This study examined the influence of two independent parameters (torrefaction temperature and residence time) on the mass and energy yield as well as on the physicochemical transformation of the corresponding biomass samples. Based on the modelling results, it was observed that temperature is a crucial parameter that significantly influences the mass and energy yield performance irrespective of the nature of the precursors. For instance, with increasing torrefaction temperature to 300 °C, the mass yield of the corresponding torrefied biomass samples declined remarkably to 75.1% for SCG and 67.5% for CH at 300 °C. The SCG-derived torrefied biomass demonstrated higher equilibrium adsorption capacity of 0.38 mmol/g than CH derived biomass sample (0.23 mmol/g) at 25 °C and in the presence of 30 vol% of CO<sub>2</sub> (balanced by N<sub>2</sub>). Comparatively the better performance of SCG than CH derived torrefied biomass could be owing to its high specific surface area and surface functional groups. The findings reveal that SCG has shown superior CO<sub>2</sub> adsorption capacity than CH but would need further thermal treatment or functionalization to tailor the surface and textural characteristics to attract more CO<sub>2</sub> molecules under a typical post-combustion scenario.

In the second phase the average activation energy calculated to evaluate the thermochemical conversion efficiency of the precursors. The average activation energy for SCG estimated were 101.6 kJmol<sup>-1</sup> (FWO method), 91.56 kJmol<sup>-1</sup> (KAS method) and 90.4 kJmol<sup>-1</sup> (Friedman method). On the other, the activation energy evaluated for CH is slightly higher at 106. 2 kJmol<sup>-1</sup> (FWO method), 96.0 kJmol<sup>-1</sup> (KAS method) and 101 kJmol<sup>-1</sup> (Friedman method). With higher volatile content, high heating value (22.3 MJ/kg), activation energy (90.4-101.6 kJmol<sup>-1</sup>),

Gibbs free energy (146.11-148.35 kJmol<sup>-1</sup>), entropy (-127 Jmol<sup>-1</sup>), lower content of N (2.3 wt%) and S (0.6 wt%) of SCG compared to CH have shown that it has higher potential for adsorbent production than CH and can also be exploited as a feedstock for the production of biochar, in an energy-efficient manner owing to the higher activity or requirement of lower activation energy.

The specific surface area was increased to over five times (539 m<sup>2</sup>/g) than the torrefied biomass prepared under the most severe conditions (100 m<sup>2</sup>/g) or over 250 times than the precursor (2 m<sup>2</sup>/g). Furthermore, the availability of N-5 (pyrrolic and/or pyridonic-N) and N-6 (pyridinic) nitrogenated functional moieties and developed aromatic structure in SCG-600, made a potential candidate to trap CO<sub>2</sub>. The highest equilibrium adsorption capacity of 2.8 mmol/g was obtained using SCG-600 at 30 °C and in presence of 30 vol% of CO<sub>2</sub> in N<sub>2</sub> owing to the synergy between the acid-base interactions and Vander Waals force of interaction between the adsorbate-adsorbent as well as the availability of high specific surface area. It was observed that to proceed for further thermal treatment like activation, biochar produced from slow pyrolysis is more feasible than torrefaction in terms of development in textural characteristics and surface functional moieties. Consequently, the AC sample derived from SCG-600 could be proposed as a promising alternative strategy to capture CO<sub>2</sub>.

To investigate the interactions between process parameters during activation, the Box–Behnken design methodology was used to study the effect of temperature (600–800 °C), reaction time (60–120 min) and gas flow rate (150–250 mL/min) on specific surface area and activated carbon yield. Maximum S<sub>BET</sub> of 1224 m<sup>2</sup>/g and yield of 57.4 % were obtained at 800 °C and 150 mL min<sup>-1</sup> of CO<sub>2</sub> in 90 min of activation time. Further the pristine AC-CO<sub>2</sub> was treated with deep eutectic solvent (choline chloride and urea) to incorporate basic functional groups on its surface. Deep eutectic solvent treated AC sample had comparatively the lower S<sub>BET</sub> (1033 m<sup>2</sup>/g), which is attributed to its recalcitrant chemical structure difficult to decompose even at lower-thermal treatment conditions as well as chemicals clogged the porous structure. However, the superior CO<sub>2</sub> capture of AC-DES-0.4 (5.5 mmol/g) compared to AC-CO<sub>2</sub> (4.34 mmol/g) at 25 °C and in presence of 15 vol% of CO<sub>2</sub> in N<sub>2</sub>. The superior performance of DES functionalised AC (AC-DES-0.4) was attributed to the presence of basic oxygenated (carboxylates, lactones, and phenols) and nitrogenated functional groups (pyrrolic and/or pyridonic-N & pyridinic) on its surface as well as the porous structure available accelerated the CO<sub>2</sub> capture performance under post-combustion scenario. Under a typical post-combustion CO<sub>2</sub> capture scenario, surface functionalities also play a significant role along with the textural

characteristics and so the presence of desired surface functionalities is desirable to enhance the CO<sub>2</sub> capture performance.

In the last phase of the study, the economic viability of the thermochemical conversion technique to synthesize AC using SCG as the potential lignocellulosic feedstock was examined. In this regard, a novel self-sustaining process designed to process 50,000 tons of SCG (dried) annually was proposed. Overall, the study compares different AC production scenarios in terms of their economic feasibility. The AC produced in scenario 1 had the lowest minimum selling price (MSP) of 0.15 U. S \$/kg. In contrast, scenarios 2-3 had MSP of AC as 0.21 U. S \$/kg and 0.28 U. S \$/kg, respectively. Furthermore, the price of the DES-treated AC sample was also compatible with the price of commercially available activated carbon (0.45 US \$/kg). Hence, the findings show that AC (Pristine and DES-treated) production from SCG is a viable and economically feasible technology. The NPV (net present value) of all the proposed three scenarios is positive, ranging from 206.4 million U.S.\$ to 131.1 million U.S.\$. Sensitivity analysis indicates that MSP of AC is mainly affected by the feedstock and utility cost.

## **9.2 Significant contribution to the knowledge**

The significant contribution of this study in extending the knowledge of the production of carbon-based adsorbents from lignocellulosic biomass to capture recalcitrant CO<sub>2</sub> under the post-combustion scenario is listed below.

- ❖ The review article in this study provides a compilation of recent advances in CO<sub>2</sub> capture technologies focusing mainly on the available post-combustion capture techniques, lignocellulose-based biomass utilized to synthesize AC, the influence of different activation agents and challenges and future perspectives. The study also comprehensively highlighted the role of activated carbon in CO<sub>2</sub> removal from the post-combustion capture facility.
- ❖ The thesis provides a detailed understanding of the influence of torrefaction parameters and the effect of precursors on physicochemical characteristics and their candidacy for CO<sub>2</sub> capture. The impact of the torrefaction conditions on the mass and energy yield was determined based on the simulated model determined.
- ❖ The study contributes to understanding the impact of pyrolysis process parameters on the thermal decomposition pattern, kinetics and thermodynamics parameters predicting the most promising feedstock for biochar generation in terms of thermochemical conversion efficiency and physicochemical properties.

- ❖ Spent coffee grounds as representative of the coffee waste was found to be a promising precursor for biochar production. Consequently, the study adds to the knowledge of biochar generation from SCG with tailored surface and textural properties required for CO<sub>2</sub> removal from simulated flue gas stream.
- ❖ The thesis provides a comprehensive understanding of the effect of the activation parameters on specific surface area and AC yield. Furthermore, the study highlighted the influence of natural deep eutectic solvent in transforming the surface chemistry for CO<sub>2</sub> capture performance.
- ❖ The techno-economic assessment of the AC production reveals that the thermochemical conversion of SCG is an economically feasible strategy. The price of AC is the most critical determining factor of an AC production plant's economic feasibility. From a financial standpoint, the proposed scenarios for the thermochemical conversion process were found to be profitable.

### **9.3 Future Recommendations**

- ❖ Compare the potential of different low-temperature thermochemical conversion techniques like hydrothermal carbonization (HTC) or hydrothermal liquefaction (HTL) to synthesize biochar using lignocellulose biomass as the starting material in terms of their physicochemical properties and CO<sub>2</sub> adsorption performance.
- ❖ To evaluate the kinetic parameters of a thermochemical conversion process like slow pyrolysis using computational fluid dynamics (CFD) technique.
- ❖ In the future, compare the conventional and microwave-assisted pyrolysis techniques to produce biochar in terms of biochar's yield and physicochemical properties and compare the CO<sub>2</sub> capture performance. Also, study the impact of co-pyrolysis on the physicochemical properties of biochar and CO<sub>2</sub> capture performance.
- ❖ In future, compare the properties of AC samples obtained by using a mixture of CO<sub>2</sub> and N<sub>2</sub> in the flue gas combination as the activating agent to make the overall activation process economically feasible.
- ❖ To reduce the energy requirement during the two-step activation technique, the microwave-assisted ultrasonic pathway could be explored to determine its candidacy in AC synthesis with desired physicochemical properties for CO<sub>2</sub> removal. Also, study the impact of particle size of the precursor and AC samples on the physicochemical characteristics and CO<sub>2</sub> removal performance.



- ❖ Studies comparing the influence of various adsorption parameters using a sophisticated tool like machine learning (artificial neural network, ANN) and validating the findings with statistical tools like (BBD or CCD) are necessary to propose the optimized CO<sub>2</sub> adsorption conditions in a pressure swing adsorption unit. The flue gas stream containing traces of moisture along with other gases (CO<sub>2</sub>, N<sub>2</sub> and O<sub>2</sub>) could help elucidate the activated carbon's hydrophobic role. Hence, investigating the effect of moisture is recommended in future.
- ❖ For potential industrial applications of AC derived from SCG, a detailed CO<sub>2</sub> capture unit in the TEA analysis and life cycle assessment (LCA) should be conducted to assess the conversion technique's overall environmental impact and economic viability. However, designing a reliable life cycle assessment would demand huge time and effort.
- ❖ A comparative evaluation of various promising solid adsorbents such as carbon nanotubes or zeolite should be examined regarding CO<sub>2</sub> removal performance and economic feasibility.

## List of References

- ❖ Abioye, A.M., Abdulkadir, L.N., Sintali, I.S., Bawa, M.A., Ani, F.N., 2020. Temperature Controlled Microwave-Induced CO<sub>2</sub> Activated Carbon: Optimization Using Box-Behnken Design 198, 129–135. <https://doi.org/10.2991/aer.k.201221.023>
- ❖ Acharya, B., Dutta, A., Minaret, J., 2015. Review on comparative study of dry and wet torrefaction. *Sustain. Energy Technol. Assessments* 12, 26–37. <https://doi.org/10.1016/j.seta.2015.08.003>
- ❖ Afolabi, O.O.D., Sohail, M., Cheng, Y.L., 2020. Optimisation and characterisation of hydrochar production from spent coffee grounds by hydrothermal carbonisation. *Renew. Energy* 147, 1380–1391. <https://doi.org/10.1016/j.renene.2019.09.098>
- ❖ Ahmad, M.S., Mehmood, M.A., Al Ayed, O.S., Ye, G., Luo, H., Ibrahim, M., Rashid, U., Arbi Nehdi, I., Qadir, G., 2017. Kinetic analyses and pyrolytic behavior of Para grass (*Urochloa mutica*) for its bioenergy potential. *Bioresour. Technol.* 224, 708–713. <https://doi.org/10.1016/j.biortech.2016.10.090>
- ❖ Akhtar, J., Saidina Amin, N., 2012. A review on operating parameters for optimum liquid oil yield in biomass pyrolysis. *Renew. Sustain. Energy Rev.* 16, 5101–5109. <https://doi.org/10.1016/j.rser.2012.05.033>
- ❖ Al-Hamamre, Z., Foerster, S., Hartmann, F., Kröger, M., Kaltschmitt, M., 2012. Oil extracted from spent coffee grounds as a renewable source for fatty acid methyl ester manufacturing. *Fuel* 96, 70–76. <https://doi.org/10.1016/j.fuel.2012.01.023>
- ❖ Al-Wabel, M., Elfaki, J., Usman, A., Hussain, Q., Ok, Y.S., 2019. Performance of dry water- and porous carbon-based sorbents for carbon dioxide capture. *Environ. Res.* 174, 69–79. <https://doi.org/10.1016/j.envres.2019.04.020>
- ❖ Al Mesfer, M.K., Danish, M., 2018. Breakthrough adsorption study of activated carbons for CO<sub>2</sub> separation from flue gas. *J. Environ. Chem. Eng.* 6, 4514–4524. <https://doi.org/10.1016/j.jece.2018.06.042>
- ❖ Alabadi, A., Razzaque, S., Yang, Y., Chen, S., Tan, B., 2015. Highly porous activated carbon materials from carbonized biomass with high CO<sub>2</sub> capturing capacity. *Chem. Eng. J.* 281, 606–612. <https://doi.org/10.1016/j.cej.2015.06.032>
- ❖ Anastopoulos, I., Karamesouti, M., Mitropoulos, A.C., Kyzas, G.Z., 2017. A review for coffee adsorbents. *J. Mol. Liq.* 229, 555–565. <https://doi.org/10.1016/j.molliq.2016.12.096>
- ❖ Ashraf, A., Sattar, H., Munir, S., 2019. Thermal decomposition study and pyrolysis kinetics of coal and agricultural residues under non-isothermal conditions. *Fuel* 235, 504–514.

<https://doi.org/10.1016/j.fuel.2018.07.120>

- ❖ ASTM D3175-11, 2011. Standard method for volatile matter in the analysis sample of coal and coke, ASTM International, Pennsylvania.
- ❖ ASTM E1755-01, 2007. Standard test method for ash in biomass, ASTM International, Pennsylvania.
- ❖ ASTM E871-82, 2006. Standard test method for moisture analysis of particulate wood fuels, ASTM International, Pennsylvania.
- ❖ Azargohar, R., Dalai, A.K., 2005. Production of activated carbon from Luscar char: Experimental and modeling studies. *Microporous Mesoporous Mater.* 85, 219–225. <https://doi.org/10.1016/j.micromeso.2005.06.018>
- ❖ Azargohar, R., Jacobson, K.L., Powell, E.E., Dalai, A.K., 2013. Evaluation of properties of fast pyrolysis products obtained, from Canadian waste biomass. *J. Anal. Appl. Pyrolysis* 104, 330–340. <https://doi.org/10.1016/j.jaap.2013.06.016>
- ❖ Azargohar, R., Nanda, S., Dalai, A.K., Kozinski, J.A., 2019. Physico-chemistry of biochars produced through steam gasification and hydro-thermal gasification of canola hull and canola meal pellets. *Biomass and Bioenergy* 120, 458–470. <https://doi.org/10.1016/j.biombioe.2018.12.011>
- ❖ Bach, Q.V., Skreiberg, Ø., Lee, C.J., 2017. Process modeling and optimization for torrefaction of forest residues. *Energy* 138, 348–354. <https://doi.org/10.1016/j.energy.2017.07.040>
- ❖ Badger, P.C., Fransham, P., 2006. Use of mobile fast pyrolysis plants to densify biomass and reduce biomass handling costs - A preliminary assessment. *Biomass and Bioenergy* 30, 321–325. <https://doi.org/10.1016/j.biombioe.2005.07.011>
- ❖ Barskov, S., Zappi, M., Buchireddy, P., Dufreche, S., Guillory, J., Gang, D., Hernandez, R., Bajpai, R., Baudier, J., Cooper, R., Sharp, R., 2019. Torrefaction of biomass: A review of production methods for biocoal from cultured and waste lignocellulosic feedstocks. *Renew. Energy* 142, 624–642. <https://doi.org/10.1016/j.renene.2019.04.068>
- ❖ Batista, M.J.P.A., Ávila, A.F., Franca, A.S., Oliveira, L.S., 2020. Polysaccharide-rich fraction of spent coffee grounds as promising biomaterial for films fabrication. *Carbohydr. Polym.* 233, 115851. <https://doi.org/10.1016/j.carbpol.2020.115851>
- ❖ Ben-Mansour, R., Habib, M.A., Bamidele, O.E., Basha, M., Qasem, N.A.A., Peedikakkal, A., Laoui, T., Ali, M., 2016. Carbon capture by physical adsorption: Materials, experimental investigations and numerical modeling and simulations - A review. *Appl. Energy* 161, 225–255. <https://doi.org/10.1016/j.apenergy.2015.10.011>
- ❖ Bernard, S., Beyssac, O., Benzerara, K., Findling, N., Tzvetkov, G., Brown, G.E., 2010.

- XANES, Raman and XRD study of anthracene-based cokes and saccharose-based chars submitted to high-temperature pyrolysis. *Carbon* N. Y. 48, 2506–2516. <https://doi.org/10.1016/j.carbon.2010.03.024>
- ❖ Biagini, E., Barontini, F., Tognotti, L., 2017. Thermal decomposition of agricultural and food residues: Comparison of kinetic models. *Can. J. Chem. Eng.* 95, 913–921. <https://doi.org/10.1002/cjce.22738>
  - ❖ Biswas, B., Pandey, N., Bisht, Y., Singh, R., Kumar, J., Bhaskar, T., 2017. Pyrolysis of agricultural biomass residues: Comparative study of corn cob, wheat straw, rice straw and rice husk. *Bioresour. Technol.* 237, 57–63. <https://doi.org/10.1016/j.biortech.2017.02.046>
  - ❖ Bonaventura, D., Chacartegui, R., Valverde, J.M., Becerra, J.A., Verda, V., 2017. Carbon capture and utilization for sodium bicarbonate production assisted by solar thermal power. *Energy Convers. Manag.* 149, 860–874. <https://doi.org/10.1016/j.enconman.2017.03.042>
  - ❖ Bora, R.R., Tao, Y., Lehmann, J., Tester, J.W., Richardson, R.E., You, F., 2020. Techno-Economic Feasibility and Spatial Analysis of Thermochemical Conversion Pathways for Regional Poultry Waste Valorization. *ACS Sustain. Chem. Eng.* 8, 5763–5775. <https://doi.org/10.1021/acssuschemeng.0c01229>
  - ❖ Bosoaga, A., Masek, O., Oakey, J.E., 2009. CO<sub>2</sub> Capture Technologies for Cement Industry. *Energy Procedia* 1, 133–140. <https://doi.org/10.1016/j.egypro.2009.01.020>
  - ❖ Braga, R.M., Melo, D.M.A., Aquino, F.M., Freitas, J.C.O., Melo, M.A.F., Barros, J.M.F., Fontes, M.S.B., 2014. Characterization and comparative study of pyrolysis kinetics of the rice husk and the elephant grass. *J. Therm. Anal. Calorim.* 115, 1915–1920. <https://doi.org/10.1007/s10973-013-3503-7>
  - ❖ Buhre, B.J.P., Elliott, L.K., Sheng, C.D., Gupta, R.P., Wall, T.F., 2005. Oxy-fuel combustion technology for coal-fired power generation. *Prog. Energy Combust. Sci.* 31, 283–307. <https://doi.org/10.1016/j.pecs.2005.07.001>
  - ❖ Cai, J., He, Y., Yu, X., Banks, S.W., Yang, Y., Zhang, X., Yu, Y., Liu, R., Bridgwater, A. V., 2017. Review of physicochemical properties and analytical characterization of lignocellulosic biomass. *Renew. Sustain. Energy Rev.* 76, 309–322. <https://doi.org/10.1016/j.rser.2017.03.072>
  - ❖ Cai, J., Xu, D., Dong, Z., Yu, X., Yang, Y., Banks, S.W., Bridgwater, A. V., 2018. Processing thermogravimetric analysis data for isoconversional kinetic analysis of lignocellulosic biomass pyrolysis: Case study of corn stalk. *Renew. Sustain. Energy Rev.* 82, 2705–2715. <https://doi.org/10.1016/j.rser.2017.09.113>
  - ❖ Ceylan, S., Topçu, Y., 2014. Pyrolysis kinetics of hazelnut husk using thermogravimetric analysis. *Bioresour. Technol.* 156, 182–188. <https://doi.org/10.1016/j.biortech.2014.01.040>

- ❖ Chand, R., Babu Borugadda, V., Qiu, M., Dalai, A.K., 2019. Evaluating the potential for bio-fuel upgrading: A comprehensive analysis of bio-crude and bio-residue from hydrothermal liquefaction of agricultural biomass. *Appl. Energy* 254, 113679. <https://doi.org/10.1016/j.apenergy.2019.113679>
- ❖ Chao, C., Deng, Y., Dewil, R., Baeyens, J., Fan, X., 2021. Post-combustion carbon capture. *Renew. Sustain. Energy Rev.* 138, 110490. <https://doi.org/10.1016/j.rser.2020.110490>
- ❖ Chapel, D.G., Mariz, C.L., Ernest, J., 1999. Recovery of CO<sub>2</sub> from Flue Gases : Commercial Trends. *Can. Soc. Chem. Eng. Annu. Meet.* 17.
- ❖ Charcoal, Activated, Norit®, Alkaline, Decolourizing | Canadawide [WWW Document], 2021.
- ❖ Chen, J., Yang, J., Hu, G., Hu, X., Li, Z., Shen, S., Radosz, M., Fan, M., 2016. Enhanced CO<sub>2</sub> Capture Capacity of Nitrogen-Doped Biomass-Derived Porous Carbons. *ACS Sustain. Chem. Eng.* 4, 1439–1445. <https://doi.org/10.1021/acssuschemeng.5b01425>
- ❖ Chen, W., Du, S., Tsai, C., Wang, Z., 2012a. Bioresource Technology Torrefied biomasses in a drop tube furnace to evaluate their utility in blast furnaces. *Bioresour. Technol.* 111, 433–438. <https://doi.org/10.1016/j.biortech.2012.01.163>
- ❖ Chen, W., Lu, K., Tsai, C., 2012b. An experimental analysis on property and structure variations of agricultural wastes undergoing torrefaction. *Appl. Energy* 100, 318–325. <https://doi.org/10.1016/j.apenergy.2012.05.056>
- ❖ Chen, W., Peng, J., Bi, X.T., 2015. A state-of-the-art review of biomass torrefaction , densification and applications. *Renew. Sustain. Energy Rev.* 44, 847–866. <https://doi.org/10.1016/j.rser.2014.12.039>
- ❖ Chen, Y., Chen, W., Lin, B., Chang, J., Chyuan, H., 2016. Impact of torrefaction on the composition , structure and reactivity of a microalga residue. *Appl. Energy* 181, 110–119. <https://doi.org/10.1016/j.apenergy.2016.07.130>
- ❖ Chen, Z., Deng, S., Wei, H., Wang, B., Huang, J., Yu, G., 2013. Activated carbons and amine-modified materials for carbon dioxide capture -- A review. *Front. Environ. Sci. Eng.* 7, 326–340. <https://doi.org/10.1007/s11783-013-0510-7>
- ❖ Cheng, F., Luo, H., Colosi, L.M., 2020. Slow pyrolysis as a platform for negative emissions technology: An integration of machine learning models, life cycle assessment, and economic analysis. *Energy Convers. Manag.* 223, 113258. <https://doi.org/10.1016/j.enconman.2020.113258>
- ❖ Chingombe, P., Saha, B., Wakeman, R.J., 2005. Surface modification and characterisation of a coal-based activated carbon. *Carbon N. Y.* 43, 3132–3143. <https://doi.org/10.1016/j.carbon.2005.06.021>

- ❖ Chiodo, V., Zafarana, G., Maisano, S., Freni, S., Urbani, F., 2016. Pyrolysis of different biomass: Direct comparison among *Posidonia Oceanica*, Lacustrine Alga and White-Pine. *Fuel* 164, 220–227. <https://doi.org/10.1016/j.fuel.2015.09.093>
- ❖ Coffey, T., Urquhart, S.G., Ade, H., 2002. Characterization of the effects of soft X-ray irradiation on polymers. *J. Electron Spectros. Relat. Phenomena* 122, 65–78. [https://doi.org/10.1016/S0368-2048\(01\)00342-5](https://doi.org/10.1016/S0368-2048(01)00342-5)
- ❖ Creamer, A.E., Gao, B., Zhang, M., 2014. Carbon dioxide capture using biochar produced from sugarcane bagasse and hickory wood. *Chem. Eng. J.* 249, 174–179. <https://doi.org/10.1016/j.cej.2014.03.105>
- ❖ Cruz, G., Crnkovic, P.M., 2016. Investigation into the kinetic behavior of biomass combustion under N<sub>2</sub>/O<sub>2</sub> and CO<sub>2</sub>/O<sub>2</sub> atmospheres. *J. Therm. Anal. Calorim.* 123, 1003–1011. <https://doi.org/10.1007/s10973-015-4908-2>
- ❖ Dai, L., Wang, Y., Liu, Y., Ruan, R., He, C., Yu, Z., Jiang, L., Zeng, Z., Tian, X., 2019. Integrated process of lignocellulosic biomass torrefaction and pyrolysis for upgrading bio-oil production: A state-of-the-art review. *Renew. Sustain. Energy Rev.* 107, 20–36. <https://doi.org/10.1016/j.rser.2019.02.015>
- ❖ Damartzis, T., Vamvuka, D., Sfakiotakis, S., Zabaniotou, A., 2011. Thermal degradation studies and kinetic modeling of cardoon (*Cynara cardunculus*) pyrolysis using thermogravimetric analysis (TGA). *Bioresour. Technol.* 102, 6230–6238. <https://doi.org/10.1016/j.biortech.2011.02.060>
- ❖ Dantas, T.L.P., Luna, F.M.T., Silva, I.J., de Azevedo, D.C.S., Grande, C.A., Rodrigues, A.E., Moreira, R.F.P.M., 2011. Carbon dioxide-nitrogen separation through adsorption on activated carbon in a fixed bed. *Chem. Eng. J.* 169, 11–19. <https://doi.org/10.1016/j.cej.2010.08.026>
- ❖ Das, S., Mishra, S., 2017. Box-Behnken statistical design to optimize preparation of activated carbon from *Limonia acidissima* shell with desirability approach. *J. Environ. Chem. Eng.* 5, 588–600. <https://doi.org/10.1016/j.jece.2016.12.034>
- ❖ Doyle, Charles D., 1965. Series approximations to the equation of thermogravimetric data. *Nature* 207.4994: 290-291.
- ❖ Dean, C.C., Blamey, J., Florin, N.H., Al-Jeboori, M.J., Fennell, P.S., 2011. The calcium looping cycle for CO<sub>2</sub> capture from power generation, cement manufacture and hydrogen production. *Chem. Eng. Res. Des.* 89, 836–855. <https://doi.org/10.1016/j.cherd.2010.10.013>
- ❖ Deng, S., Wei, H., Chen, T., Wang, B., Huang, J., Yu, G., 2014. Superior CO<sub>2</sub> adsorption on pine nut shell-derived activated carbons and the effective micropores at different temperatures. *Chem. Eng. J.* 253, 46–54. <https://doi.org/10.1016/j.cej.2014.04.115>

- ❖ di Stasio, S., Braun, A., 2006. Comparative NEXAFS study on soot obtained from an ethylene/air flame, a diesel engine, and graphite. *Energy and Fuels* 20, 187–194. <https://doi.org/10.1021/ef058019g>
- ❖ Dilokekunakul, W., Teerachawanwong, P., Klomkliang, N., Supasitmongkol, S., Chaemchuen, S., 2020. Effects of nitrogen and oxygen functional groups and pore width of activated carbon on carbon dioxide capture: Temperature dependence. *Chem. Eng. J.* 389, 124413. <https://doi.org/10.1016/j.cej.2020.124413>
- ❖ Dodevski, V., Janković, B., Stojmenović, M., Krstić, S., Popović, J., Pagnacco, M.C., Popović, M., Pašalić, S., 2017. Plane tree seed biomass used for preparation of activated carbons (AC) derived from pyrolysis. Modeling the activation process. *Colloids Surfaces A Physicochem. Eng. Asp.* 522, 83–96. <https://doi.org/10.1016/j.colsurfa.2017.03.003>
- ❖ Du, Y., Lv, Y., Zha, W., Hong, X., Luo, Q., 2020. Effect of coffee consumption on dyslipidemia: A meta-analysis of randomized controlled trials. *Nutr. Metab. Cardiovasc. Dis.* 30, 2159–2170. <https://doi.org/10.1016/j.numecd.2020.08.017>
- ❖ Edathil, A.A., Shittu, I., Zain, J.H., Banat, F., 2018. Journal of Environmental Chemical Engineering Novel magnetic coffee waste nanocomposite as effective bioadsorbent for Pb (II) removal from aqueous solutions. *J. Environ. Chem. Eng.* 6, 2390–2400. <https://doi.org/10.1016/j.jece.2018.03.041>
- ❖ El-Sayed, S.A., Mostafa, M.E., 2014. Pyrolysis characteristics and kinetic parameters determination of biomass fuel powders by differential thermal gravimetric analysis (TGA/DTG). *Energy Convers. Manag.* 85, 165–172. <https://doi.org/10.1016/j.enconman.2014.05.068>
- ❖ Fakayode, O.A., Aboagarib, E.A.A., Zhou, C., Ma, H., 2020. Co-pyrolysis of lignocellulosic and macroalgae biomasses for the production of biochar – A review. *Bioresour. Technol.* 297, 122408. <https://doi.org/10.1016/j.biortech.2019.122408>
- ❖ Feroso, J., 2018. Journal of Analytical and Applied Pyrolysis Thermochemical decomposition of coffee ground residues by TG-MS: A kinetic study 130, 358–367. <https://doi.org/10.1016/j.jaap.2017.12.007>
- ❖ Firdaus, R.M., Desforges, A., Emo, M., Mohamed, A.R., Vigolo, B., 2021. Physical and chemical activation of graphene-derived porous nanomaterials for post-combustion carbon dioxide capture. *Nanomaterials* 11, 1–14. <https://doi.org/10.3390/nano11092419>
- ❖ Fiuza-Jr, R.A., Andrade, R.C., Andrade, H.M.C., 2016. CO<sub>2</sub> capture on KOH-activated carbons derived from yellow mombin fruit stones. *J. Environ. Chem. Eng.* 4, 4229–4236. <https://doi.org/10.1016/j.jece.2016.09.025>

- ❖ Fiuza-jr, R.A., Andrade, R.C., Martins, H., Andrade, C., 2016. Journal of Environmental Chemical Engineering CO<sub>2</sub> capture on KOH-activated carbons derived from yellow mombin fruit stones. *Biochem. Pharmacol.* 4, 4229–4236. <https://doi.org/10.1016/j.jece.2016.09.025>
- ❖ Franciski, M.A., Peres, E.C., Godinho, M., Perondi, D., Foletto, E.L., Collazzo, G.C., Dotto, G.L., 2018. Development of CO<sub>2</sub> activated biochar from solid wastes of a beer industry and its application for methylene blue adsorption. *Waste Manag.* 78, 630–638. <https://doi.org/10.1016/j.wasman.2018.06.040>
- ❖ Friedl, A., Padouvas, E., Rotter, H., Varmuza, K., 2005. Prediction of heating values of biomass fuel from elemental composition. *Anal. Chim. Acta* 544, 191–198. <https://doi.org/10.1016/j.aca.2005.01.041>
- ❖ Gai, C., Dong, Y., Zhang, T., 2013. The kinetic analysis of the pyrolysis of agricultural residue under non-isothermal conditions. *Bioresour. Technol.* 127, 298–305. <https://doi.org/10.1016/j.biortech.2012.09.089>
- ❖ Garip, M., Gizli, N., 2020. Ionic liquid containing amine-based silica aerogels for CO<sub>2</sub> capture by fixed bed adsorption. *J. Mol. Liq.* 310, 113227. <https://doi.org/10.1016/j.molliq.2020.113227>
- ❖ Gascó, G., Paz-Ferreiro, J., Álvarez, M.L., Saa, A., Méndez, A., 2018. Biochars and hydrochars prepared by pyrolysis and hydrothermal carbonisation of pig manure. *Waste Manag.* 79, 395–403. <https://doi.org/10.1016/j.wasman.2018.08.015>
- ❖ Gassensmith, J.J., Furukawa, H., Smaldone, R.A., Forgan, R.S., Botros, Y.Y., Yaghi, O.M., Stoddart, J.F., 2011. Strong and reversible binding of carbon dioxide in a green metal-organic framework. *J. Am. Chem. Soc.* 133, 15312–15315. <https://doi.org/10.1021/ja206525x>
- ❖ Goel, C., Bhunia, H., Bajpai, P.K., 2016. Novel nitrogen enriched porous carbon adsorbents for CO<sub>2</sub> capture: Breakthrough adsorption study. *J. Environ. Chem. Eng.* 4, 346–356. <https://doi.org/10.1016/j.jece.2015.11.017>
- ❖ Goel, C., Bhunia, H., Bajpai, P.K., 2015. Synthesis of nitrogen doped mesoporous carbons for carbon dioxide capture. *RSC Adv.* 5, 46568–46582. <https://doi.org/10.1039/c5ra05684e>
- ❖ González, A.S., Plaza, M.G., Rubiera, F., Pevida, C., 2013. Sustainable biomass-based carbon adsorbents for post-combustion CO<sub>2</sub> capture. *Chem. Eng. J.* 230, 456–465. <https://doi.org/10.1016/j.cej.2013.06.118>
- ❖ Granite, E.J., Pennline, H.W., 2002. Photochemical removal of mercury from flue gas. *Ind. Eng. Chem. Res.* 41, 5470–5476. <https://doi.org/10.1021/ie020251b>
- ❖ Gutiérrez Ortiz, F.J., 2020. Techno-economic assessment of supercritical processes for biofuel production. *J. Supercrit. Fluids* 160, 1–15. <https://doi.org/10.1016/j.supflu.2020.104788>



- ❖ Haeldermans, T., Campion, L., Kuppens, T., Vanreppelen, K., Cuypers, A., Schreurs, S., 2020. A comparative techno-economic assessment of biochar production from different residue streams using conventional and microwave pyrolysis. *Bioresour. Technol.* 318, 124083. <https://doi.org/10.1016/j.biortech.2020.124083>
- ❖ Han, J., Zhang, L., Zhao, B., Qin, L., Wang, Y., Xing, F., 2019a. Industrial Crops & Products The N-doped activated carbon derived from sugarcane bagasse for CO<sub>2</sub> adsorption. *Ind. Crop. Prod.* 128, 290–297. <https://doi.org/10.1016/j.indcrop.2018.11.028>
- ❖ Han, J., Zhang, L., Zhao, B., Qin, L., Wang, Y., Xing, F., 2019b. The N-doped activated carbon derived from sugarcane bagasse for CO<sub>2</sub> adsorption. *Ind. Crops Prod.* 128, 290–297. <https://doi.org/10.1016/j.indcrop.2018.11.028>
- ❖ Harsono, S.S., Grundman, P., Lau, L.H., Hansen, A., Salleh, M.A.M., Meyer-Aurich, A., Idris, A., Ghazi, T.I.M., 2013. Energy balances, greenhouse gas emissions and economics of biochar production from palm oil empty fruit bunches. *Resour. Conserv. Recycl.* 77, 108–115. <https://doi.org/10.1016/j.resconrec.2013.04.005>
- ❖ Hedin, N., Chen, L., Laaksonen, A., 2010. Sorbents for CO<sub>2</sub> capture from flue gas - Aspects from materials and theoretical chemistry. *Nanoscale* 2, 1819–1841. <https://doi.org/10.1039/c0nr00042f>
- ❖ Heo, Y.J., Park, S.J., 2015. A role of steam activation on CO<sub>2</sub> capture and separation of narrow microporous carbons produced from cellulose fibers. *Energy* 91, 142–150. <https://doi.org/10.1016/j.energy.2015.08.033>
- ❖ Herawan, S.G., Hadi, M.S., Ayob, M.R., Putra, A., 2013. Characterization of activated carbons from oil-palm shell by CO<sub>2</sub> activation with no holding carbonization temperature. *Sci. World J.* 2013. <https://doi.org/10.1155/2013/624865>
- ❖ Hernández Rodríguez, M., Yperman, J., Carleer, R., Maggen, J., Daddi, D., Gryglewicz, G., Van der Bruggen, B., Falcón Hernández, J., Otero Calvis, A., 2018. Adsorption of Ni(II) on spent coffee and coffee husk based activated carbon. *J. Environ. Chem. Eng.* 6, 1161–1170. <https://doi.org/10.1016/j.jece.2017.12.045>
- ❖ Heymann, K., Lehmann Johannes, J., Solomon, D., Schmidt, M.W.I., Regier, T., 2011. C 1s K-edge near edge X-ray absorption fine structure (NEXAFS) spectroscopy for characterizing functional group chemistry of black carbon. *Org. Geochem.* 42, 1055–1064. <https://doi.org/10.1016/j.orggeochem.2011.06.021>
- ❖ Hornbostel, M.D., Bao, J., Krishnan, G., Nagar, A., Jayaweera, I., Kobayashi, T., Sanjurjo, A., Sweeney, J., Carruthers, D., Petruska, M.A., Dubois, L., 2013. Characteristics of an advanced carbon sorbent for CO<sub>2</sub> capture. *Carbon* N. Y. 56, 77–85.

<https://doi.org/10.1016/j.carbon.2012.12.082>

- ❖ Hu, M., Chen, Z., Wang, S., Guo, D., Ma, C., Zhou, Y., Chen, J., Laghari, M., Fazal, S., Xiao, B., Zhang, B., Ma, S., 2016. Thermogravimetric kinetics of lignocellulosic biomass slow pyrolysis using distributed activation energy model, Fraser-Suzuki deconvolution, and iso-conversional method. *Energy Convers. Manag.* 118, 1–11. <https://doi.org/10.1016/j.enconman.2016.03.058>
- ❖ Huang, B., Xie, X., Yang, Y., Rahman, M.M., Zhang, X., Yu, X., Blanco, P.H., Dong, Z., Zhang, Y., Bridgwater, A. V., Cai, J., 2019. Reaction chemistry and kinetics of corn stalk pyrolysis without and with Ga/HZSM-5. *J. Therm. Anal. Calorim.* 137, 491–500. <https://doi.org/10.1007/s10973-018-7962-8>
- ❖ Hussin, F., Aroua, M.K., Yusoff, R., 2021a. Adsorption of CO<sub>2</sub> on palm shell based activated carbon modified by deep eutectic solvent: Breakthrough adsorption study. *J. Environ. Chem. Eng.* 9. <https://doi.org/10.1016/j.jece.2021.105333>
- ❖ Hussin, F., Aroua, M.K., Yusoff, R., 2021b. Adsorption of CO<sub>2</sub> on palm shell based activated carbon modified by deep eutectic solvent: Breakthrough adsorption study. *J. Environ. Chem. Eng.* 9, 105333. <https://doi.org/10.1016/j.jece.2021.105333>
- ❖ Ibn Ferjani, A., Jeguirim, M., Jellali, S., Limousy, L., Courson, C., Akrou, H., Thevenin, N., Ruidavets, L., Muller, A., Bennici, S., 2019. The use of exhausted grape marc to produce biofuels and biofertilizers: Effect of pyrolysis temperatures on biochars properties. *Renew. Sustain. Energy Rev.* 107, 425–433. <https://doi.org/10.1016/j.rser.2019.03.034>
- ❖ Idrees, M., Rangari, V., Jeelani, S., 2018. Sustainable packaging waste-derived activated carbon for carbon dioxide capture. *J. CO<sub>2</sub> Util.* 26, 380–387. <https://doi.org/10.1016/j.jcou.2018.05.016>
- ❖ Igalavithana, A.D., Choi, S.W., Shang, J., Hanif, A., Dissanayake, P.D., Tsang, D.C.W., Kwon, J.H., Lee, K.B., Ok, Y.S., 2020. Carbon dioxide capture in biochar produced from pine sawdust and paper mill sludge: Effect of porous structure and surface chemistry. *Sci. Total Environ.* 739, 139845. <https://doi.org/10.1016/j.scitotenv.2020.139845>
- ❖ Ikegwu, Ugochukwu Michael, Ozonoh, M., Daramola, M.O., 2021. Kinetic Study of the Isothermal Degradation of Pine Sawdust during Torrefaction Process. *ACS Omega* 6, 10759–10769. <https://doi.org/10.1021/acsomega.1c00327>
- ❖ Ikegwu, Ugochukwu M, Ozonoh, M., Okoro, N.M., Daramola, M.O., 2021. Effect and Optimization of Process Conditions during Solvolysis and Torrefaction of Pine Sawdust Using the Desirability Function and Genetic Algorithm. <https://doi.org/10.1021/acsomega.1c00857>
- ❖ Illing, G., Hellgardt, K., Wakeman, R.J., Jungbauer, A., 2001. Preparation and characterisation

of polyaniline based membranes for gas separation. *J. Memb. Sci.* 184, 69–78. [https://doi.org/10.1016/S0376-7388\(00\)00606-2](https://doi.org/10.1016/S0376-7388(00)00606-2)

- ❖ Ismail, I.S., Singh, G., Smith, P., Kim, S., Yang, J.H., Joseph, S., Yusup, S., Singh, M., Bansal, V., Talapaneni, S.N., Vinu, A., 2020. Oxygen functionalized porous activated biocarbons with high surface area derived from grape marc for enhanced capture of CO<sub>2</sub> at elevated-pressure. *Carbon N. Y.* 160, 113–124. <https://doi.org/10.1016/j.carbon.2020.01.008>
- ❖ Jain, S., Kumar, P., Vyas, R.K., Pandit, P., Dalai, A.K., 2014. Adsorption optimization of acyclovir on prepared activated carbon. *Can. J. Chem. Eng.* 92, 1627–1635. <https://doi.org/10.1002/cjce.22026>
- ❖ Janissen, B., Huynh, T., 2018. Chemical composition and value-adding applications of coffee industry by-products: A review. *Resour. Conserv. Recycl.* 128, 110–117. <https://doi.org/10.1016/j.resconrec.2017.10.001>
- ❖ Jawad, A.H., Ismail, K., Ishak, M.A.M., Wilson, L.D., 2019. Conversion of Malaysian low-rank coal to mesoporous activated carbon: Structure characterization and adsorption properties. *Chinese J. Chem. Eng.* 27, 1716–1727. <https://doi.org/10.1016/j.cjche.2018.12.006>
- ❖ Jenkins, R.W., Stageman, N.E., Fortune, C.M., Chuck, C.J., 2014. Effect of the type of bean, processing, and geographical location on the biodiesel produced from waste coffee grounds. *Energy and Fuels* 28, 1166–1174. <https://doi.org/10.1021/ef4022976>
- ❖ Jiang, H., Ye, Y., Lu, P., Zhao, M., Xu, G., Chen, D., Song, T., 2021. Effects of torrefaction conditions on the hygroscopicity of biochars. *J. Energy Inst.* 96, 260–268. <https://doi.org/10.1016/j.joei.2021.03.018>
- ❖ Kanniche, M., Gros-Bonnivard, R., Jaud, P., Valle-Marcos, J., Amann, J.M., Bouallou, C., 2010. Pre-combustion, post-combustion and oxy-combustion in thermal power plant for CO<sub>2</sub> capture. *Appl. Therm. Eng.* 30, 53–62. <https://doi.org/10.1016/j.applthermaleng.2009.05.005>
- ❖ Karmee, S.K., 2018. A spent coffee grounds based biorefinery for the production of biofuels, biopolymers, antioxidants and biocomposites. *Waste Manag.* 72, 240–254. <https://doi.org/10.1016/j.wasman.2017.10.042>
- ❖ Karunakaran, C., Vijayan, P., Stobbs, J., Bamrah, R.K., Arganosa, G., Warkentin, T.D., 2020. High throughput nutritional profiling of pea seeds using Fourier transform mid-infrared spectroscopy. *Food Chem.* 309, 125585. <https://doi.org/10.1016/j.foodchem.2019.125585>
- ❖ Kaur, B., Gupta, R.K., Bhunia, H., 2019. Chemically activated nanoporous carbon adsorbents from waste plastic for CO<sub>2</sub> capture: Breakthrough adsorption study. *Microporous Mesoporous Mater.* 282, 146–158. <https://doi.org/10.1016/j.micromeso.2019.03.025>
- ❖ Kaur, R., Gera, P., Jha, M.K., Bhaskar, T., 2018. Pyrolysis kinetics and thermodynamic

- parameters of castor (*Ricinus communis*) residue using thermogravimetric analysis. *Bioresour. Technol.* 250, 422–428. <https://doi.org/10.1016/j.biortech.2017.11.077>
- ❖ Keiluweit, M., Nico, P.S., Johnson, M.G., 2010. Dynamic Molecular Structure of Plant Biomass-Derived Black Carbon ( Biochar ) 44, 1247–1253.
  - ❖ Kim, D., Lee, K., Bae, D., Park, K.Y., 2017. Characterizations of biochar from hydrothermal carbonization of exhausted coffee residue. *J. Mater. Cycles Waste Manag.* 19, 1036–1043. <https://doi.org/10.1007/s10163-016-0572-2>
  - ❖ Kim, Yong Sang, Kim, Young Seok, Kim, S.H., 2010. Investigation of thermodynamic parameters in the thermal decomposition of plastic waste-waste lube oil compounds. *Environ. Sci. Technol.* 44, 5313–5317. <https://doi.org/10.1021/es101163e>
  - ❖ Kishibayev, K.K., Serafin, J., Tokpayev, R.R., Khavaza, T.N., Atchabarova, A.A., Abduakhytova, D.A., Ibraimov, Z.T., Sreńscek-Nazzal, J., 2021. Physical and chemical properties of activated carbon synthesized from plant wastes and shungite for CO<sub>2</sub> capture. *J. Environ. Chem. Eng.* 9. <https://doi.org/10.1016/j.jece.2021.106798>
  - ❖ Kong, S.H., Loh, S.K., Bachmann, R.T., Zainal, H., Cheong, K.Y., 2019. Palm kernel shell biochar production, characteristics and carbon sequestration potential. *J. Oil Palm Res.* 31, 508–520. <https://doi.org/10.21894/jopr.2019.0041>
  - ❖ Kumar, A., Mylapilli, S.V.P., Reddy, S.N., 2019a. Thermogravimetric and kinetic studies of metal (Ru/Fe) impregnated banana pseudo-stem (*Musa acuminata*). *Bioresour. Technol.* 285, 121318. <https://doi.org/10.1016/j.biortech.2019.121318>
  - ❖ Kumar, A., Mylapilli, S.V.P., Reddy, S.N., 2019b. Thermogravimetric and kinetic studies of metal (Ru/Fe) impregnated banana pseudo-stem (*Musa acuminata*). *Bioresour. Technol.* 285, 121318. <https://doi.org/10.1016/j.biortech.2019.121318>
  - ❖ Kumar, R., Mangalapuri, R., Ahmadi, M.H., Vo, D.V.N., Solanki, R., Kumar, P., 2020. The role of nanotechnology on post-combustion CO<sub>2</sub> absorption in process industries. *Int. J. Low-Carbon Technol.* 15, 361–367. <https://doi.org/10.1093/IJLCT/CTAA002>
  - ❖ Kung, C.C., McCarl, B.A., Cao, X., 2013. Economics of pyrolysis-based energy production and biochar utilization: A case study in Taiwan. *Energy Policy* 60, 317–323. <https://doi.org/10.1016/j.enpol.2013.05.029>
  - ❖ Lahijani, P., Mohammadi, M., Mohamed, A.R., 2018. Metal incorporated biochar as a potential adsorbent for high capacity CO<sub>2</sub> capture at ambient condition. *J. CO<sub>2</sub> Util.* 26, 281–293. <https://doi.org/10.1016/j.jcou.2018.05.018>
  - ❖ Latham, K.G., Dose, W.M., Allen, J.A., Donne, S.W., 2018. Nitrogen doped heat treated and activated hydrothermal carbon: NEXAFS examination of the carbon surface at different

- temperatures. *Carbon* N. Y. 128, 179–190. <https://doi.org/10.1016/j.carbon.2017.11.072>
- ❖ Lee, S.Y., Park, S.J., 2015. A review on solid adsorbents for carbon dioxide capture. *J. Ind. Eng. Chem.* 23, 1–11. <https://doi.org/10.1016/j.jiec.2014.09.001>
  - ❖ Lee, Y., Park, J., Ryu, C., Gang, K.S., Yang, W., Park, Y.K., Jung, J., Hyun, S., 2013. Comparison of biochar properties from biomass residues produced by slow pyrolysis at 500°C. *Bioresour. Technol.* 148, 196–201. <https://doi.org/10.1016/j.biortech.2013.08.135>
  - ❖ León, M., Silva, J., Carrasco, S., Barrientos, N., 2020. Design, cost estimation and sensitivity analysis for a production process of activated carbon from waste nutshells by physical activation. *Processes* 8. <https://doi.org/10.3390/PR8080945>
  - ❖ Li, D., Ma, T., Zhang, R., Tian, Y., Qiao, Y., 2015. Preparation of porous carbons with high low-pressure CO<sub>2</sub> uptake by KOH activation of rice husk char. *Fuel* 139, 68–70. <https://doi.org/10.1016/j.fuel.2014.08.027>
  - ❖ Lim, H.K., Md Ali, U.F., Ahmad, R., Aroua, M.K., 2021. Adsorption of carbon dioxide (CO<sub>2</sub>) by activated carbon derived from waste coffee grounds. *IOP Conf. Ser. Earth Environ. Sci.* 765. <https://doi.org/10.1088/1755-1315/765/1/012034>
  - ❖ Lim, Y.H., Adelodun, A.A., Kim, D.W., Jo, Y.M., 2016. Surface impregnation of glycine to activated carbon adsorbents for dry capture of carbon dioxide. *Asian J. Atmos. Environ.* 10, 99–113. <https://doi.org/10.5572/ajae.2016.10.2.099>
  - ❖ Lin, H., Freeman, B.D., 2004. Gas solubility, diffusivity and permeability in poly(ethylene oxide). *J. Memb. Sci.* 239, 105–117. <https://doi.org/10.1016/j.memsci.2003.08.031>
  - ❖ Liu et al 2012-Greenhouse Gases - 2012 - Liu - Recent advances in carbon dioxide capture with metal-organic fr.pdf, n.d.
  - ❖ Liu, L., Qian, H., Mu, L., Wu, J., Feng, X., Lu, X., Zhu, J., 2021. Techno-economic analysis of biomass processing with dual outputs of energy and activated carbon. *Bioresour. Technol.* 319, 124108. <https://doi.org/10.1016/j.biortech.2020.124108>
  - ❖ Liu, S.H., Huang, Y.Y., 2018. Valorization of coffee grounds to biochar-derived adsorbents for CO<sub>2</sub> adsorption. *J. Clean. Prod.* 175, 354–360. <https://doi.org/10.1016/j.jclepro.2017.12.076>
  - ❖ Lu, C., Bai, H., Wu, B., Su, F., Hwang, J.F., 2008. Comparative study of CO<sub>2</sub> capture by carbon nanotubes, activated carbons, and zeolites. *Energy and Fuels* 22, 3050–3056. <https://doi.org/10.1021/ef8000086>
  - ❖ Lv, Y., Yu, X., Jia, J., Tu, S.T., Yan, J., Dahlquist, E., 2012. Fabrication and characterization of superhydrophobic polypropylene hollow fiber membranes for carbon dioxide absorption. *Appl. Energy* 90, 167–174. <https://doi.org/10.1016/j.apenergy.2010.12.038>

- ❖ Ma, Z., Chen, D., Gu, J., Bao, B., Zhang, Q., 2015. Determination of pyrolysis characteristics and kinetics of palm kernel shell using TGA-FTIR and model-free integral methods. *Energy Convers. Manag.* 89, 251–259. <https://doi.org/10.1016/j.enconman.2014.09.074>
- ❖ Mallick, D., Poddar, M.K., Mahanta, P., Moholkar, V.S., 2018. Discernment of synergism in pyrolysis of biomass blends using thermogravimetric analysis. *Bioresour. Technol.* 261, 294–305. <https://doi.org/10.1016/j.biortech.2018.04.011>
- ❖ Manouchehrinejad, M., Mani, S., 2019. Energy Conversion and Management: X Process simulation of an integrated biomass torrefaction and pelletization ( iBTP ) plant to produce solid biofuels. *Energy Convers. Manag.* X 1, 100008. <https://doi.org/10.1016/j.ecmx.2019.100008>
- ❖ Mashhadimoslem, A.G.H., Izadpanah, P.Z., 2022. NiO and MgO / activated carbon as an efficient - CO<sub>2</sub> adsorbent : characterization , modeling , and optimization. *Int. J. Environ. Sci. Technol.* 19, 727–746. <https://doi.org/10.1007/s13762-021-03582-x>
- ❖ Merkel, T.C., Lin, H., Wei, X., Baker, R., 2010. Power plant post-combustion carbon dioxide capture: An opportunity for membranes. *J. Memb. Sci.* 359, 126–139. <https://doi.org/10.1016/j.memsci.2009.10.041>
- ❖ Michailos, S., McCord, S., Sick, V., Stokes, G., Styring, P., 2019a. Dimethyl ether synthesis via captured CO<sub>2</sub> hydrogenation within the power to liquids concept: A techno-economic assessment. *Energy Convers. Manag.* 184, 262–276. <https://doi.org/10.1016/j.enconman.2019.01.046>
- ❖ Michailos, S., Parker, D., Webb, C., 2019b. Design, Sustainability Analysis and Multiobjective Optimisation of Ethanol Production via Syngas Fermentation. *Waste and Biomass Valorization* 10, 865–876. <https://doi.org/10.1007/s12649-017-0151-3>
- ❖ Michailos, S., Walker, M., Moody, A., Poggio, D., Pourkashanian, M., 2020. Biomethane production using an integrated anaerobic digestion, gasification and CO<sub>2</sub> biomethanation process in a real waste water treatment plant: A techno-economic assessment. *Energy Convers. Manag.* 209, 112663. <https://doi.org/10.1016/j.enconman.2020.112663>
- ❖ Mishra, R.K., Mohanty, K., 2018a. Pyrolysis kinetics and thermal behavior of waste sawdust biomass using thermogravimetric analysis. *Bioresour. Technol.* 251, 63–74. <https://doi.org/10.1016/j.biortech.2017.12.029>
- ❖ Mishra, R.K., Mohanty, K., 2018b. Pyrolysis kinetics and thermal behavior of waste sawdust biomass using thermogravimetric analysis. *Bioresour. Technol.* 251, 63–74. <https://doi.org/10.1016/j.biortech.2017.12.029>
- ❖ Mishra, R.K., Mohanty, K., 2018c. Investigation into the kinetic behavior of biomass

- combustion under N<sub>2</sub>/O<sub>2</sub> and CO<sub>2</sub>/O<sub>2</sub> atmospheres. *Bioresour. Technol.* 251, 63–74. <https://doi.org/10.1016/j.biortech.2017.12.029>
- ❖ Mittal, G., Dhand, V., Rhee, K.Y., Park, S.J., Lee, W.R., 2015. A review on carbon nanotubes and graphene as fillers in reinforced polymer nanocomposites. *J. Ind. Eng. Chem.* 21, 11–25. <https://doi.org/10.1016/j.jiec.2014.03.022>
  - ❖ Mohanty, P., Nanda, S., Pant, K.K., Naik, S., Kozinski, J.A., Dalai, A.K., 2013. Evaluation of the physiochemical development of biochars obtained from pyrolysis of wheat straw, timothy grass and pinewood: Effects of heating rate. *J. Anal. Appl. Pyrolysis* 104, 485–493. <https://doi.org/10.1016/j.jaap.2013.05.022>
  - ❖ Mondal, M.K., Balsora, H.K., Varshney, P., 2012. Progress and trends in CO<sub>2</sub> capture/separation technologies: A review. *Energy* 46, 431–441. <https://doi.org/10.1016/j.energy.2012.08.006>
  - ❖ Mukherjee, A., Borugadda, V.B., Dynes, J.J., Niu, C., Dalai, A.K., 2021a. Carbon dioxide capture from flue gas in biochar produced from spent coffee grounds: Effect of surface chemistry and porous structure. *J. Environ. Chem. Eng.* 9, 106049. <https://doi.org/10.1016/j.jece.2021.106049>
  - ❖ Mukherjee, A., Okolie, J.A., Abdelrasoul, A., Niu, C., Dalai, A.K., 2019. Review of post-combustion carbon dioxide capture technologies using activated carbon. *J. Environ. Sci. (China)* 83, 46–63. <https://doi.org/10.1016/j.jes.2019.03.014>
  - ❖ Mukherjee, A., Okolie, J.A., Niu, C., Dalai, A.K., 2022. Experimental and Modeling Studies of Torrefaction of Spent Coffee Grounds and Coffee Husk: Effects on Surface Chemistry and Carbon Dioxide Capture Performance. *ACS Omega* 7, 638–653. <https://doi.org/10.1021/acsomega.1c05270>
  - ❖ Mukherjee, A., Okolie, J.A., Tyagi, R., Dalai, A.K., Niu, C., 2021b. Pyrolysis kinetics and activation thermodynamic parameters of exhausted coffee residue and coffee husk using thermogravimetric analysis. *Can. J. Chem. Eng.* <https://doi.org/10.1002/cjce.24037>
  - ❖ Murthy, P.S., Madhava Naidu, M., 2012. Sustainable management of coffee industry by-products and value addition - A review. *Resour. Conserv. Recycl.* 66, 45–58. <https://doi.org/10.1016/j.resconrec.2012.06.005>
  - ❖ Mussatto, S.I., Machado, E.M.S., Martins, S., Teixeira, J.A., 2011. Production, Composition, and Application of Coffee and Its Industrial Residues. *Food Bioprocess Technol.* 4, 661–672. <https://doi.org/10.1007/s11947-011-0565-z>
  - ❖ Namkung, H., Park, Ju-hyoung, Lee, Y., Song, G., Won, J., Kim, J., Park, Jun-su, Hwan, B., Ho, K., Park, S., Choi, Y., 2017. Characteristics of novel synthetic fuels using coal and sewage

sludge impregnated bioliquid applying for a coal combustion system. *Fuel Process. Technol.* 167, 153–161. <https://doi.org/10.1016/j.fuproc.2017.06.030>

- ❖ Nanda, S., Dalai, A.K., Berruti, F., Kozinski, J.A., 2016. Biochar as an Exceptional Bioresource for Energy, Agronomy, Carbon Sequestration, Activated Carbon and Specialty Materials. *Waste and Biomass Valorization* 7, 201–235. <https://doi.org/10.1007/s12649-015-9459-z>
- ❖ Nasri, N.S., Hamza, U.D., Ismail, S.N., Ahmed, M.M., Mohsin, R., 2014. Assessment of porous carbons derived from sustainable palm solid waste for carbon dioxide capture. *J. Clean. Prod.* 71, 148–157. <https://doi.org/10.1016/j.jclepro.2013.11.053>
- ❖ Ngaosuwan, K., Goodwin, J.G., Prasertdham, P., 2016. A green sulfonated carbon-based catalyst derived from coffee residue for esterification. *Renew. Energy* 86, 262–269. <https://doi.org/10.1016/j.renene.2015.08.010>
- ❖ Nguyen, M., Lee, B., 2016. A novel removal of CO<sub>2</sub> using nitrogen doped biochar beads as a green adsorbent. *Process Saf. Environ. Prot.* 104, 490–498. <https://doi.org/10.1016/j.psep.2016.04.007>
- ❖ Ogungbenro, A.E., Quang, D. V., Al-Ali, K., Abu-Zahra, M.R.M., 2017. Activated Carbon from Date Seeds for CO<sub>2</sub> Capture Applications. *Energy Procedia* 114, 2313–2321. <https://doi.org/10.1016/j.egypro.2017.03.1370>
- ❖ Oke, E.O., Okolo, B.I., Adeyi, O., Adeyi, J.A., Ude, C.J., Osoh, K., Otolorin, J., Nzeribe, I., Darlinton, N., Oladunni, S., 2021. Process Design, Techno-Economic Modelling, and Uncertainty Analysis of Biodiesel Production from Palm Kernel Oil. *Bioenergy Res.* <https://doi.org/10.1007/s12155-021-10315-y>
- ❖ Okolie, J.A., Nanda, S., Dalai, A.K., Berruti, F., Kozinski, J.A., 2020a. A review on subcritical and supercritical water gasification of biogenic, polymeric and petroleum wastes to hydrogen-rich synthesis gas. *Renew. Sustain. Energy Rev.* <https://doi.org/10.1016/j.rser.2019.109546>
- ❖ Okolie, J.A., Nanda, S., Dalai, A.K., Kozinski, J.A., 2021a. Chemistry and Specialty Industrial Applications of Lignocellulosic Biomass. *Waste and Biomass Valorization* 12, 2145–2169. <https://doi.org/10.1007/s12649-020-01123-0>
- ❖ Okolie, J.A., Nanda, S., Dalai, A.K., Kozinski, J.A., 2021b. Chemistry and Specialty Industrial Applications of Lignocellulosic Biomass. *Waste and Biomass Valorization* 12, 2145–2169. <https://doi.org/10.1007/s12649-020-01123-0>
- ❖ Okolie, J.A., Nanda, S., Dalai, A.K., Kozinski, J.A., 2020b. Hydrothermal gasification of soybean straw and flax straw for hydrogen-rich syngas production: Experimental and thermodynamic modeling. *Energy Convers. Manag.* 208, 112545.



<https://doi.org/10.1016/j.enconman.2020.112545>

- ❖ Okolie, J.A., Rana, R., Nanda, S., Dalai, A.K., Kozinski, J.A., 2019. Supercritical water gasification of biomass: A state-of-the-art review of process parameters, reaction mechanisms and catalysis. *Sustain. Energy Fuels* 3, 578–598. <https://doi.org/10.1039/c8se00565f>
- ❖ Okolie, J.A., Tabat, M.E., Gunes, B., Epelle, E.I., Mukherjee, A., Nanda, S., Dalai, A.K., 2021c. A techno-economic assessment of biomethane and bioethanol production from crude glycerol through integrated hydrothermal gasification, syngas fermentation and biomethanation. *Energy Convers. Manag.* X 12, 100131. <https://doi.org/10.1016/j.ecmx.2021.100131>
- ❖ Onsree, T., Jaroenkhasemmesuk, C., Tippayawong, N., 2020. Techno-economic assessment of a biomass torrefaction plant for pelletized agro-residues with flue gas as a main heat source. *Energy Reports* 6, 92–96. <https://doi.org/10.1016/j.egyr.2020.10.043>
- ❖ Packer, M., 2009. Algal capture of carbon dioxide; biomass generation as a tool for greenhouse gas mitigation with reference to New Zealand energy strategy and policy. *Energy Policy* 37, 3428–3437. <https://doi.org/10.1016/j.enpol.2008.12.025>
- ❖ Pallarés, J., González-Cencerrado, A., Arauzo, I., 2018. Production and characterization of activated carbon from barley straw by physical activation with carbon dioxide and steam. *Biomass and Bioenergy* 115, 64–73. <https://doi.org/10.1016/j.biombioe.2018.04.015>
- ❖ Patel, M., Oyedun, A.O., Kumar, A., Gupta, R., 2019. Predicting the biomass conversion performance in a fluidized bed reactor using isoconversional model-free method. *Can. J. Chem. Eng.* 97, 1263–1273. <https://doi.org/10.1002/cjce.23397>
- ❖ Patra, B.R., Nanda, S., Dalai, A.K., Meda, V., 2021. Slow pyrolysis of agro-food wastes and physicochemical characterization of biofuel products. *Chemosphere* 285, 131431. <https://doi.org/10.1016/j.chemosphere.2021.131431>
- ❖ Pires, J.C.M., Alvim-Ferraz, M.C.M., Martins, F.G., Simões, M., 2012. Carbon dioxide capture from flue gases using microalgae: Engineering aspects and biorefinery concept. *Renew. Sustain. Energy Rev.* 16, 3043–3053. <https://doi.org/10.1016/j.rser.2012.02.055>
- ❖ Plaza, M.G., González, A.S., Pevida, C., Pis, J.J., Rubiera, F., 2012. Valorisation of spent coffee grounds as CO<sub>2</sub> adsorbents for postcombustion capture applications. *Appl. Energy* 99, 272–279. <https://doi.org/10.1016/j.apenergy.2012.05.028>
- ❖ Plaza, M.G., González, A.S., Pis, J.J., Rubiera, F., Pevida, C., 2014. Production of microporous biochars by single-step oxidation: Effect of activation conditions on CO<sub>2</sub> capture. *Appl. Energy* 114, 551–562. <https://doi.org/10.1016/j.apenergy.2013.09.058>
- ❖ Prins, M.J., Ptasinski, K.J., Janssen, F.J.J.G., 2006. Torrefaction of wood Part 2 . Analysis of

products 77, 35–40. <https://doi.org/10.1016/j.jaap.2006.01.001>

- ❖ Promraksa, A., Rakmak, N., 2020. Biochar production from palm oil mill residues and application of the biochar to adsorb carbon dioxide. *Heliyon* 6. <https://doi.org/10.1016/j.heliyon.2020.e04019>
- ❖ Pu, Q., Wang, Y., Wang, X., Shao, Z., Wen, S., Wang, J., Ning, P., Lu, S., Huang, L., Wang, Q., 2021. Biomass-derived carbon/MgO-Al<sub>2</sub>O<sub>3</sub> composite with superior dynamic CO<sub>2</sub> uptake for post combustion capture application. *J. CO<sub>2</sub> Util.* 54, 101756. <https://doi.org/10.1016/j.jcou.2021.101756>
- ❖ Raganati, F., Alfe, M., Gargiulo, V., Chirone, R., Ammendola, P., 2019. Kinetic study and breakthrough analysis of the hybrid physical/chemical CO<sub>2</sub> adsorption/desorption behavior of a magnetite-based sorbent. *Chem. Eng. J.* 372, 526–535. <https://doi.org/10.1016/j.cej.2019.04.165>
- ❖ Rahman, S., Hossain, A., Ahmed, M.B., 2020. Dioxide Capture 1–17.
- ❖ Rashidi, N.A., Yusup, S., 2021. Co-valorization of delayed petroleum coke – palm kernel shell for activated carbon production. *J. Hazard. Mater.* 403, 123876. <https://doi.org/10.1016/j.jhazmat.2020.123876>
- ❖ Rashidi, N.A., Yusup, S., 2019. Production of palm kernel shell-based activated carbon by direct physical activation for carbon dioxide adsorption. *Environ. Sci. Pollut. Res.* 26, 33732–33746. <https://doi.org/10.1007/s11356-018-1903-8>
- ❖ Rashidi, N.A., Yusup, S., 2016. An overview of activated carbons utilization for the post-combustion carbon dioxide capture. *J. CO<sub>2</sub> Util.* 13, 1–16. <https://doi.org/10.1016/j.jcou.2015.11.002>
- ❖ Rashidi, N.A., Yusup, S., Borhan, A., Loong, L.H., 2014. Experimental and modelling studies of carbon dioxide adsorption by porous biomass derived activated carbon. *Clean Technol. Environ. Policy* 16, 1353–1361. <https://doi.org/10.1007/s10098-014-0788-6>
- ❖ Rashidi, N.A., Yusup, S., Hameed, B.H., 2013. Kinetic studies on carbon dioxide capture using lignocellulosic based activated carbon. *Energy* 61, 440–446. <https://doi.org/10.1016/j.energy.2013.08.050>
- ❖ Raynal, L., Bouillon, P.A., Gomez, A., Broutin, P., 2011. From MEA to demixing solvents and future steps, a roadmap for lowering the cost of post-combustion carbon capture. *Chem. Eng. J.* 171, 742–752. <https://doi.org/10.1016/j.cej.2011.01.008>
- ❖ Ren, X., Sun, R., Meng, X., Vorobiev, N., Schiemann, M., Levendis, Y.A., 2017. Carbon, sulfur and nitrogen oxide emissions from combustion of pulverized raw and torrefied biomass. *Fuel* 188, 310–323. <https://doi.org/10.1016/j.fuel.2016.10.017>

- ❖ Ribeiro, J.M.C., Godina, R., Matias, J.C. de O., Nunes, L.J.R., 2018. Future perspectives of biomass torrefaction: Review of the current state-of-the-art and research development. *Sustain.* 10, 1–17. <https://doi.org/10.3390/su10072323>
- ❖ Rutherford, D.W., Wershaw, R.L., Rostad, C.E., Kelly, C.N., 2012. Effect of formation conditions on biochars: Compositional and structural properties of cellulose, lignin, and pine biochars. *Biomass and Bioenergy* 46, 693–701. <https://doi.org/10.1016/j.biombioe.2012.06.026>
- ❖ Sahoo, K., Bilek, E., Bergman, R., Mani, S., 2019. Techno-economic analysis of producing solid biofuels and biochar from forest residues using portable systems. *Appl. Energy* 235, 578–590. <https://doi.org/10.1016/j.apenergy.2018.10.076>
- ❖ Samanta, A., Zhao, A., Shimizu, G.K.H., Sarkar, P., Gupta, R., 2012. Post-combustion CO<sub>2</sub> capture using solid sorbents: A review. *Ind. Eng. Chem. Res.* 51, 1438–1463. <https://doi.org/10.1021/ie200686q>
- ❖ Sarker, T.R., Azargohar, R., Dalai, A.K., Venkatesh, M., 2020. Physicochemical and Fuel Characteristics of Torrefied Agricultural Residues for Sustainable Fuel Production. *Energy and Fuels* 34, 14169–14181. <https://doi.org/10.1021/acs.energyfuels.0c02121>
- ❖ Saxena, R., Singh, V.K., Kumar, E.A., 2014. Carbon dioxide capture and sequestration by adsorption on activated carbon. *Energy Procedia* 54, 320–329. <https://doi.org/10.1016/j.egypro.2014.07.275>
- ❖ Sengupta, S., Amte, V., Dongara, R., Das, A.K., Bhunia, H., Bajpai, P.K., 2015. Effects of the adsorbent preparation method for CO<sub>2</sub> capture from flue gas using K<sub>2</sub>CO<sub>3</sub>/Al<sub>2</sub>O<sub>3</sub> adsorbents. *Energy and Fuels* 29, 287–297. <https://doi.org/10.1021/ef501792c>
- ❖ Serafin, J., Narkiewicz, U., Morawski, A.W., Wróbel, R.J., Michalkiewicz, B., 2017. Highly microporous activated carbons from biomass for CO<sub>2</sub> capture and effective micropores at different conditions. *J. CO<sub>2</sub> Util.* 18, 73–79. <https://doi.org/10.1016/j.jcou.2017.01.006>
- ❖ Sethia, G., Sayari, A., 2015. Comprehensive study of ultra-microporous nitrogen-doped activated carbon for CO<sub>2</sub> capture. *Carbon N. Y.* 93, 68–80. <https://doi.org/10.1016/j.carbon.2015.05.017>
- ❖ Shafeeyan, M.S., Daud, W.M.A.W., Houshmand, A., Shamiri, A., 2010. A review on surface modification of activated carbon for carbon dioxide adsorption. *J. Anal. Appl. Pyrolysis* 89, 143–151. <https://doi.org/10.1016/j.jaap.2010.07.006>
- ❖ Shahkarami, S., Azargohar, R., Dalai, A.K., Soltan, J., 2015a. Breakthrough CO<sub>2</sub> adsorption in bio-based activated carbons. *J. Environ. Sci. (China)* 34, 68–76. <https://doi.org/10.1016/j.jes.2015.03.008>

- ❖ Shahkarami, S., Azargohar, R., Dalai, A.K., Soltan, J., 2015b. ScienceDirect Breakthrough CO<sub>2</sub> adsorption in bio-based activated carbons. *JES* 34, 68–76. <https://doi.org/10.1016/j.jes.2015.03.008>
- ❖ Shahkarami, S., Azargohar, R., Dalai, A.K., Soltan, J., 2015c. Breakthrough CO<sub>2</sub> adsorption in bio-based activated carbons. *J. Environ. Sci. (China)* 34, 68–76. <https://doi.org/10.1016/j.jes.2015.03.008>
- ❖ Shahkarami, S., Dalai, A.K., Soltan, J., 2016. Enhanced CO<sub>2</sub> Adsorption Using MgO-Impregnated Activated Carbon: Impact of Preparation Techniques. *Ind. Eng. Chem. Res.* 55, 5955–5964. <https://doi.org/10.1021/acs.iecr.5b04824>
- ❖ Shahkarami, S., Dalai, A.K., Soltan, J., Hu, Y., Wang, D., 2015d. Selective CO<sub>2</sub> Capture by Activated Carbons: Evaluation of the Effects of Precursors and Pyrolysis Process. *Energy and Fuels* 29, 7433–7440. <https://doi.org/10.1021/acs.energyfuels.5b00470>
- ❖ Shahkarami, S., Dalai, A.K., Soltan, J., Hu, Y., Wang, D., 2015e. Selective CO<sub>2</sub> Capture by Activated Carbons: Evaluation of the Effects of Precursors and Pyrolysis Process. *Energy and Fuels* 29, 7433–7440. <https://doi.org/10.1021/acs.energyfuels.5b00470>
- ❖ Shalini, R., 2018. Characteristic Study on Biochar Production from Biological Substrates by Slow Pyrolysis for Carbon Sequestration Characteristic Study on Biochar Production from Biological Substrates by Slow Pyrolysis for Carbon Sequestration. <https://doi.org/10.20546/ijcmas.2017.604.034>
- ❖ Shariff, A., Aziz, N.S.M., Ismail, N.I., Abdullah, N., 2016. Corn cob as a potential feedstock for slow pyrolysis of biomass. *J. Phys. Sci.* 27, 123–137. <https://doi.org/10.21315/jps2016.27.2.9>
- ❖ Sheng, J., Ji, D., Yu, F., Cui, L., Zeng, Q., Ai, N., Ji, J., 2014. Influence of Chemical Treatment on Rice Straw Pyrolysis by TG-FTIR. *IERI Procedia* 8, 30–34. <https://doi.org/10.1016/j.ieri.2014.09.006>
- ❖ Shewchuk, S.R., Mukherjee, A., Dalai, A.K., 2021. Selective carbon-based adsorbents for carbon dioxide capture from mixed gas streams and catalytic hydrogenation of CO<sub>2</sub> into renewable energy source: A review. *Chem. Eng. Sci.* 243, 116735. <https://doi.org/10.1016/j.ces.2021.116735>
- ❖ Sigmaaldrich, 2021. Urea ACS reagent, 99.0-100.5% | 57-13-6 [WWW Document].
- ❖ Sigmaaldrich, 2021. Choline Chloride - ZENNOH.pdf [WWW Document].
- ❖ Simonoff, J.S., 1998. Three sides of smoothing: Categorical data smoothing, nonparametric regression, and density estimation. *Int. Stat. Rev.* 66, 137–156. <https://doi.org/10.1111/j.1751-5823.1998.tb00411.x>

- ❖ Singh, J., Basu, S., Bhunia, H., 2019a. Dynamic CO<sub>2</sub> adsorption on activated carbon adsorbents synthesized from polyacrylonitrile (PAN): Kinetic and isotherm studies. *Microporous Mesoporous Mater.* 280, 357–366. <https://doi.org/10.1016/j.micromeso.2019.02.031>
- ❖ Singh, J., Bhunia, H., Basu, S., 2019b. Adsorption of CO<sub>2</sub> on KOH activated carbon adsorbents: Effect of different mass ratios 250. <https://doi.org/10.1016/j.jenvman.2019.109457>
- ❖ Siqueira, R.M., Freitas, G.R., Peixoto, H.R., Nascimento, J.F.D., Musse, A.P.S., Torres, A.E.B., Azevedo, D.C.S., Bastos-Neto, M., 2017. Carbon Dioxide Capture by Pressure Swing Adsorption. *Energy Procedia* 114, 2182–2192. <https://doi.org/10.1016/j.egypro.2017.03.1355>
- ❖ Smets, K., De Jong, M., Lupul, I., Gryglewicz, G., Schreurs, S., Carleer, R., Yperman, J., 2016. Rapeseed and raspberry seed cakes as inexpensive raw materials in the production of activated carbon by physical activation: Effect of activation conditions on textural and phenol adsorption characteristics. *Materials (Basel)*. 9. <https://doi.org/10.3390/MA9070565>
- ❖ Song, C.F., Kitamura, Y., Li, S.H., 2012. Evaluation of Stirling cooler system for cryogenic CO<sub>2</sub> capture. *Appl. Energy* 98, 491–501. <https://doi.org/10.1016/j.apenergy.2012.04.013>
- ❖ Soysa, R., Choi, Y.S., Kim, S.J., Choi, S.K., 2016. Fast pyrolysis characteristics and kinetic study of Ceylon tea waste. *Int. J. Hydrogen Energy* 41, 16436–16443. <https://doi.org/10.1016/j.ijhydene.2016.04.066>
- ❖ Spigarelli, B.P., Kawatra, S.K., 2013. Opportunities and challenges in carbon dioxide capture. *J. CO<sub>2</sub> Util.* 1, 69–87. <https://doi.org/10.1016/j.jcou.2013.03.002>
- ❖ Stephens, J.C., van der Zwaan, B., 2005. Capture and Storage (CSS): Exploring the Research, Development, Demonstration and Deployment. *BCSIA Discuss. Pap.* Harvard Un, 1–20.
- ❖ Struhs, E., Mirkouei, A., You, Y., Mohajeri, A., 2020. Techno-economic and environmental assessments for nutrient-rich biochar production from cattle manure: A case study in Idaho, USA. *Appl. Energy* 279, 115782. <https://doi.org/10.1016/j.apenergy.2020.115782>
- ❖ Tan, Y.L., Islam, M.A., Asif, M., Hameed, B.H., 2014. Adsorption of carbon dioxide by sodium hydroxide-modified granular coconut shell activated carbon in a fixed bed. *Energy* 77, 926–931. <https://doi.org/10.1016/j.energy.2014.09.079>
- ❖ Tang, H.Y., Xiao, Q.G., Xu, H. Bin, Zhang, Y., 2013. Optimization of reaction parameters for the synthesis of chromium methionine complex using response surface methodology. *Org. Process Res. Dev.* 17, 632–640. <https://doi.org/10.1021/op3002905>
- ❖ Taskin, E., Castro, C. De, Allegretta, I., Terzano, R., 2019. Chemosphere Multianalytical characterization of biochar and hydrochar produced from waste biomasses for environmental

and agricultural applications 233, 422–430.  
<https://doi.org/10.1016/j.chemosphere.2019.05.204>

- ❖ Tian, H., Zhou, T., Huang, Z., Wang, J., Cheng, H., Yang, Y., 2021. Integration of spent coffee grounds valorization for co-production of biodiesel and activated carbon: An energy and techno-economic case assessment in China. *J. Clean. Prod.* 324, 129187. <https://doi.org/10.1016/j.jclepro.2021.129187>
- ❖ Titinchi, S.J.J., Piet, M., Abbo, H.S., Bolland, O., Schwieger, W., 2014. Chemically Modified Solid Adsorbents for CO<sub>2</sub> Capture. *Energy Procedia* 63, 8153–8160. <https://doi.org/10.1016/j.egypro.2015.12.337>
- ❖ Tiwari, D., Bhunia, H., Bajpai, P.K., 2018. Development of chemically activated N-enriched carbon adsorbents from urea-formaldehyde resin for CO<sub>2</sub> adsorption: Kinetics, isotherm, and thermodynamics. *J. Environ. Manage.* 218, 579–592. <https://doi.org/10.1016/j.jenvman.2018.04.088>
- ❖ Tiwari, D., Goel, C., Bhunia, H., Bajpai, P.K., 2017. Dynamic CO<sub>2</sub> capture by carbon adsorbents: Kinetics, isotherm and thermodynamic studies. *Sep. Purif. Technol.* 181, 107–122. <https://doi.org/10.1016/j.seppur.2017.03.014>
- ❖ Trubetskaya, A., Grams, J., Leahy, J.J., Johnson, R., Gallagher, P., Monaghan, R.F.D., Kwapinska, M., 2020. The effect of particle size, temperature and residence time on the yields and reactivity of olive stones from torrefaction. *Renew. Energy* 160, 998–1011. <https://doi.org/10.1016/j.renene.2020.06.136>
- ❖ Tsai, W., Liu, S., 2013. Journal of Analytical and Applied Pyrolysis Effect of temperature on thermochemical property and true density of torrefied coffee residue. *J. Anal. Appl. Pyrolysis* 102, 47–52. <https://doi.org/10.1016/j.jaap.2013.04.003>
- ❖ Vyazovkin, S., Burnham, A.K., Criado, J.M., Pérez-Maqueda, L.A., Popescu, C., Sbirrazzuoli, N., 2011. ICTAC Kinetics Committee recommendations for performing kinetic computations on thermal analysis data. *Thermochim. Acta* 520, 1–19. <https://doi.org/10.1016/j.tca.2011.03.034>
- ❖ Wang, H., Li, X., Cui, Z., Fu, Z., Yang, L., Liu, G., Li, M., 2020. Coffee grounds derived N enriched microporous activated carbons: Efficient adsorbent for post-combustion CO<sub>2</sub> capture and conversion. *J. Colloid Interface Sci.* 578, 491–499. <https://doi.org/10.1016/j.jcis.2020.05.125>
- ❖ Wang, H., Wang, X., Cui, Y., Xue, Z., Ba, Y., 2018. Bioresource Technology Slow pyrolysis polygeneration of bamboo (*Phyllostachys pubescens*): Product yield prediction and biochar formation mechanism. *Bioresour. Technol.* 263, 444–449.

<https://doi.org/10.1016/j.biortech.2018.05.040>

- ❖ Wang, Q., Luo, J., Zhong, Z., Borgna, A., 2011. CO<sub>2</sub> capture by solid adsorbents and their applications: Current status and new trends. *Energy Environ. Sci.* 4, 42–55. <https://doi.org/10.1039/c0ee00064g>
- ❖ Wu, D., Xu, Q., Liu, D., Zhong, C., 2010. Exceptional CO<sub>2</sub> capture capability and molecular-level segregation in a Li-modified metal-organic framework. *J. Phys. Chem. C* 114, 16611–16617. <https://doi.org/10.1021/jp105899t>
- ❖ Wu, W., Mei, Y., Zhang, L., Liu, R., Cai, J., 2015. Kinetics and reaction chemistry of pyrolysis and combustion of tobacco waste. *Fuel* 156, 71–80. <https://doi.org/10.1016/j.fuel.2015.04.016>
- ❖ Xu, D., Cao, J., Li, Y., Howard, A., Yu, K., 2019. Effect of pyrolysis temperature on characteristics of biochars derived from different feedstocks: A case study on ammonium adsorption capacity. *Waste Manag.* 87, 652–660. <https://doi.org/10.1016/j.wasman.2019.02.049>
- ❖ Xu, X., Zheng, Y., Gao, B., Cao, X., 2019. N-doped biochar synthesized by a facile ball-milling method for enhanced sorption of CO<sub>2</sub> and reactive red. *Chem. Eng. J.* 368, 564–572. <https://doi.org/10.1016/j.cej.2019.02.165>
- ❖ Yadavalli, G., Lei, H., Wei, Y., Zhu, L., Zhang, X., Liu, Y., Yan, D., 2017a. Carbon dioxide capture using ammonium sulfate surface modified activated biomass carbon. *Biomass and Bioenergy* 98, 53–60. <https://doi.org/10.1016/j.biombioe.2017.01.015>
- ❖ Yadavalli, G., Lei, H., Wei, Y., Zhu, L., Zhang, X., Liu, Y., Yan, D., 2017b. Biomass and Bioenergy Carbon dioxide capture using ammonium sulfate surface modified activated biomass carbon. *Biomass and Bioenergy* 98, 53–60. <https://doi.org/10.1016/j.biombioe.2017.01.015>
- ❖ Yan, W., Perez, S., Sheng, K., 2017. Upgrading fuel quality of moso bamboo via low temperature thermochemical treatments: Dry torrefaction and hydrothermal carbonization. *Fuel* 196, 473–480. <https://doi.org/10.1016/j.fuel.2017.02.015>
- ❖ Yang, H., Xu, Z., Fan, M., Gupta, R., Slimane, R.B., Bland, A.E., Wright, I., 2008. Progress in carbon dioxide separation and capture: A review. *J. Environ. Sci.* [https://doi.org/10.1016/S1001-0742\(08\)60002-9](https://doi.org/10.1016/S1001-0742(08)60002-9)
- ❖ Yaumi, A.L., Bakar, M.Z.A., Hameed, B.H., 2017. Recent advances in functionalized composite solid materials for carbon dioxide capture. *Energy* 124, 461–480. <https://doi.org/10.1016/j.energy.2017.02.053>
- ❖ Yen, W.J., Wang, B. Sen, Chang, L.W., Duh, P. Der, 2005. Antioxidant properties of roasted coffee residues. *J. Agric. Food Chem.* 53, 2658–2663. <https://doi.org/10.1021/jf0402429>

- ❖ Yuan, Z., Xu, Z., Zhang, D., Chen, W., Zhang, T., Huang, Y., Gu, L., Deng, H., Tian, D., 2018. Box-Behnken design approach towards optimization of activated carbon synthesized by co-pyrolysis of waste polyester textiles and MgCl<sub>2</sub>. *Appl. Surf. Sci.* 427, 340–348. <https://doi.org/10.1016/j.apsusc.2017.08.241>
- ❖ Yunus, Z.M., Al-Gheethi, A., Othman, N., Hamdan, R., Ruslan, N.N., 2020. Removal of heavy metals from mining effluents in tile and electroplating industries using honeydew peel activated carbon: A microstructure and techno-economic analysis. *J. Clean. Prod.* 251. <https://doi.org/10.1016/j.jclepro.2019.119738>
- ❖ Zanco, S.E., Joss, L., Hefti, M., Gazzani, M., Mazzotti, M., 2017. Addressing the Criticalities for the Deployment of Adsorption-based CO<sub>2</sub> Capture Processes. *Energy Procedia* 114, 2497–2505. <https://doi.org/10.1016/j.egypro.2017.03.1407>
- ❖ Zhang, X., Lei, H., Zhu, L., Zhu, X., Qian, M., Yadavalli, G., Wu, J., Chen, S., 2016. Thermal behavior and kinetic study for catalytic co-pyrolysis of biomass with plastics. *Bioresour. Technol.* 220, 233–238. <https://doi.org/10.1016/j.biortech.2016.08.068>
- ❖ Zhu, X.L., Wang, P.Y., Peng, C., Yang, J., Yan, X. Bin, 2014. Activated carbon produced from paulownia sawdust for high-performance CO<sub>2</sub> sorbents. *Chinese Chem. Lett.* 25, 929–932. <https://doi.org/10.1016/j.ccllet.2014.03.039>



## Appendix A: 3-Minutes Thesis Competitions (3MT competitions, 2019-2022)

- ❖ **Mukherjee, A., Niu, C., & Dalai A.K** “CO<sub>2</sub> capture using novel activated carbon from spent coffee grounds”, 2<sup>nd</sup> U of Sask 3MT Competition, Saskatoon, March 27<sup>th</sup>, 2019 (**Honorary Mention Award**).
- ❖ **Mukherjee, A. Niu, C., & Dalai, A.K** “Carbon dioxide capture using novel activated carbon prepared from spent coffee grounds”, Food and Bioprocess Engineering Night, Saskatoon, Canada, April 10<sup>th</sup>, 2019 (**2<sup>nd</sup> prize winner**).
- ❖ **Mukherjee, A. Niu, C., & Dalai, A.K** “Valorization of spent coffee residue for value added products and CO<sub>2</sub> mitigation”, 69<sup>th</sup> Canadian Chemical Engineering Conference, Halifax, Canada, October 20-23<sup>rd</sup>, 2019.
- ❖ **Mukherjee, A., Niu, C., & Dalai A.K** “Valorization of Spent Coffee Residue for Value Added Products and CO<sub>2</sub> Mitigation” Trainee Research Competition, People Around the World (PAWS) Virtual Conference, Saskatoon, Canada, February 2<sup>nd</sup> & 3<sup>rd</sup> 2020.
- ❖ **Mukherjee, A., Niu, C., & Dalai, A.K** “Can coffee grounds contribute towards the climate Change”, 1<sup>st</sup> Engineering 3-Minute Thesis Competition, Engineering Graduate Community Council, Saskatoon, Canada, February 28<sup>th</sup>, 2020 (**People’s Choice Award**).
- ❖ **Mukherjee, A., Niu, C., & Dalai, A.K** “Utilization of Spent Coffee Grounds for Climate Change (CO<sub>2</sub> mitigation)”, 2<sup>nd</sup> Engineering 3-Minute Thesis Competition, Engineering Graduate Community Council, Saskatoon, Canada, February 25<sup>th</sup>, 2021 (**Special Mention**).
- ❖ **Mukherjee, A., Niu, C., & Dalai A.K** “CO<sub>2</sub> capture using novel activated carbon from spent coffee grounds”, U of Sask, 3MT Competition, Saskatoon, March 26<sup>th</sup>, 2021 (**3<sup>rd</sup> prize winner**).
- ❖ **Mukherjee, A., Niu, C., & Dalai, A.K.**, “Can caffeine contribute towards the climate Change- Yes or No!”, 3<sup>rd</sup> Engineering 3-Minute Thesis Competition, Engineering Graduate Community Council (EGCC), February 25<sup>th</sup>, 2022.
- ❖ **Mukherjee, A., Niu, C., & Dalai, A.K.**,” Can spent coffee grounds contribute towards climate change: yes or no!”, U of Sask 3MT Competition, Saskatoon, April 1<sup>st</sup>, 2022.

## Appendix B: Torrefaction, slow-pyrolysis, and CO<sub>2</sub> activation for production of torrefied biomass samples, biochar and activated carbon samples

Temperature and mass flow calibration curve for torrefaction, slow-pyrolysis and CO<sub>2</sub> activation set-up are presented below:

Temperature of the furnace was controlled by a temperature controller (Eurotherm 2416) and temperature calibration data of bed is shown in Figure B.1. N<sub>2</sub> and CO<sub>2</sub> flow were controlled by a mass flow controller (Brooks Instrument, 5850S A/B) and the calibration data are shown in Figures B.2 and B.3, respectively.

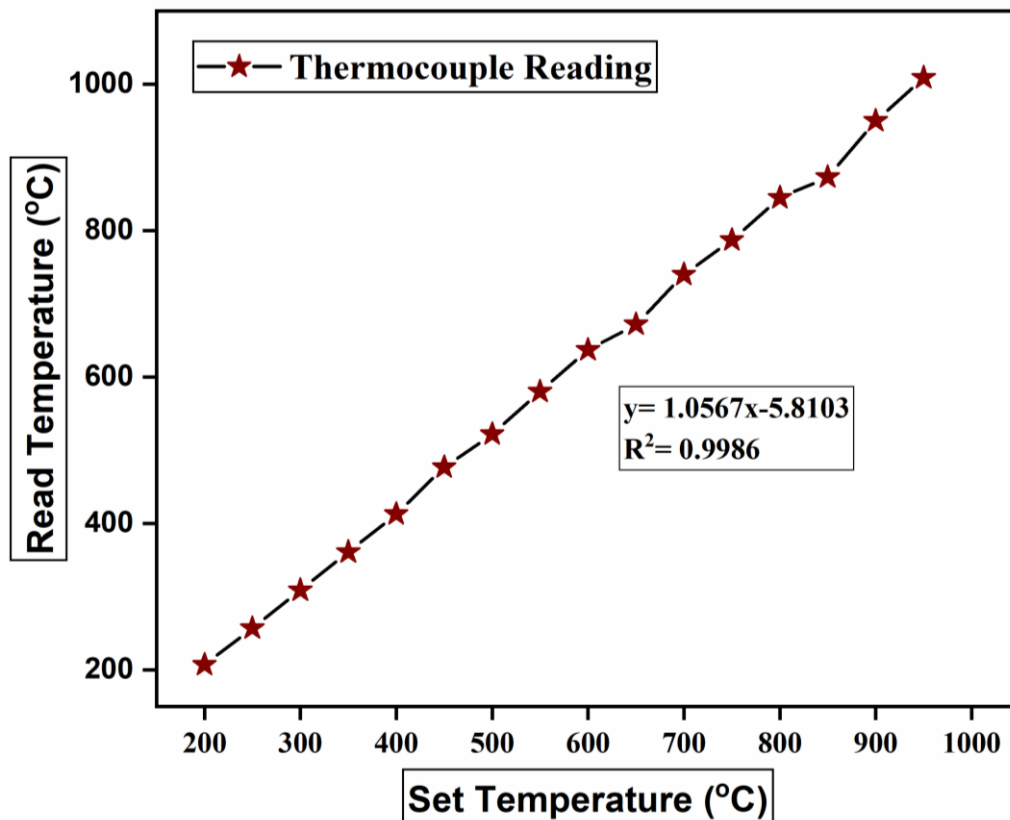


**Figure B.1:** Temperature calibration data for the furnace installed on the torrefaction, slow-pyrolysis, and CO<sub>2</sub> activation set-up.

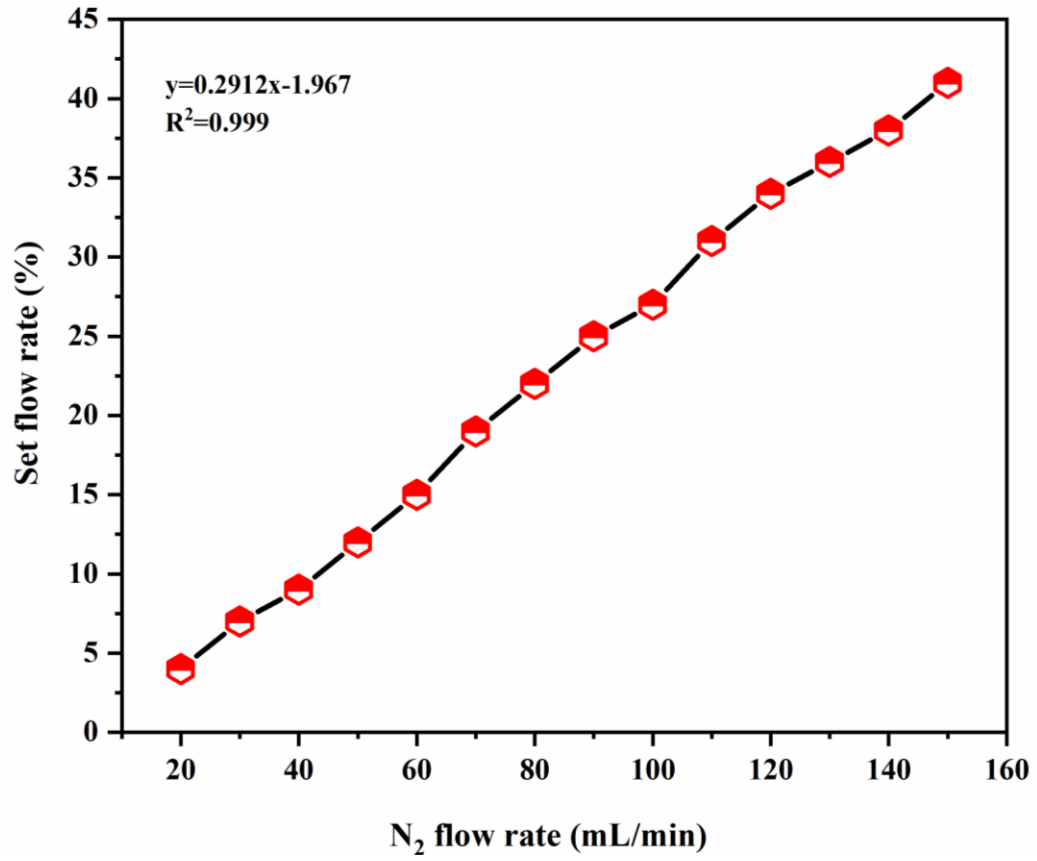


**Figure B.2:** Calibration data for N<sub>2</sub> mass flow controller used in the torrefaction, slow-pyrolysis, and CO<sub>2</sub> activation set-up.

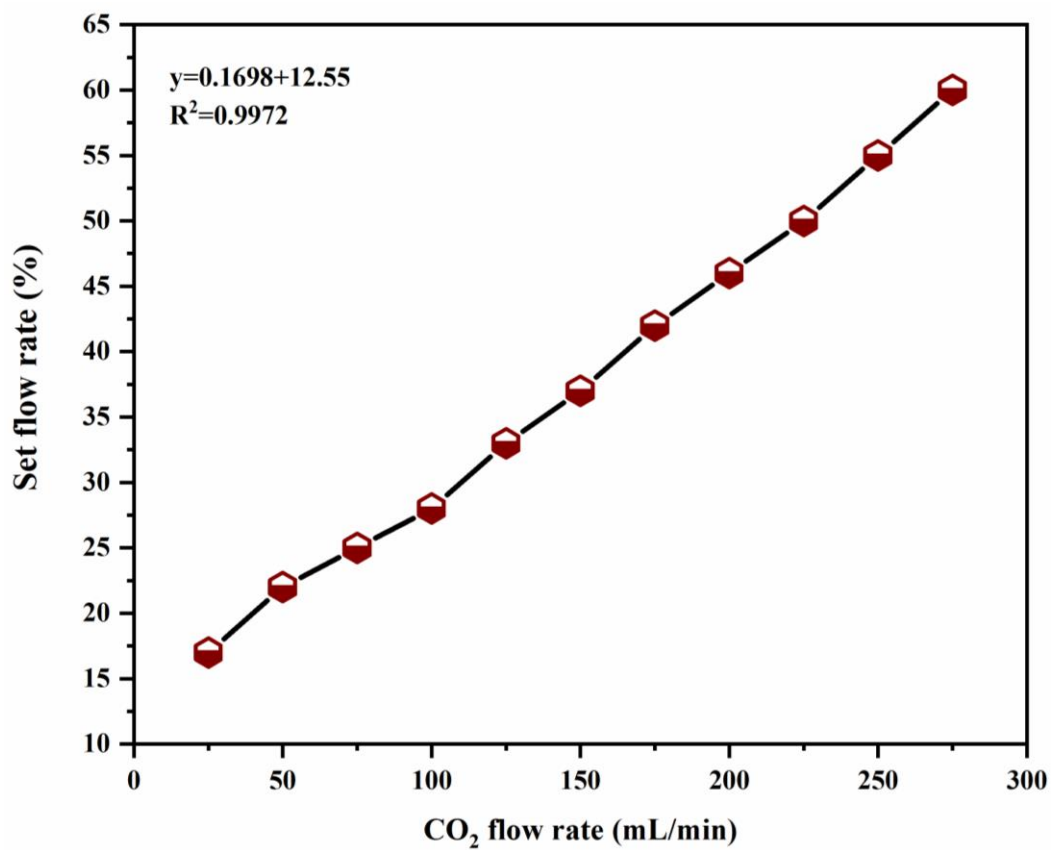


**Figure B.3:** Calibration data for CO<sub>2</sub> mass flow controller used in the CO<sub>2</sub> activation set up.

**Appendix C: CO<sub>2</sub> calibration curve and GC calibration curves for CO<sub>2</sub> adsorption experiment in Chapters 3-6**

GC calibration Date on October 22, 2020, is shown in Table C.1 and Table C.2.

**Table C.1:** Composition of standard gas used for GC calibration

0.330	1	1	9.92500e-1	19.83098	5.00480e-2	He
		2	3.97000	64.37440	6.16705e-2	
		3	7.94000	113.60070	6.98939e-2	
0.360	1	1	2.49250	83.10397	2.99925e-2	H <sub>2</sub>
		2	9.97000	256.94131	3.88026e-2	
		3	19.94000	438.80035	4.54421e-2	
0.406	2	1	1.75000	15.17665	1.15309e-1	CO <sub>2</sub>
		2	7.00000	50.32441	1.39098e-1	
		3	14.00000	90.91829	1.53984e-1	
0.429	2	1	7.72500e-1	6.88850	1.12143e-1	Ethylene
		2	3.09000	22.71481	1.36035e-1	
		3	6.18000	40.95055	1.50914e-1	
0.448	2	1	1.26000e-1	1.17740	1.07015e-1	Ethane
		2	5.03000e-1	3.87098	1.29941e-1	
		3	1.00600	6.93043	1.45157e-1	
0.481	2	1	1.28000e-1	9.25400e-1	1.38319e-1	Acetylene
		2	5.13000e-1	3.04803	1.68305e-1	
		3	1.02600	5.50436	1.86398e-1	
0.481	1	1	5.00000e-1	1.72535	2.89796e-1	O <sub>2</sub>
		2	2.00000	5.75504	3.47522e-1	

**Table C.2:** Composition of standard gas used for GC calibration

Component	Certified concentrations (molar concentration%)	Analytical accuracy
Acetylene	0.513	±2%
Carbon dioxide	7.00	±2%
Carbon monoxide	8.05	±2%
Ethane	0.503	±2%
Ethylene	3.09	±2%
Helium	3.97	±2%
Hydrogen	9.97	±2%
Methane	6.01	±2%
Oxygen	2.00	±2%
Propane	0.709	±2%
Propylene	0.504	±2%
Nitrogen	Balance	
Part Number	NI AC5000X14CAS	

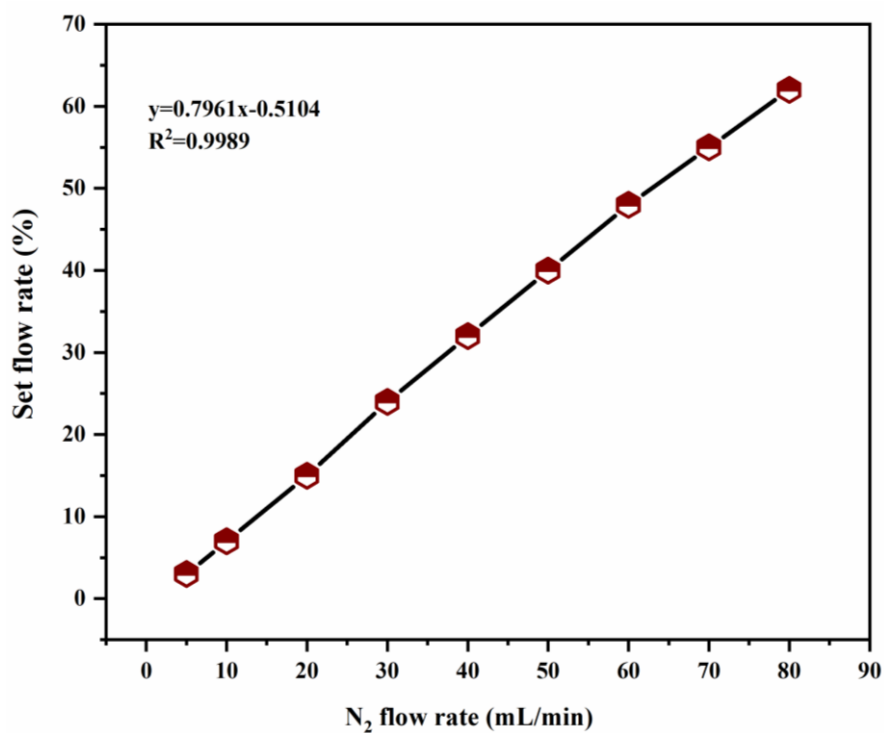


**Figure C.1:** Calibration data for N<sub>2</sub> mass flow controller used in the CO<sub>2</sub> capture set-up.

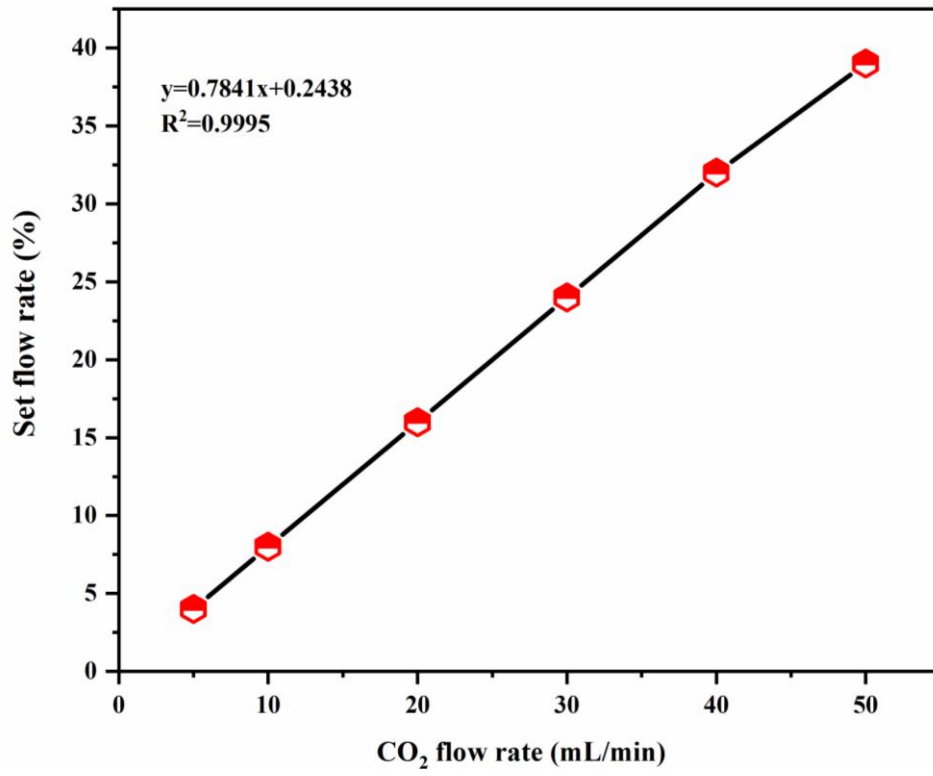


**Figure C.2:** Calibration data for CO<sub>2</sub> mass flow controller used in the CO<sub>2</sub> capture set-up.

## Appendix D Additional data for Aspen Plus simulation used in Chapter 4

C fact is the factor to convert the ultimate analysis to

C a wet basis

C NB! water is the %moisture on a wet basis, but all the other

C Components are on a dry basis.

fact = (100-water)/100

H<sub>2</sub>O = water/100

Ash = ult(1) / 100 \* fact

Carb = ult(2) / 100 \* fact

H<sub>2</sub> = ult(3) / 100 \* fact

An<sub>2</sub> = ult(4) / 100 \* fact

Cl<sub>2</sub> = ult(5) / 100 \* fact

Sulf = ult(6) / 100 \* fact

O<sub>2</sub> = ult(7) / 100 \* fact

WRITE (NTERM, 100) fact

100 FORMAT ("Conversion Factor", 4f10.2)

C Changing ash to include some unburned carbon

C Calculating the total masses leaving as carbon and ash (slag)

unbc = (1-maxcc) \* carb

carb = carb - unbc

ash = ash + unbc

C Calculating the composition of the ash (slag)

C For proximate and ultimate analysis...

C Fixed carbon:

IF (ash .GT. 0) THEN

proxfc = unbc/ash\*100

ELSE

proxfc = 100

END IF

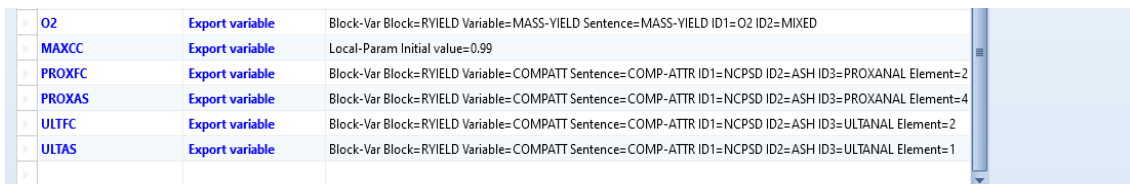
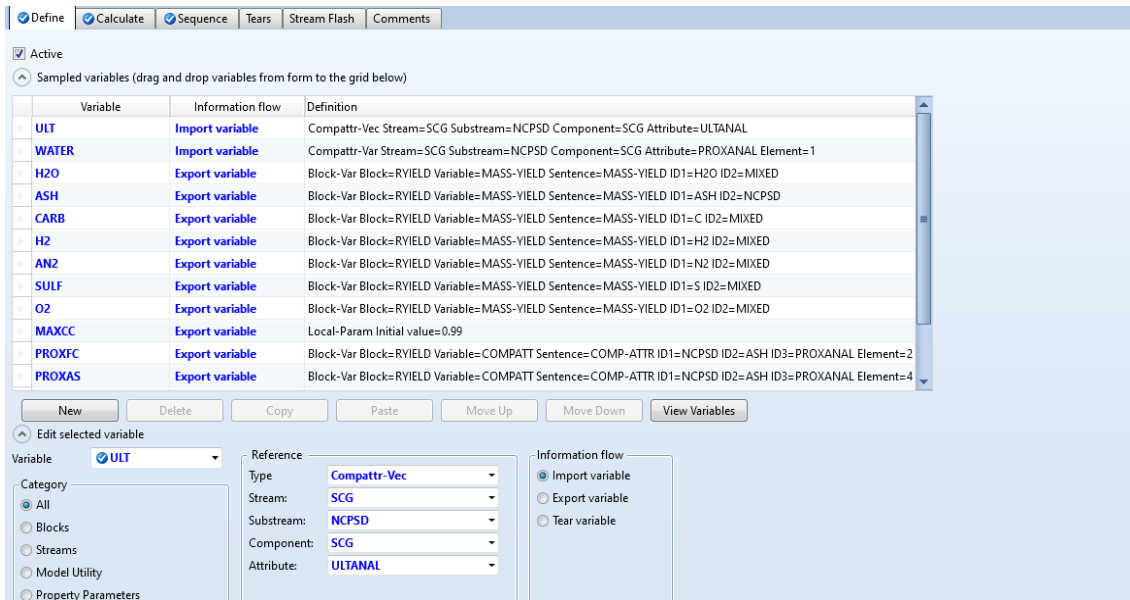
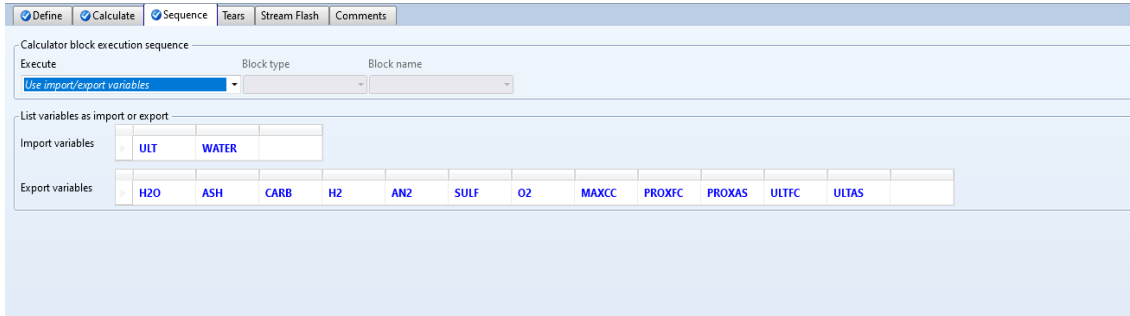


ultfc = proxfc

C Ash (as component of total ash mass):

proxas = 100 - proxfc

ultas = proxas



## Appendix E Additional data for Matlab code for kinetics used in Chapter 5

```
function d = backward(y,x,p)
% backward
%
% Calculates derivative d of vector y at point x(p) using backward difference
% approximation.
%
% y = vector containing function values
% x = vector containing increments
% p = point number where to calculate
% d = derivative of y at point p
d = (y(p)-y(p-1))/(x(p)-x(p-1));
end
```

### Forward

```
function d = forward(y,x,p)
% forward
%
% Calculates derivative d of vector y at point x(p) using forward difference
% approximation.
%
% y = vector containing function values
% x = vector containing increments
% p = point number where to calculate
% d = derivative of y at point p
d = (y(p+1)-y(p))/(x(p+1)-x(p));
end
```

### Central

```
function d = central(y,x,p)
% central
%
```

```

% Calculates derivative d of vector y at point x(p) using central difference
% approximation.
%
% y = vector containing function values
% x = vector containing increments
% p = point number where to calculate
% d = derivative of y at point p
d = (y(p+1)-y(p-1))/(x(p+1)-x(p-1));
end

derivative
function d = derivative(y,x)
% Numerically estimates the first derivative of a vector, using forward difference
% for first point, backward difference for last point, and central difference for
% all intermediate points.
y = [0 0.100129771 0.20021374 0.300002776 0.400564192 0.5003644
      0.600290146 0.700220125 0.80006211 0.900054545];
x = [443.6511 551.6034 574.0014 590.7209 605.9316 625.49 686.1234
      753.3851 833.364 951.7553
];
% d = derivative(y, x)
%
% where
% y = input vector containing function values
% x = input vector containing argument increments
% returns
% d = Numerical derivative of y. All vectors have the same length
d(1) = forward(y, x, 1);
for n = 2:size(y,2)-1
d(n) = central(y, x, n);
end
d(size(y,2)) = backward(y, x, size(y,2));
end

```

## Appendix F Additional data for Aspen plus simulation used in Chapter 8

Definition of feedstock using calculator block

- c fact is the factor to convert the ultimate analysis to
- c a wet basis
  
- c NB! water is the %moisture on a wet basis, but all the other
- c components are on a dry basis.

$$\text{fact} = (100 - \text{water}) / 100$$

$$\text{h2o} = \text{water} / 100$$

$$\text{ash} = \text{ult}(1) / 100 * \text{fact}$$

$$\text{carb} = \text{ult}(2) / 100 * \text{fact}$$

$$\text{h2} = \text{ult}(3) / 100 * \text{fact}$$

$$\text{an2} = \text{ult}(4) / 100 * \text{fact}$$

$$\text{cl2} = \text{ult}(5) / 100 * \text{fact}$$

$$\text{sulf} = \text{ult}(6) / 100 * \text{fact}$$

$$\text{o2} = \text{ult}(7) / 100 * \text{fact}$$

WRITE (NTERM, 100) fact

100 FORMAT ("Conversion Factor",4f10.2)

- c Changing ash to include some unburned carbon
  
- C Calculating the total masses leaving as carbon and ash (slag)
  - $\text{unbc} = (1 - \text{maxcc}) * \text{carb}$
  - $\text{carb} = \text{carb} - \text{unbc}$
  - $\text{ash} = \text{ash} + \text{unbc}$
  
- C Calculating the composition of the ash (slag)
- C For proximate and ultimate analysis
- C Fixed carbon:

```
IF (ash .GT. 0) THEN
  proxfc = unbc/ash*100
```

```
ELSE
```

```
  proxfc = 100
```

```
END IF
```

```
ultfc = proxfc
```

C Ash (as component of total ash mass):

```
proxas = 100 - proxfc
```

```
ultas = proxas
```

## Design specification

The screenshot shows the 'Define' tab of a software interface. At the top, there are tabs for 'Define', 'Spec', 'Vary', 'Fortran', 'Declarations', 'EO Options', and 'Comments'. Below the tabs, there is a section for 'Active' variables. A table lists the variable 'ACTC' with the definition 'Mass-Flow Stream=AP Substream=MIXED Component=C Units=kg/hr'. Below the table are buttons for 'New', 'Delete', 'Copy', 'Paste', 'Move Up', 'Move Down', and 'View Variables'. The 'Edit selected variable' section shows the variable 'ACTC' selected. On the left, there are radio buttons for 'Category' with options: 'All', 'Blocks', 'Streams' (selected), 'Model Utility', 'Property Parameters', and 'Reactions'. On the right, there are dropdown menus for 'Reference' with options: 'Type: Mass-Flow', 'Stream: AP', 'Substream: MIXED', 'Component: C', and 'Units: kg/hr'. At the bottom, there is an 'EO input' section with fields for 'Open variable' and 'Description'.

The screenshot shows the 'Spec' tab of the same software interface. At the top, there are tabs for 'Define', 'Spec', 'Vary', 'Fortran', 'Declarations', 'EO Options', and 'Comments'. Below the tabs, there is a section for 'Design specification expressions'. A table lists the variable 'ACTC' with the following values: 'Spec: ACTC', 'Target: 6584.13', and 'Tolerance: 0.1'.

<input checked="" type="checkbox"/> Define	<input checked="" type="checkbox"/> Spec	<input checked="" type="checkbox"/> Vary	Fortran	Declarations	EO Options	Comments
--	--	--	---------	--------------	------------	----------

**Manipulated variable**

Type: **Stream-Var**

Stream: **CO2**

Substream: **MIXED**

Variable: **MASS-FLOW**

Units: **kg/hr**

**Manipulated variable limits**

Lower: **500**

Upper: **700**

Step size:

Maximum step size:

**Report labels**

Line 1	Line 2	Line 3	Line 4
<input type="text"/>	<input type="text"/>	<input type="text"/>	<input type="text"/>

**EO input**

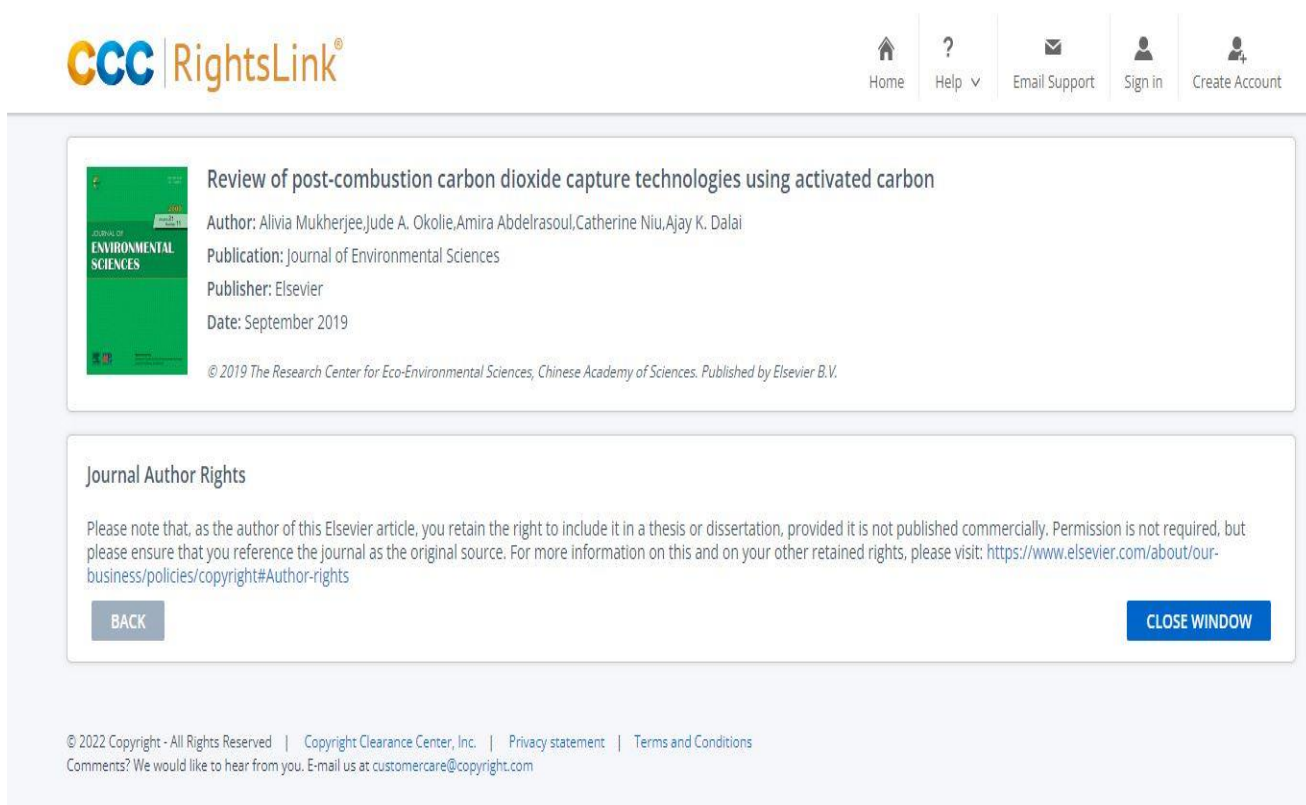
Open variable:

Description:

## APPENDIX G: Permission to use Review and Research Articles

1. Permission to use the following published manuscript entitled “**Mukherjee, A., Okolie, J. A., Abdelrasoul, A., Niu, C., & Dalai, A.K., (2019). Review of post-combustion carbon dioxide capture technologies using activated carbon. Journal of Environmental Sciences, 83, pp.46-63**”.

<https://doi.org/10.1016/j.jes.2019.03.014>



The screenshot displays the CCC RightsLink interface. At the top left is the CCC RightsLink logo. On the top right, there are navigation links: Home, Help, Email Support, Sign in, and Create Account. The main content area features a green cover image of the 'Journal of Environmental Sciences' on the left. To its right, the article title 'Review of post-combustion carbon dioxide capture technologies using activated carbon' is displayed. Below the title, the author list 'Author: Alivia Mukherjee, Jude A. Okolie, Amira Abdelrasoul, Catherine Niu, Ajay K. Dalai' is shown, followed by 'Publication: Journal of Environmental Sciences', 'Publisher: Elsevier', and 'Date: September 2019'. A copyright notice at the bottom of this section reads: '© 2019 The Research Center for Eco-Environmental Sciences, Chinese Academy of Sciences. Published by Elsevier B.V.'. Below this, a section titled 'Journal Author Rights' contains a paragraph of text: 'Please note that, as the author of this Elsevier article, you retain the right to include it in a thesis or dissertation, provided it is not published commercially. Permission is not required, but please ensure that you reference the journal as the original source. For more information on this and on your other retained rights, please visit: <https://www.elsevier.com/about/our-business/policies/copyright#Author-rights>'. At the bottom of this section are two buttons: 'BACK' and 'CLOSE WINDOW'. The footer of the page contains copyright information: '© 2022 Copyright - All Rights Reserved | Copyright Clearance Center, Inc. | Privacy statement | Terms and Conditions' and a contact note: 'Comments? We would like to hear from you. E-mail us at [customer-care@copyright.com](mailto:customer-care@copyright.com)'.

**Figure G.1:** Permission to use the published paper “Review of post-combustion carbon dioxide capture technologies using activated carbon.”

2. Permission to use the following published manuscript entitled “**Mukherjee, A., Okolie, J. A, Niu, C, Dalai, A.K., (2021). Experimental and Modeling Studies of Torrefaction of Spent Coffee Grounds and Coffee Husk: Effects on Surface Chemistry and Carbon Dioxide Capture Performance. ACS Omega, 7(1), pp. 638-653**”.
- <https://doi.org/10.1021/acsomega.1c05270>

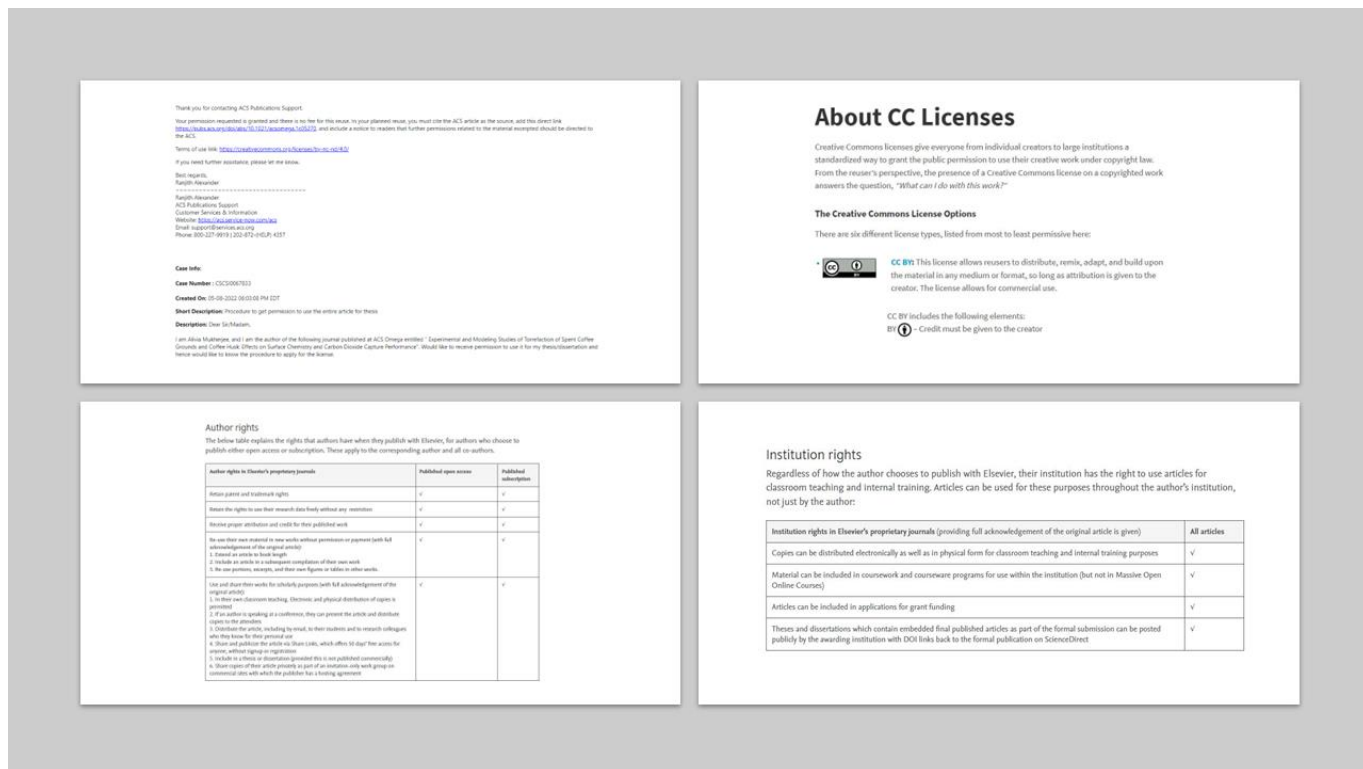



**Figure G.2:** Permission to use the published paper “Experimental and Modeling Studies of Torrefaction of Spent Coffee Grounds and Coffee Husk: Effects on Surface Chemistry and Carbon Dioxide Capture Performance.”



3. Permission to use the following published manuscript entitled “**Mukherjee, A, Okolie, J. A, Tyagi, R, Niu, C, Dalai, A.K., (2021).** Pyrolysis kinetics and thermodynamic activation parameters of exhausted coffee residue and coffee husk using thermogravimetric analysis. *The Canadian Journal of Chemical Engineering*, 99(8), pp. 1683-1695”.

<https://doi.org/10.1002/cjce.24037>



**Pyrolysis kinetics and activation thermodynamic parameters of exhausted coffee residue and coffee husk using thermogravimetric analysis**

Author: Alivia Mukherjee, Jude A. Okolie, Ramani Tyagi, et al

Publication: Canadian Journal of Chemical Engineering

Publisher: John Wiley and Sons

Date: Mar 21, 2021

© 2021 Canadian Society for Chemical Engineering

**Order Completed**

Thank you for your order.

This Agreement between Ms. Alivia Mukherjee ("You") and John Wiley and Sons ("John Wiley and Sons") consists of your license details and the terms and conditions provided by John Wiley and Sons and Copyright Clearance Center.

Your confirmation email will contain your order number for future reference.

License Number	5320320142847	<a href="#">Printable Details</a>
License date	Jun 01, 2022	

Licensed Content	Order Details	
Licensed Content Publisher	John Wiley and Sons	
Licensed Content Publication	Canadian Journal of Chemical Engineering	
Licensed Content Title	Pyrolysis kinetics and activation thermodynamic parameters of exhausted coffee residue and coffee husk using thermogravimetric analysis	
Licensed Content Author	Alivia Mukherjee, Jude A. Okolie, Ramani Tyagi, et al	
Licensed Content Date	Mar 21, 2021	
	Type of use	Dissertation/Thesis
	Requestor type	Author of this Wiley article
	Format	Print and electronic
	Portion	Full article
	Will you be translating?	No

**Figure G.3:** Permission to use the published paper “Pyrolysis kinetics and activation thermodynamic parameters of exhausted coffee residue and coffee husk using thermogravimetric analysis.”

4. Permission to use the following published manuscript entitled “**Mukherjee, A., Borugadda, V. B., Dynes, J. J., Niu, C., & Dalai, A.K., (2021). Carbon dioxide capture from flue gas in biochar produced from spent coffee grounds: Effects of surface chemistry and porous structure, Journal of Environmental Chemical Engineering, 5(9), p. 106049.**”

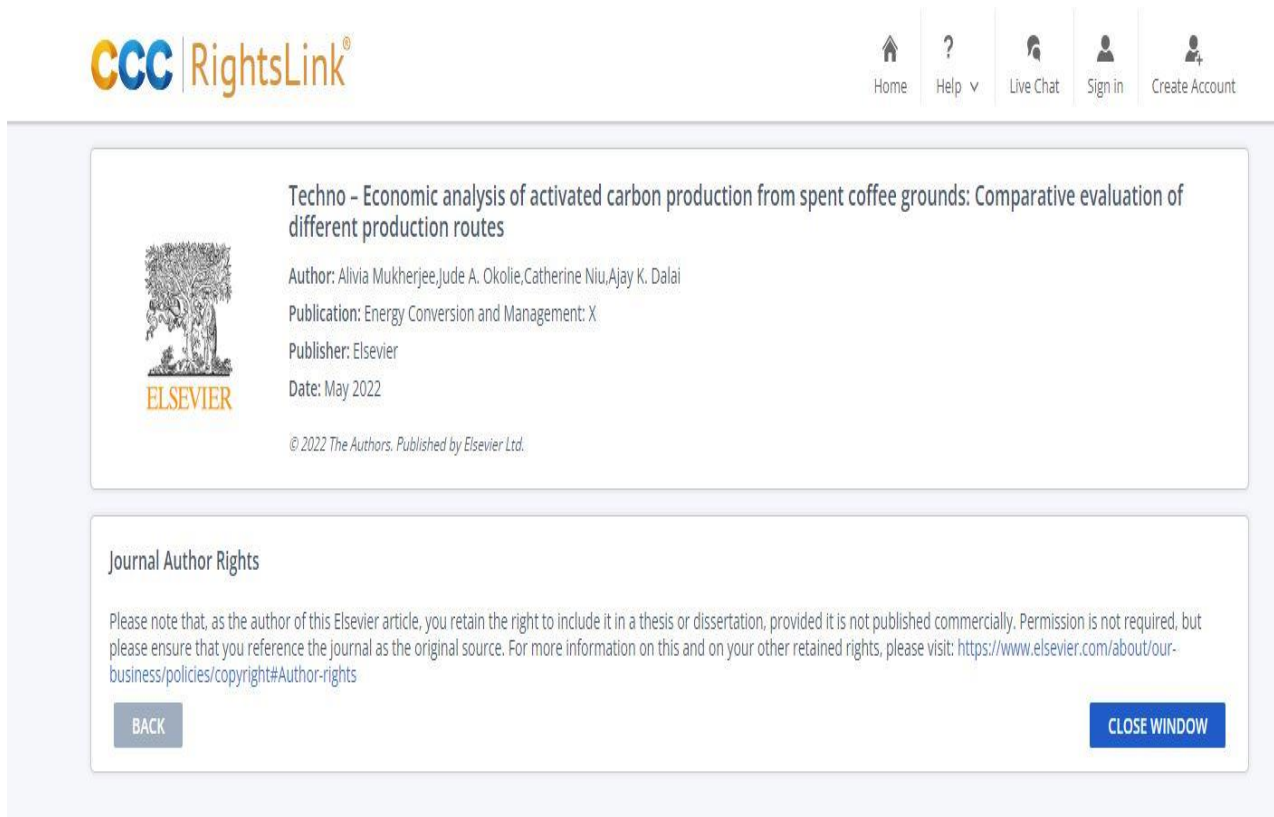
<https://doi.org/10.1016/j.jece.2021.106049>

The screenshot displays the CCC RightsLink interface. At the top left is the logo for CCC RightsLink. On the top right, there are navigation links: Home, Help, Email Support, Sign In, and Create Account. The main content area is divided into two sections. The first section, titled "Carbon dioxide capture from flue gas in biochar produced from spent coffee grounds: Effect of surface chemistry and porous structure", includes the Elsevier logo, author names (Alivia Mukherjee, Venu Babu Borugadda, James J. Dynes, Catherine Niu, Ajay K. Dalai), publication title (Journal of Environmental Chemical Engineering), publisher (Elsevier), and date (October 2021). Below this is a copyright notice: "© 2021 Elsevier Ltd. All rights reserved." The second section, titled "Journal Author Rights", contains a paragraph of text explaining that authors retain the right to include their work in a thesis or dissertation, provided it is not published commercially. It also includes a link to the Elsevier copyright policy page. At the bottom of this section are two buttons: "BACK" and "CLOSE WINDOW". At the very bottom of the page, there is a footer with copyright information and contact details for the Copyright Clearance Center, Inc.

**Figure G.4:** Permission to use the published paper “Carbon dioxide capture from flue gas in biochar produced from spent coffee grounds: Effects of surface chemistry and porous structure.”

5. Permission to use the following published manuscript entitled “**Mukherjee, A., Okolie, J.A., Niu, C., & Dalai, A.K., (2022).** Techno-Economic Analysis of activated carbon production from spent coffee grounds: Comparative evaluation of different production routes, *Energy Conversion and Management: X*, volume (14), pp. 100218.”

<https://doi.org/10.1016/j.ecmx.2022.100218>



The screenshot displays the CCC RightsLink interface. At the top left is the logo for CCC RightsLink. On the top right, there are navigation links: Home, Help, Live Chat, Sign in, and Create Account. The main content area is divided into two sections. The first section, titled "Techno - Economic analysis of activated carbon production from spent coffee grounds: Comparative evaluation of different production routes", includes the Elsevier logo, the author list (Alivia Mukherjee, Jude A. Okolie, Catherine Niu, Ajay K. Dalai), the publication name (Energy Conversion and Management: X), the publisher (Elsevier), and the date (May 2022). Below this is a copyright notice: "© 2022 The Authors. Published by Elsevier Ltd." The second section, titled "Journal Author Rights", contains a paragraph of text explaining that authors retain the right to include their work in a thesis or dissertation, provided it is not published commercially. It also provides a URL for more information: <https://www.elsevier.com/about/our-business/policies/copyright#Author-rights>. At the bottom of this section are two buttons: "BACK" and "CLOSE WINDOW".

**Figure G.5:** Permission to use the published paper “Techno-Economic Analysis of activated carbon production from spent coffee grounds: Comparative evaluation of different production routes.”